UNIVERSITEIT
GENT

Feasibility of acoustic neutrino detection in ice with the South Pole Acoustic Test Setup

Freija Descamps

Feasibility of acoustic neutrino detection in ice with the South Pole Acoustic Test Setup

Haalbaarheid van akoestische detectie van neutrino's in ijs met "The South Pole Acoustic Test Setup"

Freija Descamps

Promotor: Prof. Dr. Dirk Ryckbosch

For my mum and dad

Contents

List of Figures

List of Tables

Introduction

Once upon a time, probably over 13 billion years ago [1], there was no Universe and no time. At least, not as we define them today. Indeed, there is experimental evidence indicating that the Universe is currently expanding and that it finds its origin at a finite time in the past. This point in time, t_0, has been named "the Big Bang". It is the primordial hot and dense phase from which all that surrounds us originates. Over a long period of time after the Big Bang, the slightly denser regions of the nearly uniformly distributed matter formed gas clouds, stars, galaxies, and the other astronomical structures observable at the present time.

The Universe today is a very vast and ancient place compared to our Earth and history. As an illustration, let us assume that the whole of the Universe's lifetime is compressed in one year, with the Big Bang happening at midnight on the 1st of January. The present time is 12 pm on the 31st of December, exactly one year later. In this compressed timescale, our solar system would have been born in the second week of September, the early Homo Sapiens would have appeared around 11:50 pm on the 31st December and the recorded human history would have started about 21 seconds ago. The average human lifespan on that timescale is about 0.15 s. It is therefore easy to overlook, given this comparatively short span of human history and life, the fact that the Universe is a dynamic place. Indeed, all matter that surrounds us and all the stars and other astrophysical objects that we observe have a finite age. Stars are born and die violent deaths, galaxies collide and distant objects are moving away from us at high speeds.

Mankind has always been fascinated, and puzzled, by objects and events in the sky above. At first, all astronomical knowledge was solely based on naked-eye (later aided by optical instruments) observations of the light emitted by astrophysical objects (like stars) that reaches Earth. The Chinese, Egyptian, and Babylonian ancient cultures already had formal systems and theories that classified and explained their astronomical observations. For example, the Maya astronomical calendars include detailed tables to predict phases of the Moon and the cycles of eclipses. Chinese astronomers took careful note of the appearance in the sky of so-called guest stars. The supernova (exploding star) that created the Crab Nebula in the year 1054 (about 2.8 s ago on our compressed timescale) is an example of such a guest star.

Late in the 19th century, the discovery of X-Rays, γ rays, radio waves, microwaves, ultraviolet radiation, and infrared radiation had a big impact on astronomy, spawning the fields of infrared astronomy, radio astronomy, x-ray astronomy and finally gamma-ray astronomy. Soon afterwards, in the early 1910s, with the discovery of the particles (cosmic rays) that reach Earth from interstellar space, the field of astroparticle physics saw the light, opening an entirely new window on the Universe. Indeed, not only photons can be observed and used to investigate astrophysical objects, but also charged particles, neutrinos and other neutral particles.

Nowadays, astroparticle physics is often defined as an interdisciplinary field lying between particle physics, astronomy and cosmology. It studies elementary particles of astronomical origin, and their relation to astrophysics and cosmology, to reveal the nature and structure of matter in the Universe. Current experiments in astroparticle physics span almost the whole spectrum of charged and neutral cosmic rays (γ rays included). They make use of the detection of all these types of astrophysical messengers in order to learn about the sources of cosmic rays, the nature of the particles, as well as the properties of the interstellar medium.

The neutrino is one of these messengers. Its existence was first postulated by W. Pauli in 1930

1

when he proposed the idea of neutrinos as the particles that carry away the missing energy in the beta decay experiments. Over twenty years later, in 1956, F. Reines and C. L. Cowan finally succeeded in detecting neutrinos produced by the Savannah River Reactor in South Carolina [2]. This delay between postulation and confirmation illustrates the elusive nature of this elementary particle. It interacts only very rarely with matter and therefore, the observation of neutrino interactions requires large detector masses.

Nuclear reactions in stars and supernova explosions produce copious amounts of neutrinos. These low energy ($< 100\,\mathrm{MeV}$) neutrinos have large fluxes and can therefore be detected in statistically significant numbers by detectors consisting of man-built tanks filled with a liquid medium. The first extra-terrestrial neutrinos, originating from the Sun, were observed at the Homestake neutrino detector in 1968 [3]. The motivation for the Homestake experiment was to use the solar neutrinos to look into the interior of the Sun and thus test the theory of stellar evolution and the nuclear processes in stars. Indeed, solar neutrinos can leave the core without interacting[1].

The only other detected source of astrophysical neutrinos is the supernova SN1987A (in 1987) from which a burst of neutrinos (the actual combined neutrino count was about 24) was observed at three separate neutrino observatories. The field of solar (low energy) neutrino astrophysics is very active today. At the same time, the interest of neutrino astrophysics has also moved beyond our local neighbourhood, aiming to detect high energy neutrinos ($> 10^{12}\,\mathrm{eV}$) from distant astrophysical sources. The predicted ultra-high-energy (UHE) neutrino fluxes from both hadronic processes in these cosmic sources and interaction of high energy cosmic rays with the cosmic microwave background radiation are very low. Therefore much larger detector volumes are needed in order to detect a significant amount of these neutrinos. To this end, naturally available resources are often used as detector medium, like the oceans or the Antarctic ice sheet. The density of detectors in such UHE neutrino telescopes is dictated by the attenuation length of the observable signal that is generated by the neutrino interaction with the medium. The optically transparent ice at the geographic South Pole has optical attenuation lengths in the order of $100\,\mathrm{m}$. This has allowed the construction and operation of a kilometer-scale detector which has maximum sensitivity to ν_μ-induced muons from below with energies in the TeV to PeV range.

However, the optical attenuation length and therefore detector cost is prohibitive to a possible extension towards the even larger detector volumes that are needed to detect the astrophysical neutrinos of the highest energies. Both the attenuation length of radio and acoustic waves are predicted to be larger than $1\,\mathrm{km}$ in ice and both signatures are generated in an UHE neutrino interaction. Hence, this interaction in ice could be detected by an hybrid detector array consisting of optical, radio and acoustic sensors.

Still, the observation of UHE neutrino fluxes presents a considerable experimental challenge as there is no calibrated signal, or "test beam", at these energies and the fluxes are expected to be very low. The power of the hybrid idea lies in the "golden events": neutrino interactions that are detected by two or more different detection techniques. These coincident detections could serve as a cross-calibration opportunity and allow to investigate systematics.

Several experiments already have investigated the detection possibilities of the radio waves emitted by neutrino interaction in the South Polar ice. The aim of the presented work is to

---

[1] The light that we receive from the Sun also finds its origin in the solar core. However, it takes roughly a million years for a photon from the solar core to reach the surface. It therefore retains very little information about the solar nuclear processes due to diffuse radiation and transportation through convection.

investigate the feasibility of an acoustic neutrino detection array situated in the South Polar ice. To this end, the acoustic properties of the ice in the 1 to 100 kHz region were measured with a dedicated acoustic test setup: the South Pole Acoustic Test Setup (SPATS). This work will concentrate on the SPATS measurement of the acoustic attenuation length of the Antarctic ice. This is a fundamental quantity in determining the design and sensitivity of a future acoustic neutrino detector at South Pole.

First, Chapter 1 gives a short history and status of cosmic ray physics. Chapter 2 then introduces the theory behind acoustic neutrino detection: how does the neutrino interaction gives rise to an acoustic signature and what are the resulting signal properties? Experimental verifications, detection techniques and current acoustic neutrino detectors are presented. Subsequently, the SPATS hardware and performance is described in Chapter 3, followed by results of pre-deployment and calibration tests in Chapter 4. Chapter 5 presents inter-string data-taking and the attenuation length analysis with SPATS inter-string data. An overview of all current SPATS results is presented in Chapter 6. Finally, a discussion and outlook are presented in Chapter 7.

Motivation

This chapter gives a short history and status of cosmic ray physics, focussing on neutrino astrophysics. First, the different features in the cosmic ray spectrum and possible cosmic ray acceleration mechanisms are discussed. Subsequently, an overview of the possible astrophysical neutrino sources and limits on diffuse fluxes is given. Finally, neutrino interactions, corresponding detectable signatures and various neutrino detectors are introduced.

1.1 Cosmic rays

The discoveries of radioactivity by H. Becquerel in 1896 [4] and of the electron by J. J. Thomson in 1897 [5] are often considered as the launch of subatomic physics. The identification of the different types of radioactivity (α, β, γ) soon followed. From electroscope measurements it became clear that the air is spontaneously ionised by a highly penetrating radiation. In the quest to explain this effect, several measurements initially confirmed the Earth-radiation hypothesis: the number of ions per cubic metre decreases with increasing distance from Earth's surface. It was therefore widely accepted that this atmospheric electricity was caused only by radiation from radioactive elements in the ground.

This hypothesis was first challenged when T. Wulf measured in 1910 higher levels of radiation at the top of the Eiffel Tower than at its base [6]. Also A. Gockel [7, 8], who observed an enclosed electroscope in a balloon to a height of 4 km, reported that he found that the rate of electroscope discharge actually increased with altitude. In this context, further experiments with electroscopes in balloon flights in Austria (V. F. Hess [9, 10]) and Germany (W. Kohlhorster [11]) to a height of maximum 9 km confirmed in 1912 the existence of rays of very great penetrating power that are entering our atmosphere from above with equal intensity day or night. Hess initially assumed the rays found their origin in the atmosphere and called them "altitude radiation". These rays were renamed by R. A. Millikan in 1926, after proving their extra-terrestrial origin, as cosmic rays (CRs): charged particles that reach Earth from interstellar space. In 1936 Hess received the Nobel Prize for the discovery of cosmic rays.

In the present work, cosmic rays are defined as all extra-terrestrial particles arriving at Earth's atmosphere. This therefore also includes neutral particles like γ-rays and neutrinos.

1.1.1 The charged cosmic ray spectrum

Almost a century after Hess' balloon flight, the measured spectrum for charged cosmic rays spans over 28 orders of magnitude in flux and 13 orders of magnitude in energy (see Fig. 1.1). The flux decreases from more than 1000 particles per second and square meter at GeV[1] energies to about one particle per year and square meter at 1 PeV. Above 100 EeV, less than one particle per century and square kilometer is expected.

---

[1] 1 GeV=10^9 eV, 1 TeV=10^{12} eV, 1 PeV=10^{15} eV, 1 EeV=10^{18} eV, 1 ZeV=10^{21} eV
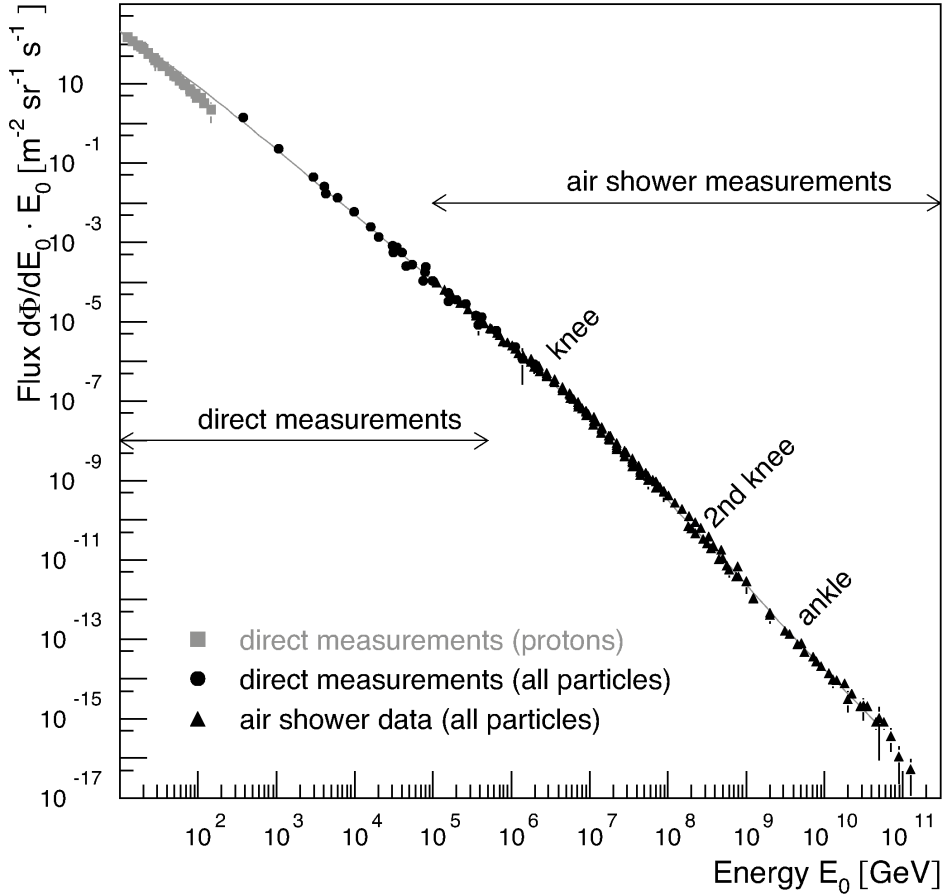
Figure 1.1: Energy spectrum of all charged cosmic rays as measured directly with detectors above the atmosphere and with air shower detectors. The flux of primary protons is shown separately at lower energies [12].

The world-data can be combined into an almost featureless power law spectrum following $\frac{dN}{dE} \sim E^{\gamma}$, where $\frac{dN}{dE}$ is the differential flux, γ is the spectral index and E is the particle energy. Its shape is an indication for non-thermal acceleration processes: the particles gain energy beyond the available thermal energy. This means that a charged CR particle must have been accelerated at the astrophysical source or on its way to Earth. It is a non-trivial exercise to formulate production models. Indeed, it is hard to imagine what mechanism can be responsible for, for example, the creation of the so-called "Oh-my-God"-particle: the most energetic CR ever observed (on October 15, 1991, the Fly's Eye detector observed a proton with an energy of $(3.2 \pm 0.9) \cdot 10^{20}$ eV) [13, 14]. What physical processes can generate these energetic particles?

Production mechanisms

There are two main types of charged CR production models. The so-called bottom-up models assume that the charged particle is accelerated from low to high energy. For example, in a Fermi acceleration [15] scenario, a charged particle will gain energy by being reflected by a magnetic mirror. Such an acceleration can take place at moving interstellar magnetised clouds. When a region of high field intensity moves towards, and collides with, a charged CR particle, the latter will gain energy[2]. The inverse is true for the case when a charged CR particle overtakes a region of high field intensity that is moving in the same direction. The probability of a head-on collision is greater than a head-tail collision. Therefore, the charged CR particles will, on average, be accelerated. This stochastic process is called second-order Fermi acceleration. A more efficient version of the Fermi acceleration (first-order Fermi acceleration) is proposed, for example, in [16]. In this model, charged particles are scattered across a shock front propagating through interstellar space, gaining energy at each crossing.

One simple acceleration criterion is the geometrical one: the CR should not leave the accelerator before it gains the required energy. If the charged particle is accelerated by the electric field and confined by the magnetic one, then the geometrical criterion is expressed in terms of the particle's Larmor radius r_L which should not exceed the linear size of the accelerator. When this Larmor radius of a charged CR particle exceeds the size of the acceleration region, it will no longer be magnetically confined. Acceleration up to higher energies then becomes impossible since the particle will leave the accelerator region. The "geometrical Hillas criterion" therefore gives an indication for the maximum energy $E_{\max}$ that can be acquired by a charged particle travelling in a medium with magnetic field $\mathcal{B}$ [17]:

$$E_{\max} \sim 2\beta c Z e \mathcal{B} r_L,\qquad(1.1)$$

where βc is the characteristic velocity of the scattering centres (shock fronts, magnetised clouds, etc.) and Z is the CR charge. Only the most violent astrophysical processes can possibly accelerate charged CR particles above 10^{20} eV, see Fig. 1.2.

The other main CR-production branch consists of the more exotic top-down models in which the (charged or neutral) particle is produced by decay of interaction of a particle with a higher energy. A number of such particle physics scenarios exist as explanations of the origin of ultra-high-energy (UHE) CRs. The basic idea is that very massive (GUT-scale[3]) unknown particles decay and generate the observed UHE CRs. In some models, the unknown particles themselves are remnants of the early Universe and have very long lifetimes, like for example magnetic monopoles [18]. Being superheavy, these particles would be gravitationally attracted to the Galaxy and to the Local SuperCluster (LSC, the irregular supercluster that contains the Local Group, which in turn contains the Milky Way and Andromeda galaxies), where their density could well exceed the average density in the Universe (see for example [19, 20]). In the Z-burst model, neutrinos of ultra high energy annihilate with cosmological neutrinos in our neighbourhood and generate bosons which decay into a local flux of nucleons, pions, photons and neutrinos [21].

After production, the CR flux propagates through interstellar space. During this diffusive process, the spectral index possibly changes. A certain fraction of CRs reaches Earth's atmosphere. The exact composition of the charged primary flux is dependent on which part of the

---

[2]As a tennis ball gains energy when colliding with a moving tennis racquet.

[3]The GUT-scale is the energy scale for the Grand Unified Theory (GUT), around 10^{14} GeV.
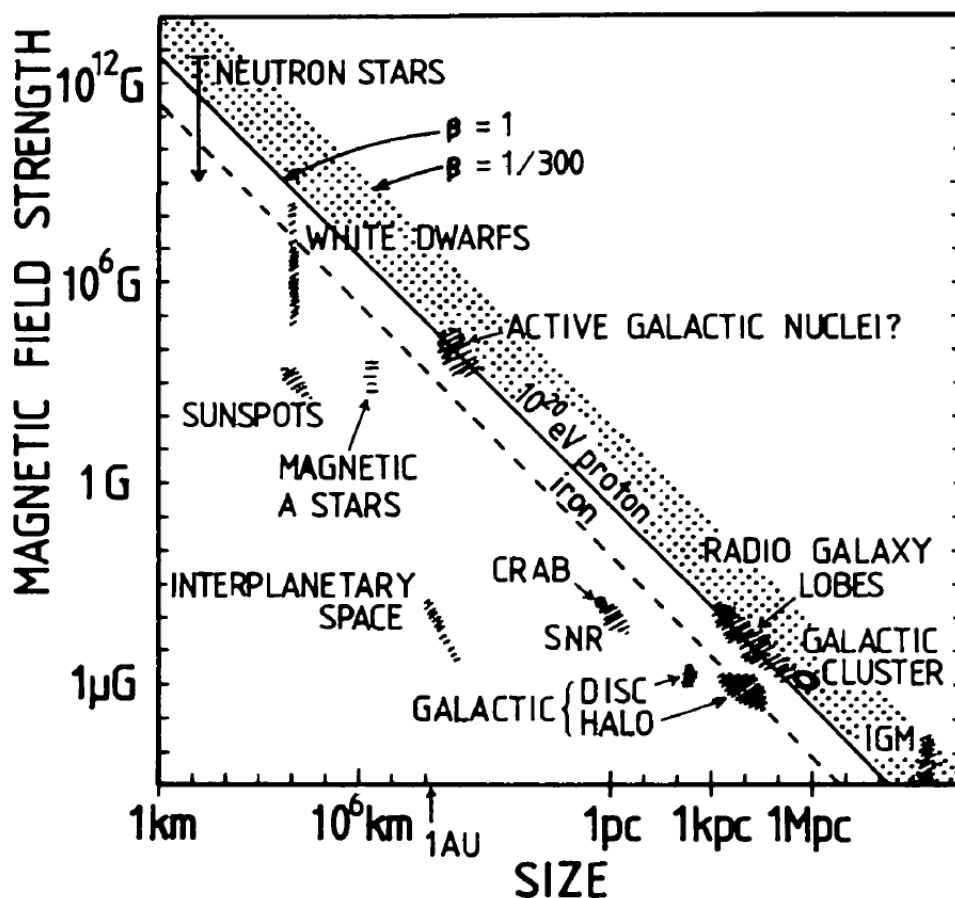
Figure 1.2: Size and magnetic field strength of possible astrophysical particle accelerators. Objects below the diagonal black line cannot accelerate protons to 10^{20} eV. IGM stands for Intra-Galactic Medium. Some of these astrophysical objects will be discussed in § 1.2.2, as they are also possible neutrino source candidates. Figure from [17].

energy spectrum is observed. However, in general, almost 90% of all the incoming charged cosmic rays are protons, about 9% are helium nuclei (α particles) and about 1% are heavier nuclei, electrons, positrons or antiprotons [22].

The spectrum transition regions

Measuring the true, or primary, charged cosmic ray spectrum and composition presents an experimental challenge. Indeed, the charged particles are sensitive to the presence of the Sun in our solar system. Both the magnetic field and the solar winds that carry it lead to effects that are visible for the less energetic cosmic rays below 10^{10} eV: the flux will be lower and the particles will lose energy. Once the particles are past the influence of the solar magnetic field and winds, they encounter the geomagnetic field. It bends their trajectories and makes the low-energy cosmic ray flux on top of the atmosphere non-isotropic. Subsequently, the primary cosmic rays interact with the atmosphere and produce cascades of particles, called Extensive Air Showers (EASs).

The properties of the EAS can be interpreted in terms of the energy spectrum and composition of the primary flux, heavily relying on particle interaction models and primary flux assumptions. It is clear that, ideally, one should detect the primary charged cosmic ray before it enters the solar system. The next best thing is to account for solar modulation at low energy and detect the primaries at the top of the atmosphere using balloons or satellites. In this case, particle identification, energy and direction reconstruction is relatively easy. For the high-energy CRs that have a much lower flux, ground based experiments observe the EASs created by CRs in the atmosphere.

The observed spectrum has three clear transition regions where the spectral index (γ) changes. γ goes from –2.7 to –3.1 for primary energies (E_p) from 10^{15} to 10^{16} eV, this region is called the "knee". A possible (no consensus exists) further steepening, also called the "second knee", occurs around $4 \cdot 10^{17}$ eV. At the location of the "ankle" between 10^{18} and 10^{19} eV, γ goes back to –2.7 (see Fig. 1.1).

- **Below the knee: $E_p < 10^{15}$ eV**
  The flux of the CR primaries below 10^{15} eV is typically large enough so that sufficient statistics can be accumulated with relatively small experimental setups deployed above or in the upper layers of the atmosphere. Stratospheric[4] balloons and satellite-based experiments have established the CR composition in the low energy region. The main proposed acceleration mechanism responsible for the acceleration of these particles is first-order Fermi acceleration at the shock fronts of galactic Supernova Remnants (SNRs) which typically predicts an initial spectral index at source of $\gamma \sim$–2. The difference with the spectral index of the measured spectrum at Earth can possibly be explained by leaky-box and re-acceleration models [23, 24]. These models assume that the charged particles are confined by the galactic magnetic fields. During propagation high energy particles have a higher chance of escaping the galaxy, thus steepening the CR spectrum to the spectral index that is observed at Earth's atmosphere.

- **From the knee to the ankle: 10^{15} eV$< E_p < 10^{19}$ eV**
  The cause for the change of the spectral index at the knee is an open question and different models have been proposed to explain this feature of the spectrum; for an overview see for example [12]. There is an indication in recent experimental data that the knee in the charged particle spectrum is caused by a suppression of the flux of light elements: the mean mass of the CRs increases in this region. It is therefore suggested that the knee marks the end of the acceleration from galactic SNRs due to the finite lifetime of the shock fronts. This limits the maximum achievable energy for particles with charge Z to $E_{max} \sim Z \cdot (0.1-5)$ PeV, which depends upon the assumed SNR properties such as magnetic field strength, available energy and ambient medium. It has even been suggested that the CR spectrum in the knee-region is dominated by the contribution of a single source [25]. The more exotic theories about the origin of the knee, such as interaction of CRs with massive neutrinos or dense photon fields are disfavoured by observations [12].
  The classic SNR models have difficulties explaining the CR flux above $\sim 10^{16}$ eV, therefore more exotic astrophysical objects, like SNR hosting rotating neutron stars, are proposed as possible CR accelerators beyond the knee. Still, the maximum energy in this type of

---

[4]The stratosphere is situated between about 10 km and 50 km altitude above the surface at moderate latitudes. At the poles it starts at about 8 km altitude.
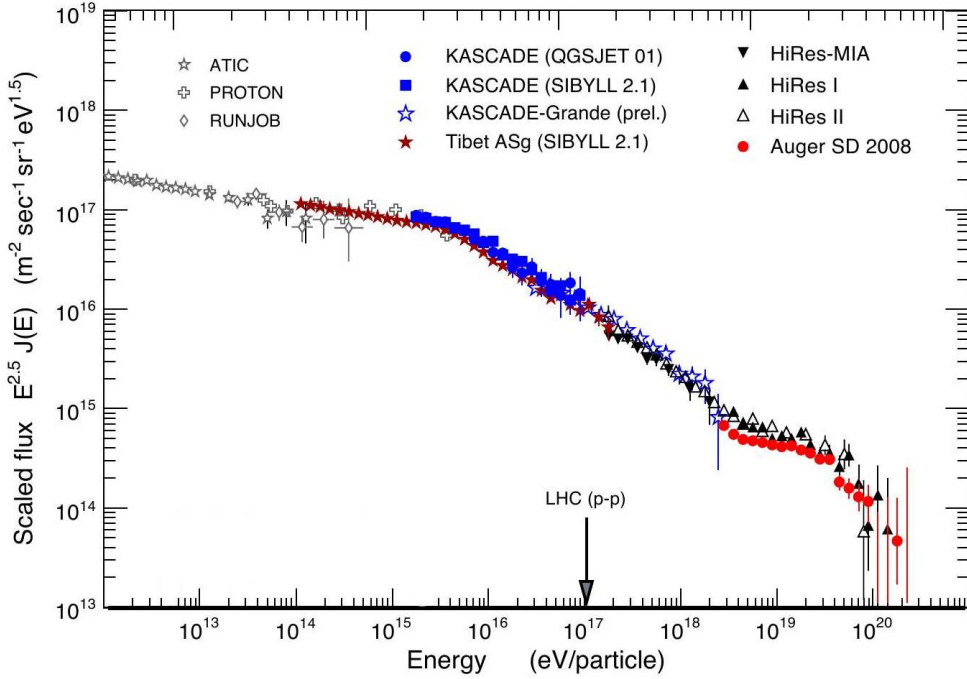
(a)
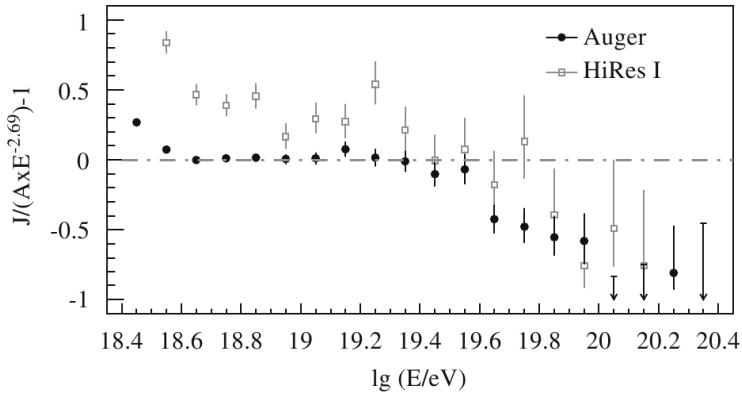
(b)

Figure 1.3: (a): Charged particle CR spectrum scaled by $E^{2.5}$ as obtained by direct measurements above the atmosphere (ATIC, PROTON and RUNJOB) as well as results from air shower experiments (Tibet ASγ, KASCADE, Akeno). The measurements at very high energies are represented by HiRes and the Pierre Auger Observatory (PAO). Figure from [12], see also this reference for data-references. (b): The fractional differences between PAO and HiRes I data [26] compared to a spectrum with a spectral index of −2.69. From [27].

model typically does not exceed $\sim 10^{19}$ eV [28].

- **Above the ankle: $E_p > 10^{19}$ eV**

  Figure 1.3(a) shows the observational data for the high-energy cosmic ray spectrum. The flattening of the cosmic ray spectrum above $\sim 10^{19}$ eV might be associated with the appearance of a contribution of an extra-galactic component [29]; this is usually referred to as the ankle model. This model is attractive since it does not require fine-tuning of fluxes: the flatter extra-galactic flux crosses the steep galactic spectrum at the ankle. On top of that, the spectral index for this flux (γ=–2 to –2.5) is not in contradiction with the predicted spectral index for Fermi acceleration. The observed dip at $1 \cdot 10^{18} \leq E \leq 4 \cdot 10^{19}$ eV is explained in the ankle model as the natural structure in a two-component spectrum. This model, however, requires a galactic and iron-dominated component in the cosmic ray spectrum that extends above $\sim 10^{19}$ eV which currently does not fit the data very well.

  Another model, the pair-production dip-model assumes CRs in the $(10^{18}$–$10^{19})$ eV energy region to be already mainly extra-galactic. The transition between the galactic and extra-galactic components is then marked by the second knee. This model typically predicts a clear transition from heavy to light dominance from the knee to the ankle.

  Observation of the suppression of the flux of cosmic rays above $4 \cdot 10^{19}$ eV by the Pierre Auger Observatory (PAO [27]) and HiRes [26] experiments has allowed the rejection of the theory that the charged CR spectrum continues with a constant slope above that energy with more than 6σ significance, see Fig. 1.3(b). The chemical composition and anisotropy of UHE cosmic rays is the centre of debate in the cosmic ray community because the experimental results appear to be in disagreement. While the HiRes data point to a proton composition above the ankle [30], the PAO data indicate an increasingly heavier composition at these energies, see also Fig. 1.5(b). The last PAO data points are consistent with the expectations for iron [31]. The PAO has rejected the hypothesis of an isotropic distribution of the UHE CRs and has suggested a correlation of the arrival direction of these particles with nearby extra-galactic objects like Active Galactic Nuclei (AGN) [32, 33], whereas HiRes has not seen any deviation from an isotropic sky [30]. In [34], the implication of the anisotropy on the possible CR composition is discussed. It is argued that one can test the chemical composition of UHE CRs by comparing the anisotropy at various energies. If anisotropies are observed above a certain threshold energy E_{th} and the flux is assumed to be composed of heavy nuclei, one should observe at energies above E_{th}/Z an even stronger anisotropy. This anisotropic signal is associated with the proton component of the primary flux. It is found that it is therefore hard to reconcile the PAO chemical composition and anisotropy measurements, although it is still very early to claim any true discrepancies.

To summarise, a standard charged CR model seems to emerge from the world-data. The measurements are compatible with the assumption that galactic (hadronic) cosmic rays are accelerated at strong shock fronts from, for example, SNRs after which they diffuse through the Galaxy. As for the origin of the knee, a combination of the maximum energy attained in galactic acceleration processes and leakage from the Galaxy seems to be favoured. CRs between the knee and the ankle originate from other galactic sources, possibly non-standard SNRs or already of extra-galactic sources (pair production dip-model). The highest-energy particles are believed to be of extra-galactic origin. A cut-off is observed at $4 \cdot 10^{19}$eV, possibly due to GZK-suppression of the flux (see 1.1.2). No consensus currently exists about the charged UHE CR composition and directionality.

1.1.2 The GZK cut-off

In 1966, after the discovery of the Cosmic Microwave Background (CMB) by Penzias and Wilson [35], two independent papers by Greisen [36], and Zatsepin and Kuz'min [37] predicted a steepening of the CR spectrum around $5 \cdot 10^{19}$ eV as the cosmic rays lose energy when propagating through the CMB. This is the so-called GZK cut-off of the CR spectrum. High-energy protons can interact with the photons of the CMB ($E_{\mathrm{CMB}} \sim 2.35 \cdot 10^{-4}$ eV) in two ways, namely via the Bethe-Heitler (BH) e^+e^- pair production,

$$p + \gamma_{\mathrm{CMB}} \rightarrow p + e^+ + e^-, \tag{1.2}$$

and pion production processes, for example through the Δ^+-resonance [38]:

$$p + \gamma_{\mathrm{CMB}} \rightarrow \Delta^+ \rightarrow N + \pi, \tag{1.3}$$

where the final state can either be $p + \pi^0$, $n + \pi^+$, $p + \pi^+ + \pi^-$, etc. Also possible Cosmic Infrared Background (CIB) can give rise to the same interactions. The energy threshold for BH pair production is $E_{\mathrm{th}}^{\mathrm{BH}} = 5 \cdot 10^{18}$ eV and for the Δ^+-resonance it is $E_{\mathrm{th}}^{\Delta} = 5 \cdot 10^{19}$ eV. The attenuation length is defined as $\lambda = E_p/(-dE_p/dx)$, where E_p is the proton energy and $-dE_p/dx$ is the mean energy loss rate. Figure 1.4 shows the energy loss length, this is the propagation length before the energy is decreased by a factor of $1/e$, of UHE protons as a function of their energy. The effect from the Hubble expansion (redshift)[5] is also shown. The BH pair production forms the main contribution to the energy loss below E_{th}^{Δ}, after which the Δ^+-resonance becomes dominant and leads to the GZK cut-off.

Heavier nuclei lose energy via photo-disintegration [39]. As high-energy CR nuclei propagate through intergalactic space, they interact with cosmic radiation backgrounds, fragmenting into lighter nuclei and nucleons. In each photo-disintegration interaction, a proton is produced (neutrons are produced too but decay relatively fast into protons). An analytic method to compute the high-energy CR energy spectrum and chemical composition at Earth resulting from the propagation through cosmic radiation backgrounds of heavy nuclei injected by extra-galactic sources is presented in [40]. No hadronic cosmic rays are expected to travel over distances larger than 100 Mpc with energies above 10^{20} eV. Moreover, the gyroradii of UHE protons in the local galactic fields are much larger than the diameter of our Galaxy (our Galaxy is approximately 30 kpc in diameter[6]) and no plausible source candidates are suspected inside it. This supports the assumption that the charged UHE CRs are of extra-galactic origin.

1.1.3 Neutral cosmic rays

Due to the influence of galactic magnetic fields, charged CRs in general do not point back to their sources. Only the highest-energy charged CRs are marginally influenced by those magnetic fields, but the GZK mechanism limits the field of view as discussed above. γ-rays and neutrinos have no, or very small, magnetic moments and will therefore not feel the influence of magnetic fields. They are products of the decays from accelerated charged particles or top-down production

---

[5] The propagation of CRs will be affected by the cosmological evolution for sources at large redshift. This leads to a redshift energy loss.

[6] The nearby galaxy, Andromeda (M31) is located at 772 ± 44 kpc [41] and the closest large cluster of galaxies is called the Virgo cluster which is at roughly 18.0 ± 1.2 Mpc and consists of possibly over 1300 galaxies [42].
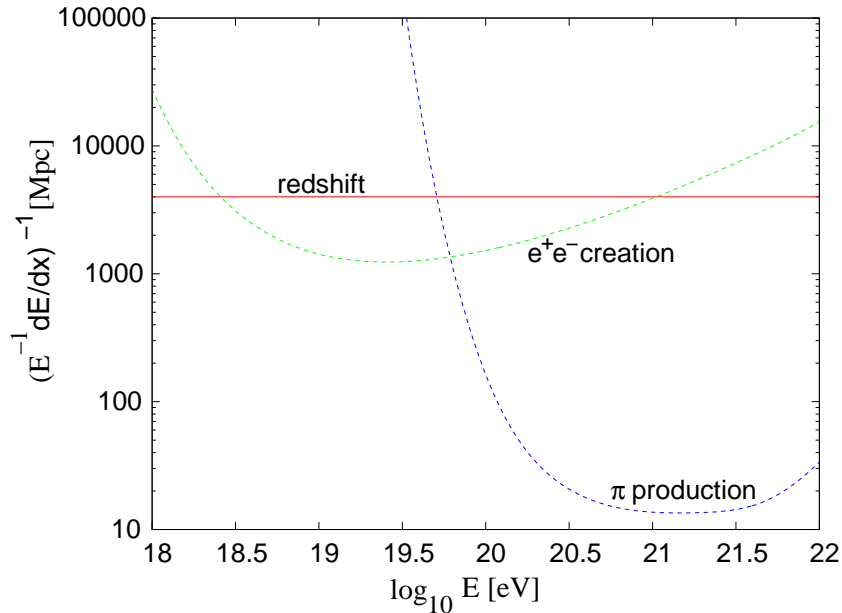
Figure 1.4: The energy loss length for UHE protons propagating through the Universe, due to e^+e^- creation and pion production. The effect from the Hubble expansion (redshift) is also drawn. Figure from [38].

scenarios. Electrons and protons are accelerated by astrophysical objects in, respectively, leptonic and hadronic accelerators. High-energy photons can be produced at both sites, whereas neutrinos are emitted solely in the case of hadronic acceleration.

Neutrinos and photons are produced in hadronic CR sources in proton-photon and proton-proton interactions via pion-production. The dominant channels are $p+\gamma \to \Delta^+ \to p+\pi^0$ (2/3) or $n+\pi^+$ (1/3) and $p+p \to p+p+\pi^0$ (2/3) or $p+n+\pi^+$ (1/3), where the target γ are available at the acceleration site and have higher energies than the CMB γ. The neutral mesons decay into photons:

$$\pi^0 \to \gamma + \gamma, \tag{1.4}$$

while charged mesons decay into, among others, neutrinos:

$$\pi^+ \to \nu_\mu + \mu^+,$$
$$\mu^+ \to \overline{\nu_\mu} + \nu_e + e^+. \tag{1.5}$$

or the charge conjugate for π^- originating from incident neutrons. If the neutrons decay before interacting, an extra flux of $\overline{\nu_e}$ is expected:

$$n \to p + e^- + \overline{\nu_e}. \tag{1.6}$$

However, inside the dense regions of the astrophysical sources, the neutrons are likely to interact before decaying. Therefore neutrinos from astrophysical sources are expected to arise dominantly from the decays of charged pions (and, for higher energies, kaons) and their muon daughters. This results in an initial flavour ratio, $(\phi_{\nu_e}:\phi_{\nu_\mu}:\phi_{\nu_\tau})$ and $(\phi_{\overline{\nu_e}}:\phi_{\overline{\nu_\mu}}:\phi_{\overline{\nu_\tau}})$, of nearly 1:2:0, assuming that pions of negative and positive charge occur in equal amounts. This implies that tau neutrinos are

not produced in astrophysical sources. The detected flavour composition at Earth, however, will be different due to neutrino oscillation whereby a neutrino created with a specific lepton flavour (electron, muon or tau) can be measured to have a different flavour. For the three neutrino species, there is strong experimental evidence from solar ([43]) and atmospheric studies, that ν_μ and ν_τ are maximally mixed and that negligible mixing from ν_e to ν_τ occurs. The current neutrino mixing angles predict that the three neutrino flavours should be observed in equal numbers at Earth for neutrinos from astrophysical sources [44]. Future verification of the actual neutrino flavour ratio could constrain astrophysical and particle physics models.

Active galactic nuclei (AGN) were among the first γ-ray sources detected at TeV energies and have remained the most abundant source population for high-energy ($E > 10^{12}$ eV) γ-ray astronomy. An intriguing recent development in the field is the discovery of a population of TeV γ-ray sources that appear to have no counterparts at longer wavelengths. The presently unidentified TeV γ-ray sources cluster around the galactic plane, possibly indicating that they are of galactic origin [45].

High-energy photons can interact with infrared or CMB photons to produce e^-e^+ pairs and are effectively absorbed. The implication is that the observable TeV gamma-ray sky does not extend very far: above 10 TeV the horizon of the photons is limited to less than 10 Mpc which is even less than for the UHE charged CRs. Possibly only neutrinos are left to open the window on the most extreme and distant events of the Universe[7].

1.2   Neutrino astrophysics

The neutrino is sometimes referred to as the ideal astrophysical messenger for the following reasons, some of which have been mentioned before.

- Unlike charged CRs, neutrinos are not subject to deflections by cosmic magnetic fields. They follow geodesic paths.

- Neutrinos do not interact with the CMB or CIB and can therefore reach Earth unattenuated, unlike photons and charged CRs.

- Due to their small interaction cross sections, neutrinos are expected to be able to escape much denser astrophysical bodies than photons or charged CRs. Therefore they can provide information that remains hidden to traditional astronomy or charged CR detectors as has been the case in the field of solar neutrino physics.

- Neutrinos provide strong evidence for hadronic acceleration processes and detection of high-energy neutrinos of astrophysical origin will reveal the importance of hadronic interactions in astrophysical objects.

It is clear that the neutrino has earned its title due to its capability to carry complementary (or even exclusive) information about the cosmos and its astrophysical objects without losing directional information or energy. Its small cross section is however a major draw-back. Large

---

[7]Gravitational waves (fluctuations in the curvature of spacetime) will also originate from binary star systems composed of white dwarfs, neutron stars, or black holes. However, no direct measurement of gravitational waves has been achieved and this messenger will not be discussed here.

target masses are needed for their detection on Earth. Natural resources, like ocean water and Antarctic ice are convenient and abundant potential detection media (see § 1.4).

The neutrino flux arriving at a neutrino detector on Earth is expected to have three contributions. First there are the atmospheric neutrinos that are generated by CR interactions in the atmosphere. This flux is not discussed in this work, see [46] for an overview of the latest results from the AMANDA [47] and IceCube [48] detectors. Second, there are the extra-terrestrial neutrinos that are associated with a specific source (point-like fluxes). Third, the extra-terrestrial neutrinos can also be associated with a diffuse flux. In the following sections a selection of the possible astrophysical neutrino sources is discussed.

1.2.1 Cosmogenic neutrinos

The predicted GZK cut-off, due to proton interactions with the CMB or photo-disintegration of heavier nuclei, implies the existence of a flux of UHE neutrinos, see Eqs. 1.5 and 1.6. These neutrinos are often referred to as cosmogenic[8] or GZK neutrinos. Predictions for the magnitude of the flux of GZK neutrinos differ by more than an order of magnitude [49, 50]. Typically, the predicted GZK neutrino energy stays below $\sim 10^{21}$ eV and the muon neutrino spectrum peaks at $\sim 10^{17.5}$ eV. The electron neutrino spectra have a more interesting double-peak shape. The higher peak, containing mostly ν_e, coincides with the muon neutrino one. The lower energy spectrum peaking at $10^{15.5}$ eV contains only $\overline{\nu_e}$ from neutron decay, see Eq. 1.6. The neutron decay length equals the photoproduction interaction length (on γ_{CMB}) at about $4 \cdot 10^{20}$ eV and neutrons of lower energy are more likely to decay than to interact.

The strength and shape of the cosmogenic neutrino flux depends on several factors [50]:

- The energy spectrum of the primary protons (or charged CR). Typically $\gamma = -2$ is chosen as the spectral index at the source (before propagation), as this is predicted by the Fermi acceleration theory. An exponential cutoff at a critical energy is usually implemented. Both AGNs and GRBs are often used as input sources for the estimation of the GZK neutrino flux. The UHE CR composition is also an important factor and in most GZK fluxmodels it is assumed that the dominant fraction of the UHE charged CR are protons. The neutrino production of heavier nuclei is less efficient and typically powered by neutron decay. The heavier the UHE CR, the lower the UHE GZK neutrino flux will be. The flux at the source is typically scaled to fit the charged CR spectrum at Earth. Also γ-ray observations can constrain the injected proton flux.

- The cross sections. These are estimated by extrapolating accelerator measurements. The fraction of the energy that goes to the neutrinos and the amount of neutrinos produced depend on this input.

- The density of the CMB photons. The photon density is well known and the spectrum can be fitted with a blackbody spectrum of $T \sim 2.7$ K. At larger redshifts the photon density is higher by $(1 + z)^3$ and both the microwave photon and proton energy are higher by $(1 + z)$. Therefore the photoproduction threshold decreases [53]. High redshift GZK neutrinos are of lower energy, because the proton interaction threshold energy decreases and the neutrinos are redshifted.

---

[8]As they are generated by the CMB.
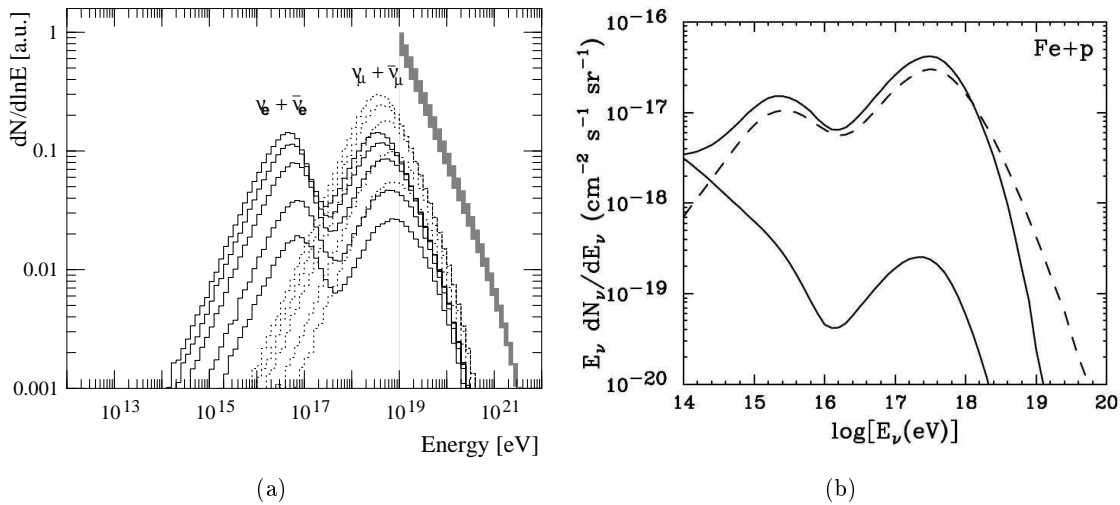
Figure 1.5: (a): Neutrino fluxes produced during the propagation of protons over 10, 20, 50, 100 and 200 Mpc (from bottom up) in a 1 nG magnetic field. The heavy grey histogram shows the assumed proton injection spectrum. Figure from [51]. (b): The range of cosmogenic neutrino spectra that are consistent with the PAO composition measurements and spectrum. The dashed curve is the prediction for an all-proton spectrum for a certain choice of model parameters, similar to the standard ESS flux [51]. The solid lines denote the modelled spectra with the highest and lowest predicted rates for the wide range of spectral parameters that fit the PAO data. For details see [52].

- The cosmological evolution of the source population. The input source density is usually assumed to follow the star formation rate and is modelled as $\rho \sim (1+z)^m$, with $z < z_{max}$ is the redshift and $m > 0$. There is a definite relation between the shape of the neutrino spectrum and the cosmological evolution of the sources. A larger m and also larger $z < z_{max}$ leads to a larger number of sources that contribute and therefore to a higher flux.

Both the deflections by interstellar magnetic fields and neutrino oscillation are usually not taken into account in GZK fluxmodels. The UHE charged CR are expected minimally deflected and the actual magnetic field strengths are not well-determined. In general it is assumed that all three neutrino flavours are present in equal amount in the GZK flux.

For a standard GZK neutrino flux from propagation UHE protons, the work of [51] is often referred to, although this flux is likely to be too high in the case of iron-dominated UHE CRs. In [51], it is shown that the energy degradation of UHE protons in the CMB is very fast. Protons with an energy of about 10^{21} eV interact on average twice or more during the first 10 Mpc of propagation and lose close to 50% of their injection energy. Of this energy loss, about 40% goes into the produced neutrinos. Therefore, the expected neutrino flux mostly originates from the first 100 Mpc of propagation [51]. Figure 1.5(a) shows the neutrino fluxes produced during the propagation of protons for several distances. The contribution from 100 Mpc to 200 Mpc is small because the proton spectrum is now deprived from particles with sufficient energy to undergo photoproduction. Therefore a source at 200 Mpc yields a fully evolved neutrino spectrum.

More recently, in [52], the PAO measurement showing a tendency towards heavier particles

for the UHE CRs is fitted as an input for models that predict the cosmogenic neutrino flux, see Fig. 1.5(b). Several different heavy nuclei such as N, Si, Fe or a combination of one of those three with protons are used as a primary spectrum and then propagated through the interstellar medium. The cosmogenic neutrino flux prediction can be suppressed as much as two orders of magnitude when going from an all-proton to a pure-iron composition. In this case, only a few of the dissociated protons that are product of the photo-disintegration of the nuclei exceed E_{th}^{Δ}. For this worst case scenario, none of the current or planned neutrino telescopes are large enough for GZK-neutrino detection [52, 50].

The detection of the cosmogenic neutrino flux is one of the main motivations for the search of UHE neutrinos. Indeed, detection or non-detection of the UHE GZK neutrino flux by current or future neutrino detectors will put constraints on the UHE CR composition of both the injected flux and the flux arriving at the Earth's atmosphere. Other HE neutrino sources also exist and are discussed in the following section.

1.2.2 Astrophysical neutrino sources

γ-ray sources are, in general, good candidates for neutrino sources since both neutrinos and high-energy photons can originate from hadronic CR accelerators. Therefore, predictions of the neutrino flux of this kind of astrophysical source depend upon the assumption that most of the observed γ-rays originate from π^0 decays.

Galactic neutrino sources are interesting because they require less luminosity than extra-galactic sources to give the same event rate at Earth. An overview of galactic neutrino point sources, like for example Supernovæ, pulsar wind nebulæ, shell-type SNRs, pulsars and magnetars, is given in [54]. However, the typical maximum energy predicted for these sources is about 200 TeV (in case of the Crab Nebula SNR). Models for astrophysical neutrino sources in our Galaxy usually assume a very efficient transfer of the energy available in the source into the accelerated hadrons. This gives rise to optimistic neutrino fluxes at relatively low energies.

The extension of the measured charged CR spectrum above the ankle is currently believed to be the result of an extra-galactic component. Again, charged CR and γ-ray observations allow predictions of the expected extra-galactic UHE neutrino flux. Several good candidates for extra-galactic particle accelerators exist:

- **Active Galactic Nuclei (AGN)**
  An AGN is a compact region at the centre of a galaxy which has substantial radiation that is not associated with the stars or gas heated by them. The active nuclei typically emit strongly over the whole electromagnetic spectrum, including radio and X-ray. There is also strong γ-ray emission, where most galaxies hardly radiate at all. Very luminous active nuclei, such as quasars, easily outshine their host galaxies and are found at large cosmological redshifts [55]. All of them have a massive central black hole and about 10% have visible jets. Unified AGN models propose that different classes of AGN, like quasars, blazars, FSRQs (Flat Spectrum Radio Quasars), FR-II (Fanaroff-Riley morphology type-II) and radio-quiet AGN, are intrinsically similar systems with different orientations to the line-of-sight of the Earth and different accretion rates. The system is then a supermassive black hole with an accretion disk around it that produces, in some cases, jets: twin highly collimated and fast outflows that emerge in opposite directions from close to the disc. In the case of blazars for example we might be directly looking into the jet.
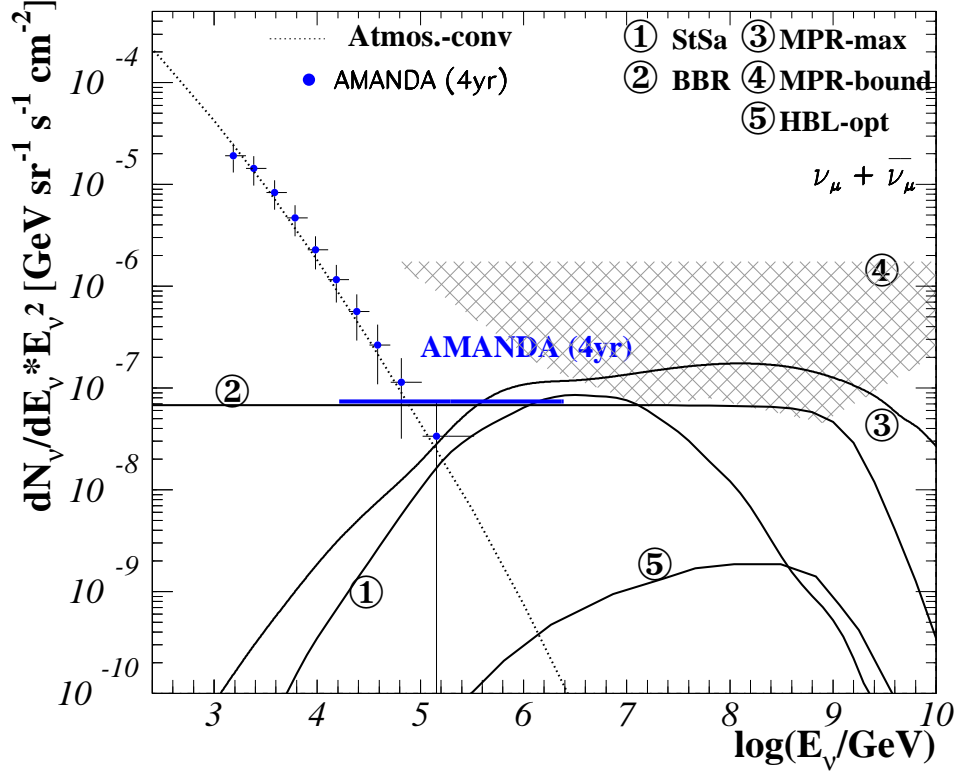
Figure 1.6: AGN neutrino flux models. (1) and (5): two predictions for blazars. (2): for FR-II type galaxies and FSRQs. (3): maximum contributions from sources that have been observed by EGRET. (4): an upper bound for the diffuse neutrino flux for optically thick (upper bound) and thin (lower bound) sources. The atmospheric prediction is shown as the dotted line, the data points and limit are from the 4-year AMANDA-II analysis. For references, see [50]

There are two possible production regions for neutrinos in AGN: the region close to the central engine and the AGN jets [53]. A shock wave can be produced in the central region due to the pressure of the accreting matter. This shock wave can accelerate protons by the Fermi acceleration mechanism. Neutrinos are then mainly the product of the energy-loss mechanism of these protons by pion production. The precise acceleration model can be constrained by detection or non-detection of neutrinos emitted by the AGN core. The other location for proton acceleration and therefore neutrino production are the AGN jets. The dominant production process is again pion production on internal synchrotron photons or on the thermal UV photon background of the accretion disk. Figure 1.6 shows a selection of predicted AGN neutrino fluxes together with data from AMANDA and the prediction for the flux of atmospheric neutrinos.

- **Gamma-ray Bursts (GRBs)**
  GRBs are the most luminous astrophysical phenomena known and are often located at large cosmological redshifts. They are short, typically several seconds long, flashes of γ-rays with energies predominantly larger than $100\,\mathrm{MeV}$. In the standard GRB fireball model [56], the energy source is assumed to be rapid mass accretion on a newly formed solar-mass black hole whose formation can be associated with a type Ib/c supernova. The associated energy release drives an ultra-relativistic plasma outflow or "fireball". This model has gained experimental support from the observation of the afterglow: γ-rays that are produced by synchrotron emission of high-energy electrons accelerated in internal shocks of the fireball. Protons are expected to be present in the fireball and to be accelerated to high energies [57].

  In [50] three phases of non-thermal emission and the expected resulting neutrino flux from the GRB source are discussed. Neutrino emission is expected prior to the GRB (precursor phase), when the pre-GRB interacts with the central pulsar or the SNR shell. The prompt emission that follows is accompanied by neutrinos if the observed UHE charged CR spectrum comes from GRBs. In that case, also the afterglow emission is expected to be accompanied by a neutrino signal [56, 57]. An experimental search for high-energy muon neutrinos from the brightest GRB ever observed (GRB080319B) with the IceCube neutrino telescope is presented in [58]. It is shown that no constraint on the GRB-models is possible with the current IceCube data.

- **Starburst Galaxies**
  A starburst galaxy is a non-active galaxy going through an exceptionally high rate of star formation. Galaxies are often observed to have a burst of star formation after a collision or close encounter with another galaxy. The neutrino emission from such astrophysical objects was suggested and calculated in [59], starting from the observed synchrotron emission from starburst galaxies which is produced by relativistic electrons in these sources. It is then assumed that (1) the presence of relativistic electrons in these sources implies the presence of relativistic protons, that (2) the protons lose essentially all of their energy to pion production, and that (3), a lower limit to the rate at which the protons lose their energy can then be obtained from the synchrotron radio flux by assuming that all of the electrons (and positrons) which are radiating are from pion decay. The predicted diffuse high-energy neutrino flux is large enough to be observable with a very large neutrino detector such as IceCube. The actual diffuse flux from starbursts is likely to be lower as, discussed in [60], where assumptions (2) and (3) are re-examined.

1.2.3 Theoretical upper bounds on diffuse neutrino emission

Unidentified neutrino sources that are not intense enough to be observed individually should contribute to a possible diffuse neutrino flux. High-energy cosmic ray observations can be used to set model-independent upper bounds on expected high-energy neutrino fluxes. However, large uncertainties exist, such as for example the poorly known magnetic field strengths in the Universe. Two predictions are discussed here: the Waxman-Bahcall (WB) and Mannheim-Protheroe-Rachen (MPR) upper bounds.

In [49], an upper bound on the diffuse neutrino flux from extra-galactic sources is derived using as input the observed spectrum of CRs with energies above $10^{18}\,\mathrm{eV}$, assuming that they

are protons of extra-galactic origin. This Waxmann-Bahcall bound assumes a generic E^{-2} spectrum for all extra-galactic sources, in particular AGN jets and GRBs, as expected from a Fermi acceleration mechanism, and predicts an upper limit of

$$E_\nu^2 \frac{d\phi}{dE_\nu} < 4.5 \cdot 10^{-8} \text{GeVcm}^{-2}\text{s}^{-1}\text{sr}^{-1}. \tag{1.7}$$

The WB limit was criticised to be not completely model-independent mainly since the assumption of the generic E^{-2} spectrum could imply a Fermi acceleration mechanism. In [61] an upper bound is derived using both the high-energy CR spectrum and the diffuse γ-ray flux. Both neutron-transparent and neutron-opaque sources are considered. The limit for opaque sources is

$$E_\nu^2 \frac{d\phi}{dE_\nu} < 2.0 \cdot 10^{-6} \text{GeVcm}^{-2}\text{s}^{-1}\text{sr}^{-1}, \tag{1.8}$$

which is about two orders of magnitude larger than the WB limit because an opaque source is assumed to let very few charged CR escape but it is transparent to neutrinos and γ-rays. This optimistic flux has been partially excluded by the AMANDA-II 2000-03 observational limit [62], see Fig. 1.6.

1.3 Neutrino interactions

1.3.1 Cross sections

High-energy neutrinos $\nu_l = \nu_e$, ν_μ, ν_τ can interact via deep inelastic scattering with a nucleon N of a nucleus of the target material, via either the charged current (CC) weak inelastic interaction [63]:

$$\nu_l + N \to l + X, \tag{1.9}$$

or the neutral current (NC) interaction:

$$\nu_l + N \to \nu_l + X, \tag{1.10}$$

where $l = e$, μ, τ is a lepton and X is the hadronic product of the interaction that will decay in the form of a hadronic particle cascade, called hadronic shower. The fraction of the energy that is not carried by the produced lepton is called the inelasticity, y. For high energies, y is roughly independent of energy and the mean value is about 0.2. This means that the hadronic cascade will, on average, carry about 20% of the total neutrino energy. The emerging charged lepton can give rise to a track and/or an electromagnetic cascade. In [64, 65] neutrino-nucleon interaction probabilities at ultra-high energy are calculated and their results are shown in Fig. 1.7. At very high energies ($E_\nu > 10^{18}$ eV) Earth becomes opaque for high-energy neutrinos [66].

The Glashow resonance

The interaction of neutrinos with the electrons from the target material atoms is in general negligible compared to the inelastic neutrino-nucleon interactions. An exception exists for the case of the annihilation by charged current of an electron anti-neutrino on an atomic electron by exchange of a W^- boson in the s-channel: $\overline{\nu_e} + e^- \to W^-$. This interaction is resonant for a centre-of-mass energy that is equal to the mass M_W of the W^- boson. In the target rest frame,
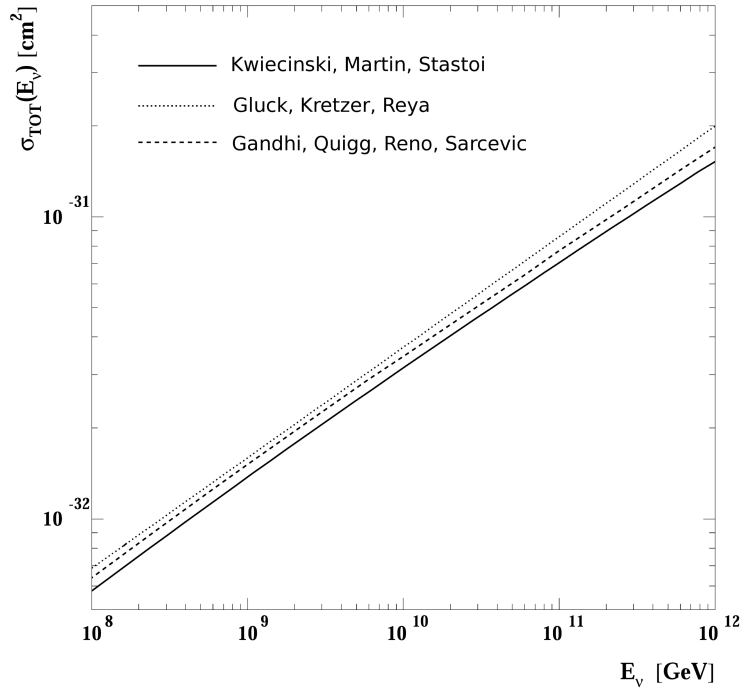
Figure 1.7: The neutrino-nucleon cross section at high energy. The prediction for the total νN cross section obtained in [65], compared to other calculations from [64, 67, 68]. Figure adapted from [65].

this corresponds to an incident neutrino energy of $E_\nu = 6.3\,\mathrm{PeV}$, where m_e is the electron mass. The $\overline{\nu_e}e$ cross section is, at this narrow resonance (width is about $1\,\mathrm{PeV}$), of the same order as the cross section for νN interactions and therefore significantly attenuates a high-energy $\overline{\nu_e}$-beam propagating through Earth.

1.3.2 Neutrino signatures

A high-energy neutrino that interacts in a medium has up to three detectable signatures, originating from the tracks of the charged leptons or the hadronic or electromagnetic cascades:

- **Optical**
  The charged particles produced by νN interactions, traversing a medium, emit Cherenkov light if travelling faster than the speed of light in that medium [69]. This light can be detected by photomultiplier tubes (PMTs). Both tracks and cascades therefore have an optical signature.

- **Radio**
  Low energy processes like Compton, Møller and Bhabha scattering and positron annihilation build up a net charge (more e^- than e^+) in the cascades, as atomic electrons in the target medium are swept up into the forward moving shower. This moving negative charge imbalance in the cascade gives rise to coherent Cherenkov radiation at radio frequencies [70] in dielectric media, this is called the radio-Cherenkov signal. The Cherenkov radiation will
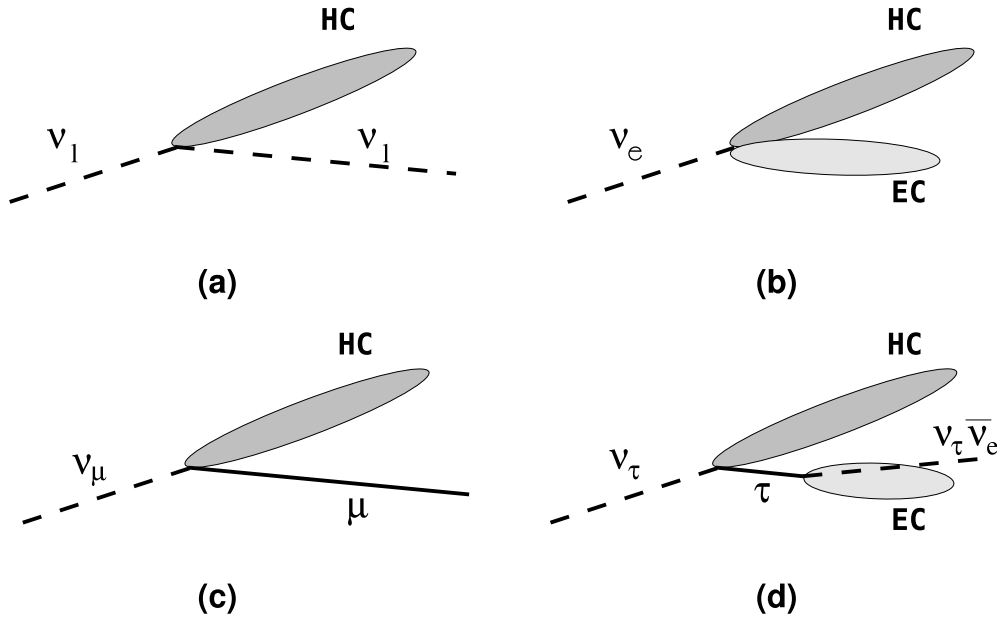
Figure 1.8: Event topologies for different neutrino flavours and interactions. (a): NC interaction producing a hadronic cascade (HC). (b): CC interaction of ν_e producing both hadronic and electromagnetic cascades (EC). (c): CC interaction of ν_μ producing a μ and a hadronic cascade. (d): example of a CC interaction of ν_τ producing a τ that decays into ν_τ, this interaction produces an electromagnetic cascade in the case of $\tau \rightarrow e\nu_\tau\overline{\nu_e}$. This is the so-called double bang signature.

become coherent when the wavelength exceeds the dimensions of the cascade. Modelling of electromagnetic showers in ice shows that coherence is maintained typically from a few hundred MHz up to a few GHz. This radio signal can be detected by radio antennas. The energy threshold for generating a detectable radio signal is still under debate but typically higher than 10^{17} eV.

- **Acoustic**
  The cascades will locally and instantaneously heat the medium, giving rise to a coherent pressure wave that is potentially detectable by acoustic sensors. The amplitude of the signal depends on the energy density inside the cascade region. This mechanism is discussed in detail in Chapter 2 and the feasibility of acoustic neutrino detection in ice, the detector medium of interest, is the subject of this work.

1.3.3 Tracks and cascades

The experimental signature of a νN interaction depends on the flavour and type of interaction (CC or NC), see Fig. 1.8. Both NC and CC interaction produce a hadronic cascade at the interaction point which carries, as mentioned before, about 20 % of the total energy. This hadronic cascade produces an optical and possibly a radio and an acoustic signature. The remaining

energy is carried by the emerging lepton which gives rise to following signatures in case of a CC interaction:

- The outgoing muons will only undergo radiation losses and leave track-like optical signatures.

- The emerging e generates an electromagnetic cascade. Indeed, the outgoing charged lepton, e or will interact with the electrons of the medium (see § 1.3.3). This electromagnetic cascade can generate both a radio and an acoustic signature in addition to the optical signal.

- In the case of ν_τ, instead of a single cascade, multiple cascades are produced due to the regeneration of the τ. The branching ratio of the common purely leptonic τ decays are 17.85% for decay into $e\nu_\tau\overline{\nu_e}$ and 17.36% for decay into $\mu\nu_\tau\overline{\nu_\mu}$. For example, the CC interaction with ν_τ can produce a very specific "double-bang" signature if the τ decays into $e\nu_\tau\overline{\nu_e}$, where the emerging electron will form an electromagnetic cascade, giving rise to a radio and possibly an acoustic signal. For the τ, the energy loss per unit length is smaller than for the muon, therefore they will produce a dimmer optical track.

Electromagnetic cascades

When a high-energy electron or photon interacts with a target material, it initiates an electromagnetic cascade as pair production and Bremsstrahlung generate more electrons and photons with lower energy. Indeed, in the case of an incident electron for example, a photon will be produced by Bremsstrahlung which can itself generate a e^+e^- pair. This pair will in its turn radiate photons by Bremsstrahlung if their energy is sufficiently large. The longitudinal development is governed by the high-energy part of the cascade, and scales as the radiation length X_0 in the material. The transverse development of electromagnetic showers in different materials scales fairly accurately with the Moliere radius R_M, which is,for example, about 13 cm in ice, the medium of interest for this work[9]. After reaching a critical energy E_c, when the energy loss due to Bremsstrahlung is equal to the energy loss due to ionisation, e^+ and e^- lose their energy mostly due to ionisation and the cascade eventually stops. A rough estimate of the critical energy is $E_c \sim 605/Z$ MeV where Z is the atomic number of the medium [71].

Hadronic cascades

The hadronic fragments X that remain after the inelastic collision of the neutrino with the nucleon will also be at the origin of a cascade of particles. The hadronic fragments X are composed of mainly high-energy pions that will maintain the direction of the initial neutrino because their transverse momentum is expected to be around a few hundred MeV. The cumulative angular deviations will remain small for several generations of hadronic particles. Therefore the hadronic shower will consist of a very penetrating central core that feeds electromagnetic subshowers through the decay of π^0 into a photon pair if the pion energy is low enough. If all pions roughly have equal energy, then about 1/3 of the energy is converted into electromagnetic subshowers in each interaction. Several papers discuss the longitudinal and transverse profiles of the hadronic shower [73, 74].

---

[9]R_M for lead and iron is 1.6 cm and 2.1 cm respectively. In air, at sea-level, the Moliere radius is about 78 m.
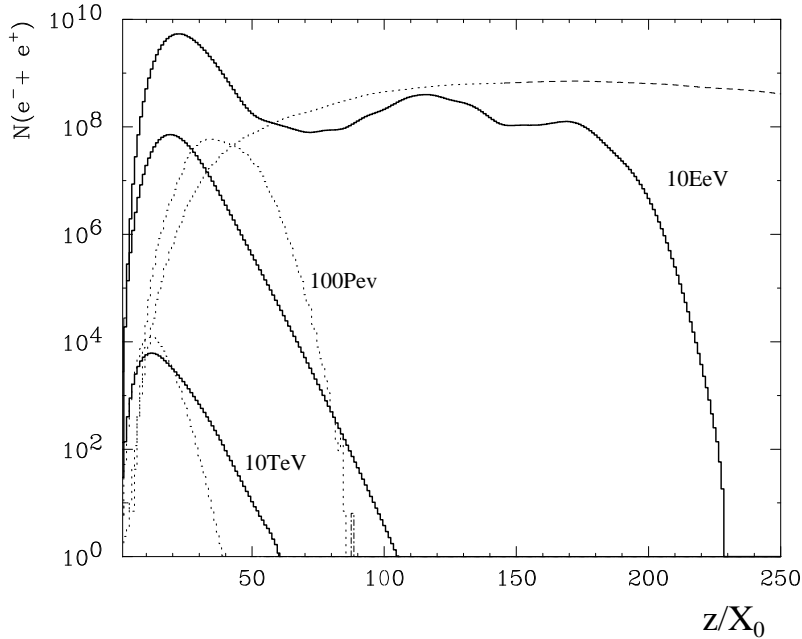
Figure 1.9: Longitudinal development of electromagnetic (dashed curves) and hadronic (solid curves) cascades in ice. The energies shown are from bottom to top 10 TeV, 100 PeV and 10 EeV. The radiation length X_0 is 36.08 g cm^{-2}. Figure adapted from [72].

The LPM effect

The Landau-Pomeranchuk-Migdal (LPM) [75, 76] effect, which is the reduction of the cross sections for electron Bremsstrahlung and photon e^+e^- pair production above a certain threshold energy E_{LPM} (for example, about 2 PeV for ice), is known to increase the electron and photon interaction lengths. The LPM effect becomes important for the cascade development at the highest energies, $E_\nu > 10^{18}$ eV.

The electromagnetic shower is elongated by about a factor of 10 at $E_\nu \sim 10^{20}$ eV. This stretching means that the energy density goes down. Also, due to the stochastic nature of the shower development, the different energy density maxima of the individual subshowers initiated by the initial particles will become separated. These effects mean that the expected acoustic signal from such an UHE electromagnetic shower is likely much lower than what one would naively expect from the initial conditions (the EM shower takes on average 80% of the incident neutrino energy.)

Hadronic showers show a much smaller elongation because most of the electrons and photons in the shower come from the decays of π^0 produced in hadronic interactions. Pion decay in ice above 40 PeV is suppressed because they are more likely to interact. This means that, even for EeV showers, only a small fraction of the shower is subject to LPM elongation [77]. Figure 1.9 shows the comparison between the simulated longitudinal developments of hadronic and electromagnetic cascades in ice. Even for EeV energies, the hadronic cascades will still deposit a large fraction of their energy within $50\, X_0$. This region can therefore still generate an acoustic signal.

1.4 Neutrino detectors

This section gives an overview of the current optical and radio high-energy neutrino detectors. The status of acoustic neutrino detection projects is presented in Chapter 2.

1.4.1 Optical neutrino detectors

Markov's paper in the 1960 Rochester Conference Proceedings [78] is often cited as the first reference to a deep ocean neutrino detector i.e. the first reference to using natural resources as a medium for large-scale high-energy neutrino detection. Markov proposed to install detectors deep in a lake or sea and to determine the direction of the incident charged particles with the help of Cherenkov radiation. However, the idea of an ocean-based neutrino detector seems to have occurred to several people simultaneously. The early design-proposals were all focused on the detection of atmospheric and/or solar neutrinos. The idea of neutrino astronomy outside our solar system was first made concrete with the design of the Deep Underwater Muon and Neutrino Detection (DUMAND) detector, first discussed at the 1973 Cosmic Ray Conference.

The DUMAND collaboration existed from about 1976 through 1995 [79, 80]. The goal was the construction of the first deep ocean high energy neutrino detector, to be placed at a depth of 4800 m in the Pacific Ocean. Many preliminary studies were carried out, from technology to ocean optics. A prototype vertical string of instruments suspended from a special ship was employed to demonstrate the technology, and measure the cosmic ray muon flux in the deep ocean. In 1995 all funds and further efforts on DUMAND were stopped but it has served as a benchmark project that inspired many other projects (see references below): several sea-based experiments like (in order of age) NESTOR, ANTARES, and NEMO, all located in the Mediterranean, as well as the Lake Baikal Project in Russia, and the AMANDA and IceCube projects at the South Pole. For an overview of the birth of experimental high-energy neutrino astronomy and the DUMAND project, see [81].

Water

The Baikal Neutrino Telescope [82] operates in Lake Baikal, Russia, at a depth of 1.1 km. It was the first installed underwater neutrino detector and also the first to reconstruct a muon-track generated by an interacting atmospheric neutrino. The initial configuration NT-200 started operation in 1998 and contained 192 Optical Modules (OM). It was upgraded to NT-200+ in 2005 and plans for a gigaton detector are currently under discussion. The ANTARES [83] project was set up in 1996 and the detector was completed in May 2008. It consists of 900 photomultipliers distributed along 12 lines that are installed in the Mediterranean Sea, at 2.5 km depth, about 40 km off the shore of Toulon, France. Both the NESTOR [84] and NEMO [85, 86] collaborations have carried out R&D activities aimed at the development of technologies for a deep-sea km^3-scale detector. NESTOR is located in the Ionian Sea ,near the Greek coastline, at about 3.8 km depth. It has deployed a single instrumented tower at a proposed site for a possible future km^3-scale detector. The NEMO project has deployed a technological demonstrator at a depth of 2.0 km at a test site off the coast of Capo Passero, in Sicily. The ANTARES, NESTOR and NEMO collaborations have joined their efforts in a consortium, KM3NET, that has the goal to construct a km^3-scale detector in the Mediterranean Sea [87].
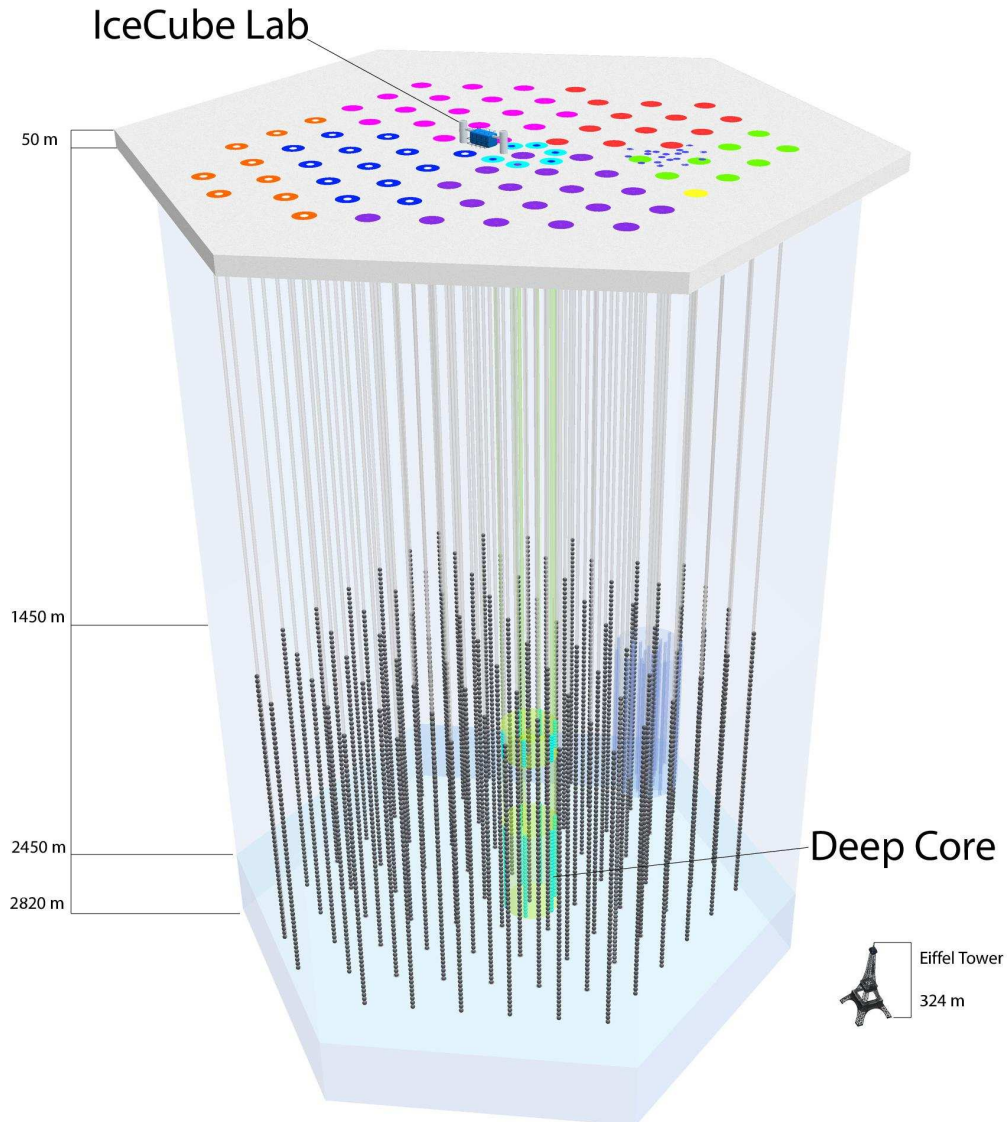
Figure 1.10: The IceCube detector: the IceTop cosmic-ray EAS detector is situated on top of the ice. 80 IceCube strings will each have 60 Digital Optical Modules (DOM) instrumenting in total $1\,\mathrm{km}^3$ of ice. A DeepCore of 6 additional strings (also carrying 60 DOMs) forms the low-energy extension in the heart of the detector.

Ice

The IceCube [48] neutrino telescope is currently under construction in Antarctica, at the site of the South Pole Amundson-Scott station (see Fig. 1.10). The end of construction is foreseen in February 2011, after 7 austral construction summers. IceCube builds on the successful deployment and operation, since 1996, of the AMANDA neutrino telescope [47]. The IceCube neutrino observatory will consist of 4800 Digital Optical Modules (DOMs) installed between a depth of 1450 m and 2450 m on a hexagonal array of 80 strings with horizontal spacing of 125 m. In addition, a DeepCore of 6 additional strings will be deployed in the coming seasons. The DOMs digitise the signals directly in the ice to minimise loss of information from degradation of analogue signals sent over long distances. The in-ice array is complemented by a surface array, IceTop, which is an Extensive Air Shower (EAS) detector that will consist of 160 ice-tanks, in pairs, near the top of each IceCube string.

The large scale high-energy neutrino detectors like IceCube, AMANDA and ANTARES are sensitive to neutrinos with energies between 1 TeV and 1 PeV. No extra-terrestrial neutrinos have been detected up to now with these detectors but several optimistic neutrino fluxes from galactic and extra-galactic sources have been excluded with current data. Many of the source classes are still unexplored due to limited experimental sensitivities. IceCube will be entering, upon completion, a region with realistic discovery potential although theoretical estimates suggest that this km^3-scale detector will still only scratch the surface of potential neutrino fluxes. Even assuming an optimistic GZK-neutrino flux, IceCube is not expected to see more than 1 GZK-neutrino each year [88]. If IceCube has the capability to identify neutrino species [89], deviations from the expected flavour composition could be measured. In the Glashow resonance scattering it is possible to discriminate between ν_e and $\overline{\nu_e}$. The normalised $\overline{\nu_e}$ signal could be used to differentiate between the two primary neutrino-production interactions ($p\gamma$ and pp collisions) [90] for optically thin CR sources.

1.4.2 Radio neutrino detectors

In order to survey the UHE neutrino sky above 10^8 GeV, even larger detectors are needed. Currently, the radio Cherenkov technique is being used as a tool to survey vast amounts of target material, like the Antarctic or Greenland ice shelf or the Moon's regolith. The energy threshold for this type of experiment is typically very high. No radio Cherenkov neutrino event has been observed and the current limits are starting to cut into the optimistic GZK-neutrino flux models. Most current radio Cherenkov experiments rely on Antarctic ice as their detection medium:

- **RICE**
  The Radio Ice Cherenkov Experiment (RICE, [91]) was an array of 16 antennas with a bandwidth of (0.2–1) GHz buried about 150 m deep in the Antarctic ice at the South Pole. It looked for the radio signal from neutrino-induced cascades in the ice; no neutrino candidate was found. The derived upper limit on the high-energy flux is indicated in Fig. 1.11.

- **ANITA**
  The ANtarctic Impulsive Transient Array (ANITA) is an Antarctic balloon experiment that consists of an array of 32 broadband horn antennas that look down at the ice surface. The first ANITA flight was launched in December 2006 and ANITA-II flew in the 2008–2009
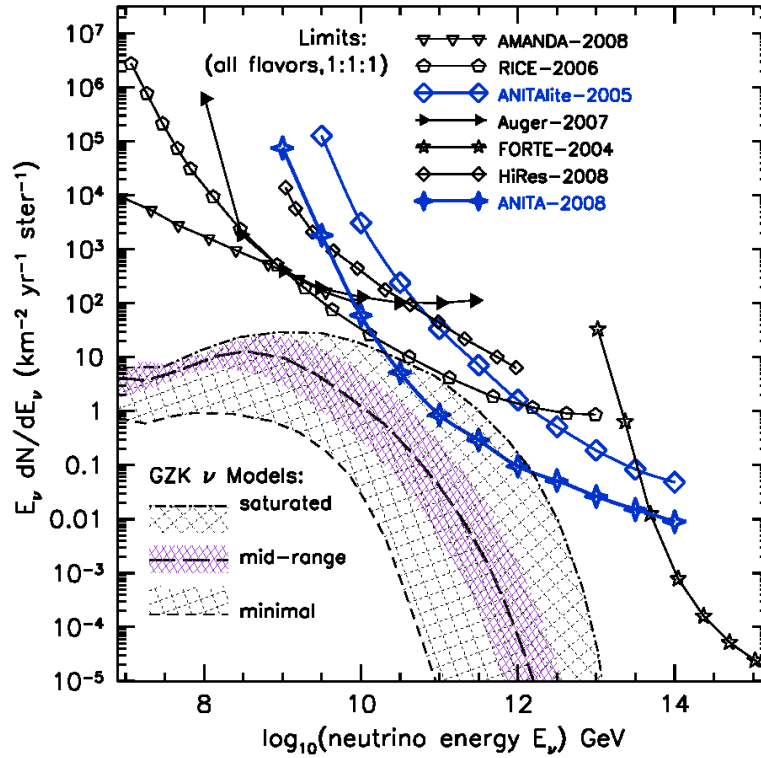
Figure 1.11: Ultra-high-energy neutrino flux limits. ANITA-I limits based on no surviving candidates for 18 days of lifetime. Other limits are from AMANDA [47], RICE [91], ANITA-lite [92], Auger [93], HiRes [94], FORTE [95]. The GZK neutrino model range is determined by a variety of models, see [96] for details.

Antarctic season. The limit on the UHE neutrino flux obtained with the 2006–2007 data is shown in Fig. 1.11. It is currently the best available limit on the neutrino flux for energies from 10^{10} to 10^{14} GeV [96].

But also the lunar regolith, the upper layer of loose and heterogeneous material covering the solid moon bedrock, is being observed in the radio frequencies:

- **Lunar radio Cherenkov experiments**
  The first attempt to use the lunar regolith in the search for UHE neutrinos was made at the 64 m Parkes radio telescope which was used to observe the Moon using a wide-bandwidth. No neutrino event candidates were identified [97]. Subsequently, several independent experiments utilising the technique also recorded null results, like the Goldstone Lunar Ultra-High-Energy Neutrino Experiment (GLUE, [98]), the Kalyazin Radio Astronomical Observatory [99] and the LUNASKA project [100]. These were used to place limits on the UHE neutrino flux (Fig. 1.11). Recently, low-frequency lunar observations have started with the Westerbork Synthesis Radio Telescope [101] and similar observations are planned with the future LOFAR (LOw Frequency ARray) antenna array [102].

- **FORTE satellite experiment**
  The FORTE (Fast On-orbit Recording of Transient Events) satellite records bursts of electromagnetic waves arising from near Earth's surface in the radio frequency (RF) range of 30 MHz to 300 MHz with a dual polarisation antenna. A search for RF signatures of UHE neutrinos originating from coherent Cherenkov emission induced by cascades in the Greenland ice sheet was performed with the FORTE satellite over a ∼2-year period, see [95] and Fig. 1.11.

A number of future radio neutrino detectors are currently under investigation:

- **IceCube-centred radio arrays**
  Currently, several IceCube-centred arrays are under investigation but neither geometry nor design has been fixed. The South Pole location offers the possibility of hybrid neutrino detection using IceCube and radio antenna coincidences. IceRay [103] proposes to deploy a large two-dimensional array of antenna stations near the surface close to the South Pole. AURA (Askaryan Under ice Radio Array) is an ongoing project that aims to deploy a shallow UHE neutrino detector at the South Pole in a similar way to RICE.

- **ARIANNA**
  The Antarctic Ross Iceshelf ANtenna Array (ARIANNA, [104]) is a proposed array of antenna stations on the surface of the Ross Ice Shelf (situated near McMurdo, Antarctica) and is designed to be sensitive to radio signals from neutrino-induced showers in the ice-layer. It has the advantage that the radio signals will be reflected at the ice-water interface so that the detection probability increases. A prototype station has been deployed in 2007 and further R&D efforts are ongoing.

- **SALSA**
  The SALt dome Shower Array (SALSA) has been proposed as a possible neutrino detector that could be deployed in a large salt formation [105, 106, 107]. Salt has the advantage of
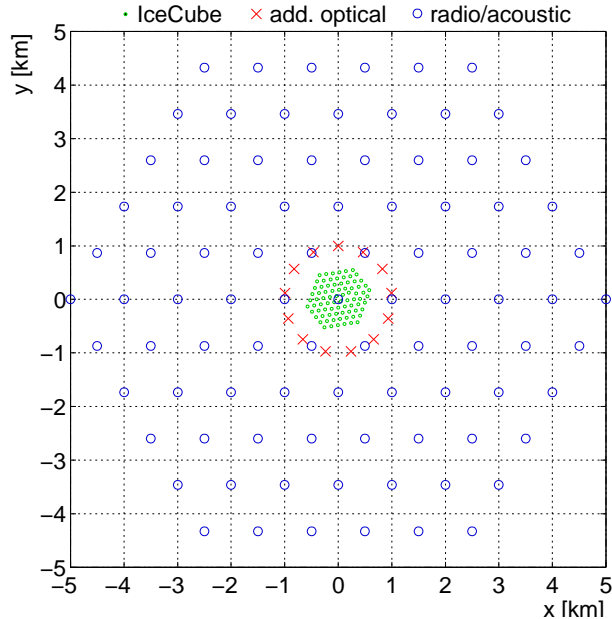
Figure 1.12: Geometry of the simulated hybrid array as presented in [88].

being much denser than ice so that the interaction probability is larger. Currently, attenuation length measurements and other feasibility studies (like drilling costs and procedures) are ongoing.

1.4.3 Acoustic neutrino detectors

Askaryan and Dolgoshein and, independently, Bowen proposed during the DUMAND-76 conference, the use of the expected acoustic signature from a high-energy particle cascade for the detection of neutrinos with energies in excess of 10^{16} eV at a great depth in the ocean. Many of the current large optical neutrino detectors have a dedicated acoustic R&D agenda and there are also a number of stand-alone acoustic neutrino detectors, all of which are discussed in §2.3.

1.4.4 Hybrid neutrino detection

Ice is the only naturally available target material on Earth that allows detection of all three neutrino-interaction signatures as radio waves do not propagate in water and the attenuation length for light is very short in both salt and permafrost. These are two other potential target media for acoustic neutrino detection (see §2.3.2). Ice therefore offers a possibility of hybrid neutrino detection. Where a single radio signal in ice by itself might not be a convincing neutrino candidate, a coincident acoustic and/or optical signature could eliminate all doubt and help calibrate the new experimental techniques.

IceCube is currently already the largest neutrino telescope. The simulations presented in [88, 108], despite using optimistic GZK-neutrino fluxes [51], have shown that the fully constructed IceCube detector is expected to detect less than 1 GZK-neutrino during one year of operation. It is therefore clear that IceCube does not have the required sensitive volume to detect or accumulate

the essential statistics of GZK-neutrinos in order to study spatial and energy distributions. Larger detector volumes are needed. The relatively short optical attenuation length [109], of the order of 120 m makes building a detector much larger than IceCube prohibitively expensive since it requires a high detector density. The idea of a hybrid optical-radio-acoustic detector at South Pole has been first suggested in [88] (see Fig. 1.12) and further adapted to an intermediate design in [108]. The simulations for the extensive hybrid array as presented in [88] showed an increased total event rate: 16 GZK neutrinos per year are expected to be detected by the acoustic array and 8 by both the acoustic and radio arrays using the optimistic neutrino flux from [51].

1.5   Conclusion

The current UHE CR experimental data still leaves room for speculation about the astrophysical sources of these high-energy charged particles and their exact nature. The detection of UHE neutrinos could open a new window into the Universe, increasing the understanding of the nature of the UHE CR composition and origin. The, sometimes called guaranteed, GZK neutrino flux is one of the main motivations to search for these neutrinos but other sources have also been suggested. However, the current and planned optical neutrino detectors do not yield sufficiently large rates in order to define the GZK spectrum amplitude and shape.

Indeed, the predicted UHE neutrino fluxes are extremely small and new experimental techniques, like radio Cherenkov and acoustic neutrino detection, may offer the possibility to cheaply instrument the required large volumes of target material due to the expected low attenuation of these signals. On top of that, they offer the unique possibility to detect a neutrino interaction in ice with three different experimental techniques: optical, radio and acoustic. Indeed, unlike the atmospheric neutrinos in the case of the lower energy optical arrays, the large radio or acoustic detectors will not have a calibration beam. Until now, no neutrino interaction has been detected by its radio or acoustic signature. The hybrid approach finds its strength in the possible cross-calibration of the different experimental techniques.

Therefore the acoustic neutrino detection technique, still in its infancy, is worth further consideration and investigation. In the next chapter, the thermo-acoustic model is discussed in detail and an overview of current acoustic neutrino detection projects is given. Also medium properties are reviewed, mainly for the Antarctic ice. It will be shown why this specific target material is possibly the most interesting for the acoustic (and hybrid) detection of UHE neutrinos.

Acoustic neutrino detection

The field of radiation-acoustics studies the conversion of energy that is deposited by penetrating radiation into sound energy. The precise mechanism for this sound generation depends on the specific type and intensity of radiation, the medium properties and the mode of energy release. The possibility of detecting the acoustic signal generated by a beam of charged particles in water was first suggested by G. A. Askarian in 1957 ([110]). His thermo-acoustic model was then further discussed by G. A. Askarian and B. A. Dolgoshein [111], and J. G. Learned [112]. More recent work presents computational methods to calculate the acoustic signature of UHE neutrino interactions in ice and water [74]. In this chapter, the thermo-acoustic theory and its experimental verification are presented. Furthermore, ice properties and current acoustic neutrino detection projects are discussed.

2.1 The thermo-acoustic model

2.1.1 Thermo-acoustic principles

The thermo-acoustic model states that an acoustic signal originates from the thermal stress caused by local heating due to ionisation energy loss by charged particles in electromagnetic or hadronic cascades. When a charged particle or beam of charged particles traverses a medium, it deposits energy along its path. The particle velocity in a cascade is on the order of the speed of light c and the speed of sound is typically at least 3 orders of magnitude smaller. The total energy deposition happens on a time-scale $\tau = L/c$, where L is the length of the track or cascade. Therefore, the energy deposition can be regarded as being instantaneous relative to slower energy dissipation processes. This thermal energy can then transform into sound wave energy in different ways. At moderate released energy densities, where no phase changes occur, the fastest and main contribution to the sound generation process is due to the thermal expansion of a region of the medium where the radiation is absorbed. The extent of this thermal expansion depends on the density distribution of the deposited energy. This is the thermoradiation (thermoelastic) mechanism of sound generation. In this case the generated sound fields can be described within the framework of the linear sound theory.

Liquids

In liquids, one can write the wave equation as follows [112, 111, 113]:

$$\Delta p(\vec{r}, t) - \frac{1}{c_l^2} \cdot \frac{\partial^2 p(\vec{r}, t)}{\partial t^2} = -\frac{\alpha}{C_e} \cdot \frac{\partial^2 q(\vec{r}, t)}{\partial t^2}, \tag{2.1}$$

where $p(\vec{r}, t)$ is the hydrodynamic pressure at a given place and time, c_l is the longitudinal sound speed in the liquid, C_e is the specific heat, α is the thermal expansion coefficient and $q(\vec{r}, t)$ is
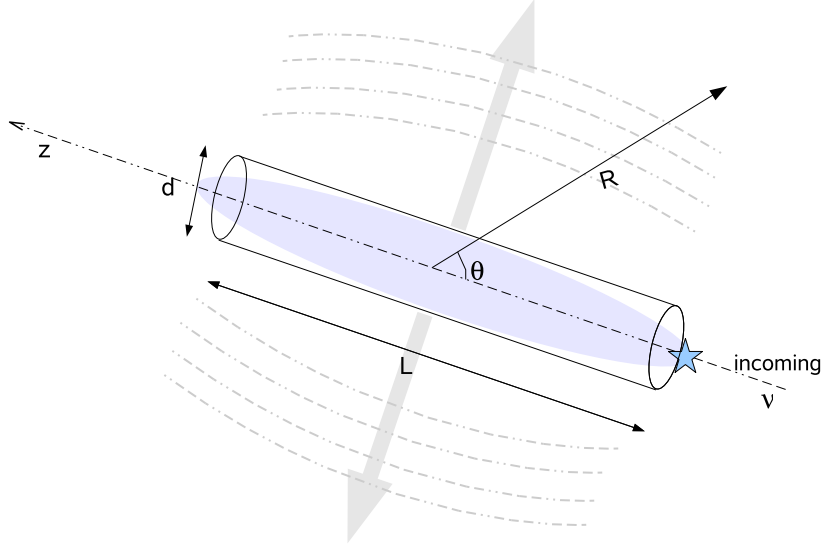
Figure 2.1: Illustration of the energy deposition and generation of sound by a UHE cascade originating form a neutrino interaction.

the energy deposition density. Therefore, the pressure field depends on the spatial distribution of the energy deposition of the particles in the cascade and on the temperature-dependent material properties α, c_l and C_e, as is also the case for solids (see next section). In [114] Eq. 2.1 takes the following form:

$$\frac{\partial^2 p(\vec{r}, t)}{\partial t^2} - c_l^2 \Delta p(\vec{r}, t) = \Gamma \frac{\partial Q(\vec{r}, t)}{\partial t}, \qquad (2.2)$$

where $Q(\vec{r}, t)$ is the function that characterises the energy release of the penetrating radiation and $\Gamma = c_l^2 \alpha / C_e$ is the Grüneisen parameter. The shape of the function $Q(\vec{r}, t)$, and therefore the energy density of the cascade, determines the shape and strength of the acoustic signal. A solution to Eq. 2.1 is given by the Kirchhoff integral [111]:

$$p(\vec{r}, t) = -\frac{\alpha}{4\pi C_e} \int \frac{dV'}{|\vec{r} - \vec{r}'|} \frac{\partial^2}{\partial t^2} q\left(\vec{r}', t - \frac{|\vec{r} - \vec{r}'|}{c_l}\right). \qquad (2.3)$$

The energy deposition can be regarded as being instantaneous compared to the timescales of the other processes involved:

$$\frac{\partial}{\partial t} q(\vec{r}, t) = q(\vec{r}) \delta(t), \qquad (2.4)$$

such that:

$$p(\vec{r}, t) = -\frac{\alpha}{4\pi C_e} c_l^2 \frac{\partial}{\partial R} \int_{S_r^R} \frac{q(\vec{r})}{R} d\sigma, \qquad (2.5)$$

where the integration is performed over the surface of a sphere with radius $R = c_l t$, at a time t, and whose centre is at the detection point with spatial coordinates $\vec{r}$. In order to calculate the acoustic signal at large distances (far-field), a frequency-dependent attenuation needs to be

included. The acoustic signal properties can then be calculated for a certain assumption of energy deposition density $q(\vec{r})$.

In [111], the cascade of particles is assumed to deposit its energy homogeneously inside a cylindrical volume $V = \pi a^2 L$, where L and $a = d/2$ are the effective longitudinal and transversal dimensions respectively, see Fig. 2.1. In the near-field at an optimal angle $(L\cos\theta/\lambda < 1)$, the frequency component of the sound pressure will be:

$$|p(f)| \sim \frac{f}{a\pi^2}\frac{\alpha}{C_e}\frac{E}{\sqrt{R}}, \tag{2.6}$$

where f is the frequency and E is the cascade energy. The frequency component of the sound pressure for the far-field is derived in [111]:

$$|p(f)| = \frac{f}{4\pi^2}\frac{\alpha}{C_e}\frac{E}{R}\frac{\sin X}{X}, \tag{2.7}$$

where $X = \lambda/2\pi < \cos\theta$. In the cylindrical approach, the radiation will be coherent for $f < f_{\text{peak}} = c_l/(2\pi\lambda)$, where $2\pi\lambda \sim 2a$ approximates the diameter of the energy deposition region. For a shower diameter in water of $(4\text{--}6)\,\text{cm}$, the peak frequency f_{peak} is about $25\,\text{kHz}$ [111]. The duration of the pulse is $\tau \sim 2a/c_l = 1/f_{\text{peak}}$, which is about $10^{-5}\,\text{s}$ in the case discussed here.

Solids

When an arbitrary disturbance takes place in an infinite solid, two types of bulk waves[1] are found to be possible. One type corresponds to the longitudinal wave motion and involves volume change of the medium. This type of wave is therefore called a dilatational or compressional wave. The second type does not involve any change in volume but involves shearing motions and can be identified with a transverse wave motion. This type of wave is known as transversal, rotational, solenoidal or shear wave. These two types of waves are also often referred to as P (primary) and S (secondary) waves.

In the linear theory of elasticity only the deformation for which stress is linearly related to strain is considered, see for example [115]. Stress is the force divided by the area on which the force acts and is represented by a 3-dimensional matrix (σ_{ik}). Deformation of a deformable body is said to be elastic when the body regains its original shape and size after the forces are removed. The displacement vector $\vec{u}$ has components that are defined as $u_i = x_i' - x_i$, where x_i and x_i' are the coordinates of a certain point respectively before and after displacement.

$$\epsilon_{ik} = \frac{1}{2}\left(\frac{\partial u_i}{\partial x_k} + \frac{\partial u_k}{\partial x_i}\right) \tag{2.8}$$

is called the strain tensor and describes the change in volume and shape of the body. For a perfect elastic body one can write Hooke's law, linking stress to strain, in a generalised form[2]:

$$\sigma_{ik} = c_{iklm}\epsilon_{lm}, \tag{2.9}$$

where c_{iklm} is a fourth rank tensor called the elastic constant tensor. In the most general case this tensor has 81 components. An isotropic solid is a solid for which the physical properties do

---

[1]Surface waves are not considered here.
[2]The Einstein summation convention is used, i.e. repeated suffixes imply summation.

not depend on the orientation of the solid. There are only two independent components in the elastic constant tensor for an isotropic body, these are often expressed in the form of the Lamé constants λ and G[3]. Eq. 2.9 can then be rewritten as [115]:

$$\sigma_{ik} = 2G\epsilon_{ik} + \lambda\theta\delta_{ik}, \tag{2.10}$$

where $\theta = \epsilon_{11} + \epsilon_{22} + \epsilon_{33} = \nabla \cdot \vec{u}$ is the dilatation.

The equation of motion relates the force, resulting from internal and external stresses, to the product of acceleration and density:

$$\frac{\partial\sigma_{ik}}{\partial x_k} + \Phi_i = \rho\frac{\partial^2 u_i}{\partial t^2}, \tag{2.11}$$

where ρ is the volume density and Φ_i is the external stress on the solid body[4]. So we find in vector notation combining Eq. 2.10 and Eq. 2.11:

$$\rho\frac{\partial^2\vec{u}}{\partial t^2} = (\lambda + G)\nabla(\nabla \cdot \vec{u}) + G\nabla^2\vec{u} + \vec{\Phi}. \tag{2.12}$$

This equation can be rewritten when neglecting the body forces and using the vector relationship $\nabla^2\vec{u} = \nabla(\nabla \cdot \vec{u}) - \nabla \times \nabla \times \vec{u}$ as:

$$\rho\frac{\partial^2\vec{u}}{\partial t^2} = (\lambda + 2G)\nabla(\nabla \cdot \vec{u}) - G\nabla \times \nabla \times \vec{u}. \tag{2.13}$$

This is an equation of motion and it can be separated in two parts: the dilatational part, for which $\theta = \nabla \cdot \vec{u}$ is finite but $\nabla \times \vec{u} = 0$, and the rotational part, for which $\nabla \cdot \vec{u} = 0$ and $\nabla \times \vec{u}$ is finite [115]. In the first case, when $\nabla \times \vec{u} = 0$, Eq. 2.13 simplifies to:

$$\rho\frac{\partial^2\vec{u}}{\partial t^2} = (\lambda + 2G)\nabla(\nabla \cdot \vec{u}) = (\lambda + 2G)\nabla^2\vec{u}. \tag{2.14}$$

If we now define c_l as:

$$c_l^2 = \frac{\lambda + G}{\rho}, \tag{2.15}$$

then we find:

$$\nabla^2\vec{u} = \frac{1}{c_l^2}\frac{\partial^2\vec{u}}{\partial t^2}. \tag{2.16}$$

By taking the divergence of each side we then find:

$$\nabla^2(\nabla \cdot \vec{u}) = \frac{1}{c_l^2}\frac{\partial^2}{\partial t^2}(\nabla \cdot \vec{u}), \tag{2.17}$$

or

$$(\nabla^2 - \frac{1}{c_l^2}\frac{\partial^2}{\partial t^2})(\nabla \cdot \vec{u}) = 0, \tag{2.18}$$

---

[3]Lamé used the Greek letter μ instead of G.

[4]The most common body force, for example, is gravity for which $\Phi_i = \rho g_i$, where g_i is the gravity acceleration vector.

showing that, when $\nabla \times \vec{u} = 0$, a wave type is obtained which involves a change in the volume of the medium. This type of wave is therefore called a dilatational or compressional wave. In plane wave solution of Eq. 2.16, $\vec{u}$ only depends on x_1 and on the time t. The only displacement will be u_1. This is in the direction of propagation and such a wave is called a longitudinal wave. c_l can then be interpreted as the longitudinal wave velocity.

If we now take the second case, where $\nabla \cdot \vec{u} = 0$, then the following equation can be found in a similar way:

$$(\nabla^2 - \frac{1}{c_t^2} \frac{\partial^2}{\partial t^2})(\nabla \times \vec{u}) = 0, \tag{2.19}$$

where c_t is defined as:

$$c_t^2 = \frac{G}{\rho}. \tag{2.20}$$

In the plane wave solution, we find that two plane waves will propagate in the x_1 direction, but with displacements in perpendicular directions, opposite of each other. This type of plane wave is named transverse wave or shear wave and c_t is the shear wave velocity. It is interesting to note that in an ideal fluid, for which $G = 0$, no shear wave can propagate.

In the case of thermo-acoustic sound generation, the deposition of thermal energy gives rise to stress. When the distance from the region of sound generation to the free boundaries of a body is large, the waves reflected from these boundaries can be excluded. This is the case for the acoustic field generated by a high-energy particle that interacted in the 3 km thick ice layer at the South Pole. Then, assuming a certain energy-release characterising function $Q(\vec{r}, t)$ in the case of an isotropic solid, the following relation (for the longitudinal wave) can be derived [114, 116]:

$$\left(\Delta - \frac{1}{c_l^2} \frac{\partial^2}{\partial t^2} \right) (\nabla \cdot \vec{u}) = \frac{(3 - 4n^{-2})\alpha}{C_e \rho} \int \Delta Q(\vec{r}, t) dt, \tag{2.21}$$

where $n = c_l/c_t$, ρ is the medium density, α is the linear thermal expansion coefficient and C_e is the specific heat of the solid. There are no external forces of interest here: only thermal sound sources are taken into account. Since the energy-release characteristic time is very short compared to the characteristic times of the other processes involved, one can approximate the spatial dependence of the function of energy evolution Q as:

$$Q(x, y, z) = \frac{\mu E}{\pi a^2} e^{-\frac{x^2 + y^2}{a^2}} e^{-\mu z} \Theta(z), \tag{2.22}$$

where E is the cascade energy, μ^{-1} is the effective cascade length, a is the effective cascade radius and Θ is the Heaviside function[5]. Equation 2.22 approximates the energy absorption along the cascade axis (z) to be exponential and the radial intensity distribution in the (x, y) plane (perpendicular to the axis of shower development z) of the cascade of particles is assumed to be Gaussian.

The expressions for the longitudinal component of the stress tensor in a boundless solid elastic medium is [116][6]:

$$\sigma_{RR} = -\frac{(3 - 4/n^2)\alpha E}{8\pi C_e R \tau_\mu^2} e^{\frac{\tau_a^2}{4\tau_\mu^2}} e^{-\frac{R - c_l t}{c_l \tau_\mu}} \text{Erfc} \left(\frac{\tau_a}{2\tau_\mu} - \frac{R - c_l t}{c_l \tau_a} \right), \tag{2.23}$$

---

[5]$\Theta(x) = \int_{-\infty}^{x} \delta(t) dt$

[6]$\text{Erfc}(z) = 1 - \text{Erf}(z) = \frac{2}{\sqrt{\pi}} \int_{z}^{\infty} e^{-t^2} dt$

	ocean	ice	salt
T [°C]	15	–51	30
c_l [m s^{-1}]	1530	3920	4560
α [K^{-1}]	2.555×10^{-4}	1.25×10^{-4}	1.16×10^{-4}
C_e [J kg^{-1} K^{-1}]	3900	1720	839
$\Gamma = c_l^2 \frac{\alpha}{C_e}$	0.15	1.12	2.87

Table 2.1: Grüneisen parameter Γ for ocean-water, ice and salt. Γ is a figure of merit for each medium that indicates the efficiency of conversion of ionisation energy into acoustic energy for water, ice and salt [117]. It therefore gives an indication for the relative acoustic pulse heights for the different media.

R is the distance to the middle of the cascade measured in meters. $\tau_a = a \sin(\theta)/c_l$ and $\tau_\mu = \cos(\theta)/\mu c_l$, where θ is the angle between the shower axis z and line linking the point of observation with the point of interaction (at the start of the cascade), see [116]. For Antarctic ice it is assumed in [116], for a cascade energy of $E = 10^{15}$ eV, that $1/\mu \sim 4$ m, $a \sim 2$ cm, $c_l = 4 \cdot 10^2$ m/s, $n = 2$, $\alpha = 5 \cdot 10^{-5} \mathrm{s}^{-1}$ and $C_e = 2 \cdot 10^3$ J/(kg·C) (for an ambient temperature of –20 °C). In the near-field case ($R < 100$ m), the effective longitudinal sound pressure in ice (in Pa) can then be derived [116]:

$$p_{\text{eff}} \sim \frac{E}{E_0} \frac{1}{\sqrt{R}}, \tag{2.24}$$

where $E_0 = 10^{16}$ eV.

In the far-field case ($R > 100$ m) when $\tau_a \gg \tau_\mu$ (observation point close to the (x,y) plane that is perpendicular to the cascade axis), an estimation for the effective sound pressure in ice (in Pa) is:

$$p_{\text{eff}} \sim 10^{-1} \frac{E}{E_0} \frac{1}{R}. \tag{2.25}$$

In the far-field case when $\tau_a \ll \tau_\mu$, i.e. the observation point does not have an small angle to the (z-axis):

$$p_{\text{eff}} \sim 10^{-5} \frac{E}{E_0} \frac{1}{R}. \tag{2.26}$$

Therefore the far-field effective pressure drops significantly when the observation point is not close to the plane that is perpendicular to the (x,y) plane z-axis: the pressure field has a "pancake-shape". In [116] it is also shown that the level of shear stress caused by transverse waves originating from the thermo-acoustic mechanism of sound generation is approximately five orders of magnitude smaller than the corresponding longitudinal wave pressure for the same observation point.

The same near-field and far-field behaviour is found in liquids and in solids. The acoustic signal scales linearly with the total deposited energy in both cases. Also, in both media, a strong focusing of the emission in the place perpendicular to the cascade axis is observed. This is a ring-shaped bipolar pressure front that radially expands in the (x,y) plane. The effective sound pressure created at the shower in ice is expected to be approximately one order of magnitude higher than the effective sound pressure in water, other conditions (like shower length and radius) being close to equal. For the simulations presented in [74], the in-ice pulses are about a factor 6

larger than the in-water pulses. This difference is mainly caused by the fact that the Grüneisen parameter ($\Gamma = \alpha c_l^2 / C_e$) for ice is about a factor 7 larger than that for ocean water (see Table 2.1).

The specific solutions discussed for liquids (like the cylindrical approximation) are also applicable to the in-ice calculations [116]. This means that pulse duration τ and peak frequency f_{peak} both scale with the sound speed in ice. Therefore the pulse length in ice is expected to be shorter than for water. Similarly the expected peak frequency is higher for ice than for water.

In an anisotropic crystal there is often no simple relation between the direction of propagation of a wave and the direction of particle displacement. In other words, in general, the waves are not pure longitudinal or transverse types but are some form of mixed type (for a review on crystal acoustic, see for example [118]). Inhomogeneities and grain boundaries in the ice allow the scattering of longitudinal into transverse waves. The presence of transverse waves from a cascade in ice can provide additional information on the distance to the cascade due to the difference in propagation speeds for longitudinal and transversal waves, but this information can be lost due to the scattering effects. Many polycrystalline materials behave as if they were isotropic although they are actually composed of a more or less random arrangement of small crystals or grains. This is the case, in first approximation, of the ice at the South Pole which is the material of interest to this work.

2.1.2 Signal properties

When considering the design of future acoustic high-energy neutrino detectors, it is important to understand the expected signal properties of an acoustic pulse that originates from a high-energy cascade. Also the propagation through the detector medium need to be investigated. The following signal properties are expected from a neutrino-induced high-energy cascade, using the results from the simulations presented in [74]:

- The expected pressure pulse has a bipolar shape with a duration that depends on the radial dimension of the shower and the sound velocity, see Fig. 2.2. The pulse is narrower in ice than in water. The bipolar shape can be understood as follows. The energy deposition along the line of sight of the sensor can be approximated by a Gaussian. The pressure pulse is proportional to the derivative of this energy deposition.

- The signal peak frequency is expected to be higher in ice than in the ocean water. In ocean water, the mean frequency at 1 km distance is about 20 kHz. This depends on distance due to the frequency-dependent absorption effects in the ocean water. For ice, the mean frequency is claimed to be around 40 kHz in [74] and 90 kHz in [116].

- The maximum amplitude of the bipolar pulse grows linearly with the cascade energy, E_ν.

- Once outside the plane perpendicular to the shower axis (x, y) by more than a few degrees, the amplitude of the pressure will follow a $1/\sin^2 \theta$ distribution, where θ is defined as the angle between the line of observation and the plane perpendicular to the shower axis.. See also Fig. 2.3. The resulting pressure field is "pancake-shaped": the acoustic energy is concentrated in a flat disc perpendicular to the shower axis which narrows further with increasing energy.

- Three main propagation regions can be distinguished: the near-field, the far-field and the attenuation region. In the near-field, the distance to the shower is such that the shower is
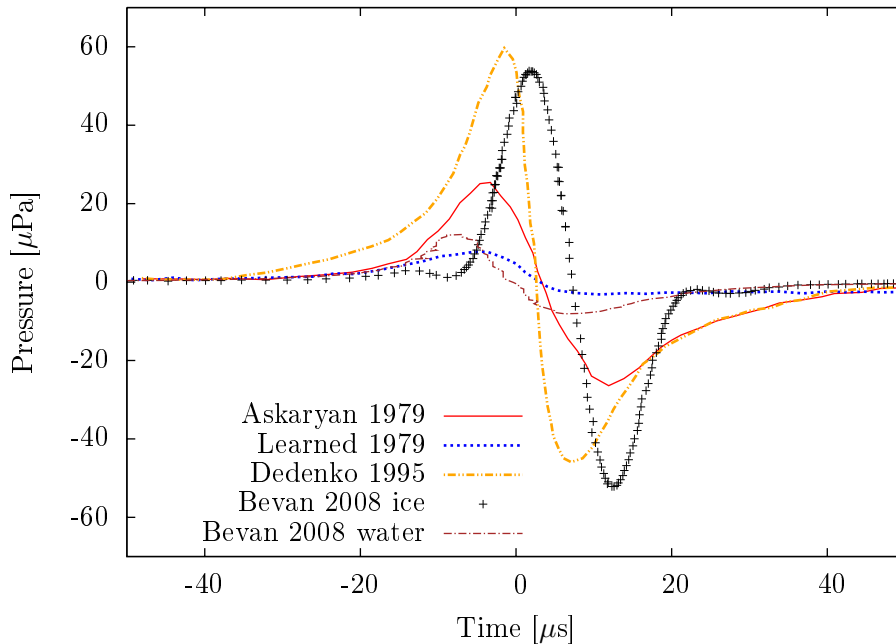
Figure 2.2: The acoustic bipolar pulse originating from a high-energy neutrino interaction in water at 400 m distance for a primary neutrino energy of E_ν=10 PeV (Dedenko, Learned and Askaryan) and in ice and water at 1 km for E_ν=10 PeV (Bevan). The in-ice pulse was delayed and scattering-dominated attenuation was applied. Adapted from [74] and [119].

still seen as a line-source. In this regime, the amplitude will scale with $1/\sqrt{r}$, where r is the distance to the cascade. In the far-field, the shower is seen as a point-source and the amplitude scales with $1/r$. At a certain distance, depending on the medium and the signal mean frequency, an exponential attenuation needs to be taken into account: $\exp(-r/\lambda)$, where λ is the attenuation length.

In this section, it was shown that a cascade that originates from a UHE neutrino interaction in water or ice will generate a clearly recognisable acoustic signature. A pancake-shaped shock front will propagate perpendicularly to the cascade-axis and the neutrino direction can then be reconstructed. The acoustic signal amplitude scales linearly with the cascade energy (and therefore also with the primary neutrino energy) and the pulse has a bipolar shape with a distinct frequency-content. Depending on the acoustic properties of the target material, the signal will be deformed and attenuated.

2.1.3 Experimental verification

Initial experimental verification of the thermo-acoustic model was driven by the first publications by Askarian, Dolgoshein and Learned and then also by the proposed DUMAND experiment in the 1970s. The experimental approach is to use accelerator beams or lasers to simulate a cascade generated by an UHE neutrino interaction in a dense medium. This requires high intensities so that the the energy depositions are close to what is expected in a UHE neutrino-induced cascade.
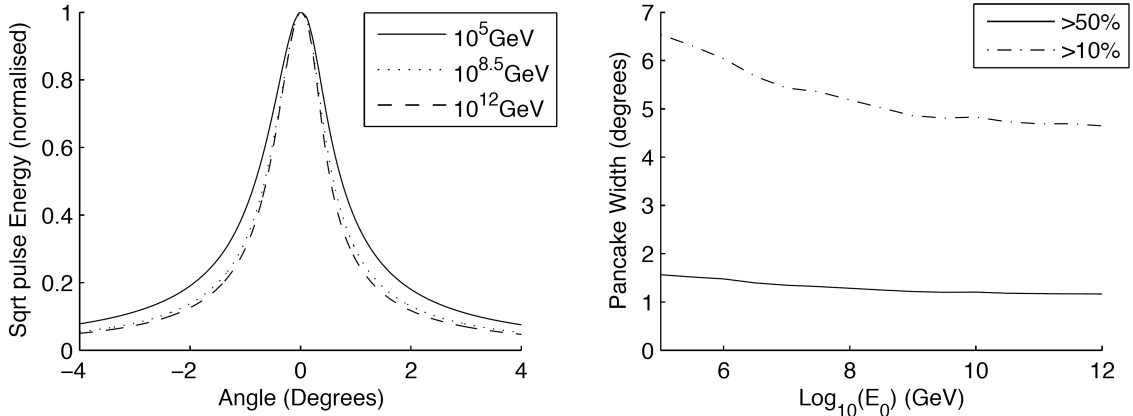
Figure 2.3: Variation of acoustic pulse energy with angle in ice. Left: Square root of the pulse energy versus angle. Right: Full width for 10 and 50% of maximum versus energy. From [74].

The comparison of the experimental results with the theoretical calculations and simulations indicates that the thermo-acoustic generation of sound has been confirmed experimentally. An overview of experiments that investigate acoustic signals originating from radiation interacting with matter can be found in [116]. Several signatures allow to confirm the thermo-acoustic nature of a detected acoustic pulse in accelerator experiments:

- For water, an important signature of thermo-acoustic sound generation is that the signal amplitude is expected to fall to zero when the water is at the critical temperature $T_c = 4\,^\circ$C. This is due to the fact that water has the largest density at that temperature. Therefore the expansion coefficient α will be positive above T_c and negative below T_c. The signal amplitude is expected to scale with the ratio α/C_e and should vanish at T_c where a inversion of the phase of the pulse occurs.
- Theory predicts a linear dependence of the amplitude of the acoustic signal on the deposited energy.
- A $1/\sqrt{r}$ dependence is expected in the near-field and a $1/r$ dependence in the far-field.

Proton and laser beam

Sulak [120] reports on experiments on sound excitation by a beam of protons in water at the linear accelerator of the Brookhaven National Laboratory (BNL) in 1977. The dimensions of the water enclosure were much larger than the proton beam track length so that the direct acoustic signal could be clearly distinguished from reflections.

In a first run, the proton track length in water was about 30 cm and the beam was pulsed with pulse lengths from (3–200) μs. The energy release from a single pulse varied from (10^{10}–10^{21}) eV within a constant diameter of 4.5 cm. For a second series of experiments at the same accelerator, the energy of the protons in the beam went up to 28 GeV. In this second run, a pulse typically shorter than 2 μs consisted of $3 \cdot 10^{11}$ protons that travelled a distance of 20 cm. The beam diameter was varied from (5–20) mm. All the above mentioned signatures of thermo acoustic sound generation were confirmed in the experiments presented in [120], clearly proving
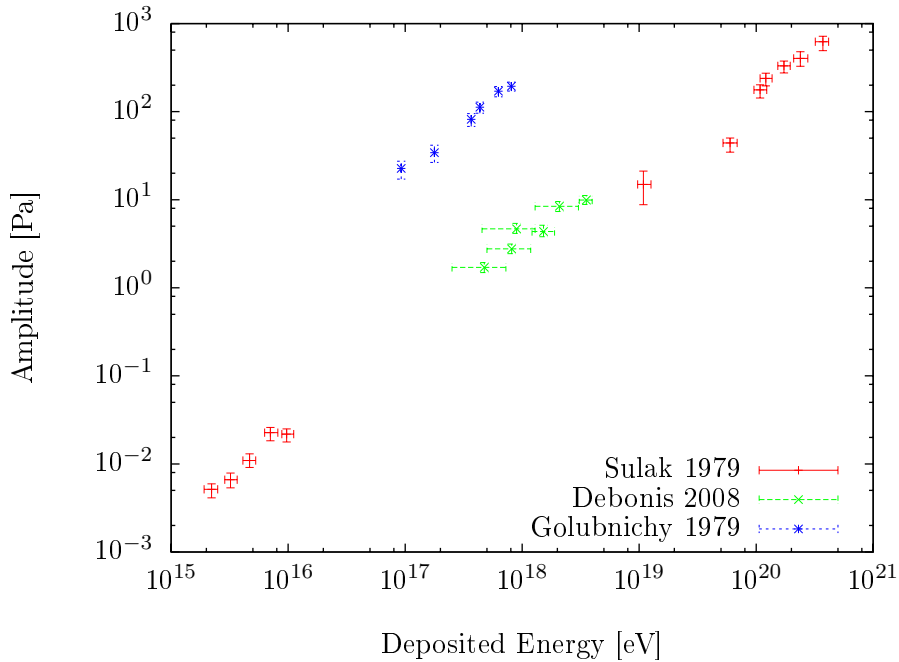
Figure 2.4: Linearity of the signal amplitude with the total deposited energy for the [120] (two independent data sets), [121] and [124] data. Adapted from [121] and [124].

the thermo-acoustic nature of the observed acoustic pulses. More recently, a similar series of measurements for water were performed with the proton beams of the Institute of Theoretical and Experimental Physics (ITEP, Moscow, Russia) accelerator [121] and the Theodor-Svedberg laboratory cyclotron [122]. Figure 2.4 shows the amplitude of the acoustic signal as a function of total deposited energy for both BNL and ITEP measurements. The proton beam of the Theodor-Svedberg laboratory cyclotron was also aimed at a block of ice containing acoustic transducers [123] thus verifying the thermo-acoustic sound generation mechanism in ice.

Lasers can also be used to generate an acoustic field in liquids. In [124], a solid state laser heated a cylindrical region with a diameter up to 4 mm and a length up to 7.5 cm in water. The results show a clear phase inversion at a water temperature of 4 °C and are in agreement with the proton beam experiments, see Fig. 2.4. In this figure, the three experiments had hydrophones positioned at different distances from the beam axis and this difference in geometry explains the fact that the three data-sets lie on three different lines.

In [122], experiments in water at both an infrared laser facility and at a proton accelerator are presented. The measured bipolar pulses and the signal dependence on beam energy, beam width and sensor distance from the beam axis were found to be in good agreement with the expectations from the thermo-acoustic theory.

Electron beam

Table 2.2 shows an overview of three experiments that investigated the acoustic signal originating from the interaction of an electron beam-pulse in water.

Year	Accelerator	e^- energy	Beam diameter	Spill time	Current	Reference
1987	NRI-RAS	10–70 MeV	$\sim 2\,\text{cm}$	$1.4\,\mu s$	0–$10\,\mu A$	[125, 116]
2006	MSU-SINP	50 MeV	max. 1.0 cm	$8.0\,\mu s$	2 mA average	[126]
2007	UGent LINAC	3–15 MeV	max. 1.0 cm	1–$16\,\mu s$	2 mA average	[127]

Table 2.2: Overview of electron beam radiation acoustic experiments
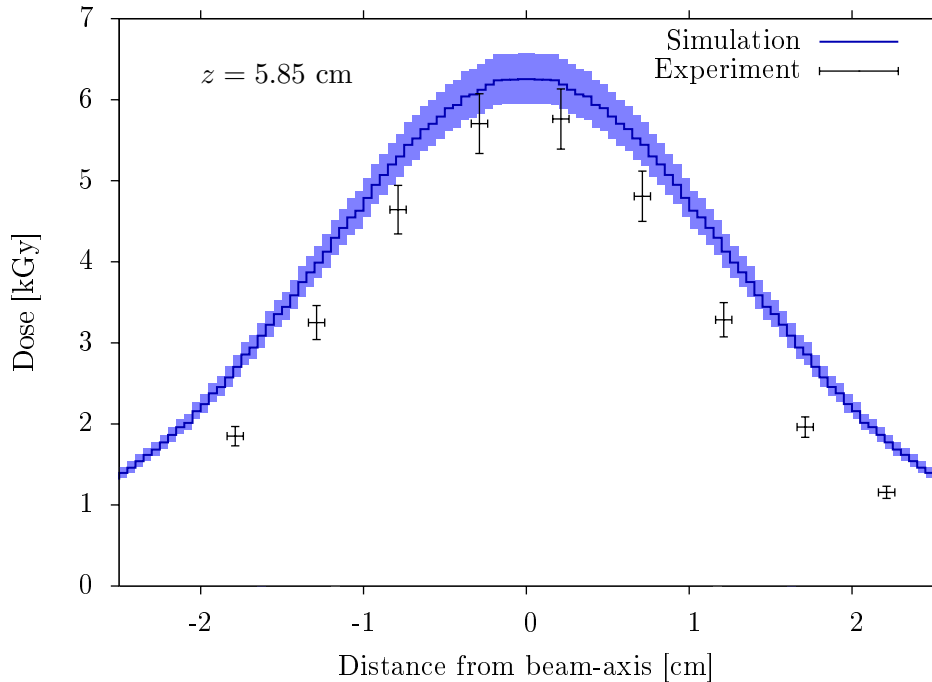
Figure 2.5: The UGent LINAC electron beam deposited dose in water. The simulated (blue line with light-blue 5% error-band) and measured (black points with 3σ error bars) deposited dose for a distance of 5.6 cm along the beam axis. Adapted from [127].

The UGent electron LINAC [128, 129] was used in 2007 in order to verify the thermo-acoustic model in water; this is reported upon in detail in [127]. The experiment took place at the e^--exit of the accelerator (see Fig. 2.6(a)), where electrons of (3–15) MeV in bunches of (1–10)μs were delivered. The maximum average current achieved was 2 mA. First, the (x-z) shower energy profile was measured with radiochromic dosimeters[7], and compared to a simulation of the e^--energy deposition. It was found that the transverse shower profiles can be fitted with Gaussians. Figure 2.5 shows an example of a deposited dose transverse profile. The dose was absorbed within a cylinder of about 10 cm length and 4 cm radius. The simulated (x-z) deposited dose is shown in Fig. 2.6(b). The simulation yields a systematically larger absorbed dose with a broader transverse spread. A possible explanation for this is the loss of electrons outside the radiated water volume during the experimental dosimetric measurement. The simulated energy density profiles were used to calculate the expected thermo-acoustic pulse ([127]) emitted by the

---

[7]FWT-70-83m
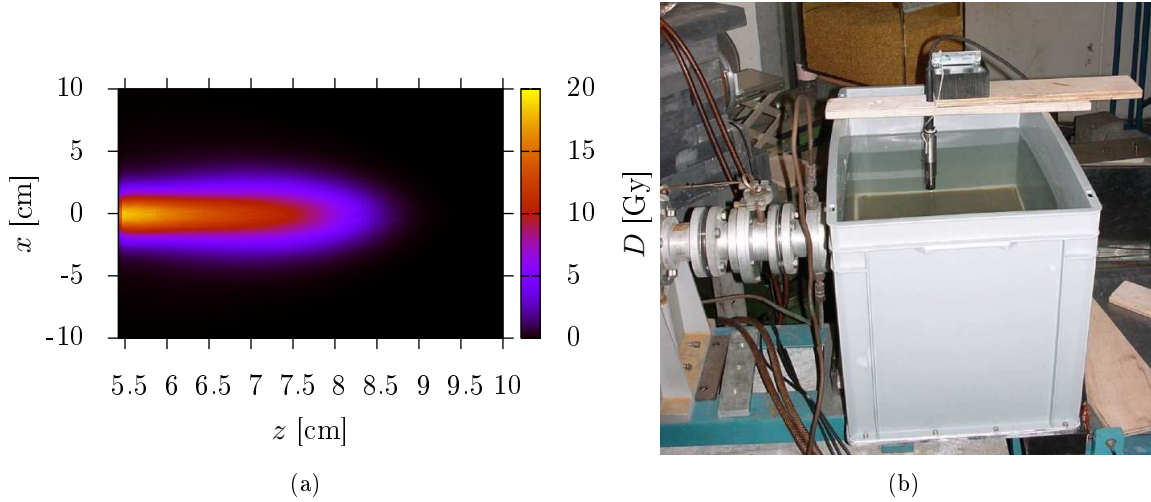
Figure 2.6: (a): The simulated deposited dose in (x, z) plane, where z is the beam axis. (b): The UGent e^- LINAC thermo-acoustic setup. A commercial hydrophone was placed inside the plastic vessel in the water at different positions relative to the beam axis. Both from [127].

cylindrical acoustic antenna that is formed by the energy deposit in the water.

Next, a plastic vessel filled with water was then placed at the same location and a positioning system was used to hold the submerged hydrophone in place. Figure 2.6(a) shows the experimental setup. The commercial hydrophone[8] with a flat frequency response in the (4–65) kHz region was then placed at several distances and angles from the beam axis and the recorded signal was compared to the simulated pulses (Fig 2.7(a)). The 50 Hz repetition rate allowed for the thermo-acoustic pulses to be clearly distinguishable from reflected waves originating from the vessel walls. The UGent LINAC test has yielded the following results:

- Bipolar acoustic pulses generated by the absorption of radiation in water have been observed by a commercial hydrophone.

- Simulation and data agree qualitatively on the shape of the bipolar pulse.

- No final conclusion on the near- or far-field behaviour is possible, although the $1/\sqrt{d}$, with d the distance to the shower axis seems to fit the data better. See Fig. 2.7(b)).

- The results are in agreement with previous thermo-acoustic experiments using e^- beams in water, see Table 2.3.

However, the UGent LINAC test presented here did not scan a temperature or energy range and therefore the purely thermo-acoustic nature of the pulses was not verified for that setup. Nevertheless, there is a good qualitative agreement between the simulated and experimentally measured acoustic pulse and both are in agreement the results of previous experiments.

---

[8]SensorTech SQ03 from Sensor Technology Limited, see http://www.sensortech.ca/userfiles/file/SQ03(4).pdf
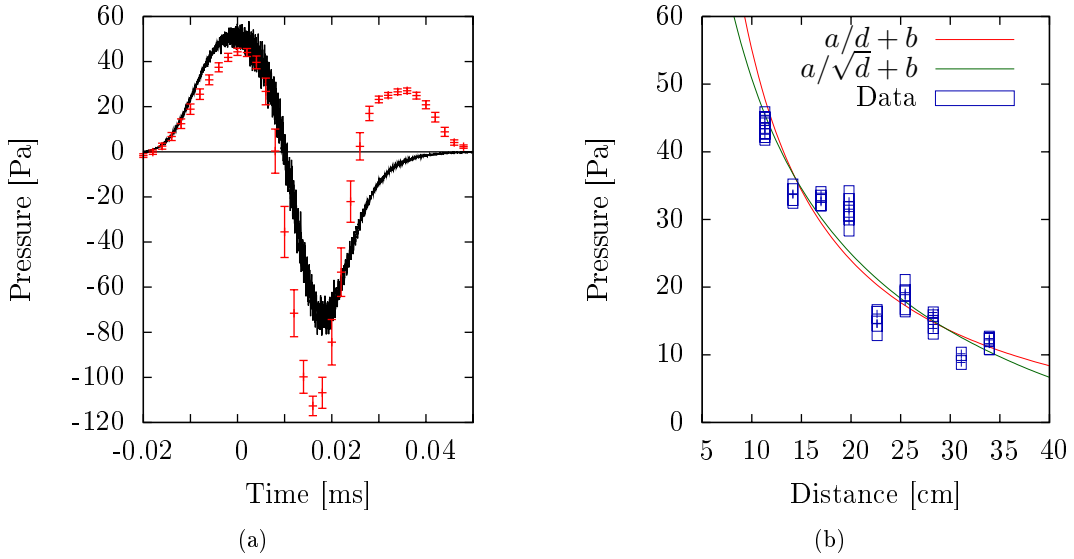
Figure 2.7: The UGent LINAC electron beam thermo-acoustic signal. (a): Comparison between the simulated (black band) and measured (red data points) acoustic bipolar pulses for $x = z = 8$ cm. (b): The maxima of the acoustic bipolar pulses as a function of the distance d to the beam axis. Both near-field and far-field behaviours have been fitted. Both figures from [127].

Experiment	Total Energy [eV]	Acoustic Pulse Length [μs]	Acoustic Pulse Height
[125, 116]	$\sim 10^{18}$	60	[-30,30] Pa
[126]	$\sim 10^{18}$	60	[-0.2,0.1] V
[127]	$\sim 10^{19}$	60	[-110,40] Pa

Table 2.3: Overview of electron beam radiation acoustic pulse characteristics. N o absolute pressure value was given in [126].

2.2 Detection principles

An acoustic detector in general consists of a sensitive element which generates an electrical signal that is linearly dependent on the incident pressure wave. It is also called a transducer[9]. This output then goes to an amplifier or a chain of amplifiers. The transducing element is often a piezo-electric element, typically followed directly by a preamplifier.

2.2.1 Piezoelectric material

Piezo-electricity is a property that certain di-electric materials (like certain crystals and ceramic materials) possess to generate an electric potential in response to applied mechanical stress. The

---

[9]A transducer is an electronic device that converts energy from one form to another, in this case acoustic to electric energy or the other way around

collective charge then induces a voltage across the material. Piezoelectric materials also show the opposite effect, called converse piezoelectric effect, where the application of an electrical field creates mechanical deformation in the material. The first demonstration of the direct piezoelectric effect was in 1880 by the brothers Pierre and Jacques Curie. Piezoelectricity occurs in certain natural materials, like cane sugar and dried bone for example.

Nowadays, man-made piezoelectrical materials are used in a large variety of applications from medicine to musical instruments. These industrially manufactured materials can be shaped on demand and are either crystals (like gallium orthophosphate) or ceramic materials. Lead zirconate titanate ($Pb[Zr_x Ti_{1-x}]O_3$ where $0<x<1$), more commonly known as PZT, is the most common piezoelectric ceramic in use today.

PZT-based compounds are composed of the chemical elements lead and zirconium, and the chemical compound titanate which are combined under extremely high temperatures and the resulting hard, dense ceramics can be manufactured in almost any given shape or size. The piezoelectric effect for a manufactured item then depends on the PZT-type and the orientation of the mechanical and electrical axes. These axes are set during "poling"; the process that induces piezoelectric properties in the ceramic.

The orientation of the DC-poling field determines the orientation of the mechanical and electrical axes. Indeed, the individual PZT crystallites are piezoelectric (see Fig. 2.8) but because of the random distribution of the Weiss domain[10] orientations in the ceramic material no macroscopic piezoelectric behaviour is observable. During poling, the different domains are permanently aligned using a strong electric field, sometimes at elevated temperatures. The material then has a remnant polarisation and exhibits piezoelectric properties. The remnant polarisation can be degraded by exceeding the mechanical, thermal and electrical limits of the material. For example, if such an element is brought above its Curie temperature[11], a phase transition will occur and the piezoelectric properties will be lost.

The behaviour can be described by the electromechanical properties of the PZT material in the case where the dependence on temperature and magnetic fields can be neglected. It is then possible for small electrical and mechanical amplitudes to be described by linear relationships between the mechanical strain

Figure 2.8: Perovskite-type lead zirconate titanate (PZT) unit cell in the tetragonally distorted configuration below the Curie temperature.

(S) or mechanical stress (T)[12] components and the components of the electric field E or the dielectric displacement D. These linear relationships are derived using dielectric, piezoelectric and elasticity "constants". Because they depend on the anisotropy of the piezoelectric material, these physical quantities can only be defined in terms of tensors which reflect the directionality of

---

[10] Groups of unit cells with the same orientation are called Weiss domains.

[11] The Curie temperature for piezoelectric materials is the temperature above which the material loses its spontaneous polarisation and piezoelectric characteristics.

[12] Stress is force per area and strain is deformation of a solid due to stress.

the electric field, the mechanical stresses, etc. In simplified form, the basic relationships between the electrical and elastic properties (for a static or quasi-static application) can be represented as follows:

$$D = dT + \epsilon_T E, \qquad (2.27)$$

$$S = s_E T + dE, \qquad (2.28)$$

where d is the piezoelectric charge (or strain) constant, ϵ_T the permittivity and s_E is the elasticity constant. d is a measure of the electric charge induced in response to a mechanical stress, or the achievable mechanical strain when an electric field is applied ($T = $ constant). For example, an important material constant is d_{33}, which is the charge density developed per mechanical stress, or, alternatively, strain developed per unit of electric field strength, all in the polarisation direction. "Soft" piezo-ceramics are characterised by a comparatively high domain mobility and a resulting relatively easy polarisation. In contrast, ferro-electrically "hard" PZT materials can be subjected to high electrical and mechanical stresses.

2.2.2 Acoustic impedance

The characteristic acoustic impedance is equal to the product of the density of the medium ρ and of the speed of sound c_l in the medium [130]:

$$Z_l = \rho c_l, \qquad (2.29)$$

and a similar relation also exists for the shear waves. Acoustic impedance is measured in Rayles ($1 \, \mathrm{Rayle} = 1 \, \mathrm{kg}/(\mathrm{m}^2\mathrm{s})$). At the boundary of two different materials with different impedances, the acoustic transmission and reflection are dictated by the difference in acoustic impedance. This difference in Z is commonly referred to as the impedance mismatch. The greater the impedance mismatch, the greater the fraction of energy that is reflected at the interface or boundary between one medium and another. Impedance matching is therefore important for the design of acoustic sensors, since minimal distortion of the acoustic waves is desirable.

The fraction of the incident wave intensity that is reflected can be derived since particle velocity and local particle pressures must be continuous across the boundary. The reflection coefficient R is the ratio of the amplitudes of the reflected A_r and incident wave A_i [130]:

$$R = \frac{A_r}{A_i} = \frac{(Z_2 \cos \phi_i - Z_1 \cos \phi_t)}{(Z_2 \cos \phi_i + Z_1 \cos \phi_t)}, \qquad (2.30)$$

and

$$\sin \phi_t = \left(\frac{c_2}{c_1} \right) \sin \phi_i, \qquad (2.31)$$

where c_1 and c_2 are the medium velocities, Z_1 and Z_2 are the medium acoustic impedances, ϕ_i is the incident angle and ϕ_t is the angle of the transmitted wave relative to the line orthogonal to the boundary (transmitted angle). In solids, this relation applies for both the longitudinal and shear waves (with their respective sound speeds and impedances).

In the generalised case of an acoustic wave incident on an impedance boundary, mode conversion can occur (if one of the two media is a solid). This means that shear waves will be created at for example water-ice boundaries. The amount of energy going into the shear wave depends on the

Material	c_l [m/s]	ρ [kg/m^3]	Z [Rayle]	R rel. ice
ice	3980	920	3.6×10^6	0
air	343	1.2	412	~ 1
fresh water	1480	1000	1.48×10^6	0.41
steel	5940	7800	4.7×10^7	0.85
PZT	5000	7700	3.85×10^7	0.83

Table 2.4: Overview of acoustic characteristic impedance for ice, air, water, steel and PZT.

exact geometry (incident angles for all planes). Table 2.4 gives the characteristic impedances for a selection of materials. Also the reflection coefficient in case of a normally incident longitudinal wave is calculated. Steel and PZT have well matched impedances whereas ice/air boundaries will almost completely reflect all acoustic waves.

2.2.3 Detector selfnoise

To an even greater extent than a sensor's sensitivity, which can in principle be arbitrarily increased by internal or external amplification, a sensor's detection capabilities are limited by its intrinsic noise. This noise has two distinct components:

- Intrinsic noise of the piezo-element resulting from thermal movement which induces voltage signals on the electrodes.

- Noise from the amplifier, both from active components (operational amplifier, transistors) and from passive components (resistors).

In a multi-stage architecture, everything except the first amplifier stage can be neglected as long as the initial gain is high enough.

The resulting total in-situ noise can be divided in two types: the continuous and transient noise. The continuous noise is defined as having a continuous distribution, such as for example a normal distribution. A transient noise event is an event that is localised in time. It is a short pulse which represents a sudden change compared to the continuous background.

2.3 Acoustic neutrino detectors

Here we give a short overview of the results of a selection of the acoustic neutrino detection projects in water and discuss possible other target materials.

2.3.1 In-water acoustic experiments

The following acoustic projects operate in water:

- **AMADEUS**: The AMADEUS (Antares Modules for Acoustic DEtection Under the Sea) project is integrated into the ANTARES [83] Cherenkov neutrino telescope. Its main goal is to evaluate the feasibility of a future acoustic neutrino telescope in the deep sea operating in the UHE regime [131]. Their latest results show good transient reconstruction

capabilities but no overall transient trigger rate is given. The majority of the transients can be correlated with the ANTARES acoustic positioning system or are downgoing events originating from above the array [132, 133]. An 80% correlation coefficient between wind speed and the mean detected noise rate was found, leading to conclude that the deep-sea noise level is dominated by the state of the sea-surface. The mean power spectral density[13] was 21.8 mPa over an 8-week data taking period.

- **Lake Baikal**: An acoustic module, designed to allow common operation with the Baikal neutrino telescope NT200+, was installed in April 2006 at a depth of 150 m. Acoustic signals are recorded by commercial hydrophones. High noise contributions were observed during the freezing and unfreezing of Lake Baikal. In stable noise conditions, the recorded noise was about 6 mPa [134]. Transient sources have been recorded and localised from both the ice-camp[14] and a calibration device.

- **SAUND**: The Study of Acoustic Ultra-high-energy Neutrino Detection (SAUND, [135]) is an ocean-based acoustic neutrino detection project that uses part of a large ($\sim$250 km^2) military hydrophone array in the Bahamas. SAUND was the first acoustic neutrino detection project that has published a neutrino flux limit [135]. The limit is not competitive with the best limits (obtained with radio techniques) but it represents the first UHE acoustic neutrino detector proof of principle.

- **ACORNE**: The Acoustic COsmic Ray Neutrino Experiment (ACORNE) project is based in the UK and has access to the military ranging array situated between the Scottish mainland and the island of Rona. The data have enabled a limit on the sensitivity to neutrino fluxes as a function of incident neutrino energy [136].

Figure 2.9 shows the sensitivities for both the SAUND and ACORNE arrays. Both experiments used military hydrophone arrays, therefore the detector geometry was far from ideal and the obtained datasets do not yield competitive sensitivities. In [137] the sensitivity of large hydrophone arrays is investigated. It is found that, in order to observe and successfully reconstruct GZK-neutrinos, a gigantic hydrophone array encompassing several thousands of cubic kilometers and operating at very low, and possibly unrealistic, pressure thresholds ($\sim$5 mPa) is needed.

2.3.2 Other target materials

Table 2.1 also shows the material properties ice and NaCl (salt).

The acoustic signal amplitude in salt is expected to be more than a factor of 2 larger than in ice and therefore natural salt domes have been proposed as a possible medium for acoustic neutrino detection. The attenuation of an acoustic wave in pure salt is predicted to be dominated by scattering at the boundaries of recrystallised grains that have random orientation. The predicted scattering length is about 1.4 km at 30 kHz [139]. There was no report on any activity on acoustic neutrino detection in salt at the last ARENA (Acoustic and Radio EeV Neutrino Detection Activities) workshop in 2008. An interesting new target material candidate is proposed in [140], namely permafrost. It has a larger density than water and exists in natural and large volumes.

---

[13]The power spectral density describes how the power of a signal is distributed with frequency.

[14]The Baikal ice-camp is a winter camp situated on the frozen lake surface.
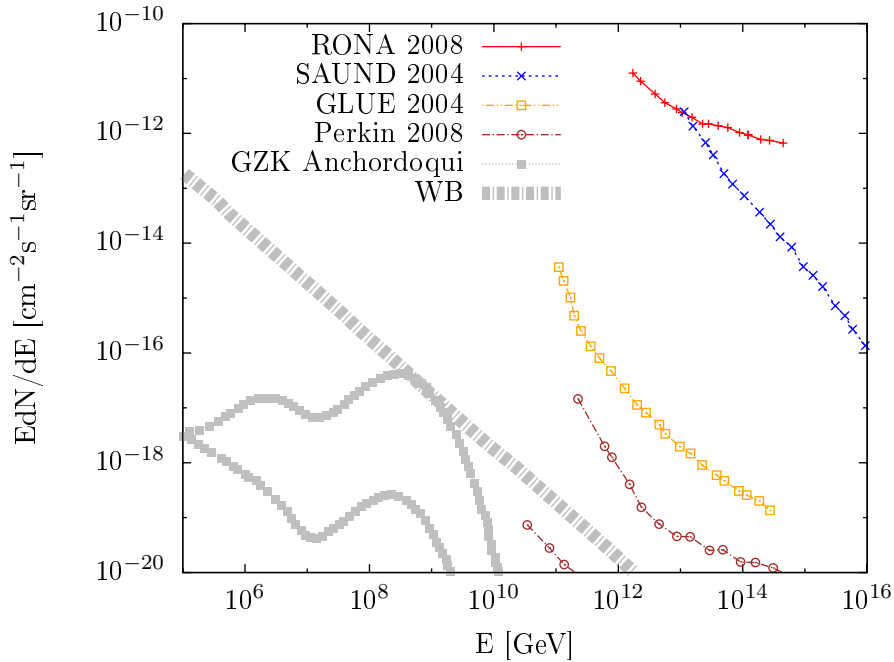
Figure 2.9: SAUND [135], ACORNE [136] (acoustic) and GLUE [138] (radio) (see also Sec. 1.4) sensitivities. The predicted sensitivity of a simulated stand-alone acoustic array of 1000 hydrophones deployed in a $1\,\mathrm{km}^3$ volume of water with a trigger threshold of $35\,\mathrm{mPa}$ and 1 year of operation (lowest sensitivity of Perkin 2008) is indicated. Also shown is the sensitivity of a $1500\,\mathrm{km}^3$ array with 100 hydrophones per cubic kilometer at a pressure threshold of $5\,\mathrm{mPa}$ for 5 years (highest sensitivity of Perkin 2008) [137]. The Waxman-Bahcall (WB) bound is indicated [49] and the GZK-flux region is taken from [52], see § 1.2.

Laboratory measurements yielded signal amplitudes in artificial permafrost that are typically an order of magnitude larger than for water.

Ice is clearly also an excellent medium candidate for acoustic neutrino detection and is worth investigating further. In the next sections, an overview of the measured and theoretically predicted ice-properties is given.

2.4 In-ice signal propagation and background

2.4.1 Medium properties

Hexagonal ice (ice-Ih, see Fig. 2.10(a) and [141, 142]) has a density of $0.917\,\mathrm{g/cm}^3$ at $0\,^{\circ}\mathrm{C}$ and is the form of all natural snow and ice on Earth with the exception only of a small amount of ice-Ic (cubic ice) which was found to be present in the upper atmosphere. Ice-Ih has a lower density than liquid water due to the ephemeral structure of its crystal lattice, see Fig. 2.10(b). The density of ice-Ih increases very slightly with decreasing temperature (the density of ice at $-180\,^{\circ}\mathrm{C}$ is $0.9340\,\mathrm{g/cm}^3$). Large volumes of ice are usually polycrystalline: they are made up out of monocrystals that have random orientation and various sizes.
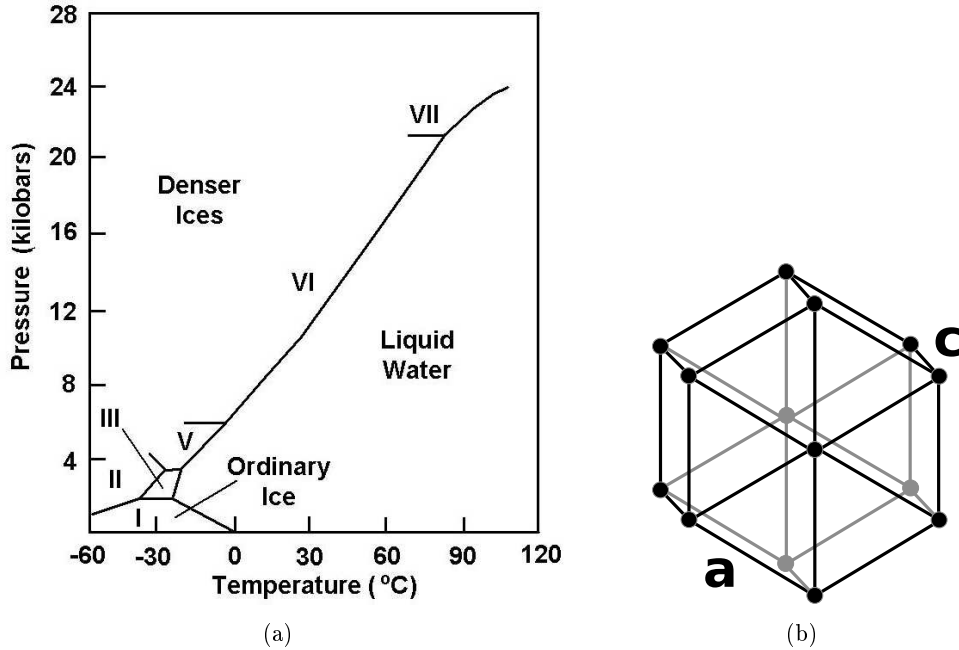
Figure 2.10: (a): The phase diagram of water, illustrating the pressure and temperature conditions under which different crystal structures of ice are stable. Hexagonal ice is less dense than liquid water whereas the other ices found in equilibrium with water are all denser with phase changes occurring on the approach of the liquid and solid densities. (b): The hexagonal structure of ice-Ih with the c and a axis indicated.

Nearly all of Antarctica is covered by an ice sheet that is, on average, at least 1.6 km thick. The glacier at the South Pole is about 2800 m thick and flows in the direction of the coast with a speed of about 10 m/year. It can be described as a slab with parallel top and bottom surfaces with a slope of only ∼0.0015 radian. The South Pole has a desert climate, almost never receiving any precipitation. Air humidity is near zero. Due to the extreme cold, all humidity in the air forms crystals that precipitate at a rate of about 2.5 cm/year. The snow then densifies with depth due to pressure until it reaches maximum density at a depth of around 200 m. This upper region of the ice-sheet where the snow compactifies to ice is called the firn. In this region, the ice becomes increasingly stiff due to scintering [143, 144, 145].Hence, small crystals fuse together in larger crystals. Figure 2.11(a) shows the comparison of firn and ice-core measurements with the density estimated using seismic data. The temperature profile of the ice cap at the South Pole is dominated by heating due to the natural heat originating from Earth's crust. The temperature is therefore lowest at shallow depth and increases with depth. The seasonal and long-period temperature changes from the surface have no short-term effect on the temperature of the ice below 10 m. Changes in temperature at the surface are attenuated exponentially with depth, so that only very-long period climatic variations can penetrate to the glacier bottom with very low amplitude [148]. The temperature of the ice at the South Pole has been experimentally determined to increase from ∼ −51 °C just below the surface to an extrapolated ∼ −9 °C at 2800 m depth, close to the bedrock, see Fig. 2.11(b).

Below 1400 m depth, all airbubbles will have converted into the solid clathrate phase [149].

(a)

(b)
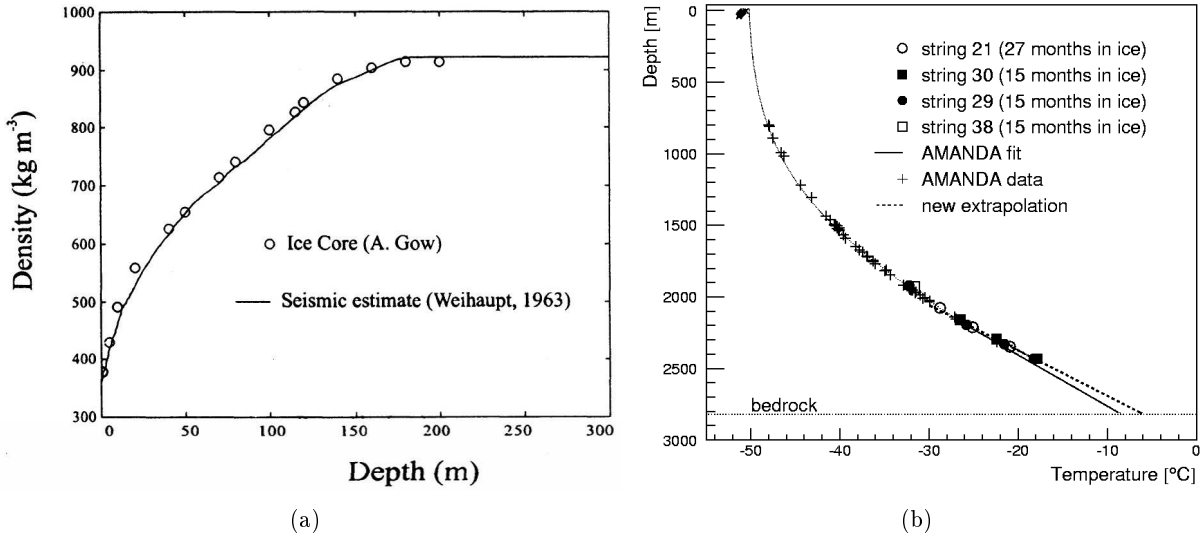
Figure 2.11: (a): Comparison of firn and ice core density measurements (circles) with density estimated (solid line) using seismic data [146]. Graph taken from [147]. (b): South Pole ice-cap vertical temperature profile. Temperatures measured in AMANDA boreholes and shallow boreholes, compared with best-fit temperature profile for the deepest 1000 m (IceCube internal document).

Clathrate, also called gas hydrates, occur when water molecules form a cage-like structure around smaller "guest molecules". Water then crystallises in the cubic system in clathrate, rather than in the hexagonal structure of normal ice. The hydrate should exist from this depth to comprise 0.06 % of the ice. Measurements of the dissociation pressure of nitrogen hydrate and oxygen hydrate show that the clathrate hydrate of air with the formula $(N_2,O_2)\cdot 6H_2O$ should start to exist below about 800 m in the Antarctic ice sheet.

2.4.2 Sound speed

The sound speed depends on the density and temperature of the medium. From the surface to the bulk-ice, in the firn region, the ice becomes gradually more rigid (stiffer) due to the increasing density. Therefore the sound speed rapidly increases in this ice layer. A sound speed profile for the firn layer was experimentally obtained by J. G. Weihaupt [146] in 1963 using seismic refraction surface measurements (see Fig. 2.12).

For greater depths, the density is constant and the sound speed can be modelled assuming a certain temperature-dependent coefficient. The profile for the pressure wave speed below 180 m and the shear wave speed profile were modelled by D.G. Albert [147] using a model for the temperature-dependent coefficient (−2.3 m/(s°C)) and Weihaupt's firn measurements.

In single-crystal ice the sound speed depends on the direction of propagation relative to the c-axis. But the South Pole ice is polycrystalline, with crystal sizes on the order of 0.1 cm and with a random distribution of c-axis orientations, so that this effect averages out [148]. The frequency dependence of the sound speed is also negligible so that the comparison with sound speed results obtained from much lower, seismic, frequencies is possible.

Refraction

Refraction of acoustic waves depends on the gradient of the sound speed. If only variation in the vertical direction is assumed and provided that the refraction index does not change significantly over one wavelength.
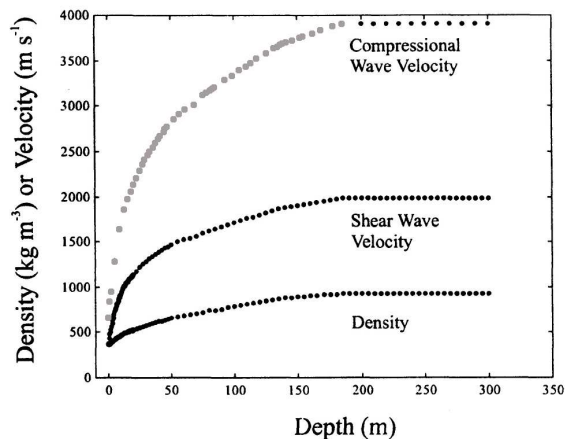
Figure 2.12: The pressure wave velocity measurements at the South Pole in light gray ([146]), along with the extrapolation to larger depths and the shear wave velocity and density values that were derived from the pressure wave measurements. From [147].

The curvature of the acoustic ray, i.e. $d\theta/ds$, is proportional to the sound speed gradient [117]:

$$\frac{d\theta}{ds} = -\frac{\cos\theta_0}{c_0}\frac{dv}{dz} = \frac{1}{R},\qquad(2.32)$$

where s is the coordinate along the ray, θ_0 and c_0 are the initial angle and sound speed respectively and R is the radius of curvature. If the sound speed gradient is constant then the curvature for all rays is constant so that the ray will follow the arc of a circle. Waves are bent toward regions of lower propagation speed. A sound speed maximum is predicted around a depth of 200 m, creating a region in the ice from which all rays are bent away. This means that the surface noise is expected to refract back up, and a much smaller and downward refraction for the noise originating from the bedrock is expected. At the same time this also means that, for a source located inside the firn region, all rays will be bend upwards from a certain emission angle. Human activity on the surface is a very likely source of background noise, but the sound will not propagate to the region of interest for acoustic neutrino detection.

The firn region is not ideal for acoustic neutrino detection due to the large sound speed gradient. Moreover, the signal amplitude scales with the square of the longitudinal sound speed c_l so that the energy threshold for neutrino interaction is higher in the firn. Also, the interaction probability is lower due to the lower density.

2.4.3 Attenuation length

Absorption

Energy loss (absorption) of an acoustic wave in a solid can be due to several processes [150]. Each of these processes is characterised by a mechanical relaxation time τ_m which depends on the temperature T following the relation $\tau_m = \tau_0 e^{U/kT}$ (Arrhenius relation), where U is the activation energy. The logarithmic decrement due to an incident acoustic wave is then given by:

$$\delta = \frac{\delta_m 2\pi f \tau_m}{(1 + 4\pi^2 f^2 \tau_m^2)},\qquad(2.33)$$

where δ_m is an experimentally determined constant that is dependent on the wave mode and the propagation direction but not on the frequency f. The attenuation coefficient is $\alpha_l = \delta f/c_l$.

There are two main absorption mechanisms for longitudinal waves in the South Pole ice: proton reorientation dominates for the upper 2000 m in the cold ice and grain boundary sliding dominates in the warmer ice near the bedrock. The contribution from proton reorientation is independent of grain size and consists of the rotation of the H_2O dipole moment into favoured positions. In this case, measurements have determined that $U = 0.58\,\mathrm{eV}$ and $\tau_0 = 3 \cdot 10^{-16}\,\mathrm{s}$.

Rotation is achieved by the repositioning or migration of orientational defects when an acoustic wave passes by. The concentration of these defects increases with increasing temperature. The proton-relaxation peak is positioned at the frequency f_m which is anticorrelated with the relaxation time τ_m following the relation $2\pi f_m = 1/\tau_m$. f_m is therefore strongly dependent on the temperature. Figure 2.13(a) shows curves of absorptivity as a function of frequency at a selection of temperatures. Two data-points are indicated originating from seismic measurements in an Antarctic glacier (solid circle) and Greenland ice (solid triangle). The range of predicted absorption lengths at near-surface temperature (–51 °C) in South Pole ice, calculated from different measurements of U, τ_0 and $\delta_{\max}$, is roughly from 5 km to 11 km.
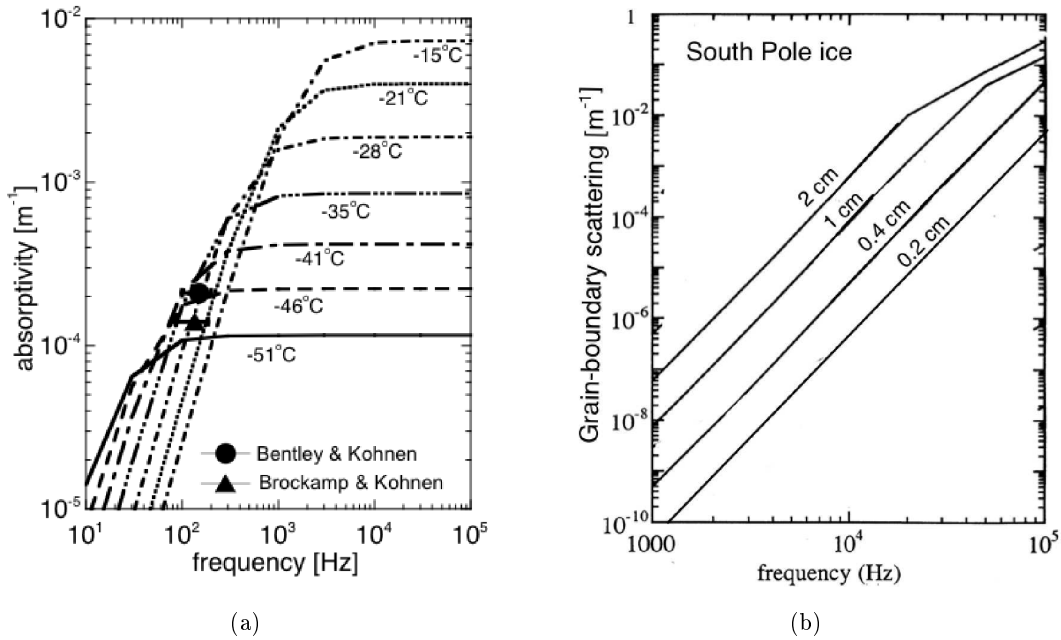
Figure 2.13: (a): Contribution to absorptivity due to molecular reorientation in glacial ice. See [117] for references. (b): Scattering off grain boundaries as a function of frequency and grain diameter in South Pole ice. From [150]

Scattering

Two possible scatterers exist in the South Pole ice cap: air bubbles and grain boundaries. In a 2164 m deep core taken at Byrd Station[15] the maximum density of scatterers was reached at a depth of ∼100 m where the ice contained air bubbles with a concentration n_0 of about

---

[15] Byrd Station was a U.S. Research Station located in the hinterland of Bakutis Coast, Marie Byrd Land in West Antarctica, 500 km from the coast.

$200\,\mathrm{cm^{-3}}$ [150]. n_0 stayed constant up to a depth of 800 m after which it decreased monotonically. The mean bubble diameter, d_b, for the Byrd Station ice core was found to be $\sim0.05\,\mathrm{cm}$ near the surface and $\sim0.008\,\mathrm{cm}$ at about 1000 m depth. Results from an early AMANDA drill hole concluded that the mean bubble size at South Pole had to be smaller than a few microns at a depth of 800 m. The mean bubble diameter decreases monotonically with depth they all have converted into the solid clathrate phase (below 1400 m). The density of clathrate crystals is similar to that of ice-Ih so that the clathrate do not contribute as scatterers. In ice layer where bubbles do occur, the individual bubbles act as independent scatterers because the mean spacing between the bubbles is many times larger than their mean dimensions. For the frequencies of interest for the acoustic detection of neutrinos (up to 100 kHz) it is clear that the scattering is situated in the Rayleigh regime: the dimensions of the scatterers are much smaller than the acoustic wavelength. The attenuation coefficient for scattering off air bubbles in the upper layer of the South Pole ice for a certain frequency f is then [117, 150]

$$\alpha_{\mathrm{bubble}} = 2.68 \cdot 10^{-10} \left(\frac{n_0}{200\,\mathrm{cm^{-3}}}\right) \left(\frac{d_b}{0.02\,\mathrm{cm}}\right)^6 \left(\frac{f}{10\,\mathrm{kHz}}\right)^4 \,[\mathrm{m^{-1}}]. \qquad (2.34)$$

If we take a worst case scenario (close to the surface) with n_0=200 $\mathrm{cm^{-3}}$, d_b=0.05 cm and f=30 kHz, we find an attenuation length from scattering off bubbles of about 18 km. Scattering off bubbles is therefore not expected to be the dominant attenuating effect.

The properties of hexagonal ice-Ih are non-isotropic and depend on 5 elastic constants c_{11}, c_{12}, c_{13}, c_{33} and c_{44}. Also the sound speed depends on the specific direction of the wave relative to the crystal axis. The polycrystalline ice at the South Pole consists of monocrystals that have random orientation and a certain mean grain diameter d_g, therefore scattering of the acoustic waves will happen at the grain boundaries where the sound speed changes abruptly. At the same time, reflection and mode conversion (from longitudinal to transversal mode or vice versa) occurs. Here we only consider the attenuation of the longitudinal waves. There are three scattering regimes for scattering at grain boundaries in ice, depending on the relative sizes of the grains and the wavelength under consideration [117, 150].

1. Rayleigh regime: $\lambda/2\pi d_g > 1$, where λ is the wavelength.
   In this case: $\alpha_l = 5 \cdot 10^{-1} \left(\frac{d_g}{0.2\,\mathrm{cm}}\right)^3 \left(\frac{f}{10\,\mathrm{kHz}}\right)^4 \,[\mathrm{km^{-1}}]$. This formula assumes a random orientation of the c-axis. It therefore overestimates the scattering for depths where there is a strong alignment of the c-axis.

2. Stochastic regime: $0.5 < \lambda/2\pi d_g < 1$, where $\alpha_l = 6.2 \left(\frac{d_g}{0.2\,\mathrm{cm}}\right) \left(\frac{f}{500\,\mathrm{kHz}}\right)^2 \,[\mathrm{m^{-1}}]$. The weaker dependence on the d_g and the frequency (f) is due to the coherent nature of the scattering process since there will be a noticeable phase-shift of the acoustic wave over a distance $\sim d_g$.

3. Geometric regime: $\lambda/2\pi d_g < 0.5$, where $\alpha_l = \langle R \rangle /d_g$. $\langle R \rangle$ is the average reflection coefficient. In this scattering regime, the scattering mechanism approaches a diffusion process and the resulting scattering is independent of frequency and proportional to $\langle R \rangle$. For the case of ice, for which the elastic anisotropy of individual crystal grains is small, the average reflection coefficient is given by $\langle R \rangle R = 0.068$ [150], and $\alpha_l = 6.0/(d_g\,[\mathrm{cm}])\,[\mathrm{m^{-1}}]$.

In ice with $d_g = 0.2\,\mathrm{cm}$, scattering is low. The expected scattering length is $2000\,\mathrm{km}$ at $10\,\mathrm{kHz}$, $25\,\mathrm{km}$ at $30\,\mathrm{kHz}$, and $2\,\mathrm{km}$ at $60\,\mathrm{kHz}$. In [117, 150] the acoustic attenuation length in the shallow ice below the firn is predicted to be dominated by the proton reorientation absorptive effect and to be $9 \pm 3\,\mathrm{km}$. Currently a core-sample from a SPRESO (South Pole Remote Earth Science Observatory) drill hole about $8\,\mathrm{km}$ distance from the South Pole is under investigation [151].

2.4.4 Background noise

The ambient noise in the South Pole ice is expected to be low and stable. The seismic station QSPA (Quiet-zone, South Pole, Antarctica), located at SPRESO situated $8\,\mathrm{km}$ from the South Pole station, is deployed at a depth of $200\,\mathrm{m}$ and measures at $30\,\mathrm{Hz}$ the lowest noise of the entire Global Seismic Network (GSN)[16] [117]. Most of the shear in the glacier at South Pole happens at the bedrock where plastic deformation occurs more easily due to the warm temperatures. The expected acoustic emission from the bedrock is from $\sim 0.01\,\mathrm{MHz}$ to $1\,\mathrm{MHz}$ [117], localised in time. This bedrock-noise is not expected to reach the depths that are relevant for acoustic neutrino detection due to the temperature and sound speed gradient. The South Pole ice is predicted to be much quieter than ocean water at the relevant frequencies because there are no waves, currents or animals. As mentioned before, all anthropogenic surface noise is expected to be waveguided back up to the surface due to the sound speed gradient in the firn.

2.5   In-ice acoustic neutrino detection

The feasibility of acoustic neutrino detection in ice depends on the acoustic properties of the ice in the relevant frequency range, roughly from $1\,\mathrm{kHz}$ to $100\,\mathrm{kHz}$. These characteristics of the ice determine the feasibility and design of a large self-triggering acoustic neutrino detection array at South Pole.

From Table 2.1, it is clear that ice is an excellent candidate for acoustic neutrino detection, since the signal amplitude is expected to be about 1 order of magnitude larger than in water. Especially the cold upper layer of the ice (but below the firn) is expected to be optimal for the conversion of radiation energy to acoustic energy. However, the theoretical predictions presented in this chapter are relying on extrapolations and assumptions of the ice structure and properties. Before considering the construction of a large acoustic neutrino detection array, the predicted properties need to be experimentally verified.

Before the deployment and results of the South Pole Acoustic Test Setup (SPATS), the topic of this work, it was unclear if the ice was indeed the predicted suitable medium for acoustic neutrino detection. The aim of SPATS is to measure the three critical acoustic parameters of the Antarctic ice sheet:

- The speed at which a pressure wave propagates through the South Pole ice is an important factor in event reconstruction and transient background rejection. Not only obtaining knowledge about the absolute value of the sound speed in the ice, but also mapping the vertical sound speed profile are important. Acoustic waves are bent towards regions of lower propagation speed and the profile dictates the refraction index and the resulting radius of curvature. The emission disk is deformed more for larger sound speed gradients

---

[16] http://www.iris.washington.edu/hq/programs/gsn

(smaller radii of curvature), making the direction reconstruction for the hadronic shower more difficult. Also, a precise measurement of the P- and S-wave speeds would allow to use the delay between the P and S-wave arrivals to calculate the distance to the source. If an UHE hadronic shower gives rise to a detectable shear waves, a single sensor could be sufficient for a distance measurement.

- The in-situ temporal (and spatial) background noise sets the possible trigger level for a particular design of an acoustic array and therefore dictates the energy threshold. A stable noise level allows for a fixed trigger level and a more straightforward transient analysis.

- The attenuation length determines how sparsly a possible future detector volume can be instrumented. The economical feasibility of an acoustic neutrino detector strongly depends on the spacing between the acoustic sensors. If the attenuation length is dominated by absorption, the pancake-shaped shock front will be preserved. For a scattering-dominated attenuation length this typical signature will be lost, making a self-triggering acoustic neutrino detection array infeasible.

SPATS was deployed in the 2006/2007, 2007/2008 and 2008/2009 Antarctic summers in the upper 500 m of the South Pole ice cap.

SPATS Hardware

The South Pole Acoustic Test Setup (SPATS) is designed to investigate the feasibility of acoustic neutrino detection in the South Pole ice. The three main acoustic characteristics (see § 2.5) that require experimental verification are the sound speed, background noise (both transient and continuous) and attenuation length of the expected acoustic neutrino signal. To that end, acoustic sensors and powerful transmitters that operate at the expected frequencies, from 1 to 100 kHz, were installed in the ice at various distances and depths. All the equipment that freezes in after deployment needs to be able to withstand temperatures down to $-60\,^{\circ}$C and pressures over 100 bar.

SPATS grew from December 2006 to January 2009, from having no hardware deployed to 4 fully functional instrumented acoustic cables, called strings (labelled A, B, C and D), deployed in the upper 500 m of IceCube holes and 10 successful runs with a retrievable transmitter, called pinger. After a productive long range test in water in April 2006, expectations were that the initial data-taking with strings A, B and C would yield the science goals swiftly. Confronted with the in-ice data (for first-year performance and results, see [152, 153]), it became clear that the different systematic effects were impossible to disentangle. The Gaussian noise levels could be studied, but the attenuation length could not be constrained and a complex timing-scheme prohibited a straightforward sound speed analysis. String D and the retrievable transmitter (pinger) were then designed, and deployed in the 2007/2008 season, in order to answer the questions raised by that first set of results and to achieve the rest of the SPATS science goals. String D was assembled and tested at the INW laboratory (UGent) in Ghent, Belgium. The first pinger data showed unexpected and large variations in signal amplitudes with depth and hole number. The main influence was suspected to be the position of the pinger relative to the hole walls. An improved pinger, with a position-centering system, generated perfectly reproducible signals in the 2008/2009 season. Strings A, B and C have been operating for close to 3 years at the time of writing. They have survived transport to the South Pole Amundson-Scott station, refreezing of the water-filled holes and several power-outages. String D has proven to be a robust addition to the permanently deployed system for almost 2 years. Together they have accumulated close to 500 GB of data, of which roughly 100 GB is pinger-data.

The complete SPATS hardware is discussed in this chapter, with specific detail for elements and limitations that are important for the data analysis.

3.1 Geometry

The permanently installed hardware of SPATS today consists of four vertical instrumented strings that were deployed in the upper 500 m of selected IceCube [48] holes to form a trapezoidal array. The current geometrical configuration (see Fig. 3.1 and Fig. 3.2) is the result of a compromise between the geometry necessary to achieve the physics goals and the IceCube geometry and personnel availability at the time of deployment. Measuring, for example, the acoustic properties
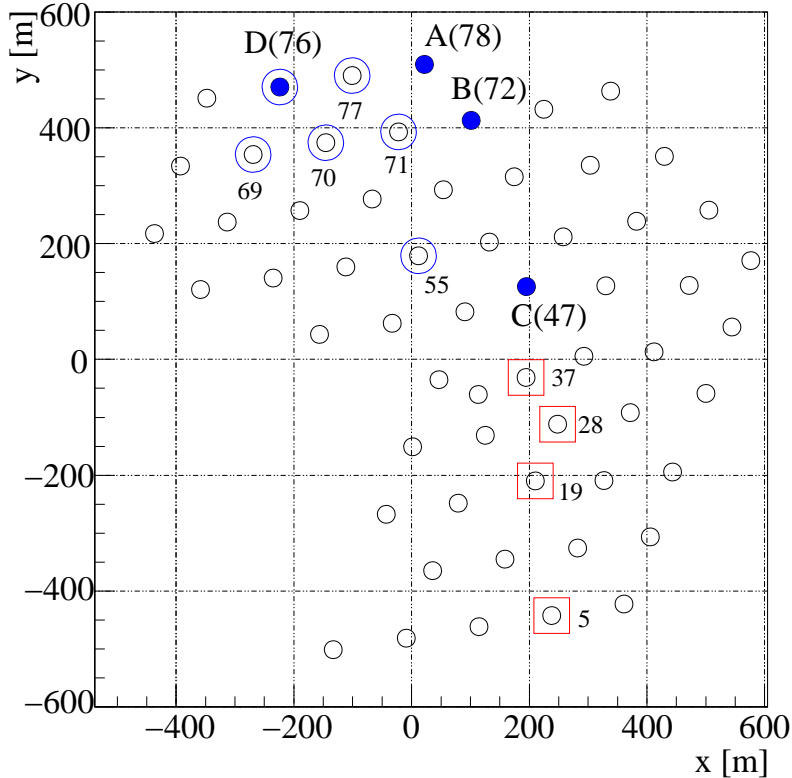
Figure 3.1: The IceCube strings as of February 2009 (black circles) with the SPATS geometry. The permanently deployed hardware is indicated by blue filled circles with the string-ID (ABCD) and corresponding IceCube hole number. The blue open circles and red open squares show respectively the position of the 2007/2008 and 2008/2009 pinger holes with the corresponding IceCube hole number.

of the ice both parallel and perpendicular to the flow of the glacier permits the investigation of possible anisotropies of the acoustic properties of the ice. Therefore a good horizontal coverage is needed. For an attenuation length analysis, it is important to have sufficient variation in transmitter to sensor distances so that the fit of the amplitude versus distance is well defined. The error on the horizontal position of each string is fixed and known to be $\pm 0.5\,\mathrm{m}$, so that the relative error decreases with increasing string-to-string distance (called baseline). Long baselines therefore allow for a more precise measurement of the arrival times of the signal for example. Strings A, B and C were positioned in such a way that three clearly distinguishable baselines were obtained: $125\,\mathrm{m}$ (between strings A and B), $302\,\mathrm{m}$ (between strings B and C) and $421\,\mathrm{m}$ (between strings A and C). String B was deployed on 11 January 2007, A on 14 January 2007 and C on 22 January 2007. String D was deployed on 24 December 2007, increasing the maximum baseline to $543\,\mathrm{m}$. The vertical distance between the acoustic transducers (transmitters and sensors) was chosen to increase with depth following the measured and expected temperature and density profiles of the ice [148, 147]. Figure 3.2 shows a schematic of the SPATS array and

its in-ice and on-ice components. Each of the four strings has 7 acoustic stages, each of which contains a transmitter and a sensor module. Strings A, B and C have instrumented levels at 80, 100, 140, 190, 250, 320 and 400 m depth. String D has instrumented levels at 140, 190, 250, 320, 400, 430 and 500 m depth. It was decided for string D to place the top acoustic stage at 140 m depth, omitting the 80 m and 100 m depth levels after less optimal acoustic conditions in those upper levels (high background noise and short attenuation length) were found in the 2007 data-set. Moreover, String D has second-generation SPATS transmitters and sensors. Also, two out of the seven acoustic stages of string D have HADES (Hydrophone for Acoustic Detection at South Pole [154]) sensors instead of SPATS sensors. The acoustic modules are discussed in more detail in § 3.2.

The retrievable transmitter was deployed in 10 water-filled IceCube holes down to a maximum depth of 500 m. 6 holes were pinged in December 2007 and January 2008. In the 2008/2009 season when 4 more holes were pinged using an optimised pinger design, the maximum baseline achieved was 1023 m.

3.2 In-ice components

3.2.1 Acoustic stages

A schematic drawing of a SPATS acoustic stage is shown in Fig. 3.2. Each acoustic stage consists of a transmitter and a sensor module. All the electronic circuits are located in steel[1] pressure housings with an outer diameter of 10.2 cm and an inner diameter of 10 cm. The modules are discussed in detail below. The transmitter and sensor modules are joined together with three ropes, allowing the transmitter module to be mounted about 45 cm above the sensor module. The ropes are joined at the top and bottom at a steel nut that is threaded and mounted on a bolt that runs through a plastic perforated hollow separation sphere, called spacer ball. The holes allow for water to flow in so that the spheres remain intact at least until freeze-in. These spacer balls are 16 cm in diameter and assure a minimum distance of the stage to the Icecube main cable and the wall of the hole. An entire stage is about 1.5 m long and maximum 16 cm wide[2] with a total weight of 10 kg. Each acoustic stage is connected to an acoustic junction box (AJB), located at the surface, by two shielded cables (one for each module) each consisting of four twisted wire pairs. All in-ice cables are twisted around a support rope which carries the weight of the stages. The depth of the string was monitored during deployment by directly reading out the pressure sensor that is inside each of the lowest transmitter modules. The stages are assumed to be positioned on the nominal depths with an error of ± 2 m (see also § 4.3.3).

The SPATS transducers all use the same lead zirconium titanate (PZT) material, namely PIC151, manufactured by PI-ceramics[3]. This is a soft piezo-ceramic material with a high piezo-electric charge constant ($d_{33} = 500$ pC/N), high permittivity, high coupling factor. It is traditionally used for low-power ultrasonic transducers and low-frequency sound transducers.

---

[1]Stainless steel grade 304/1.4301.
[2]The minimum diameter of a typical IceCube hole after drilling is about (50–60) cm.
[3]http://www.piceramic.com
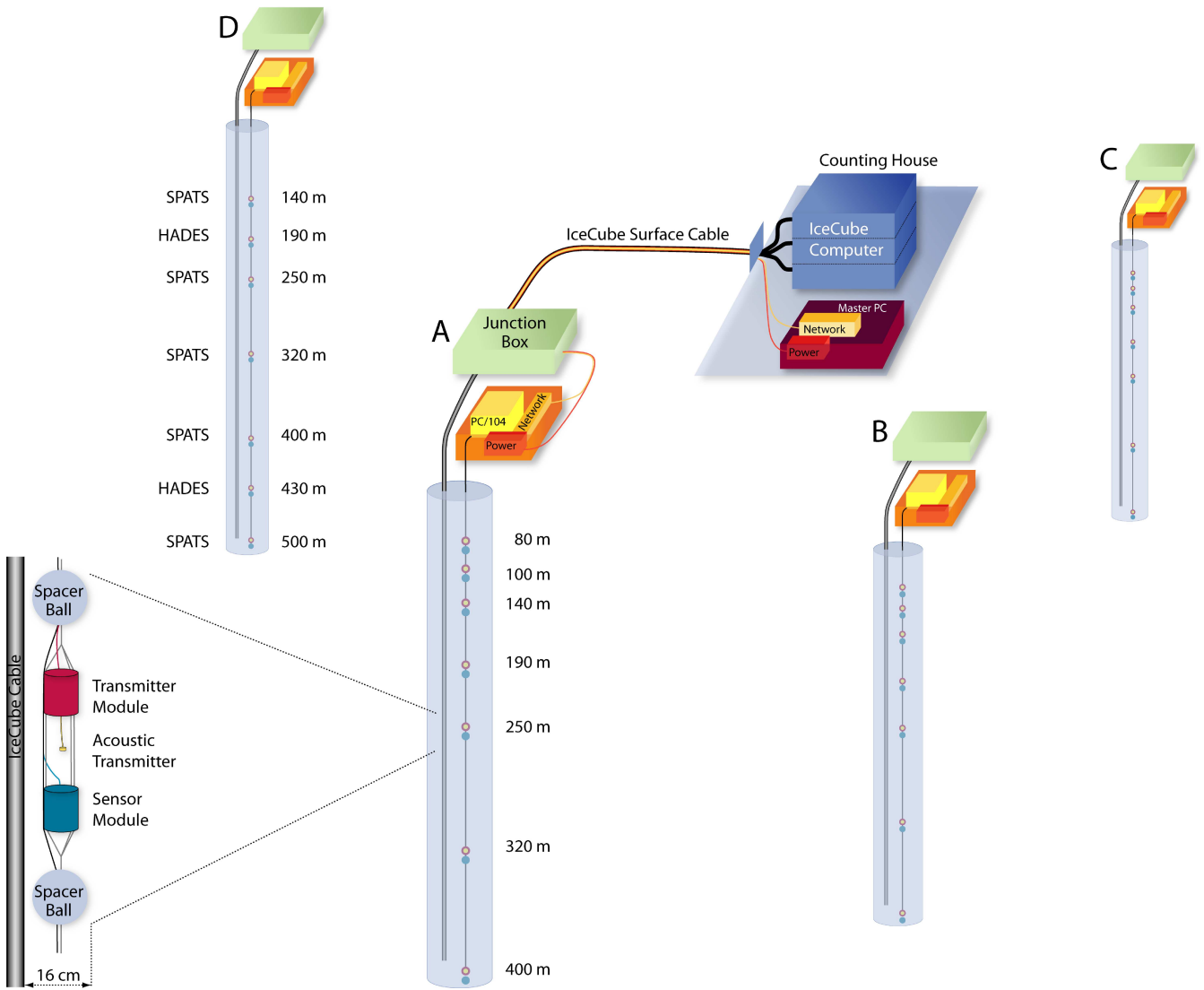
Figure 3.2: Schematic of the SPATS array, showing strings A, B, C and D, each with 7 acoustic stages. Also shown are the stage design, on-ice SPATS DAQ and power supply connectivity.
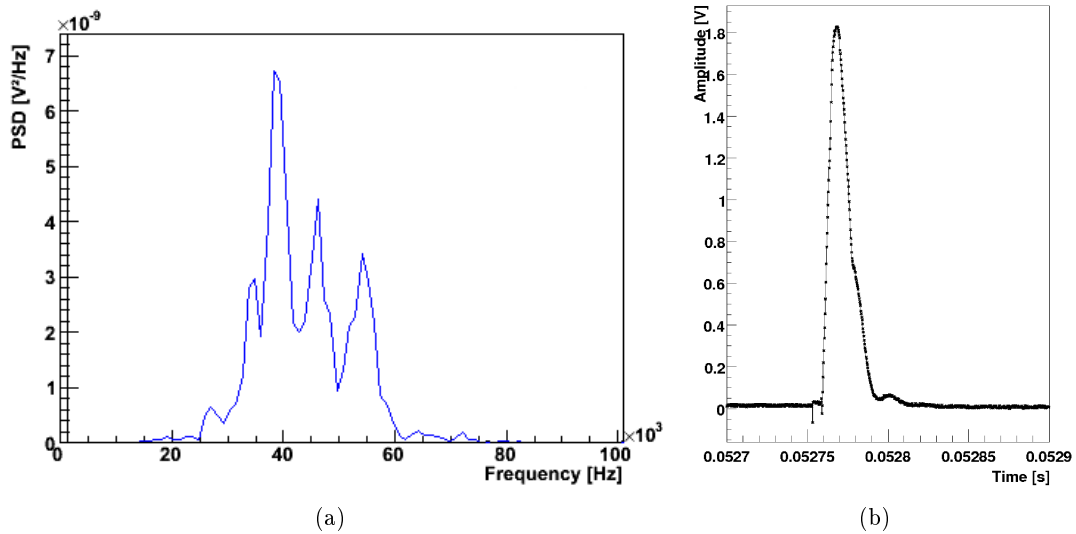
Figure 3.3: (a): Fourier spectrum for a string B transmitter as seen by one of the string D HADES sensors (from [156]). (b): An example of a string D (SPATS second-generation) transmitter HVRB recording. The y-axis is scaled down by a factor 500.

3.2.2   The transmitter module

A SPATS transmitter module consists of a steel pressure vessel and an external piezo-ceramic transmitting element that is positioned roughly 15 cm below the vessel and connected by a rigid high-voltage (HV) cable. The pressure vessel houses a HV pulse generator board (see [155]) and a temperature sensor[4]. For the deepest stages, the temperature sensor is replaced with a commercial pressure sensor. Both sensors give a linear output current range of (4–20) mA, which translates to a temperature range of –70 °C to +10 °C and a pressure range of (0–60) bar. The HV-board comprises a charging circuit parallel to an LC-circuit. A TTL (Transistor-Transistor Logic) pulse starts the charging, and its length determines the charge duration. When the charging circuit is turned off, the LC-circuit discharges over the capacitance of the attached piezo-ceramic transmitting element. The charging voltage is variable and is provided by a voltage regulation board. This way, a unipolar high voltage pulse with a FWHM (full width at half maximum) of about 17 μs and a variable maximum up to 1.5 kV is sent to the piezo-ceramic element. Both the steering voltage which determines the charging voltage and the TTL pulse length can be set externally. The resulting HV pulse can be read-back (HVRB); this allows the effects of cable length and temperature to be studied and taken into account. The HVRB is mainly used to check if the transmitters are functioning as expected. These pulses have a very high repetition stability and are triggered by TTL signals of optimally 5 ms duration. The HV pulses are sent to the transmitting element (capacitance of $\sim$16 nF) which is ring-shaped in order to have an isotropic azimuthal emission. It is cast in epoxy-resin for electrical insulation and positioned $\sim$13 cm below the steel housing. The actual emission directivity of such an element was measured in azimuthal and polar directions; all details are in [155] and a short overview is given in § 4.1.1.

The ring-shaped piezo-ceramic element is least isotropic in the polar plane. The HV cable

---

[4]Based on PT1000 resistors.

that connects this element to the transmitter module has limited flexibility and an extra rigidity was added before deployment to avoid bending. Still, it can be expected that the piezo-ceramic element has a certain angle to the horizontal plane. In this case the amplitude variation in the horizontal plane will be much larger than expected from the azimuthal isotropy measurement. Figure 3.3(a) shows the Fourier spectrum for a waveform from a string D HADES sensor listening to a string B transmitter. The SPATS transmitters typically output most power in the (20–60) kHz range although the differences in the actual shape of the emission spectra are large [156].

The SPATS second-generation transmitters of string D have an optimised HV-circuit design which results in HV pulses with a FWHM of about $50\,\mu s$ and higher pulse amplitudes than the first-generation transmitters. These pulses are triggered by TTL signals of typically 2 ms duration. Figure 3.3(b) shows an example of a string D transmitter HVRB.

3.2.3 The sensor module

A SPATS sensor module has three piezo-ceramic elements, each placed 120° apart to ensure good angular coverage. A so-called SPATS sensor channel consists of a cylindrical (10 mm diameter and 5 mm height) piezo-ceramic element (same PZT-type as for the transmitter) that is pressed against the steel housing. The piezo-ceramic element is directly soldered to a 3-stage amplifier. The first stage consists of a low-noise amplifier[5] with an amplification factor of 100, a large bandwith and a 5 kHz high-pass filter to suppress low frequencies. The second amplifier stage is an AC coupled inverted amplifier which amplifies the signal by a factor of 100 and supresses the frequencies above 500 kHz. The last stage is a line driver: it prepares the signal for transport over the long in-ice cable by providing a differential output with a gain of 1. Two twisted wires then transport the complementary signals to the differential input of an Analogue-to-Digital Converter (ADC) in the string-PC (see §3.3). This aids noise reduction by rejecting common-mode interference. The total amplification factor of the chain of amplifiers is therefore of the order of 10^4. The amplification varies about 5% in the (10–80) kHz relevant frequency range with a peak at 10 kHz, see [123].

The 21 SPATS first-generation sensor modules that were deployed on strings A, B and C have each a central bolt that is connected to three screws. These preload screws put pressure on the piezo-ceramic element through the amplifier board to ensure good contact with the steel housing and avoid deformation of the module. This introduces a mechanical coupling between the three different channels of the sensor module. It was therefore decided to replace the preload screws with a metal ring in the SPATS second-generation sensor modules on string D. Figure 3.4 shows pictures of open SPATS first (a) and second (b) generation sensor modules. 25 SPATS first-generation sensor modules were calibrated in water (see §4). String D water calibration data also exist.

HADES, see [154], was developed in order to offer an alternative in-ice sensor with a different dynamical range. HADES-A and HADES-B were respectively deployed at 190 m depth and 430 m depth on string D. A ring-shaped piezo-ceramic element is connected to a 2-stage differential amplifier that is placed inside the ring. The assembly is then coated with resin (two-component hard polyurethane). The choice of resin was made after a series of laboratory tests that investigated the resistance of the material to temperatures down to –85 °C. Also the acoustic impedance matching was calculated from the measured sound speed for each material. The

---

[5]AD754JR.

(a) SPATS first-generation sensor module.

(b) SPATS second-generation sensor module.
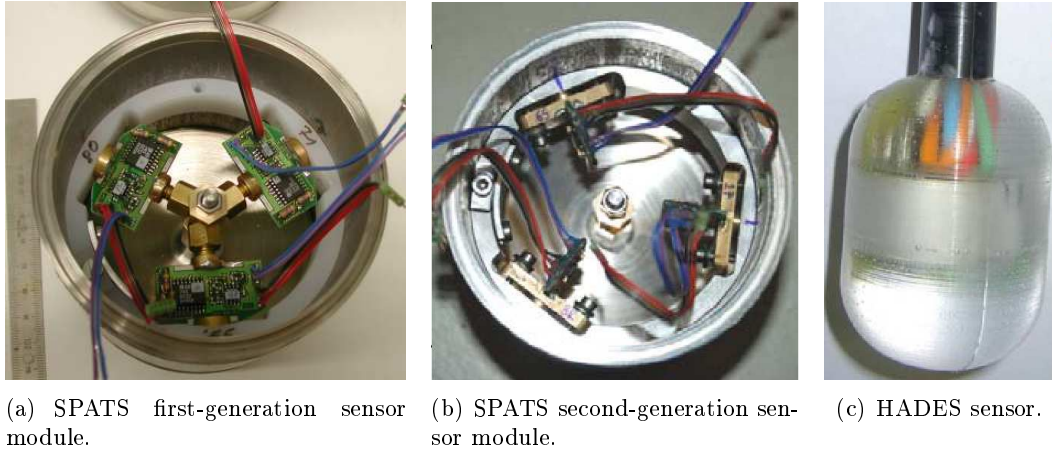
(c) HADES sensor.

Figure 3.4: Pictures of the SPATS and HADES sensors. The SPATS first- (a) and second- (b) generation sensor modules have 3 channels, each consisting of a piezo-ceramic element followed by an amplifier board. The HADES sensor (c) consists of a cylindrical piezo-ceramic element with an amplifier board cast in resin.

initial in-ice results for HADES are presented in [154]. Figure 3.4(c) shows a picture of a HADES sensor.

3.3 On-ice components

3.3.1 The acoustic junction box

The acoustic junction box (AJB, see Fig. 3.5(a)) is a robust aluminium box (dimension: $(30 \times 50 \times 80)$ cm for strings A, B and C and slightly larger for string D) buried under roughly 3 m of snow. It is split into two compartments. The first one holds the connectors from the in-ice cables. These are connected to wall-mounted connector-sockets (patch wall). The second compartment is watertight and contains the electronic components. All in-ice signals are first routed through a printed circuit board (PCB) from where they are distributed to the data acquisition (DAQ) boards of a low-power industrial PC, called the string-PC. A power distribution unit (PDU) consists of low-noise DC/DC converters and filters. It provides ground, $+5$ V, $+15$ V and $+24$ V to the string-PC and the in-ice components through the PCB. The PCB also routes the GPS timing signal and converts the currents from the in-ice pressure and temperature sensors to voltages.

The string-PC (see Fig. 3.5(b)) is a stack of IDAN (Intelligent Data Acquisition Node) PC/104 modules by RTD[6]. It has a compact modular design and its splash-proof rugged aluminium enclosure acts as a heatsink so that no fan is needed. It is rated to perform from -40 °C to $+85$ °C. The peripheral components are controlled by a CPU module[7] with a 600 MHz processor and 512 MB RAM. The linux operating system is installed on a flash-memory (wide temperature

---

[6]http://www.rtd.com/

[7]IDAN-CML47786HX650ER-260D

(a)
(b)
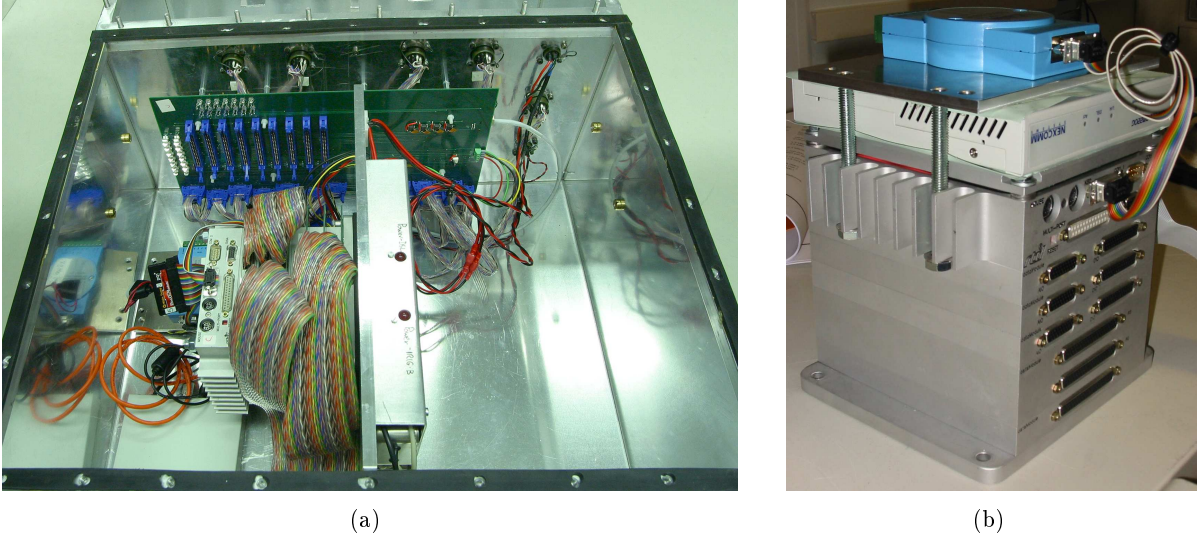
Figure 3.5: (a): The watertight part of the acoustic junction box with the PCB, power distribution board, string-PC and modems. (b): The string-PC stack. From top to bottom are the serial and DSL modems, the CPU board, 3 fast-ADC boards, 1 slow-ADC board and 1 relay module.

disk-on-module (DOM)[8]). This type of solid-state memory has the advantage that there are no moving parts, unlike a regular hard drive. The drawback is that each memory-cell of the DOM can be accessed for reading or writing a limited number of times. If too many cells fail the disk will become unaccessible, as it happened during the pre-deployment testing of string-PC B. For this reason, all data is stored locally on a temporary RAM disk. This means that part of the RAM memory of the CPU module is treated as if it were a disk drive. Hence, the read-write cycles of the DOM are kept to a minimum. The 12-bit Fast-ADC (FADC) boards[9] have a maximum sampling frequency of 1.25 MHz. There are three FADCs for each string, which means that all three channels of one sensor module can be read out simultaneously at a maximum sampling frequency of 1.25 MHz. Theoretically, the FADCs should be able to read out all 21 sensor-channels of the string at maximum ∼179 kHz sampling frequency. However, this is not feasible for the SPATS DAQ system as will be discussed in §3.6.2. The three boards are linked through a SyncBus (RTD) connection which allows the simultaneous recording of samples by the three boards (they will use the same ADC clock of one of the boards). Together with one slow ADC board[10] with a sampling frequency of 500 kHz, the transmitters can be controlled and the temperature and pressure sensors read out.

A relay board[11] has 16 relay switches which allow the power for each sensor, transmitter, temperature and pressure sensor to be switched on and off separately. The average power consumption per string is low and varies from ∼35 W (no in-ice modules powered on) to ∼96 W (all in-ice modules powered on). All these components were tested at the expected low temperatures

---

[8] DJ0010G44TK02P10; operating temperatures: $-40\,^\circ$C to $+85\,^\circ$C (http://www.pqimemory.com/)

[9] IDAN-SDM7540HR-8

[10] IDAN-DM6420HR-1-62S

[11] IDAN-DM6952HR-62D
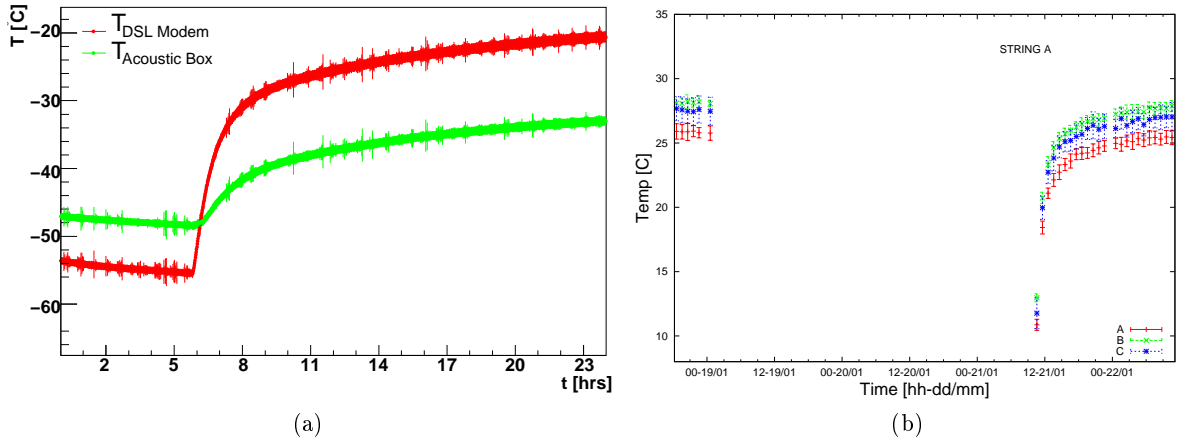
Figure 3.6: (a): the evolution of the DSL modem (red) and AJB-air (green) temperatures, the string-PC was switched on at 5:30 hrs (from [157]). (b): FADC-temperatures of string A as measured by their internal temperature sensors; there was a long power-outage on 19/01/2007.

(around –55 ^{o}C) and several cold boot cycles of the system were successfully performed prior to deployment (see for example [157] and Fig. 3.6(a)). The string-PCs have also powered on without problems after power-outages at South Pole (Fig. 3.6(b)).

The AJB allows over 90 analogue channels to be controlled and read-out without the need to transport the analogue signals over dedicated surface cables to the IceCube Laboratory (ICL). The total cable cost and signal losses are therefore kept to a minimum. Each AJB is connected to the "master-PC" (see §3.3.2) located in the ICL by two cables (quads) of the IceCube surface cable-assembly. They each have 2 twisted wire-pairs: DC-power and SDSL[12] communication go on one quad and DC-power and GPS signal on the other quad. All patch cables are shielded. This way the EMI (electromagnetic interference) shield remains intact and the interferences are minimised. The DC-power is automatically inhibited in hardware and firmware if the shield is not intact.

3.3.2 The master-PC

The master-PC (see Fig. 3.7) is a rackable 4U HP Proliant DL380 series with dual 1GHz Pentium-3 processors and a 12-slot PCI backplane[13]. Two Acopian[14] switching regulated power supplies connected in series supply 96 V, one 0 to +48 V and the other one 0 V to –48 V. They are cooled independently by internal dual fans. A symmetric DSL connection is assured by Nexcomm Nexpeed NM220G modems. These SDSL modems provide symmetrical data rates of maximum 2.3 Mbps for a distance of 3 km over a regular wire-pair. In-situ testing has shown the baseline ping-delay to be around 1.5 ms for all four strings. A GPS-based IRIG-B (100 pulses per second (pps), see Fig. 3.8) time coding signal, provided by a Meinberg GPS PCI card (GPS169PCI) guarantees absolute timestamping. The GPS clock is specified to produce IRIG-B rising edges

---

[12]A symmetric DSL connection has the same bandwith for the upstream and downstream connections.

[13]retrofitted IceCube Rev 1 DOM Hub.

[14]W48NT370, http://www.acopian.com/
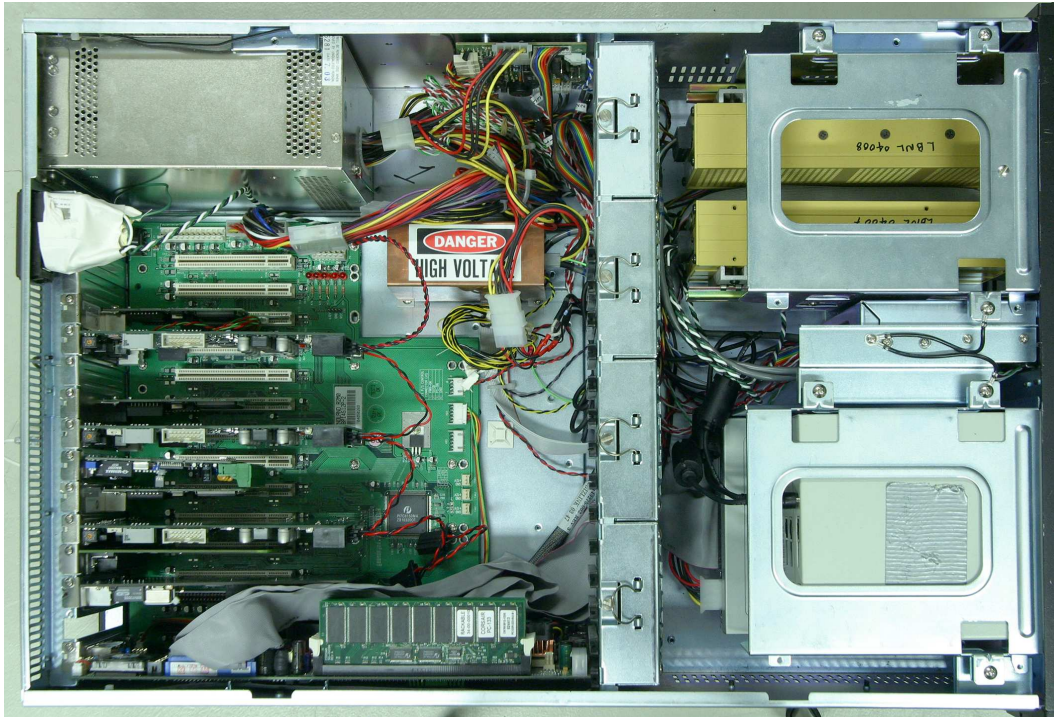
Figure 3.7: Top view of the master-PC.

within $\pm 2\mu$s of absolute GPS time. The delay introduced in the IRIG-B signals during propagation from master-PC to string-PC is a few μs. Each string has a dedicated PCI control board (SPATS Hub Service Board: SHSB) and ethernet card. The SHSB routes the DSL communication, GPS signal and power to the two surface cable quads. The SHSB firmware can be used to power on and off the strings, as well as to monitor the status of the wire-pairs. All minimum and maximum voltages and currents can be set individually and the power is automatically inhibited the instant one of the thresholds is crossed (see [158]). The master-PC is accessible through the local IceCube Lab (ICL) network. Remote access to that network is only possible when the satellite link with the South Pole Amundson-Scott station is active. Currently, all communication and data-transfer for the entire station are executed over two different satellites[15] that have a total of eight hours of visibility per day. All SPATS-data is compressed immediately from the string-PCs to the master-PC where it is stored until transferred. A specialised script then prepares different data streams for both satellite transfer and tape archiving. Each South Pole experiment has a limit on the total data-transfer and SPATS has been assigned a maximum of 150 MB of satellite-transferred data a day. It can take up to five days for the data to arrive on the IceCube data-servers after the data is retrieved by the satellite system. All data that is not transferred goes automatically to tapes that are brought back from South Pole every year. It has been possible to transfer large amounts of data during special data-taking (as, for example, during the inter-string data taking) periods.

Apart from the SPATS system at South Pole, two test-systems also exist: string Z and

---

[15] For satellite times, see for example http://ice.rsmas.miami.edu/access.phtml
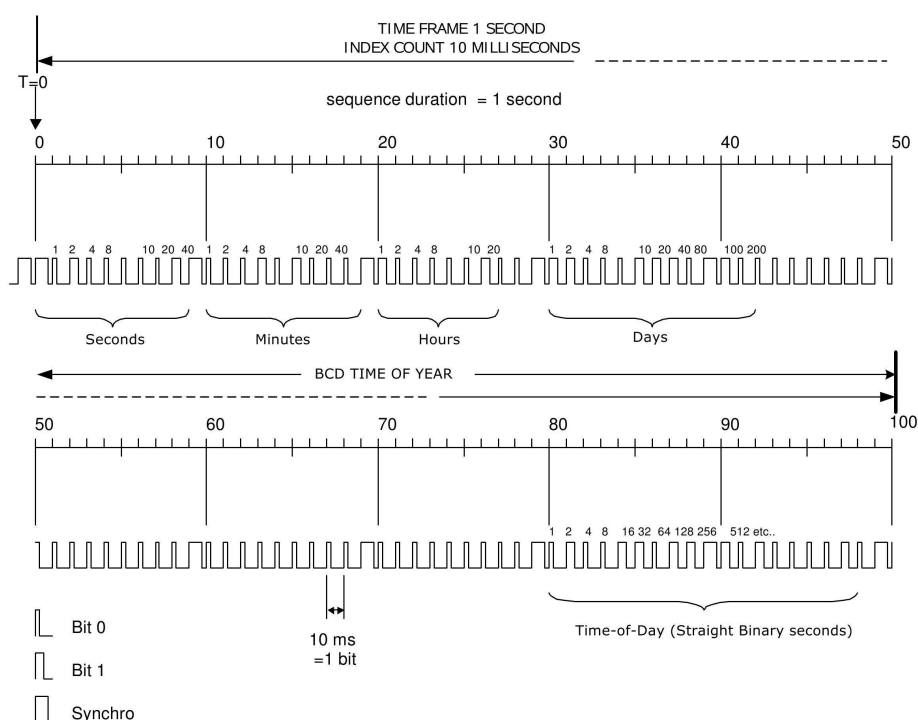
Figure 3.8: The IRIG-B 100 pps timing signal. In 1 second of data, there are 100 rising edges separated by 0.01 s. The start of the sequence is indicated by two 8 ms high separated by 2 ms low, the start of the GPS second is aligned with the second rising edge.

string E. String Z is located at DESY (Zeuthen, Germany) and consists of a complete string-PC that is connected to a desktop-PC (simulating the master-PC) through an SDSL connection. It is possible to connect SPATS sensors and transmitters or a function generator. String E was previously located at the University of California (Berkeley, USA) and has recently moved to UGent (Ghent, Belgium). It consists of a CPU-board and one FADC board to which a function generator can be attached directly. Both test-systems have been extensively used for DAQ software development.

3.3.3   Naming conventions

As mentioned before, SPATS consists of 4 instrumented cables, called strings. They have been named string A, B, C and D. Each string has 7 stages at different depths. Each string has three FADC boards: board 0 ("A"), board 1 ("B") and board 2 ("C"). Each sensor module has three sensor channels and each of these channels is read out by a different FADC, therefore the sensor channels are named channel 0, 1 or 2, after the FADC board that is connected to them. Table 3.1 shows the numbering scheme of the stages and the corresponding depths. The naming convention for transmitter is XTN , the transmitter on string X position N. For example, AT2 is the transmitter at 100 m depth on string A. A sensor is named YSM-Z, this stands for the sensor channel Z (FADC board Z) of the sensor module at position M on string Y. For example, AS2-0

is the sensor channel 0 of the sensor module that is positioned at 100 m depth on string A.

String	Depth [m]								
	80	100	140	190	250	320	400	430	500
A	1	2	X	4	5	6	7	NI	NI
B	1	2	3	4	5	6	7	NI	NI
C	X	2	3	4	5	6	7	NI	NI
D	NI	NI	1	2 (H-A)	3	4	5	6 (H-B)	7

Table 3.1: Overview of SPATS numbering conventions. NI stands for Not Instrumented. H-A and H-B are the HADES sensors. The dead sensor modules are marked by a cross.

3.4 The retrievable transmitter

The retrievable transmitter (pinger), is an autonomous sound source which can be deployed in any available IceCube hole. In the 2007/2008 and 2008/2009 austral summers, the pinger was lowered successively in 10 water-filled IceCube holes before the actual deployment of the IceCube optical equipment. The pinger, pulsing at a fixed repetition rate, went down to 400 m or 500 m depth and was then raised back to the surface. The movement was stopped for maximum 5 minutes at selected instrumented SPATS levels. During that stop, the installed SPATS strings recorded at least 1 event with each sensor channel.

The pinger setup consists of three main parts. First, an acoustic pinger box (APB) at the surface provides the battery power, the GPS synchronised trigger and a pressure-sensor readout. This box is connected to the second main part which is the cable of the Robertson winch[16] (RW). Finally, the end of the RW cable connects to a pressure housing. A transducer is connected to, and positioned below, that pressure housing.

3.4.1 The acoustic pinger box

The acoustic pinger box (APB, see Fig. 3.9(a)) on the surface contains a total of 4×6 V lead acid rechargeable batteries[17] connected in series to provide 24 V. The batteries are recharged regularly between operations. The APB is connected to an external GPS receiver. The first-generation pinger directly used the 1 pps pulse from this GPS as trigger for the HV-pulse and the maximum repetition rate was therefore 1 Hz. For the second-generation pinger, the APB routes the 1 pps signal to a GPS-synchronised pulse generator (frequency-multiplying) board called the LG-board[18]. This LG-board can be set from 1 Hz to a maximum of 50 Hz trigger rate. It is known from initial tests that the acoustic emission from the pinger becomes erratic above about 15 Hz, due to an insufficient time between pulses to restore the ground level for the electronics. The maximum repetition rate was therefore set to 10 Hz for the second pinger season. All holes during the 2008/2009 season were pinged with a 10 Hz repetition rate except for the last hole which was pinged at a rate of 8 Hz.

---

[16] http://www.geologging.com/

[17] Hawker-Cyclon, resistant to low temperatures.

[18] After its designer, Leif Gustafsson.

(a)
(b)
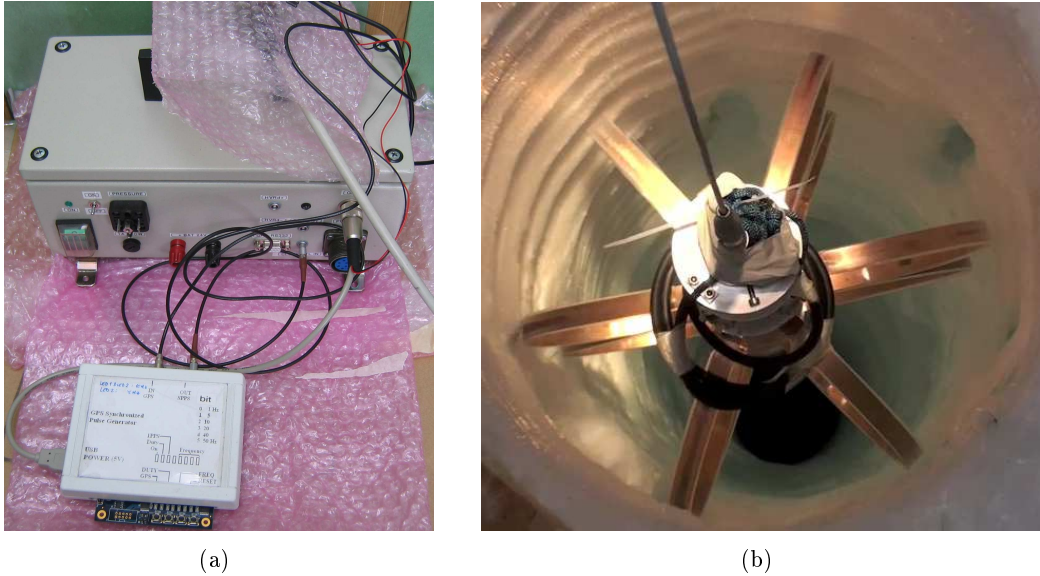
Figure 3.9: The pinger setup. (a): Pictures from the APB with the LG-board. (b): Top view of the pinger going down in a water-filled IceCube hole.

3.4.2 The retrievable stage

The APB is connected to a 2700 m long armoured 2 wire-pair cable (i.e. 4 conductors) that is spooled onto the RW. Power, ground and trigger are routed to a steel pressure vessel that contains a HV pulse generator board. The remaining conductor can be used to read out the current of a pressure sensor situated inside the steel vessel. A spherical (diameter 10.8 cm) omnidirectional piezo-ceramic transducer[19] is electrically connected to the pressure housing and positioned about 2 m below it. The transducer transmitting voltage response is about 149 dB re. V/μPa @ 1 m for a frequency around 18 kHz[20]; it is rated to a maximum depth of 1219 m and the capacitance is 62000 pF. It has a broadband omnidirectional transmitting response and has a resonance frequency of 16.5 kHz. Figure 3.10(a) shows the directivity pattern of the ITC-1001 at 18 kHz. Upon arrival of a trigger signal, a 30 μs electric pulse of 400 V is sent to the ITC-1001 piezo-ceramic element which then emits a broadband pulse. Most of the power is concentrated in the (10–30) kHz range. An example of a noise-subtracted Fourier spectrum of the pinger signal as seen by a HADES sensor is shown in Fig. 3.10(b). It was verified with simulations that the frequency content from the pinger-signal as seen by the HADES and SPATS sensors reflects the true emitted spectrum from the pinger [159].

The pinger stage that was deployed in the 2007/2008 austral summer had limited rigidity so that pendulum movements of the piezo-ceramic element were possible. Therefore there was no control over the position of the pinger transducer relative to the hole walls. This resulted in an unpredictable interference with the reflections of the pulse inside the hole. On top of that, the water/ice interface has a large impedance mismatch and creation of shear waves was expected at

---

[19]Model ITC-1001 from the International Transducer Corporation. http://www.itc-transducers.com/

[20]The traditional standard for calibration sensitivity is dB with respect to V/μPa. A sensitivity of –160 dB (re 1V/μPa) is equivalent to 10 μV/Pa of voltage sensitivity.
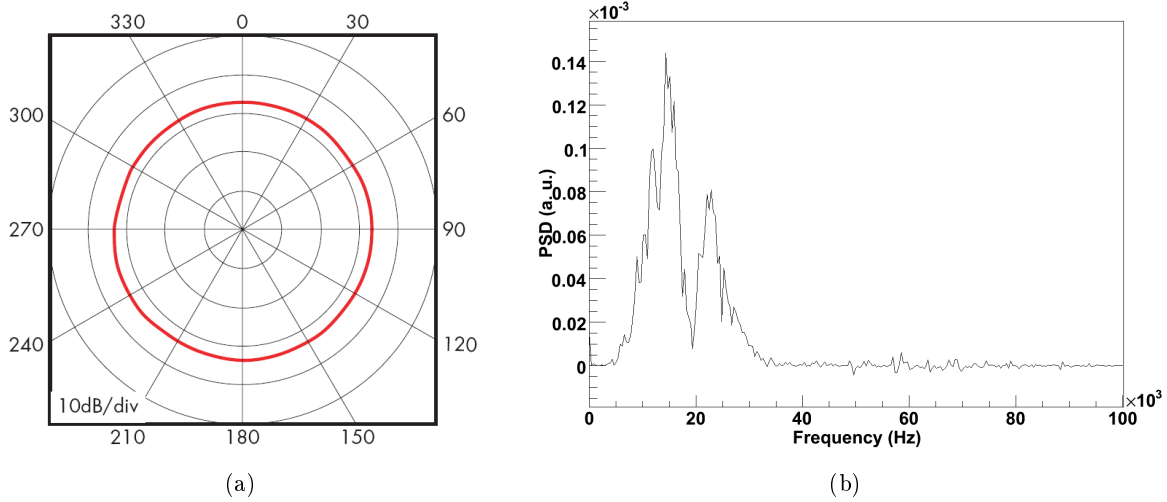
Figure 3.10: (a): The ITC-1001 transducer directivity pattern at 18 kHz. (b): The ITC-1001 frequency content for an event seen by the string D HADES DS6 sensor, from [156].

the boundary. The precise amount of energy that went into shear and pressure waves depended on the angles involved. The 2007/2008 pinger data indeed showed complicated interferences, shear wave contributions and therefore irreproducible pulses. For these reasons, it became desirable to maintain a fixed pinger position inside the hole during the stops. To that end, the stage was redesigned and fitted with centralisers so that the piezo-ceramic element would be always positioned in the centre of the hole and no oscillating movements in the horizontal plane could be possible, see Fig. 3.9(b).

3.4.3 Trigger and GPS timing

During pinger data-taking, both the SPATS array and the pinger are GPS synchronised so that the precise arrival times and therefore the speed of the pinger-pulses can be determined. This synchronisation also allows for easy averaging of the individual pulses. On the surface, a GPS clock (Garmin model GPS 18 PVC) is used to generate a 1 pps signal. The rising edge of the signal is aligned to the start of each GPS second within $1\,\mu s$ for all conditions in which the receiver has reported a valid and accurate position from the satellites for at least the previous 4 seconds.

The default pulse width is 100 ms, programmable between 20 ms and 980 ms in steps of 20 ms. The rising edge of the trigger signal initiates charging of the HV pulse generator circuit, followed by discharge that immediately results in acoustic emission. The emission time delay introduced by the HV circuit has been measured in the laboratory to be $t_e = 1.90 \pm 0.05$ ms over the range of temperatures in which the pinger operated ($-20\,°C$ to $+20\,°C$). The electrical pulse-to-pulse variation of the HV board is negligible. The electrical signal propagation speed through the 2700 m cable is 67 % of the speed of light in vacuum according to the manufacturer specifications, resulting in a $13\,\mu s$ predicted cable delay time. This delay has indeed been verified in the laboratory to be on the order of $10\,\mu s$, still negligible compared with other contributions to the timing uncertainty.

In the 2008/2009 pinger season, it was verified that no audible irregularities in repetition rate or amplitude were present before the pinger deployments. Some erratic behaviour, as was the case for repetition rates above 15 Hz, was observed after the deployments but this was not recorded in the SPATS sensor waveforms. The water level inside the IceCube holes is roughly 70 m below the surface. This means that the pinger stage could have suffered from the low temperatures (around –55 °C) inside the hole while it was travelling between the water level and the surface. In the low-level verification of the pinger-data it was found that an extra pinger-pulse was produced on rare occasions, possibly due to an erroneous trigger signal from the GPS.

3.4.4 Depth measurement

First pinger season

During the 2007/2008 season, the pressure sensor could unexpectedly not be read out during deployment. Five independent SeaStar sensors were installed on the pinger stage. These SeaStar sensors are miniature stand-alone data loggers that record temperature and pressure. Recorded data is then stored in the logger's internal memory with a real time reference for each measurement. It is the world's smallest temperature and pressure logger but it does not allow real-time monitoring of the depth of the pinger. The only way to estimate the depth during deployment was by counting the turns on the RW during the lowering of the pinger. Due to incorrect estimation of the decrease of the diameter of the RW spool, this depth was systematically overestimated. Therefore the pinger was always stopped above the nominal SPATS stage depths with a deviation that increases with depth. This became clear after analysing the data of the SeaStar sensors. It was, for example, found that the maximum depth of the pinger was 477 m, instead of the target depth of 500 m. The 5 SeaStar sensors that were used in this season sometimes disagreed by over 30 m. The corrected turn-counting estimate and the SeaStar measurements were averaged in order to get a pinger-depth estimate. The error on the 2007/2008 pinger depth is ±5 m [160].
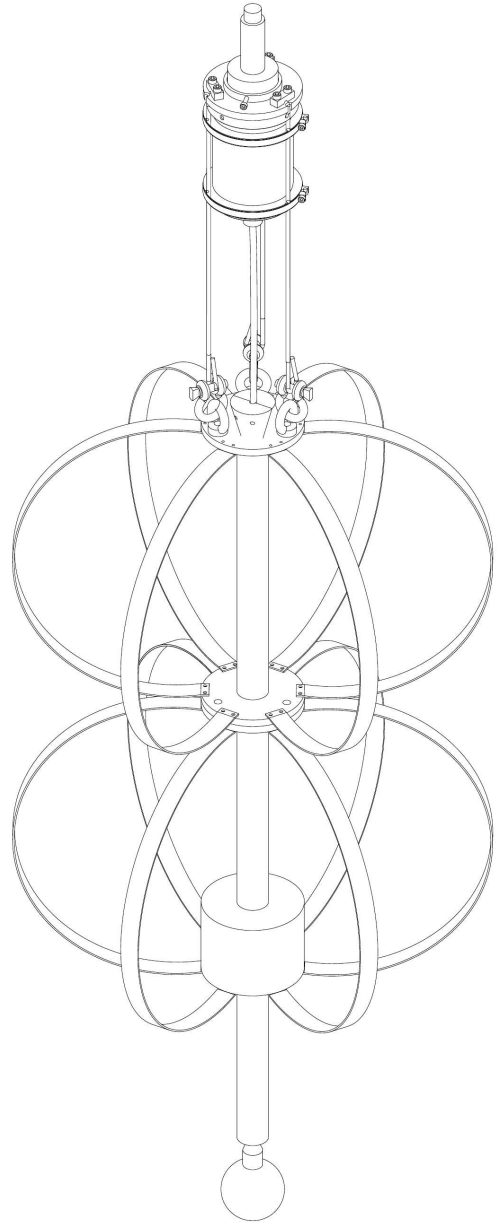
Figure 3.11: Shematic of the 2008/2009 pinger stage. The total stage has a length of roughly 2 m and a diameter of about 0.6 m.

Second pinger season

During the 2008/2009 season, three methods to measure the depth were used: the RW turn-counting, the new RW cable payout system and again the SeaStar sensors[21]. The payout depth measurement consists of a small wheel that is resting on top of the RW cable close the RW winch. The wheel turns along when the cable is lowered or raised. A counter then indicates the length of cable that has been unspooled. The SeaStar sensors were always attached to the pinger stage at the same location: about 1.4 m above the pinger piezo-ceramic element. Each second, the pressure and temperature were recorded and the time was synchronised with a GPS-synchronised NTP (Network Time Protocol) server. The SeaStar raw data states the pressure in bar. To get the actual depth of the pinger transducer, the following formula is applied:

$$D_p = (P - P_0)C - D_w - l, \tag{3.1}$$

where P is the raw pressure data recorded by the SeaStar sensor, P_0 is the pressure when the SeaStar is at about $0.4\,°C$ but not in water before the actual deployment. D_w is the distance from the floor of the Tower Operation Structure (TOS) to the surface of the water in the hole (well-depth), l is the distance from the SeaStar to the pinger piezo-ceramic element (1.4 m on all occasions) and C is the conversion constant (1 bar $=$ 10.19716213 m of water). The maximum discrepancy between the depth measurements by SeaStar sensors was about 15 m. This can be due to differences in calibration and possibly different temperature-dependences. A reasonable error on the mean of the SeaStar data is 10 m; Fig. 3.12 shows the SeaStar data for IceCube hole 19 (Fig. 3.1).

The payout was set to 0 when the pinger transducer was positioned at TOS floor-level. A possible systematic error on this depth measurement can come from slipping of the cable over the wheel. This means that the cable will go over without turning the wheel, thus making the payout underestimate the amount of cable that passed by. Slippage can happen both in the down-going and up-going movement of the cable. Therefore, the payout offset, when the pinger transducer is back at TOS floor-level after pinging, could be interpreted as the maximum error due to slippage. This offset was recorded for two different holes and was found to be less than 1 m in both cases. It is, however, more likely that the slipping of the cable occurs in equal amount but different direction and this would not be noticeable. Another possible source of error in the payout depth measurement is the fact that the payout device could be badly calibrated. The calibration was checked by estimating the pinger depth using the RW turn-counting technique and cross-checking it with the payout depth measurement. This was done for the first hole in which the pinger was deployed, at the first depth where it was stopped. Since the payout and turn-counting depth measurements agreed, it was then decided to no longer count the turns. A different device (hole-logger), which also used the RW, was deployed down to 1400 m in an IceCube hole. At that time the TOS payout system was also available. The RW and TOS payout readings were consistent.

Therefore, the payout depth measurement is more accurate than the SeaStar measurement. The two measurements are always in agreement with each other if the error on the SeaStar measurement is taken as the spread between the 3 SeaStar sensors. As a result, it is reasonable to take the payout measurement value as the pinger depth, with a conservative error of $\pm 5\,m$. Most likely a more realistic error is on the order of $\pm 2\,m$.

---

[21] In the 2008/2009 season, three SeaStar sensors were used with serial numbers 3387, 3504 and 3570.
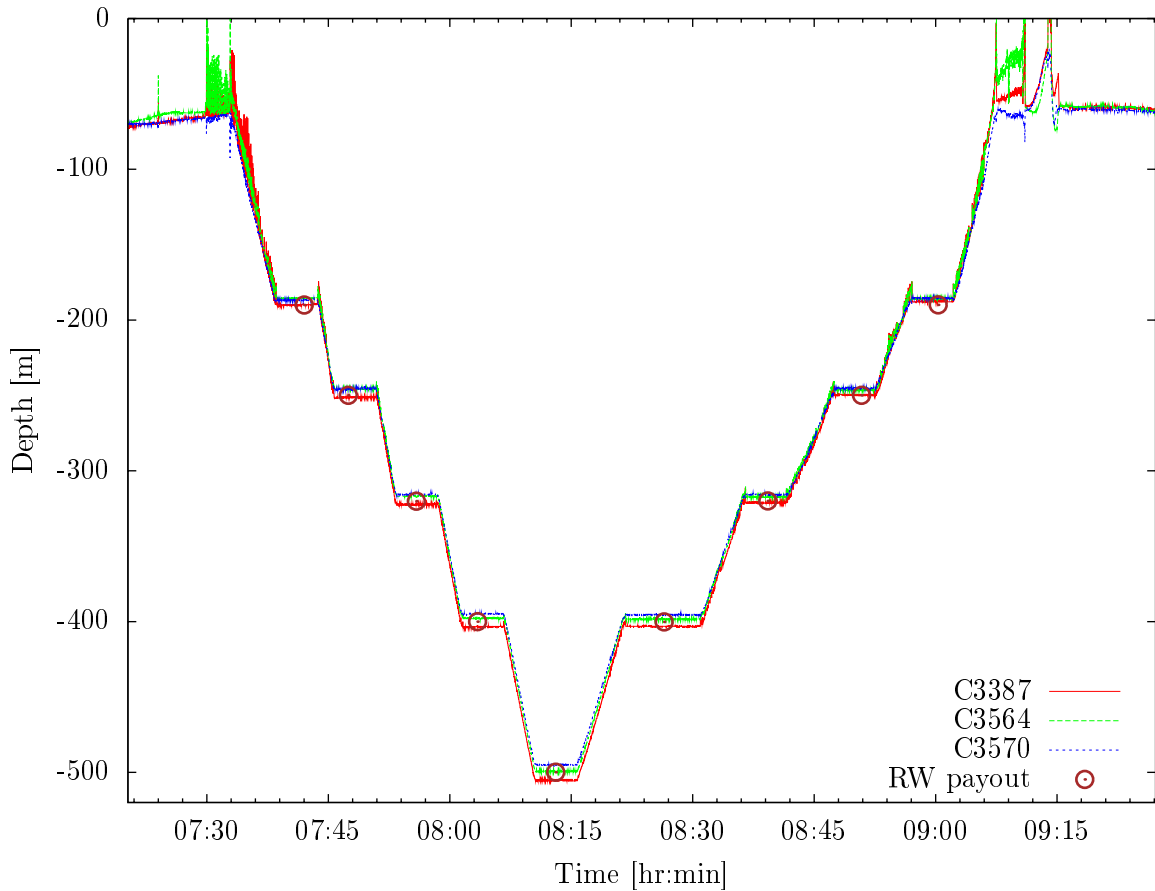
Figure 3.12: The SeaStar (C3387, C3504 and C3570) and RW payout depth measurements for hole 19. The two depth measurements are in agreement. The SeaStars behave erratically before and after deployment due to the fact that the pressure measured by the SeaStar sensors is sensitive to temperature changes. The pinger stage is positioned above the hole at those instances, exposed to the cold air ($\sim$−55 °C) that is coming up from the hole. Once the pinger is in the water, the temperature remains stable at 0.4 ± 0.4°C .

3.5   Data acquisition

3.5.1   Data format

A complete overview of the SPATS DAQ can be found in the data acquisition internal report [158]. The SPATS DAQ software is version-controlled using the Concurrent Versions System (CVS). Therefore, all strings run exactly the same software at any given time. An electronic logbook keeps track of all activity on the master-PC and string-PCs.

The SPATS data-taking software consists of compiled C-code that is controlled by shell scripts locally on each string-PC. All waveform data are recorded in a well-defined binary format (run). Such a SPATS run consists of a certain number of events that can each contain a sensor waveform and/or a transmitter HVRB waveform. A waveform consists of samples that contain both the

IRIG-B and ADC counts so that each sample has precise timestamping. A run number is assigned and incremented automatically and the daily runlog keeps track of the start- and stop-times of all runs.

3.5.2 System monitoring data-taking

The monitoring data allow to control the basic system parameters for both the master-PC and the string-PCs. The string-PC monitoring script runs each hour and collects the following data:

1. PT monitoring: the temperature (T) and pressure (P) sensors inside the transmitter modules,
2. FADC temperatures: the internal temperature sensor is read-out for all FADC boards,
3. Network Time Protocol (NTP) variables: for example, the jitter on the system time NTP synchronisation is monitored. The jitter is a measure of the phase noise in the time received from the server. If the time queries happen at irregular intervals, the jitter is high,
4. the string-PC DOM and RAM disk status (`df` and `du` queries).

The master-PC monitoring script also runs each hour and collects the following data:

1. power monitoring: the status of the wire-pairs for all SPATS surface cables,
2. ping-delays: the average ping time between the string-PCs and the master-PC,
3. the master-PC hard disk status (`df` and `du` queries),
4. the status of the NTP server on the master-PC (`ntpq -p` query).

The results of the system monitoring data-taking is compiled in a mail (monitor-mail) and sent over the so-called Iridium-network, which is a cellular satellite network, during downtime of the regular satellites. This way, action can be taken right from the start of the next satellite pass.

On top of that, all data-transfer details are compiled in another mail. Herein, the total data-transfer rate for that day and the amount of data that went to the local taping system without being transferred over satellite are detailed.

3.5.3 Acoustic data-taking

There are two main C-programs, namely `triggered-run.c` and `trigreadcont.c`, that can be used for a variety of acoustic data-taking modes.

- **Untriggered noise** (`trigreadcont.c`), or transient data. The noise waveform is recorded for a short duration (currently 0.1 s) at 200 kHz sampling frequency. These full waveforms are used for the absolute noise level analysis since they retain all frequency information up to 100 kHz.

- **Untriggered noise histograms** (`monitor-noise.c`, based on `trigreadcont.c`). It became desirable to have a way of monitoring the noise level for all sensor channels without having to save the entire waveform for each of them. Indeed, this last option takes a large amount of disk space and SDSL transfer time. Therefore the noise is recorded in the form of an ADC-count histogram (i.e. the number of times a certain ADC bin occurs), examples of which can be seen in Appendix A.
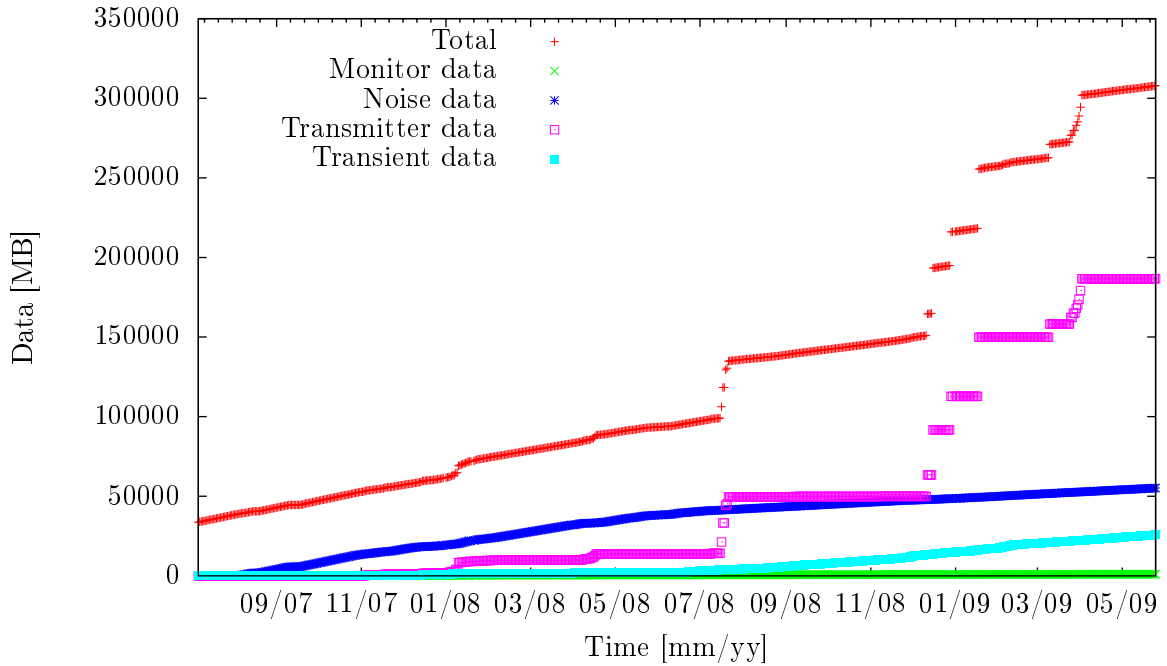
Figure 3.13: Cumulative SPATS data; most of the pinger data is not included since it was not transferred using the satellite system but carried North by hand.

- **Intra-stage** (`trigreadcont.c`). A sensor records the acoustic pulse originating from the transmitter on the same stage. This type of data has been used to investigate the freeze-in process during commissioning.

- **Intra-string** (`trigreadcont.c`). A sensor records the acoustic pulse originating from a transmitter on the same string.

- **Inter-string** (`trigreadcont.c`). A sensor records the acoustic pulse originating from a transmitter on a different string. In a typical inter-string data-taking schedule, one transmitter will be triggered while the other strings loop over their sensors. This way, all transmitter-sensor combinations are obtained. The inter-string data provide the possibility of investigating the attenuation length. The analysis of these data is the subject of Chapter 5 and data-taking will be explained in more detail there.

- **Pinger runs.** A sensor records the acoustic pulse originating from the pinger. For the 2008/2009 pinger season, the pinger signal was recorded for 18 s at a sampling frequency of 200 kHz by all three channels of a same sensor module simultaneously. A string could complete a loop over all sensor modules in less than 4 min. On top of that, the 4 SPATS strings recorded data from the same sensor module at the same time within 1 s thanks to the NTP synchronisation and the fact that the data-taking script would be restarted every 4 min.

- **Triggered noise** (`triggered-run.c`). If the number of ADC counts on any of the twelve monitored sensor channels (three channels on each of the 4 SPATS strings) exceeds a certain level above noise, we record a 5 ms window of data (1001 ADC samples at 200 kHz) around the trigger on that channel. This is a transient event. The resulting trigger rate is roughly stable and on the order of a few triggers every minute for each of the monitored channels. Most of these events are Gaussian noise events, where only one sample is outside the trigger boundaries. The transient events are processed offline and analysed for time-coincidence clustering. `triggered-run.c` also allows monitoring of the FADC clockdrifts (see § 3.6.2 and § 5.2.1) and the recording of noise-histograms during transient data-taking. These options are currently disabled.

At the present time, the SPATS data-taking is concentrating on transient data-taking: 45 minutes of each hour are dedicated to transient data-taking, the remaining 15 min are reserved for noise data-taking and system monitoring. The thresholds for each channel that takes part in transient data-taking are chosen so that the total data-rate for SPATS remains below 150 MB/day under normal trigger circumstances. In total, over 500 GB of data has been accumulated over the past ~3 years. Figure 3.13 shows the cumulative data versus time.

3.6   System performance

3.6.1   System monitoring

The SPATS monitoring website[22] has been operational since April 2007. It is updated daily with the latest available SPATS data or with the data of the monitor-mail. It also hosts an online plot-generator: the Gaussian noise data can be plotted for any sensor and any period. The availability of the data depends on the satellite-transfer queue. A normal delay is 1 to 2 days, although delays of 10 days or more have occurred in the past. Currently the monitoring website shows the following system and acoustic monitoring variables:

- **Noise level monitoring**
  Since the observed noise in the SPATS sensors is Gaussian, the noise levels can be monitored looking at the evolution of the standard deviation of the Gaussian ADC-count distributions for each channel. The SPATS noise levels are very stable, with a few exceptions. First, the noise was found to increase during the first few weeks after a SPATS string was deployed. It is possible that this is an effect of a better coupling of the hole-ice to the bulk ice. Second, the noise levels increase and fluctuate during the IceCube drilling season. In fact, it was shown that the drill can clearly be heard by the SPATS sensors if it is close enough. Indeed, Fig. 3.14 shows the Gaussian noise level for all available sensor channels of string B (bottom 7 plots) for a period during which the IceCube drill was passing by at the depths of the stages (upper plot). The noise levels are elevated only when the drill is in the upper 600 m of the ice. Third, the noise levels are in general higher just after powering up the sensor. Therefore, the sensors are kept on continuously. The recorded noise levels are not dependent on the FADC board temperatures, see Fig. 3.15.

---

[22] http://inwfsun1.ugent.be/~freija/Moni-SPATS/ Restricted website, please contact author for access.
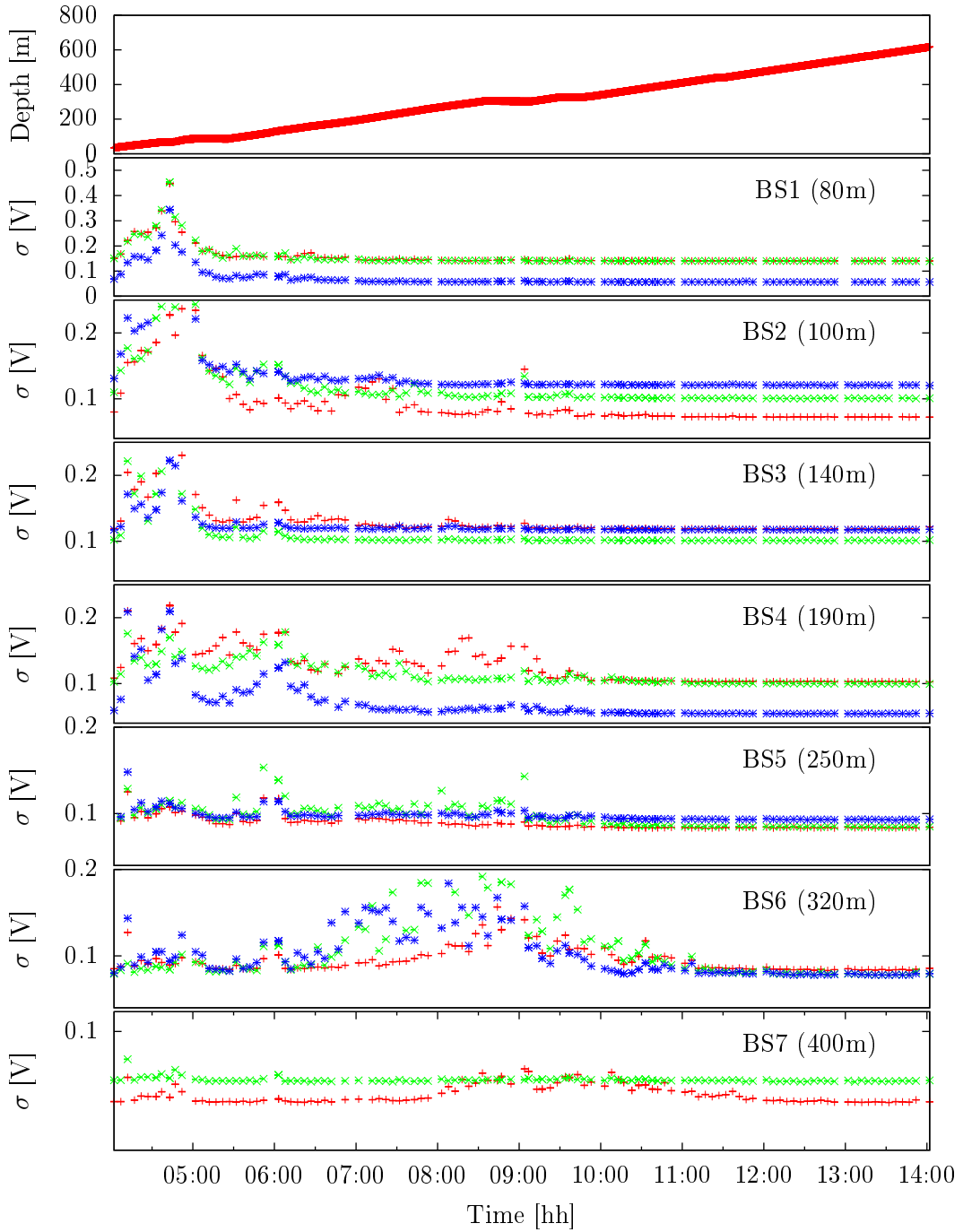
Figure 3.14: Evolution of the SPATS noise levels for string B during drilling at IceCube hole 64, at a distance of roughly 128 m. The upper plot shows the depth of the IceCube hot-water drill versus time as measured by a pressure sensor attached to the drill head. The σ of the Gaussian fitted to the histogram of the ADC voltages is shown for all available sensor channels for string B. For each depth, the σ is plotted for the 3 sensor channels (3 different colours). One of the channels of BS7 was not operational at that time.
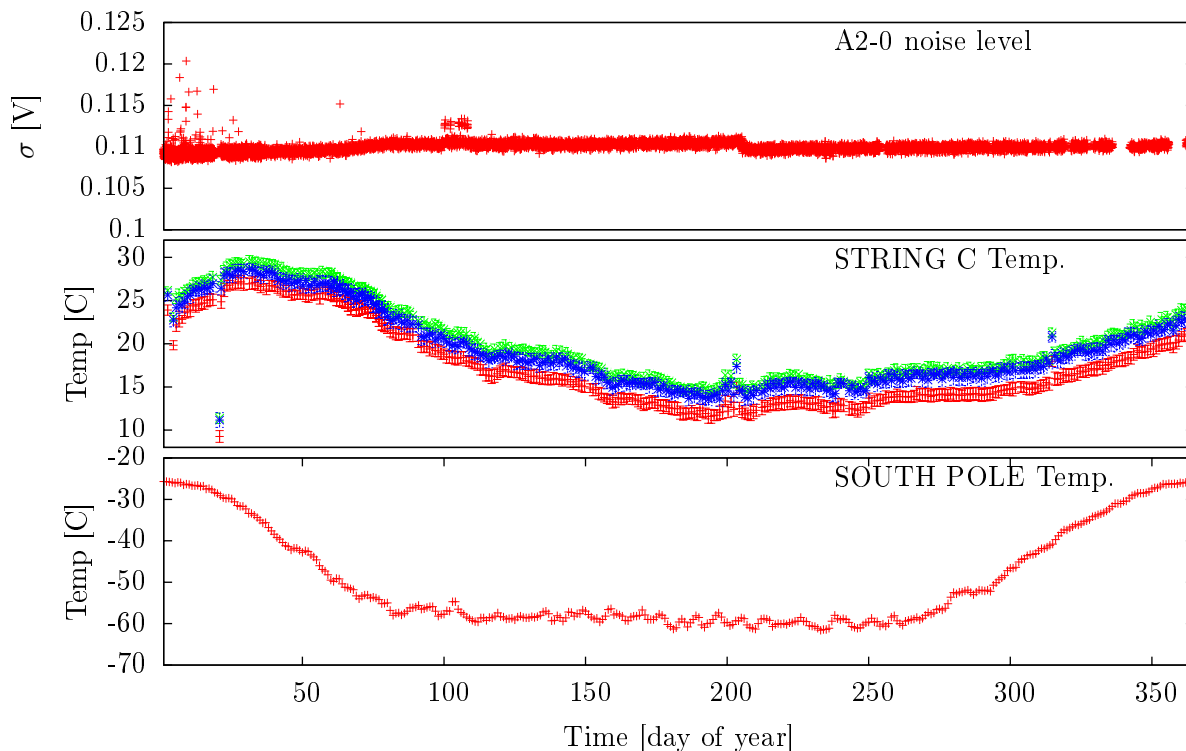
Figure 3.15: Evolution of the temperatures of the three FADC boards (3 different colours) from string C (middle panel) and AS2-0 noise levels (top panel) compared to the average surface temperature at South Pole (bottom panel). The AS2-0 sensor channel is located at 100 m depth, right between the firn and the bulk ice.

- **Transient monitoring**
  The raw transient data-rate is plotted for each hour. This includes all the Gaussian and true transient triggers.
- **Power monitoring**
  The voltage and current of each string is monitored using the daily monitor-mail.
- **FADC temperature monitoring**
  All FADC temperatures are recorded and plotted versus time, an example of which can be seen in the middle panel of Fig. 3.15.

The SPATS monitoring website has played a vital role in understanding the SPATS data stream. For example, it was noticed that the SPATS noise levels change during inter-string data taking. After investigation it became clear that the change in noise level was related to the powering off of the sensors between inter-string runs. The reason for this is that for the transmitting string, only the transmitter is turned on and the sensors are not. After the inter-string data taking, the noise monitoring code turns on all sensors at the same time. This was consequently changed so that the sensors are not powered down when transmitting. All available monitoring data is reviewed every day in order to detect anomalies as soon as possible. To this end, a dedicated monitoring logbook and monitoring-shifts were put into place.
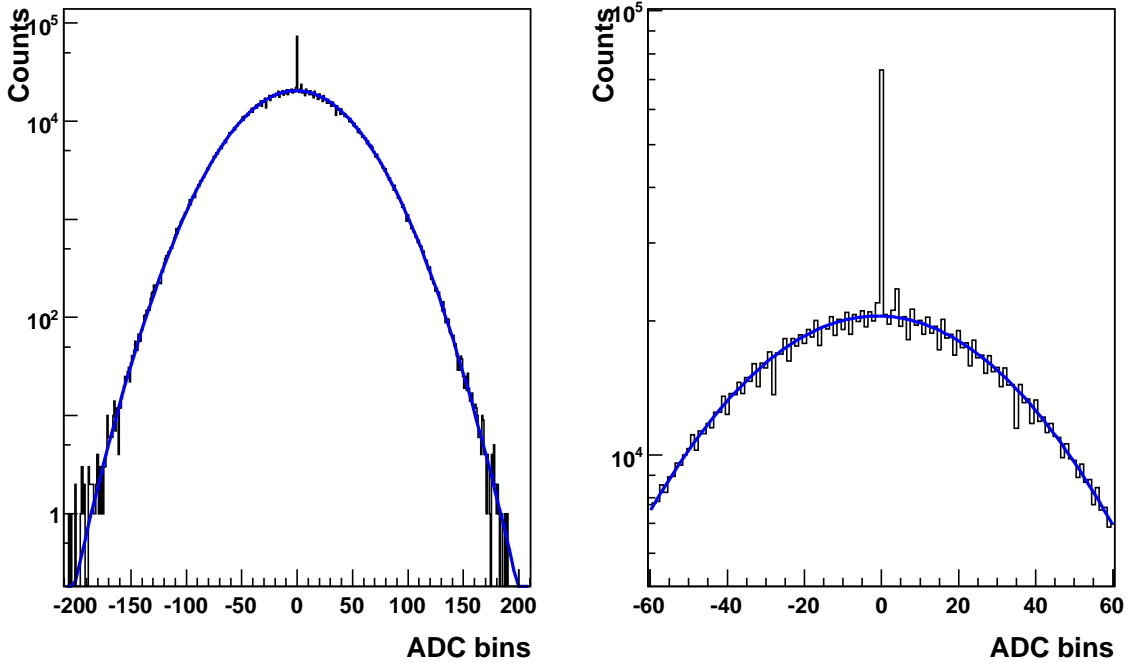
Figure 3.16: The histogram of about 10^6 ADC counts (5 s at 200 kHz) for channel AS4-2 on the left with a zoom on the central bins on the right. A Gaussian is fitted to the distribution.

3.6.2 The FADC boards

Temperature behaviour

The temperature of each FADC board is influenced by both external (weather, station-wide power outages) and internal (data-taking modes) factors. The FADC temperatures (and therefore the AJB temperature) take about 12 hours to stabilise after an extended power outage. Over the course of an entire year, the FADC temperature changes by a maximum of 20 °C whereas the South Pole surface temperature fluctuates by over 35 °C. The isolating snow that surrounds the AJB acts as a buffer to the extreme temperatures: the FADC temperature fluctuations are smaller and have a delay of about 1 month, see Fig. 3.15.

FADC limitations

It is important to have a good understanding of the FADC boards and their limitations. There are certain features in the SPATS data that are purely FADC artefacts. Figure 3.16 illustrates one of the FADC artefacts, a so-called quantisation-error that is due to the finite resolution of the FADC. It shows an ADC histogram for sensor channel AS4-2, with a zoom on the central bins. There is an excess in the bin at 0 ADC channel and a saw-like structure. The range of expected statistical fluctuations in the histogram is much smaller than the observed structure which shows bin contents that are alternating above and below the expected counts. This feature is has been investigated and it was found the ADC has a bias towards certain bins. The FADCs

can be trusted up to a precision of 1 ADC bin.

The FADC has a maximum sampling frequency of 1.25 MHz. However, when an FADC board is run for long duration and/or high sampling frequency, some runs hang with a "dma time-out" kernel message. This error is handled by wrapping binary executable runs in a shell script that kills the job if it does not finish in the expected time. However, for high enough sampling frequency or duration, practically all runs hang. There is a clear dependence of the failure rate on the sampling frequency and duration. The problem is worse when writing data to file during acquisition and better when writing after acquisition. The problem is also worse when we sample with multiple boards simultaneously or when a user is logged on the string-PC. This shows that the success rate depends on the load that is exercised on the CPU of the string-PC.

The FADC clocks were found to drift. This means that the FADC will not sample the waveform at the requested (nominal) frequency but a slightly higher or lower one. The cumulative amount of drift causes decoherence in the averaging of SPATS transmitter and pinger pulses if the nominal rather than true sampling frequency is used. This clockdrift effect can be accounted for by using the IRIG-B GPS signal since the latter is recorded synchronously with each sensor channel recording. It is therefore possible to determine the actual sampling frequency at the time of the recording. This actual sampling frequency then needs to be used if data is averaged (see § 5.2.1).

New FADC driver

In 2008, RTD released an updated Linux driver for the FADC boards for which they claimed better performance. It was therefore decided that the SPATS DAQ performance should be tested with the new driver on the test-system string E. The main change is that this new driver is designed to use an interrupt[23] handler to retrieve the data from the board. This introduces a new vulnerability: the application may miss or lose interrupts, especially if interrupts occur quickly enough. A board may enter an inconsistent state if interrupts are not acknowledged reasonably. During the tests it was found that the ADC FIFO (First In, First Out) fills up because the data of the unhandled interrupts is never retrieved and this causes the system to freeze. A way to avoid unhandled data is to lower the sampling frequency and/or to change the buffer size. It was found that the new driver performed well at a maximum of 400 kHz. This is not a major improvement on the old driver. On top of that, at a certain point during testing, the FADC became irresponsive and could no longer be accessed even after a full string-PC reboot. It was therefore decided not to install the new driver since the risks involved were too high.

3.6.3   Current status

SPATS sensor status

The status of the SPATS sensor channels can easily be assessed by investigation of the ADC histogram for noise. In Appendix A, these noise-histograms, using 10^6 ADC counts, is plotted for each of the SPATS sensor channels using the noise data taken on 20 August 2009. Currently 6 out of a total of 80 sensor channels are continuously saturated (AS3 and CS1). This saturation is presumably caused by the possible detachment of one of the piezo-ceramic elements from the

---

[23]An interrupt is an signal indicating a need or possibility for action.

housing. Some of the channels have had larger variations in their Gaussian noise levels, as, for example, AS1-2. The complete available noise data can be found in Appendix B.

SPATS transmitter status

The status of the transmitters can be assessed by looking at their HVRB. Most of the transmitters from strings A, B and C have evolved from displaying smooth HVRB-pulses to more structured ones. The pulses remain very reproducible although the amplitudes typically have decreased. Currently, all SPATS transmitters are operational, except for DT6 which failed a few weeks after deployment.

SPATS calibration and testing

The field of water (oceans) and air (atmospheric) acoustics is well developed and calibration methods for acoustic transducers in air and liquids are mature and reliable[1]. SPATS is the first project to install acoustic devices in the South Pole ice. Sensors and transmitters can only be calibrated in water since no calibration method or calibrated source exists for ice. The goals of the SPATS testing and calibration efforts are threefold:

- To understand how the absolute sensitivity[2] of a sensor channel in water translates to the absolute sensitivity in ice.
  All sensors of strings A, B and C were calibrated in water [155] and the influence of temperature and pressure on the sensitivity has been quantified in dedicated laboratory tests [161]. A short summary of the results is given in § 4.1. Combining all these results allows the recorded voltage output from the amplifier to be translated into a pressure reading.

- To understand relative variations between the transducers in the ice.
  The relative differences in waveform energy between single transmitter-sensor (T,S) combinations are due to the differences in sensitivity of the sensor channels and transmittivity of the transmitters. This can be called the intrinsic variability of the transducers. The in-water calibration data can indicate the difference in sensitivity of the sensor channels. On top of that, the sensitivity of a sensor channel varies with azimuthal or polar angle. Also the transmitter's emission strength is angular dependent. This is called the angular variability of the transducers. Both laboratory and in-situ tests have given insight into the angular behaviour of our transducers. However, the effect of the refrozen ice around the transducers is unknown. It is possible that bubbles have formed around the transmitting elements or the sensor module housings. The presence of the IceCube main cable could have a large effect on the transmitted and received amplitudes due to shadowing. Therefore, applying the in-water calibration results for the azimuthal and polar variation estimations is possibly an underestimation of the true in-ice variations.

- To check the correct installation and behaviour of all parts of the system.
  Some tests are designed to understand specific features in the data. Certain data-taking streams exist solely for system monitoring. An example is the noise-histogramming which was presented in § 3.6.1.

In this chapter, SPATS testing and important calibration results are presented, showing how these results have increased the understanding of the in-ice data and confidence in the SPATS

---

[1]The main motivation for the development of high-pressure hydrophones are the military applications, such as sonar technology for submarines.

[2]The absolute sensitivity of an acoustic sensor indicates what the absolute level is of the pressure for a certain voltage output of the sensor.
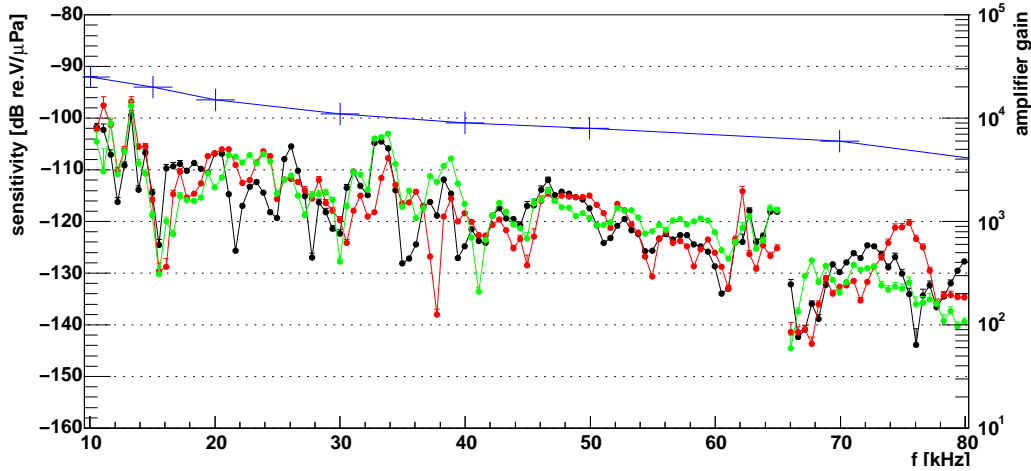
Figure 4.1: Sensitivity frequency spectrum of SPATS sensor module #3 for all three channels (3 different colours/lines). The amplifier gain is indicated by the upper line (blue). Statistical errors are also plotted but are mostly too small to see. Figure from [157].

physics results. More specifically, the systematics that are of importance to the inter-string analysis presented in Chapter 5 are discussed.

4.1 Calibration

4.1.1 In-water calibration

The in-water calibration of the 25 initial SPATS sensors took place in a large water tank at the Hamburger Schiffbauversuchsanstalt (HSVA, Germany [162]). The water was at $\sim$0.5 °C. The setup and results are described in detail in [155]; here only a short summary is given.

SPATS sensors

In order to determine the frequency dependent sensitivities for the SPATS sensors, a reference with known absolute sensitivity is necessary so that the pressure spectrum of an acoustic field can be obtained. Our reference hydrophone (Sensortech-SQ03) had a working range from 1 Hz up to 65 kHz and was delivered with a nominal frequency independent sensitivity of −163.3 ± 0.3 dB re. 1 V/μPa. Recalibration, however, showed a decrease in sensitivity 3 years after production: −167.5 ± 0.3 dB re. 1 V/μPa. The hydrophone variation in sensitivity with respect to azimuth was measured to be very small.

Ring-shaped piezo-ceramic elements, similar to the transducers of the SPATS transmitters, were used to generate a broadband pulse. The sensors were mounted at a depth of 2 m and the spacing between transmitter and sensor was $\sim$1 m to avoid near-field effects and interference from reflections. The generated pressure pulses were first recorded with the reference hydrophone and the pressure frequency spectrum was derived. The SPATS sensor modules were then consecutively positioned in the same acoustic field. Three measurements were taken for each sensor module with each time one of the three sensor channels oriented towards the transmitter.

The signal amplitudes were then derived from the Fourier coefficient distributions and the sensitivity frequency spectra for all channels were obtained by division of the amplitude frequency spectra by the pressure frequency spectrum. Fig. 4.1 shows the sensitivity spectra of the three channels inside a same SPATS module. It illustrates a typical trend that could be found in all sensor channels: the sensitivity decreased with increasing frequency. This is partly an effect of the decrease in amplifier gain. In addition, each sensitivity spectrum showed a complex structure above statistical fluctuation. The three channels from the same module do showed the same general structure which could be related to the complex mechanical design of the module which resulted in a number of resonance modes.

Moreover, five seconds of self-noise were recorded for each SPATS sensor module channel. This means that noise data were taken with minimal external influence. From this data, the self-noise frequency spectra were derived. The equivalent noise level was then extracted by taking the ratio of the self-noise frequency spectrum over the sensitivity frequency spectrum. In this way the equivalent noise level (i.e. the minimal detectable acoustic signal for any given transducer) was obtained for all 75 channels. The average values of the equivalent noise level for all channels were between 12 mPa and 83 mPa. Due to a normalisation error, the equivalent self-noise levels were initially off by a factor of 23.72. Therefore, the equivalent self-noise, for the first generation SPATS channels in water, is lower than initially extracted and is (1–10) mPa.

To summarise, all sensor channels were placed in the same acoustic field. If all sensor channels had the same sensitivity, the same output voltage would have been expected. However, this was not the case and the sensitivity for each sensor channel was extracted. The observed variations in intrinsic sensitivity were typically larger than one order of magnitude. The sensor channels were typically performing better than the commercial hydrophone, both in sensitivity and in detection capability. The sensitivity of the hydrophone, however, had a flatter dependence on frequency.

The obtained SPATS sensor channel sensitivities are only valid in water. From the material impedances presented in Table 2.4, one could expect to see an higher sensitivity for the SPATS sensors after they are frozen-in in the Antarctic ice. Indeed, the impedance matching is better between ice and steel than between water and steel. This means that a smaller fraction of the incoming pressure wave will be reflected at the ice-steel interface than at a water-steel interface.

The static pressure will be higher in ice and the temperature will be lower. In the next section the results from dedicated labtests, investigating the influence of these two external factors on the sensor channel sensitivity, are presented.

SPATS transmitters

The ring-shaped piezo-ceramic elements that are used in the SPATS transmitters are expected to have an isotropic azimuthal emission. The actual emission directivity of one ring-shaped piezo-ceramic element was measured in azimuthal and polar direction. To measure polar variations, the piezo-ceramic element was rotated around an axis perpendicular to the ring axis. The pulses were recorded by the reference hydrophone at a distance of 1 m. For the transmitters that are deployed in the South Pole ice, there is no control over the azimuthal orientation. One can expect to see variations in the amplitude of around 40% due to this systematic effect. For ±10° polar orientation uncertainty, the amplitude variation is expected to stay below 10%, see Fig. 4.2.

(a) Azimuthal directivity   (b) Polar directivity
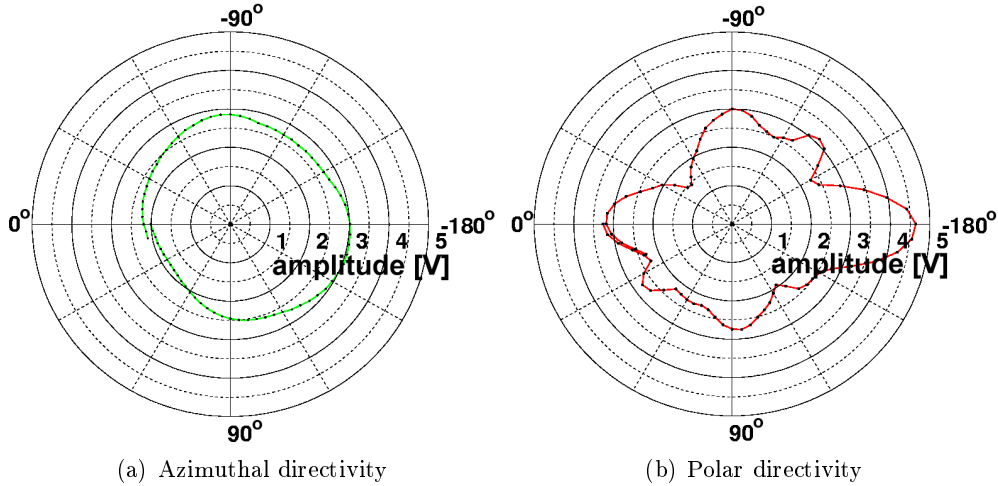
Figure 4.2: The azimuthal (a) and polar (b) directivity measurement results for a SPATS-type transmitter; in both cases the peak pulse amplitude was measured as a function of the angle. The observed asymmetry could be due to a skew mounting of the ring-shaped piezo-ceramic element. From [155].

In a different experimental setup, the pulse amplitude as a function of the steering voltage[3] was measured for all SPATS transmitters, showing a stable and similar behaviour between the different HV modules [155].

4.1.2 Pressure and temperature dependence

Pressure

The deepest SPATS stage is deployed at a depth of 500 m and the ambient pressure is expected to exceed the static pressure due to the depth (expected to be maximal ~ 50 bars) by at least a few 10 bars. This is due to the fact that the water inside the IceCube hole refreezes first at the surface, creating over-pressure during the freeze-in. The SPATS steel pressure housings have been tested at pressures up to 120 bar, which is roughly the equivalent of 1200 m of water. The housings are not expected to be deformed by more than roughly $50\,\mu$m at a tension of $15\,\text{N/m}^2$ [163], it is possible that a slight deformation gives rise to a change in sensitivity. For example, the preload on a piezo-ceramic element could change due to deformation of the steel housing.

In order to quantify the change in sensitivity due to the increase of ambient pressure, two pressure test sequences were done at Uppsala University, in Sweden, in August 2008 and February 2009. A large (40.5 cm inner diameter) pressure vessel was used in which SPATS or HADES sensors were consecutively installed. The commercial transmitter (SQ9) was mounted inside the pressure vessel during the first data taking period and failed at high pressure. It was subsequently decided to mount the SQ9 transmitter outside the pressure vessel for the February 2009 tests. That last data-set consisted of pressure dependent measurements of the transmitter pulse at different operating voltages of the transmitter at a fixed frequency (20 kHz) and of different

---

[3] As a reminder, the steering voltage determines the charging voltage of the LC circuit of the SPATS transmitter. This allows to change the amplitude of the emitted acoustic pulse.
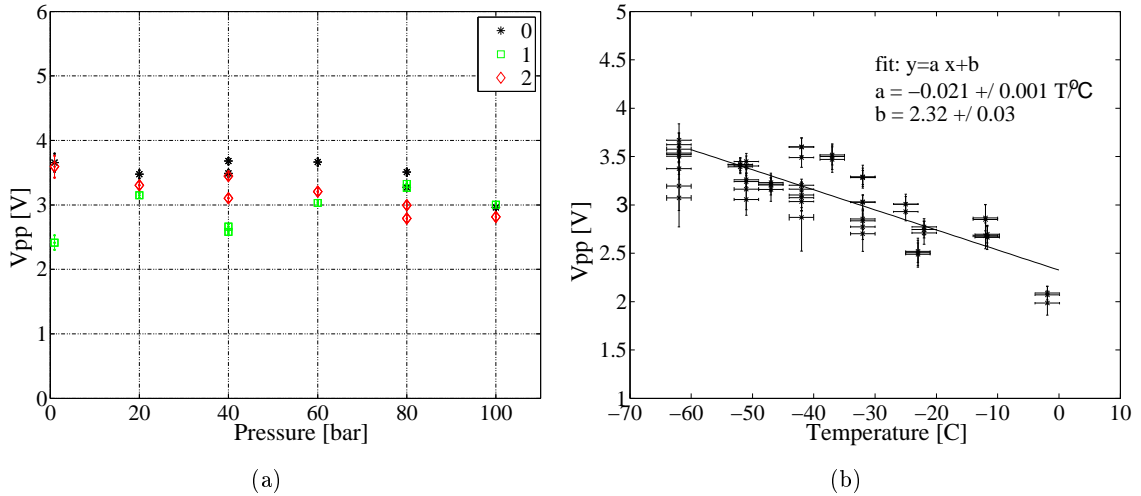
Figure 4.3: (a): The peak-to-peak voltage (Vpp) as a function of applied static pressure for the three channels of the same SPATS sensor listening to a transmitter external to the pressure vessel. (b): Vpp as a function of temperature for the three channels of the same SPATS sensor in air with a linear fit to the data (black line). From [164].

output frequencies at fixed operating voltage. These signals were recorded by the sensors inside the pressure vessel at a maximum pressure of 100 bar. The typical step in pressure was 20 bar. The recorded peak-to-peak voltage (Vpp) served as a measure of sensitivity at the various pressure levels. Figure 4.3(a) shows the measured Vpp for the three channels of a SPATS sensor as a function of ambient pressure: no systematic variation with pressure, common to all three channels, is visible. The complete pressure data set indicated that the variation of sensitivity of a SPATS sensor channel with static pressure was less than 30% between 1 bar and 100 bar [164].

Temperature

The mean ambient temperature in the South Pole ice in the upper few hundred meters is expected to be around –50 °C. Therefore, several temperature tests have investigated the temperature dependence of the SPATS sensors. To this end, industrial freezers capable of reaching temperatures below –60 °C were used. In [155], a first measurement of this dependence was presented. In a second experimental verification, performed in 2009, the ITC1001 transmitter (see § 3.4.2) was pulsed in air while being suspended near the freezer at the DESY laboratory in Zeuthen, Germany. A SPATS sensor was positioned on a support at the bottom of the freezer. The position of the sensor was not changed between the different measurements. The temperature for each measurement was taken with a thermocouple and a digital thermometer which were both in contact with the steel housing of the sensor. The difference between the two temperature measurements was typically 2.5 °C which was used as the error. The peak-to-peak amplitudes were extracted as the mean of 100 events with the standard deviation as the statistical error. Figure 4.3(b) shows the extracted Vpp as a function of temperature for the three channels of a same SPATS sensor module. A linear fit was made to the data and it was concluded that there was a gain in the sensitivity of 1.5 ± 0.2 when the temperature was lowered from 0 °C to –50 °C [164]. This result

was in agreement with the earlier measurements.

4.2 The Abisko long-range lake test

4.2.1 Setup

A SPATS system test ran in April 2006 with the following goals:

- Test different transmitter modules and piezo-ceramic transmitting transducers and check for differences in performance between different modules.
- Demonstrate that the range of a SPATS transmitter-sensor pair (i.e. the distance over which the SPATS transmitter pulse can be detected by a SPATS sensor) is sufficient to meet SPATS requirements.
- Compare the performance of the SPATS sensor modules to that of the Sensortech-SQ03 commercial hydrophone.
- Reconstruct the direction of an acoustic pulse using the difference in arrival time between the different sensor channels.
- Test the pressure sensors that are mounted inside some of the transmitter modules.
- Test the DAQ software and hardware under real deployment conditions.

Most of these goals require a large, and relatively quiet, volume of water since the signal of the SPATS transmitter needs to be recorded over large distances. The acoustic impedance mismatch between water and air (and in a lesser degree ice) is responsible for an almost total reflection of any acoustic signal. A minimum depth of the water is therefore needed in order to have a clear separation between direct and reflected pulses for all distances. Initial tests at the frozen Zeuthen lake (Germany) suffered from large background noise and the shallow depth of the lake at the test location [157]. The April 2006 testing site was chosen to be lake Torneträsk in Abisko (northern Sweden). It is the seventh largest lake in Sweden with a total area of $330\,\text{km}^2$ and a length of $70\,\text{km}$. The lake goes as deep as $168\,\text{m}$ with an average depth of $52\,\text{m}$ [165]. The lake was between $40\,\text{m}$ and $60\,\text{m}$ deep at the test location. It is typically covered with ice from December to June. In that period, the expected background noise is low since no boat traffic is possible and traffic of other vehicles is also typically limited.

In April 2006, the lake was covered with about $90\,\text{cm}$ of ice and could therefore easily be used as a testbed for the SPATS system. Accommodation and infrastructure (among which a snowmobile and a motorised ice-drill) was provided by the Abisko scientific research station [166]. The "Temporary Counting House" (TCH, see Fig. 4.4(a)), a small fishing caravan on skis, was hauled to a spot on the lake where snowmobile traffic was suspected to be minimal. It was secured with wooden poles and used as a shelter and data-acquisition (DAQ) centre. Then, holes were drilled through the ice layer at various distances on a straight line parallel to the typical snowmobile route.

Subsequently SPATS transducers were lowered down in the water at specific depths, typically with vertical intervals of $2\,\text{m}$. Different combinations of first-generation SPATS transmitter and sensor (either first-generation SPATS sensor or commercial hydrophone) were deployed and connected to an AJB (Acoustic Junction Box, see § 3.3.1) by $420\,\text{m}$ long cables (from the same type as the SPATS in-ice cables). The data-taking was controlled by a DAQ laptop that was directly connected to the string-PC with a LAN connection. Two sensor-channels were read out

(a)   (b)
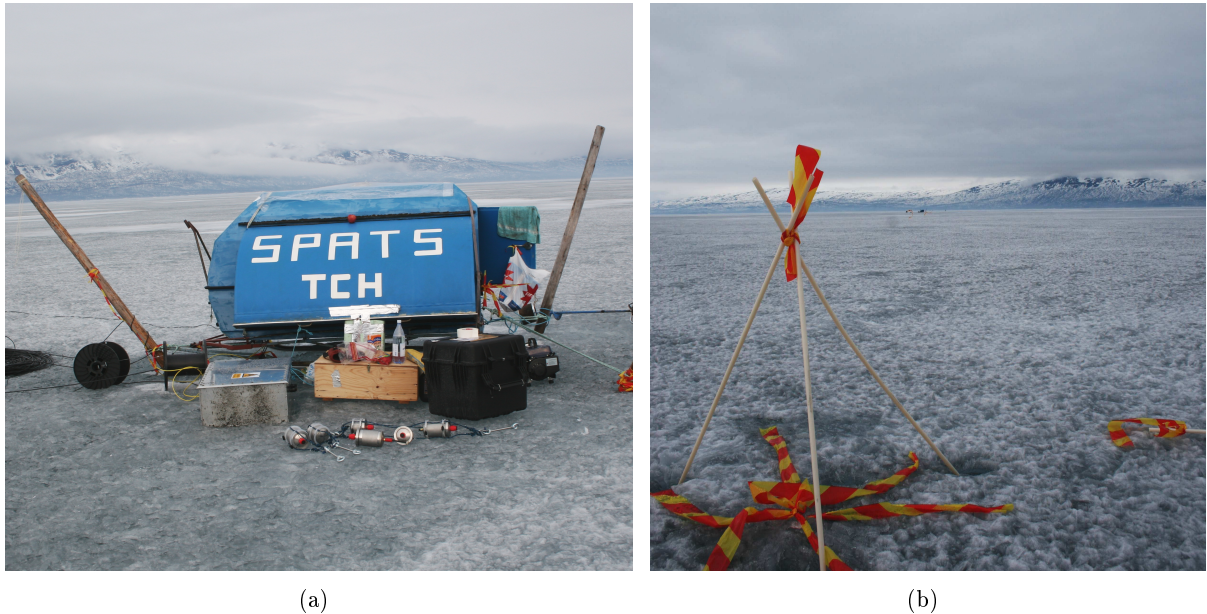
Figure 4.4: (a): The SPATS TCH with the AJB, SPATS stages, cables and power generator. (b): The TCH as seen from the 400 m South hole.

simultaneously. A typical run contained 10 events. Power was provided by a small generator on the ice next to the TCH. The holes were located on a straight line from North to South, with a maximum distance of about 800 m. Two holes were drilled at 400 m West and 400 m East, see Fig. 4.4(b). Table 4.1 gives an overview of the available SPATS Abisko in-water data.

Several temperature measurements were also taken at different locations down to a maximum depth of 60 m. It was found that the temperature increased slightly from the surface to the bottom of the lake as expected (water has the largest density at $4\,°\mathrm{C}$), although the temperature at the bottom (about $0.4 \pm 0.4\,°\mathrm{C}$) was lower than might have been expected[4]. The total change in temperature was found to be maximum of $1\,°\mathrm{C}$ so that refractive effects were expected to be small. Figure 4.5 shows the measured temperature versus depth.

4.2.2 Results

For each measurement of a SPATS transmitter pulse at a certain distance and a certain depth, 10 events were recorded by ei-
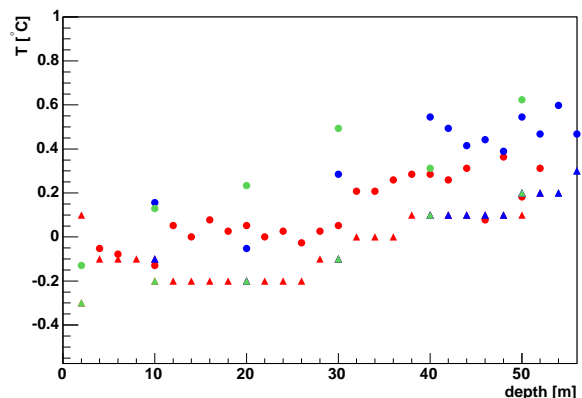
Figure 4.5: Water temperature vs. depth for the Abisko lake test; different colours indicate different measurement sequences.

---

[4]One could expect to see a temperature of about $4\,°\mathrm{C}$ at the bottom of the lake.

H/S	T	Distance [m]	$(x,y)_T$ [m]	Depth T [m]	$(x,y)_{H/S}$ [m]	Depth S/H [m]
H	T	5	(0,0)	−30	(-5,0)	[−2,−42]
H	T	100	(100,0)	−30	(0,0)	[0,−42]
H	T	400	(400,0)	−30	(0,0)	[−46,−16]
S#21	T	400	(400,0)	−30	(0,0)	−30
S#21	T	100	(100,0)	−30	(0,0)	[−2,−60]
S#21	T	400	(400,0)	−30	(0,0)	[−6,−60]
S#21	T	580	(400,0)	−30	(−180,0)	[−6,−52]
S#21	T	800	(400,0)	−30	(−400,0)	[−6,−46]
S#21	T	220	(400,0)	−30	(180,0)	[−6,−52]
H	T	400	(400,0)	−30	(0,0)	[−6,−46]
S#21	T#8	400	(0,0)	[−42,−12]	(−400,0)	−30
S#21	T#7	400	(0,0)	[−12,−42]	(−400,0)	−30
S#21	T#14	400	(0,0)	[−42,−12]	(−400,0)	−30
S#21	T#22	400	(0,0)	[−12,−42]	(−400,0)	−30
S#21	T#14+P#6	400	(0,0)	[−12,−42]	(−400,0)	−30
S#21	T#14+P#12	400	(0,0)	[−12,−42]	(−400,0)	−30
S#21	T#14+P#20	400	(0,0)	[−12,−42]	(−400,0)	−30
S#21	T#14+P#17	400	(0,0)	[−12,−42]	(−400,0)	−30
S#21	T#14+P#25	400	(0,0)	[−12,−42]	(−400,0)	−30
S#8	T#7	400	(400,0)	−30	(0,0)	−30
S#8	T#7	400	(0,−400)	−30	(0,0)	−30
S#8	T#7	400	(−400,0)	−30	(0,0)	−30
S#8	T#7	400	(0,400)	−30	(0,0)	−30

Table 4.1: Overview of the acoustic data-set of the Abisko SPATS test. H stands for Hydrophone, S for first-generation SPATS sensor, T for first-generation SPATS transmitter module and P for SPATS piezo-ceramic transmitting element. The x axis goes from North to South and the position of the TCH is (0,0). 3 main sets of data exist: a distance-dependent measurement, a transmitter-variability measurement (using a single SPATS sensor listening to different SPATS transmitters) and an angular measurement (using the same SPATS transmitter and SPATS sensor at different angles). On top of that, a commercial hydrophone was deployed for comparison.
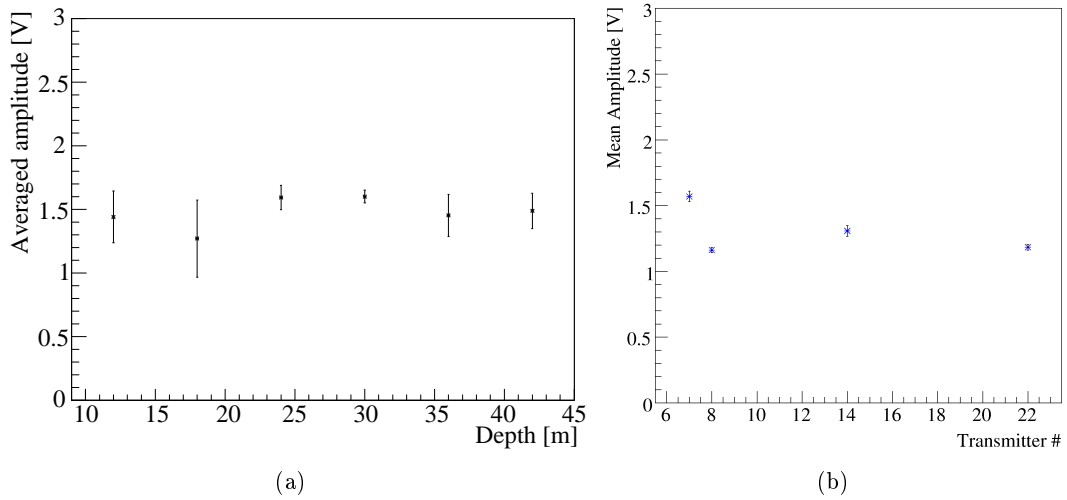
Figure 4.6: (a): The variation in the maximum amplitude (averaged over 10 events with statistical error bars) with depth for one transmitter (T7) at 400 m distance from a SPATS sensor. The sensor is positioned at 30 m depth. (b): The mean maximum amplitude averaged over all depths versus transmitter number.

ther a commercial hydrophone or a SPATS sensor. Different effects contributed to shifts in the arrival time of the acoustic signals. Underwater currents made the devices swing, or torsion in the support rope makes them spin. The signals therefore needed to be shifted in time, so that the first amplitude maxima coincide, before averaging the pulses. Lake Torneträsk was found to be a silent testing environment with a stable and low background noise level of ~120 mV for the SPATS sensors, excluding occasional snowmobiles and strong wind or hail.

Transmitter variability

At first, a SPATS sensor was placed at a depth of 30 m and different transmitter modules (or a single module with subsequently different piezo-ceramic elements attached) were then lowered in a hole at 400 m distance (at the TCH), starting from the surface to maximum 64 m depth. Signals from all tested transmitters were clearly visible at a distance of 400 m. The maximum change in polar angle was about 9° in this geometry. The expected amplitude variations due to the deviation of the position of the transmitter compared to the horizontal plane was therefore about 10%. No significant variation in sensitivity of the sensor module was expected. In this case we assumed that the orientation of the sensor-channel did not change noticeably during the transmitter testing. This is a reasonable assumption since the sensor had enough time to stabilise itself so that it did not rotate anymore at the time of the measurement.

There was no control over the azimuthal orientation of the transmitter, as is also the case for the permanently deployed strings in the ice. It was expected that the stage could rotate so that the azimuthal angle changed during the test and therefore the variability of the amplitude due to the azimuthal orientation could be probed. The amplitudes of the registered pulses for the same transmitter at different depth seen by the same sensor were compared. An example can be

found in Fig. 4.6(a). As expected, the amplitude variation with depth is small (polar systematic effect is not dominant).

At this large distance, the azimuthal orientation of the transmitter was the dominant systematic effect on the amplitude. Fig. 4.6(b) shows the signal amplitudes averaged over depth with statistical errors, there is about 35% variation in the transmitter amplitudes. A maximum variability of 40% is expected, due to the random azimuthal orientation as was discussed in § 4.1.1. Therefore, it is possible to conclude that the observed variations in amplitude lie within the expectations and are mainly due to the uncertainties on the azimuthal orientation of the transmitter (see § 3.2.2). The complete set of amplitude versus depth graphs can be found in Appendix C.

Transmitter range

A maximum distance of 800 m between transmitter and sensor was achieved, the limiting factor was the available cable length. In Fig. 4.7(a) the transmitter signal as recorded by the SPATS sensor is shown. The signal-to-noise ratio (S/N) is still high ($\sim$5) at this large distance. Assuming an acoustic attenuation length of 1 km, an extrapolation from the signal to noise ratio gives an expected range for the SPATS transmitter and sensor pair in water over 1800 m.

There is a second pulse visible $\sim$1 ms after the signal. This "afterpulse" is present in all waveforms. Figure 4.7(b) shows the difference in arrival time between the first and second pulse, Δt, as function of the depth of the SPATS sensor. The transmitter remained at fixed depth and horizontal distance. The second pulse has inverse polarity (i.e. the first peak is be inverted compared to the first peak of the first pulse). Both the linear behaviour of Δt as a function of the sensor depth and the phase inversion support the theory that the second pulse is a reflection originating from the ice surface. For vertical movements that are small compared to the distance between the sensor and the transmitter, Δt as a function of sensor depth can be approximated by a linear function. No reflections from the bottom of the lake have been observed.

Sensor performance

The contrast in performance between a commercial hydrophone and a SPATS sensor becomes clear in Fig. 4.8(a) and Fig. 4.8(b), where the significant difference in vertical scale should be noted. A SPATS transmitter was placed at 100 m distance and 30 m depth after which a hydrophone and a SPATS sensor were successively lowered to a depth of 30 m. The signal as recorded by the SPATS sensor is much higher than that of the commercial hydrophone. In fact, the hydrophone was uncapable of detecting a transmitter signal at 400 m distance at maximum gain setting. Figure 4.8 also shows the typical oscillation behaviour: the short pulses are followed by an exponentially fading oscillation. The SPATS sensor typically has a longer pulse, likely because of the many mechanical resonances which are not present for the hydrophone.

The three sensor channels are each separated by $\sim$10.5 cm of steel so that the difference in arrival time between different channels can easily be observed at the maximum sampling frequency of 1.25 MHz. A SPATS sensor was placed at a depth of 30 m and a SPATS transmitter was lowered to the same depth at a position subsequently 400 m North, West, South and East from the sensor location. The orientation of the sensor module was obtained by reading out two channels for each position of the transmitter [160].

(a)

(b)
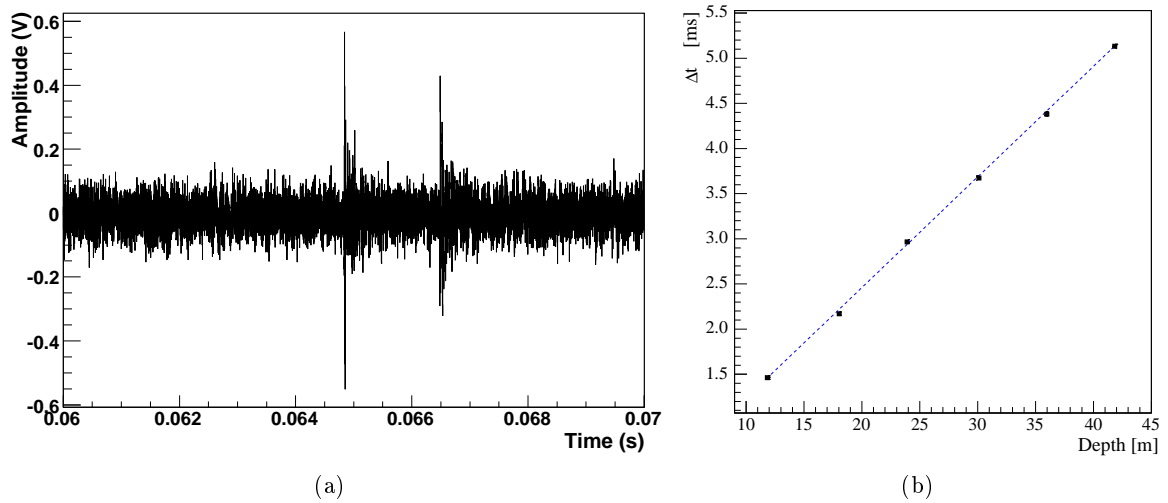
Figure 4.7: (a): The transmitter signal (T#7) as seen by a SPATS sensor (S#21) at 800 m distance. (b): The difference in arrival time between the direct and the reflected signal as a function of the depth of the SPATS sensor. The transmitter was positioned at 30 m depth.

(a) Hydrophone
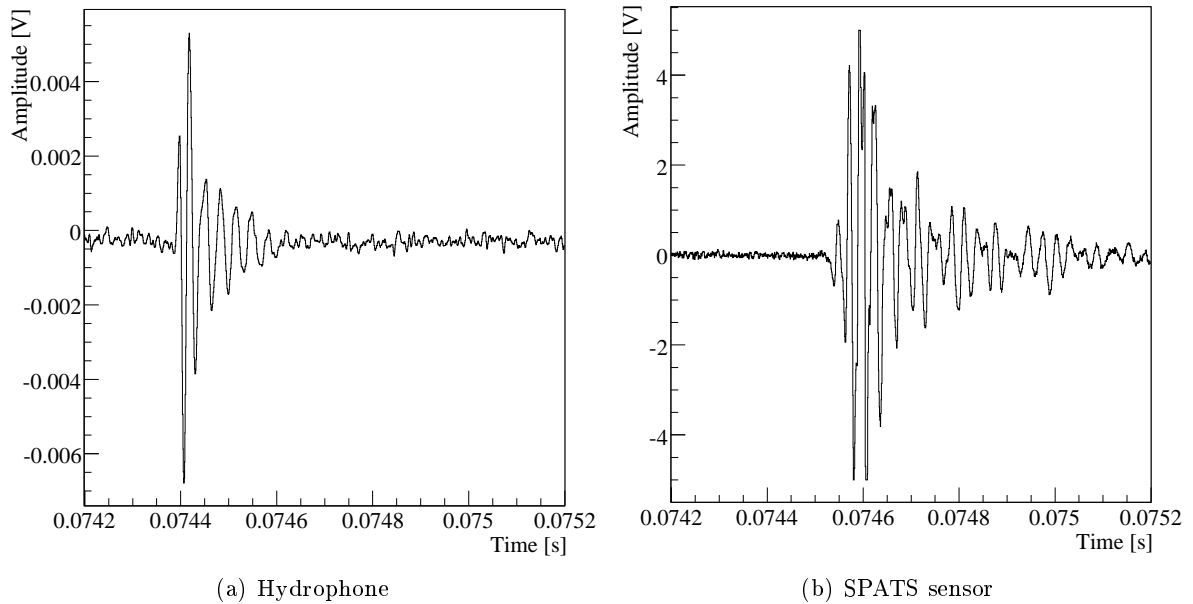
(b) SPATS sensor

Figure 4.8: Sensor results from the Abisko lake test: comparison between the signals received by a commercial hydrophone (a) and a SPATS sensor (b) at 100 m distance of the transmitter. Note the difference in vertical scale.
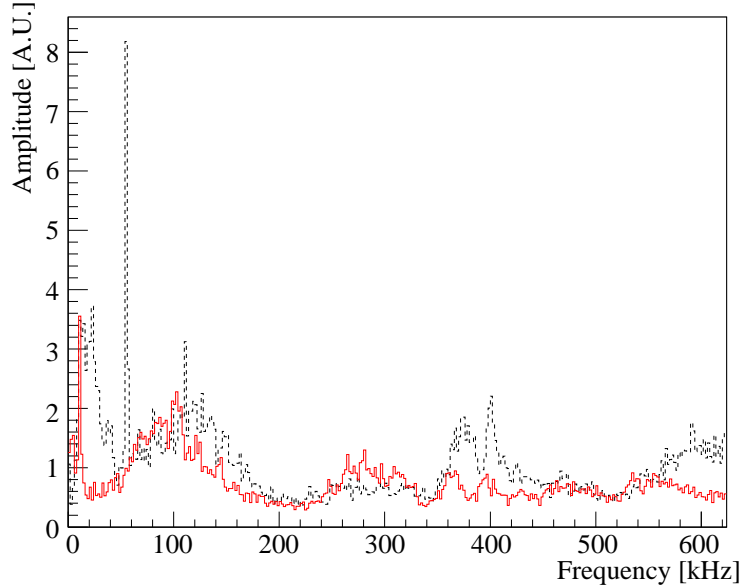
Figure 4.9: Comparison between the noise spectra from lake Torneträsk (red line) and 320 m deep in the South Pole ice (black dashed line).

	σ(S#8-0) [V]	σ(S#21-0)[V]
lake Torneträsk in-water	0.0509 ± 0.0002	0.0510 ± 0.0001
South Pole in-ice	0.0722 ± 0.0002	0.0602 ± 0.0001

Table 4.2: Comparison between the standard deviations of the Gaussian noise distribution of lake Torneträsk (water) and South Pole (ice). S #8-0 and S #21-0 are now located in the SPATS array at positions AS6-0 and BS7-0 respectively.

It is interesting to compare the in-water and in-ice noise data for the same SPATS sensor. For example, one of the SPATS sensor used in the lake Torneträsk was later deployed on string A at 320 m depth. Figure 4.9 shows the Fourier spectra for 1.25×10^3 samples of noise for both locations. The frequency amplitudes above 80 kHz can not directly be compared and interpreted since the SPATS sensor amplifier board has only been tested in the (1–80) kHz range, where the variation in amplification was about 5%, see § 3.2.3. The noise in the South Pole ice has a narrow peak at around 60 kHz and seems to have a high-frequency component.

The noise ADC-histograms were fitted with Gaussians for two different SPATS sensors for both lake Torneträsk and the South Pole ice. The results in terms of the extracted σ of the noise are shown in Table 4.2. The increase in standard deviation σ of the Gaussian noise is compatible with the expected factor of 1.5 of increase in sensitivity due to the decrease in temperature and the 30% systematic due to the increase of pressure. Both of these possible systematic effects were discussed in § 4.1.2.

4.3   In-ice calibration and tests

4.3.1   In-ice transmitter systematics estimation

The variability of the transmitter intrinsic amplitude and the variation with azimuthal and polar angle have been investigated in water. The deployment of the transmitters in IceCube holes filled with water that later refreezed around them possibly increases this variability due the following factors:

- Hole ice.
  The IceCube hole refreezes first at the top of the hole as the temperatures are lower in the upper layers of the ice layer. The hole ice has most likely a higher concentration of bubbles and cracks than the bulk ice.

- IceCube main cable position.
  The IceCube main cable runs next to the SPATS string and is about 10 cm thick. The presence of this cable possibly increases the variation of the transmittivity with the azimuthal angle.

- Transmitter tilt.
  If the HV-cable between the transmitter module and the transmitting piezo-ceramic element is bended during freeze-in, that can lead to a larger variation with azimuthal angle.

There is no independent way of assessing the effect of the above mentioned factors on the inter-string data, as is the case for the sensors (see next section). Therefore, for the inter-string analysis presented in this work, the estimates of the systematic effects from the in-water calibration measurements are used, keeping in mind that this is possibly an underestimation.

4.3.2   In-ice sensor systematics estimation

The 2008/2009 pinger data can be used to investigate the in-ice variation in sensitivity of the sensor channels. In [161], $y = \ln(A_{\mathrm{eff}} \times d)$ is plotted as a function of d for each sensor channel individually, where A_{eff} is the effective amplitude ($A_{\mathrm{eff}} = \sqrt{E}$, where E is the waveform energy, see also Chapter 5) and d is the distance between the pinger and the sensor channel. Then a linear fit is performed, fitting $y = ax + b$ for each of the available SPATS sensor channels. Figure 4.10(a) shows an example of a fit for the single sensor channel AS6-0 listening to the pinger signal. The constant b is an offset which is different for each individual sensor channel. The channel-to-channel variation of b is an estimate of the systematic uncertainty due to the channel-to-channel sensitivity variation. e^b gives an in-situ determination of the channel sensitivity for that particular pinger direction (see [161] for an overview of all extracted b-values). The spread of these values depends on the choices of data selection criteria and integration windows in the pinger analysis. The initially extracted value for the spread on e^b was about 68% [160] and the spread on b was 0.86. Taking the energy analysis of the full waveform from [164], the histogram in Fig. 4.10(b) is obtained and the spread on e^b is in this case 64%. In order to allow a straightforward comparison between the different inter-string analyses, the spread on e^b is taken to be 68%.

The values for b for each channel are presumably different for acoustic pulses coming from different angles. But the systematic variation from channel to channel is likely to be similar for acoustic signals coming from any direction, i.e. the sensor modules are randomly oriented.

97
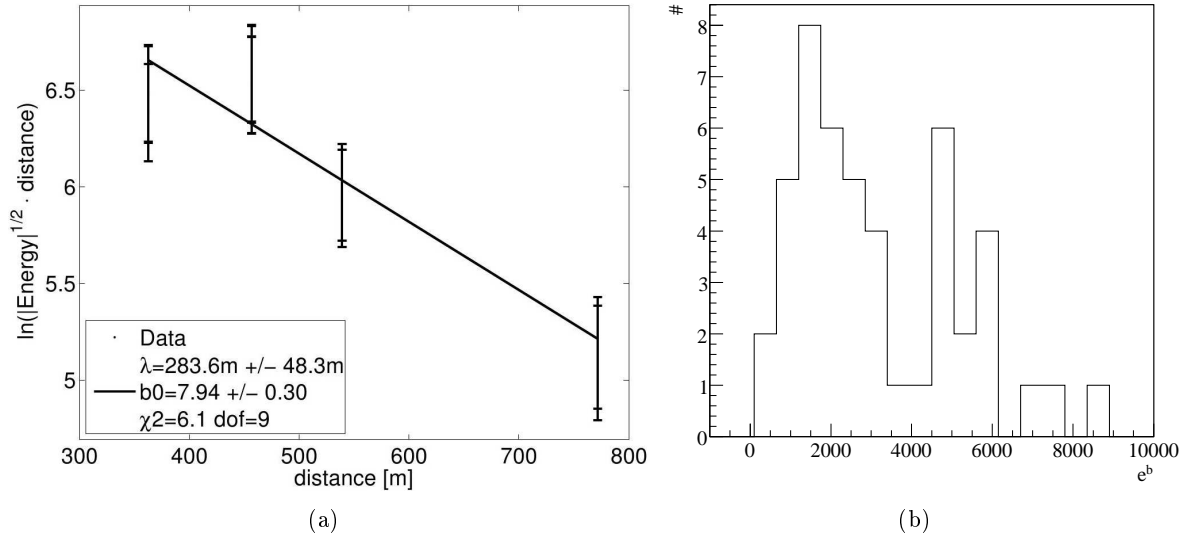
Figure 4.10: Using the 2008-2009 pinger data for in-ice sensor systematic estimation. (a): An example of a fit for the single sensor channel AS6-0 listening to the pinger signal. (b): The histogram of the extracted e^b values.

Also, even if the hole ice or IceCube main cable are affecting the spread on the amplitudes, it is a reasonable assumption that this effect is similar from different directions. So, although the individual b values cannot necessarily be used from other directions, the 68% variation in amplitude can be used as a systematic error on a single, uncalibrated, amplitude measurement with a single SPATS sensor channel.

4.3.3 String D depth

String D was deployed on 24 December 2007 in IceCube hole 76 during the austral summer of 2007/2008, about one year after strings A, B and C. It was foreseen to go down to a maximum depth of 500 m. However, there was some doubt about the actual depth of string D after deployment since the pressure readout was suspected to be unreliable and the amount of excess cable was different from expectations. It was even feared that the string could have been installed 60 m too shallow. The last pinger hole was IceCube hole 69 located at about 125 m horizontal distance from string D. Therefore the pinger data from that hole was used to verify the depth of the acoustic stages on string D. When the pinger was lowered down hole 69, all sensors from string D were continuously taking data (as were the other strings).

Method

Figure 4.11(a) shows a pinger pulse as seen by DS7-1 (sensor channel 1 of the deepest stage on string D), together with the GPS-synchronised SPATS IRIG, see also Fig. 3.8). The pinger module was triggered every second precisely at the start of the GPS second as received by the stand-alone GPS unit that was connected to the APB (see § 3.4). The arrival time t_a was defined as the time elapsed from the start of the GPS second to the first rising edge of the received pinger waveform. This edge corresponded to the first sample above a certain threshold that depended
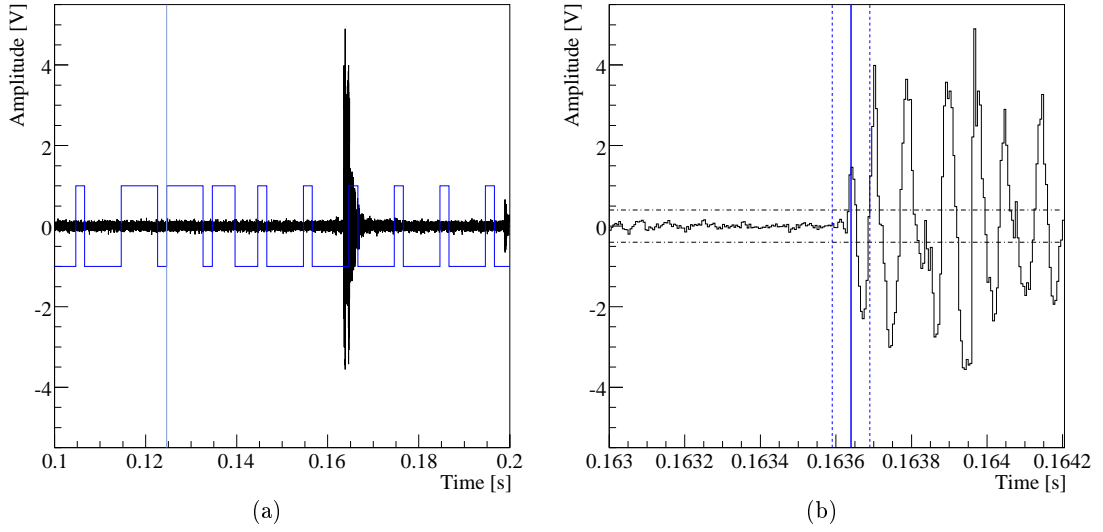
Figure 4.11: (a): Pinger pulse from hole 69 as seen by sensor DS7-1 (black waveform) with the GPS-synchronised IRIG-B (blue logic signal). The start of the GPS second (based on the IRIG-B signal) is indicated by the blue vertical line. (b): Zoom on the start of the detected pinger pulse (black waveform). The extracted arrival time is indicated (blue solid vertical line) together with the error band (blue dashed vertical lines). The trigger levels are indicated by the black horizontal dot-dashed lines.

on the background noise level of that specific sensor channel. The start of the pulse could be determined in this way with a maximum error of about 1 oscillation or 0.05 ms, see Fig. 4.11(b). The delay due to cable and electronics t_m was defined at the pinger-side as the delay from the start of the GPS second to the actual acoustic emission. This delay needs to be subtracted from the arrival time in order to obtain the actual transit time t_t and was measured in a laboratory setup to be 1.90 ± 0.05 ms [164]. From this we could find the transit time: $t_t = t_a - t_m$ with corresponding quadratically added errors: $\sigma(t_t) = \sqrt{\sigma(t_a)^2 + \sigma(t_m)^2} = 0.07$ ms. The delay in the cable ($\sim 10\,\mu s$) and the uncertainty on the start of the GPS second ($\sim 1\,\mu s$) were negligible and were not taken into account in this analysis.

	DS3	DS4	DS5	DS7
Nominal Depth [m]	250	320	400	500
Fitted Depth [m]	252.4 ± 3.0	321.9 ± 3.0	403.1 ± 2.7	502.4 ± 2.4
χ^2/NDF	0.1037/3	0.0686/3	0.2661/4	0.3019/4

Table 4.3: Depths of sensors DS3, DS4, DS5 and DS7 obtained with the pinger data from hole 69.

DS3-0

DS4-0

(a)

(b)

DS5-0

DS7-0

(c)

(d)
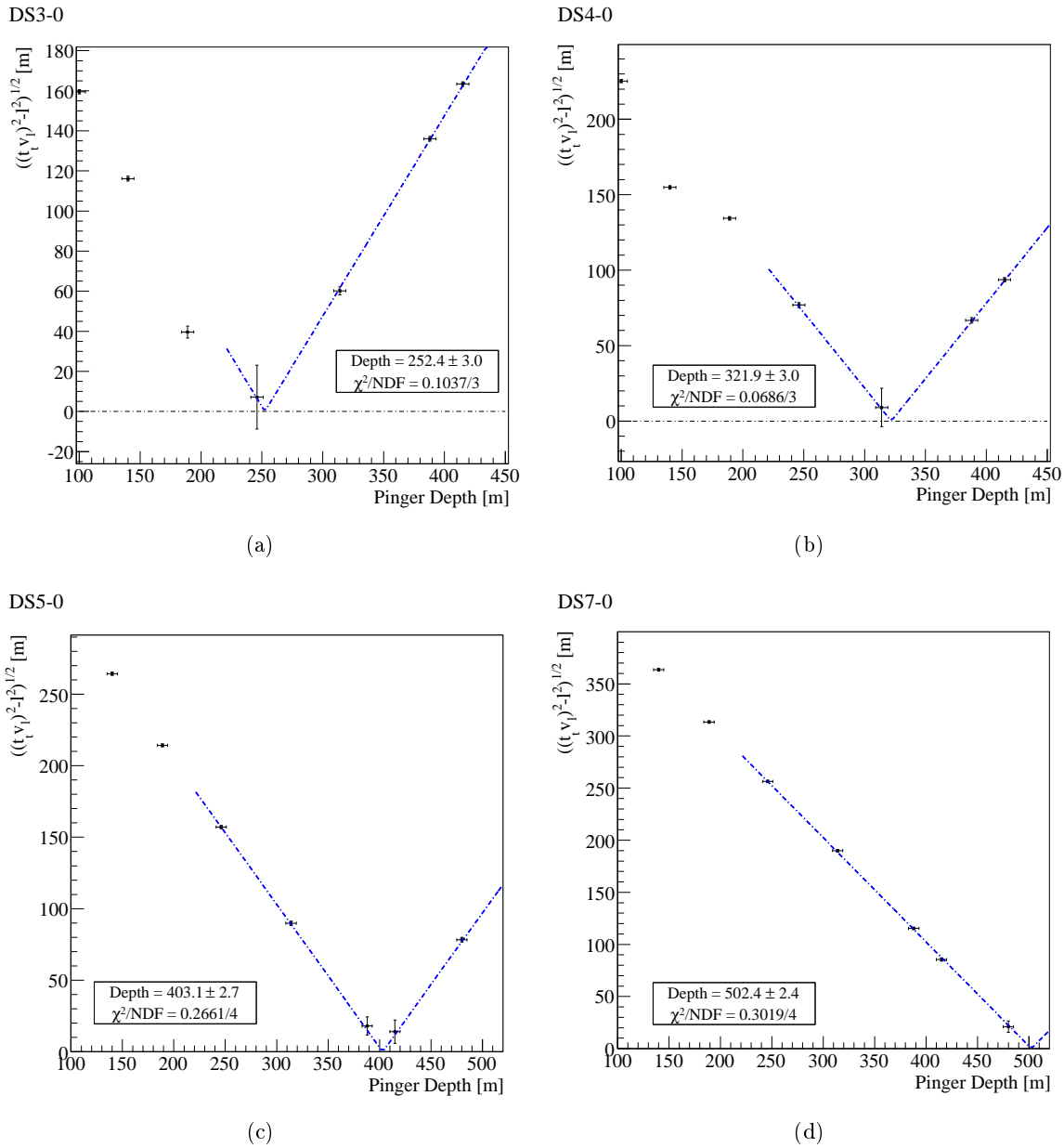
Figure 4.12: The fit to t_t for the depth of sensors DS3, DS4, DS5 and DS7 (channel 0). The blue dashed line is the fit to the pinger data (hole 69) from 240 m to 500 m depth.

100

Results

As the pinger goes down hole 69, it will approaches the bottom sensor of string D and t_t decreases and follows:

$$t_t = \frac{\sqrt{(d-D)^2 + l^2}}{v_l},$$

(4.1)

where d is the depth of the sensor, D is the depth of the pinger, l is the horizontal distance between the pinger hole and string D, and v_l is the longitudinal sound speed averaged over the fitted vertical range. Therefore the extracted transit times t_t versus pinger depth D can be fitted for the depth of the sensor assuming a certain sound speed. In the SPATS sound speed analysis, presented in detail in [167], it is shown that the sound speed gradient below 200 m is consistent with zero and the corresponding sound speed is 3878 ± 12 m/s. Therefore, only the data-points below 200 m are fitted here in order to remove any effect of varying sound speed with depth.

The position of each IceCube hole is determined by a GPS survey and the coordinates of the centre of the hole are known with a maximum error of 0.5 m. The horizontal distance between string D and pinger hole 69 is then obtained using the IceCube coordinates and found to be 124.9 ± 0.7 m. The error on D is taken as 5 m, following the RW turn-counting and SeaStar results (see § 3.4.4).

This method was subsequently also used to determine the depths of stages DS3, DS4, DS5 and DS7 (DS6 has a HADES sensor for which the signal-to-noise ratio is insufficient for this analysis). $\sqrt{(v_l t_t)^2 - l^2}$ (i.e. the difference in depth netween the pinger and the String D sensor) is plotted as a function of pinger depth D and fitted for the sensor depth d. The corresponding fits can be seen in Fig 4.12 and the resulting depths are listed in Table 4.3. The depth of sensor DS7 is found to be 502.4 ± 2.4 m ($\chi^2/\text{NDF} = 0.3019/4$). The data can also be used to give an estimate for the sound speed below 200 m by fitting a 2-parameter function. The sound speed result agrees with the result obtained in [167], see Table 4.4.

	$l = 124.9 - \sigma_l$	$l = 124.9$	$l = 124.9 + \sigma_l$
$d(\text{DS7})$	502.3 ± 5.2 m	503.6 ± 5.6 m	504.9 ± 5.7 m
v_l	3864 ± 51 m/s	3892 ± 55 m/s	3920 ± 58 m/s
χ^2/NDF	$0.228/3$	$0.274/3$	$0.373/3$

Table 4.4: Fitparameters for string D depth measurement for the 2-parameter fit.

This analysis proves that string D was effectively deployed down to its target depth, the other stages are also deployed roughly to their nominal depths within 3 m uncertainty. There is an indication that they are even deployed slightly too deep. The tiny χ^2/NDF for all fits indicates that the error on the pinger depth is possibly overestimated. To illustrate this point, the 1-parameter for DS7 was also done with a 1 m error on the pinger depth. The result is in this case 502.7 ± 0.8 m ($\chi^2/\text{NDF} = 2.8025/4$), also possibly indicating that DS7 was deployed slightly too deep.

4.4 Conclusion

Compiling all test and calibration results permits estimates to be extracted for the errors in positioning, intrinsic (and angular) sensor and transmitter variations, and absolute sensitivities of the SPATS sensor channels. Table 4.5 gives an overview of the errors and systematics that will be used in the SPATS inter-string attenuation length analysis presented in Chapter 5. The azimuthal variation that was measured with the pinger analysis is still folded with the intrinsic differences in sensitivity. The error on the SPATS stage depth is taken to be $\pm 2\,\mathrm{m}$. It can be argued that this is slightly too small, since the string D depth analysis results indicate that the string D stages were possibly systematically deployed too deep. Still, this error does not dominate the inter-string analysis and raising it to $\pm 3\,\mathrm{m}$ does not change the final attenuation length results presented in Chapter 5.

Measurement	Uncertainty	Source
SPATS stage depth	nominal $\pm 2\,\mathrm{m}$	pressure and pinger data
Horizontal position	GPS coordinates $\pm 0.5\,\mathrm{m}$	IceCube GPS survey
T azimuthal	40% if $0° < \phi < 180°$	Abisko and lab calibration
T polar	40% if $0° < \theta < 30°$	lab calibration
S azimuthal+intrinsic	68%	pinger analysis
S polar	60%	Abisko data

Table 4.5: Estimation of the errors involved in the inter-string attenuation length analysis.

To summarise, for the sensors, the in-ice estimation with the pinger 2008-2009 data of the systematic error in the azimuthal plane is used. For the transmitters, no in-ice estimation of their variation with polar and azimuthal angles exists and extra external factors could increase the angular variability of the transmitted signal. However, for the inter-string data, the polar effect will be assumed to be the dominant one and the in-water estimation will be used. This means that the systematic error on a single (T,S) combination is estimated by independent calibration measurements. The χ^2/NDF of the fits in the inter-string analysis will give an indication of the possible over- or underestimation of the systematic error.

SPATS inter-string analysis

It is possible to trigger a SPATS transmitter positioned on one of the four SPATS strings and to record the emitted short pulse with sensors that are installed on the other three strings. These type of data are called inter-string data. A typical inter-string datafile contains a sensor waveform of several seconds long in which a certain number of transmitter signals are recorded. These signals are in some cases not above noise, especially for horizontal distances larger than 125 m. The repeated pulses can be averaged in order to increase the signal-to-noise ratio. On top of that, the FADC clockdrift allows to effectively double the sampling frequency offline. The inter-string data taking, processing and analysis is presented here.

5.1 Inter-string data

The set of inter-string data used in this analysis has the following settings: the sensors are read out using the `trigreadcont.c` program. All three channels of one sensor module are recorded simultaneously at a sampling frequency of 200 kHz for 20.5 s, of which 0.5 s is imposed deadtime at the start of the recording. A shell script is started every minute for a different combination (T, S) of one transmitter (T) and one sensor (S) module, situated on two different SPATS strings.

Transmitters are also triggered using the `trigreadcont.c` program. The transmitters of the shallowest stages are not included in this data taking since they are controlled by a different steering program[1] and therefore not easily integrated in an automated data taking script. The transmitters are triggered for a duration of 40 s. At the same time, data is being recorded at a sampling frequency of 200 kHz using channel 2 one of the sensor that is positioned on the same stage as the triggering transmitter. The wait time for the transmitter trigger was set to 38 ms and the charge time was 2 ms. This means that there is one trigger every 40 ms. Therefore the transmitters produce acoustic pulses at a nominal repetition rate of 25 Hz. The steering voltages are set to the maximum acceptable level. There is a 10 s delay between the start of the transmitter triggering and the start of the data taking with the sensors on the three non-transmitting strings. This way, the transmitter HVRB has stabilised and the emitted acoustic pulses are very reproducible.

For every (T, S) combination we have the following data:

- 40 s of IRIG-B timing data taken at 200 kHz sampling frequency, sampled with the FADC clock that drives the transmitter triggering. These data enable the calculation of the clockdrift of the FADC that is used on the transmitting string. This way, the true repetition rate of the transmitter can be determined.

---

[1] Since there are only 3 FADC boards for each string, one transmitter on each string will not be attached to a FADC but to the slow ADC.

(c)   (d)
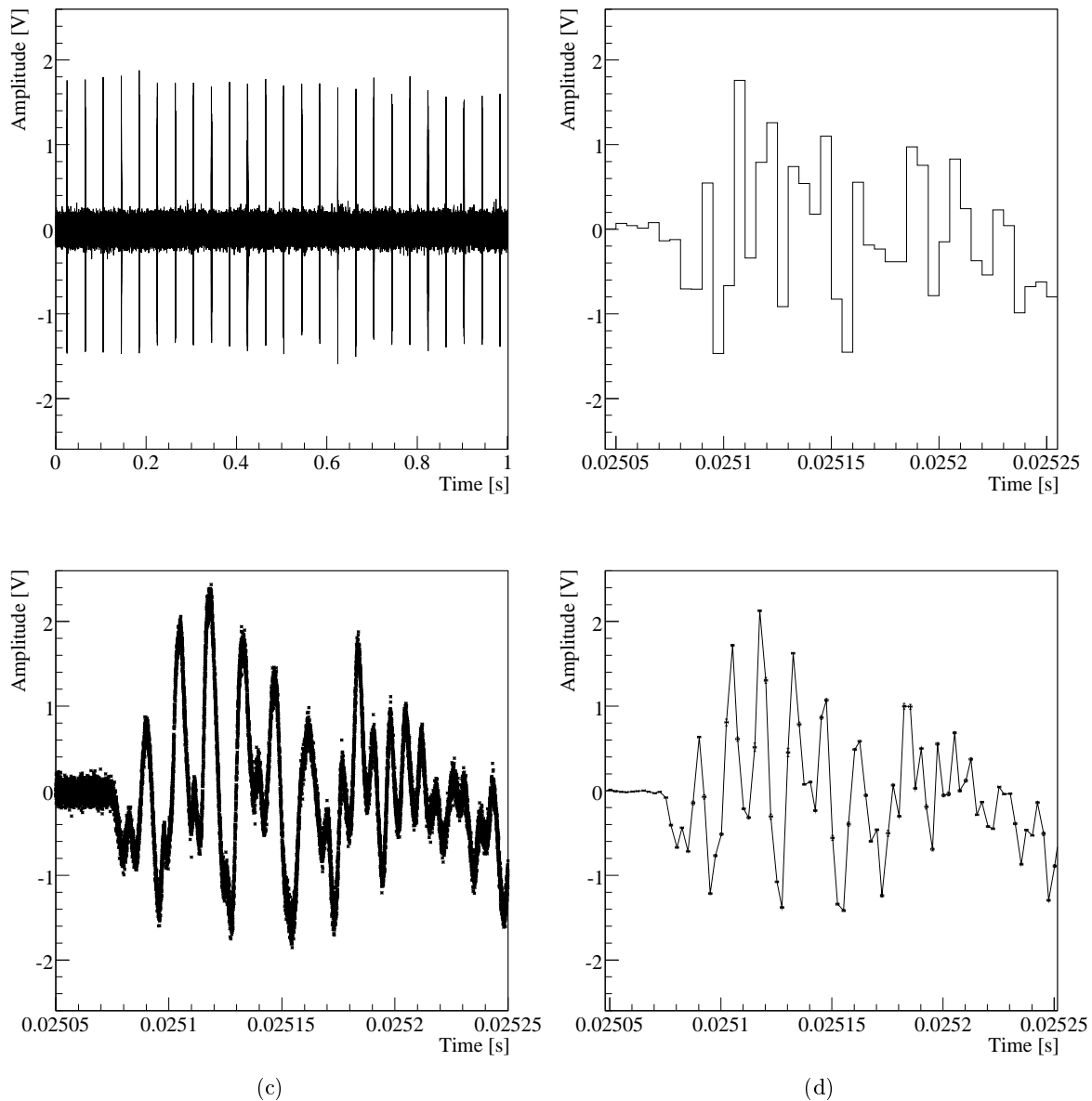
Figure 5.1: An example of processing of an inter-string waveform for transmitter-sensor combination (BT6, AS6-2). (a): 1 s of inter-string data with 25 clear transmitter pulses above noise. The fluctuations in amplitude are mainly due to the FADC clockdrift. (b): Zoom on the first 2 ms of a single transmitter pulse sampled at 200 kHz. (c): The first 2 ms of the clockdrift-corrected transmitter pulse constructed from all 500 transmitter amplitudes that were recorded in the 20 s of data. See text for details. (d): The first 2 ms of the resulting averaged transmitter pulse. Each point is the average of 250 consecutive points in (c). Therefore the transmitter pulse is now de facto sampled at 400 kHz. The statistical errors are plotted and are too small to be seen on this scale.

- 20 s of IRIG-B timing data taken at 200 kHz sampling frequency, sampled with the FADC clock used by the active sensor. These data enable the calculation of the clockdrift of the FADC that drives the sensor waveform sampling. As a result, the true sampling frequency of the sensor waveform can be determined.

- 40 s of sensor data taken at 200 kHz sampling frequency. The sensor is located on the same string and stage as the triggered transmitter and only channel 2 is recorded. These data have only been used to verify the clockdrift-correction algorithm. It has no use in the inter-string attenuation length analysis since all recorded pulses are saturated.

- 20 s of signal sensor data (3 channels simultaneously) sampled at 200 kHz while a transmitter was transmitting. The clockdrift corrections are applied to the waveforms prior to the averaging of the transmitter pulses. These averaged waveforms subsequently are used to determine the corresponding energy of the recorded transmitter signal. The noise contribution is still included at that point. See Fig. 5.1(a) for an example of 1 s of raw inter-string data with 25 pulses above noise.

- 20 s of noise sensor data (3 channels simultaneously) sampled at 200 kHz taken while no transmitter was transmitting. The noise levels are very stable for all channels that are used in the inter-string analysis. From this, the noise energy is determined so that it can be subtracted for each (T, S) combination.

As a reminder, the naming convention for transmitter-sensor combinations is (XTN, YSM-Z), where XTN stands for the transmitter on string X position N and YSM-Z stands for the sensor channel Z of the sensor module at position M on string Y.

5.2 Waveform processing

Figure 5.1 shows an example of the inter-string waveform processing. All steps are explained in detail in the following sections. First, the FADC clockdrift and its effect on the inter-string data is explained.

5.2.1 Clockdrift correction

FADC clockdrift

An ADC pacer clock is an on-board clock that paces actions such as analogue-to-digital conversions. For the SPATS FADC boards this timing is based on FPGA/EPLD (Field-Programmable Gate Array and Erasable Programmable Logic Device) and a programmable interval timer (CMOS 82C54). The data taking of a single (T, S) inter-string combination requires the use of two different FADC clocks: one on the transmitting string and one on the recording string. The three sensor channels are sampled simultaneously with the FADC clock of one of the three FADC boards. The DAQ code was modified in such a way that all sensors and transmitters on the same string always use the same FADC clock. Thus, there are in total 4 different FADC clocks used for the entire inter-string data set.

The pacer clock has a finite accuracy, and therefore a drift. This means that the true sampling frequency f_t is slightly different from the requested, or nominal, sampling frequency f_n.
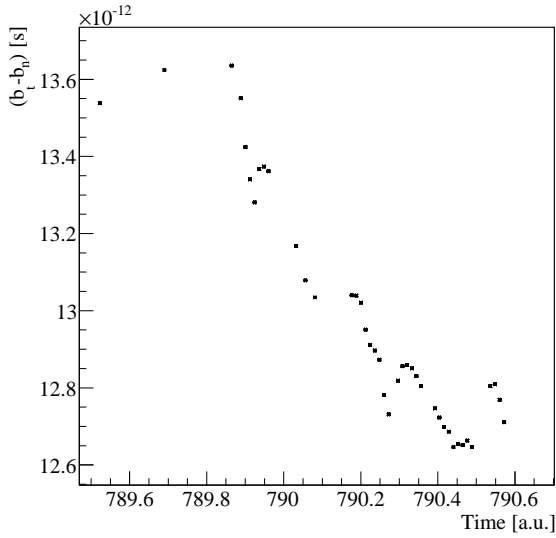
(a) string A
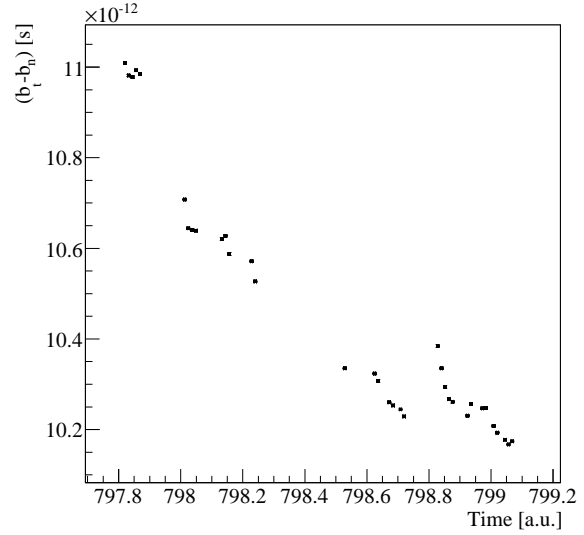
(b) string B
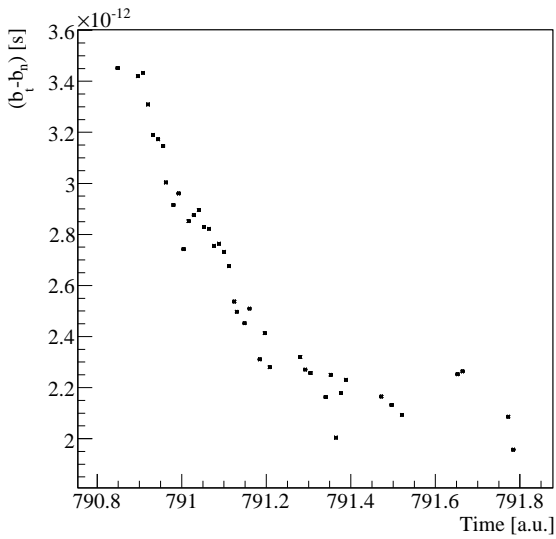
(c) string C
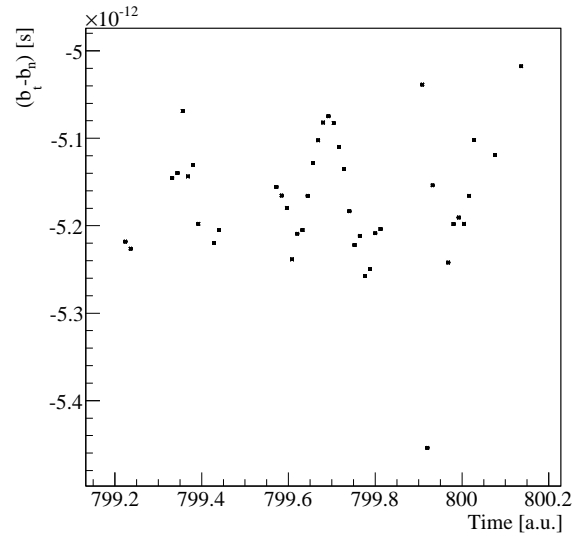
(d) string D

Figure 5.2: The difference between the true bin width b_t as calculated by the clockdrift algorithm and the nominal bin width b_n for all strings and available inter-string data. There is one plot for each string. The total duration is about 3 hours.

Therefore, the delay between 2 samples (bin width) is shorter or longer than what is expected from the nominal sampling frequency. Figure 5.2 shows the difference between the true (b_t) and requested (b_n) bin width, $b_t - b_n$, for the 4 clocks that were used during the inter-string data taking. The differences are small and the true sampling frequency did not differ by more than $2.5 \cdot 10^{-5}\,\%$ from the nominal sampling frequency during the inter-string data taking. Although these are tiny deviations, the resulting effects are clearly visible in the inter-string data set. For example, in Fig. 5.1(a), one can see the oscillation in the maxima of the different pulses. This can be understood as follows. Ideally, the two FADC boards that drive the transmitter triggering and the sensor waveform sampling are perfectly synchronised and pacing at the nominal frequency. The transmitter waveform will, in this case, always be sampled at exactly the same positions. Therefore, the fluctuation on the maxima will only be due to different noise contributions, assuming that the transmitter has a stable output. In reality, the two FADC pacer frequencies will be different from each other and from the requested value. This means that the transmitter waveform will not be sampled at always the same positions and the maxima will oscillate.

The deviation of the FADC sampling frequency is not constant in time, see Fig. 5.2. But the change in clockdrift is rather slow, only becoming important for durations on the order of hours (not seconds). Therefore b_t is assumed to remain constant throughout the recorded waveform. This means that the FADC clockdrifts are assumed to be constant within the same 20 s waveform, but different for each waveform. The two clockdrifts, for both the transmitter and the sensor, were extracted for each (T, S) combination and used to obtain the averaged waveform.

Extracting the clockdrift

The IRIG-B 100 pps signal is depicted in Fig. 3.8 and an example of the IRIG-B waveform as recorded by one of the FADC boards can be seen in Fig. 4.11(a). The IRIG-B signal has 100 rising edges per second. The time as given by the IRIG-B signal is assumed to be the true time and the rising edges to be exactly 0.01 s apart. Therefore the true elapsed time t_t from the first rising edge throughout the waveform is $0.01n$, where n is the number of rising edges since the first rising edge. The IRIG-B waveforms for both sensor and transmitter are sampled at 200 kHz, therefore the nominal bin width b_n is $5 \cdot 10^{-6}\,\mathrm{s}$. This means that the number of bins between IRIG-B rising edges should nominally correspond to 2000 ADC samples. The true bin width can then be obtained by plotting the true elapsed time since the first rising edge as a function of the bin number N, where bin number 0 corresponds to $t_t = 0$. Fitting $t_t = b_t \cdot N + c$ then yields b_t. There is one point for every rising edge in the IRIG-B waveform. Figure 5.3 shows an example of the true time as a function of bin number for 1 s of

Figure 5.3: True IRIG-B time since first rising edge as a function of number of bins since first rising edge for the first second of IRIG-B data from a recorded AS6-2 inter-string waveform.

IRIG-B data for sensor channel AS6-2.

The extracted b_t for the sensor FADC is then used to calculate the true delay since the start of the sensor waveform for each bin j (with amplitude A_j) in the sensor waveform:

$$t_t(j) = j \cdot b_t + c. \tag{5.1}$$

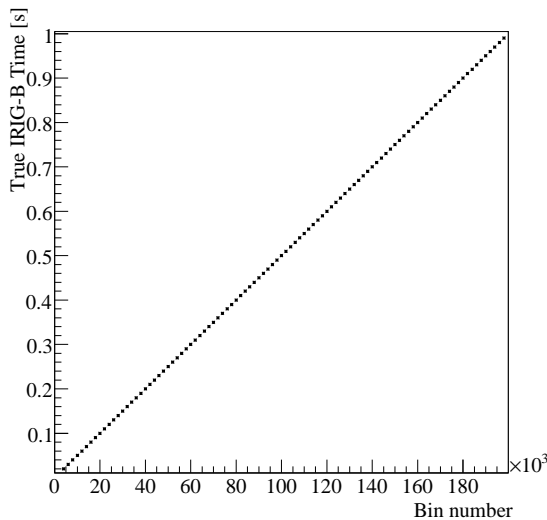The true transmitter repetition rate (i.e. the true delay between two transmitter pulses) is then calculated by applying the FADC clockdrift correction of the transmitting string. Then, each A_j in the sensor waveform is assigned a time between $0\,\mathrm{s}$ and the true length of 1 transmitter event. All $(A_j, t_t(j))$ are then sorted in time. This way, the total of 500 single transmitter pulses (25 pulses per second for a duration of $20\,\mathrm{s}$) are used to construct a single pulse, called the resampled pulse (since the clockdrift was used to increase the sampling frequency). Figure 5.1(c) shows the resulting transmitter pulse as recorded by a SPATS sensor, corrected for the sensor FADC clockdrift and wrapped in time using the true transmitter repetition rate. The clockdrift effectively raises the sampling frequency. A smooth pulse with fluctuations due to the Gaussian background noise is obtained.

5.2.2 Averaging

The example shown in Fig. 5.1 is for a (T, S) combination with a horizontal distance of roughly $125\,\mathrm{m}$. All transmitter pulses are clearly visible above the Gaussian background noise. However, most inter-string combinations do not have visible transmitter pulses above noise. The noise is random in time and can be reduced by averaging the clockdrift-corrected recorded transmitter pulses. The noise level will then be reduced by a factor $1/\sqrt{l}$, where l is the number of averaged transmitter pulses, whereas the transmitter amplitude will remain constant.

The most straightforward way to average the transmitter pulses is to rebin the resampled pulse. Each set of l consecutive samples can be grouped together to form one single data point (A_{av}, t_{av}), where t_{av} and A_{av} are the mean time and amplitude for those samples. The error on the amplitudes is underestimated for the bins where the change in amplitude is larger than the noise fluctuation, for example on the steep rising or falling sections. This effect is negligible compared to the other errors involved in this analysis.

Figure 5.4 show examples of averaged waveforms (see also Fig. 5.1(d)), using $l = 250$, also compared to the raw waveforms. After averaging, a second, smaller, pulse becomes visible above noise for the (BT6, AS6-2) combination, see Fig. 5.4(a). This pulse is the shear wave that also originates from the transmitter. The piezo-ceramic excites the surrounding ice in both the transverse and longitudinal mode. The shear wave is expected to arrive later than the pressure wave since the shear wave sound speed is about half the pressure wave sound speed. For this example, the distance between transmitter and sensor is about $125\,\mathrm{m}$. The expected delay between the two pulses is therefore roughly $0.032\,\mathrm{s}$, using the pinger sound speed results of [167]. This expected delay corresponds to the delay observed in Fig. 5.4.

5.2.3 Energy extraction

The waveforms of all available (T, S) combinations were processed using the extracted FADC clockdrifts to obtain the averaged signal waveform together with an averaged noise waveform. Because the SPATS sensor and transmitter combinations do not always produce the same pulse shapes, it is difficult to use a specific amplitude (for example the highest amplitude) of the
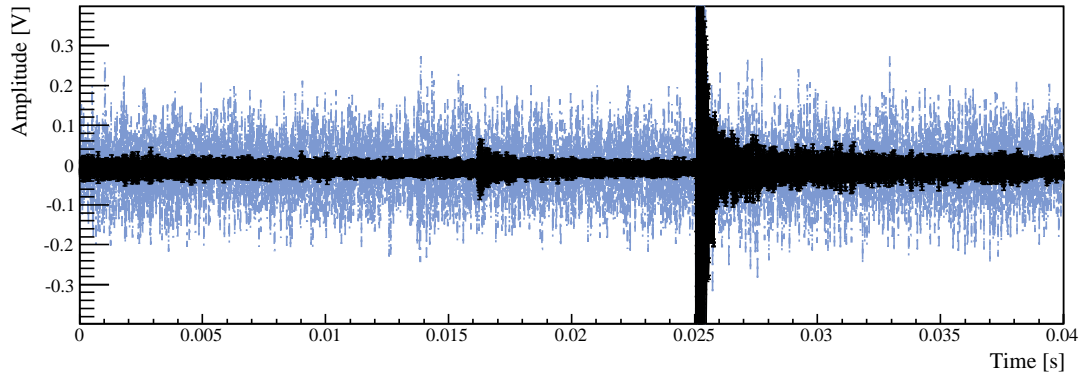
(a)
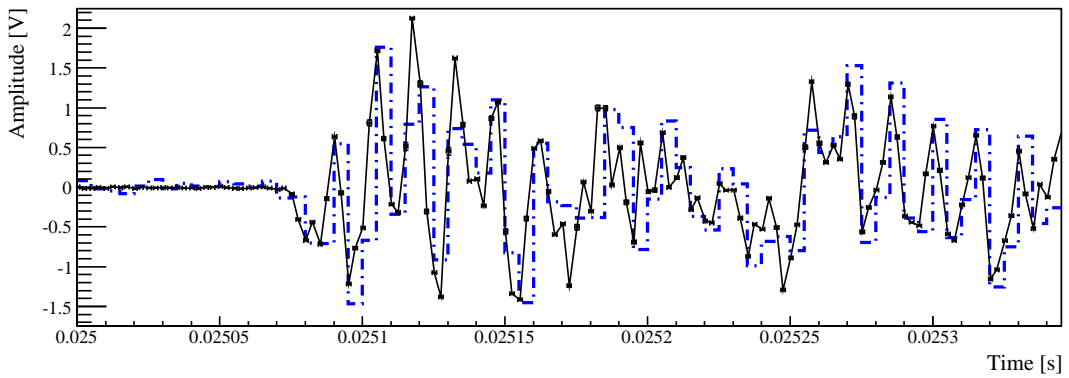
(b)
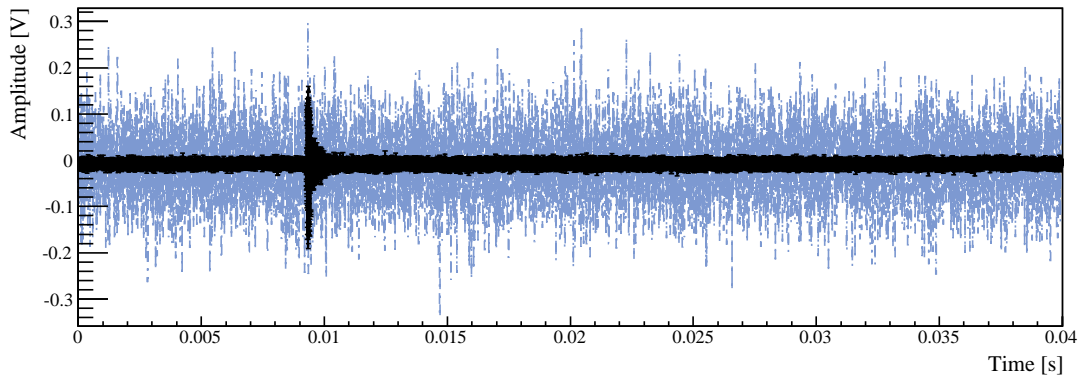
(c)

Figure 5.4: The averaged (black full line, foreground) and raw (blue dashed line, background) waveforms for sensor channel AS6-2 listening to transmitters BT6 and DT4. (a): The full waveform, zoomed in on the y-axis, for sensor channel AS6-2 listening to transmitter BT6. The shear wave is only visible in the black averaged waveform, about 0.032 s after the main pulse. Due to the arbitrary starting time of the waveform, the shear wave finds itself in front of the pressure pulse in this example. (b): Zoom on the start of the pressure wave pulse. The clockdrift correction and averaging procedures doubled the number of data points in the waveform. (c): The full waveform for sensor channel AS6-2 listening to transmitter DT4. Note the difference in amplitude scale. No pulse was visible before averaging.

(a)   (b)
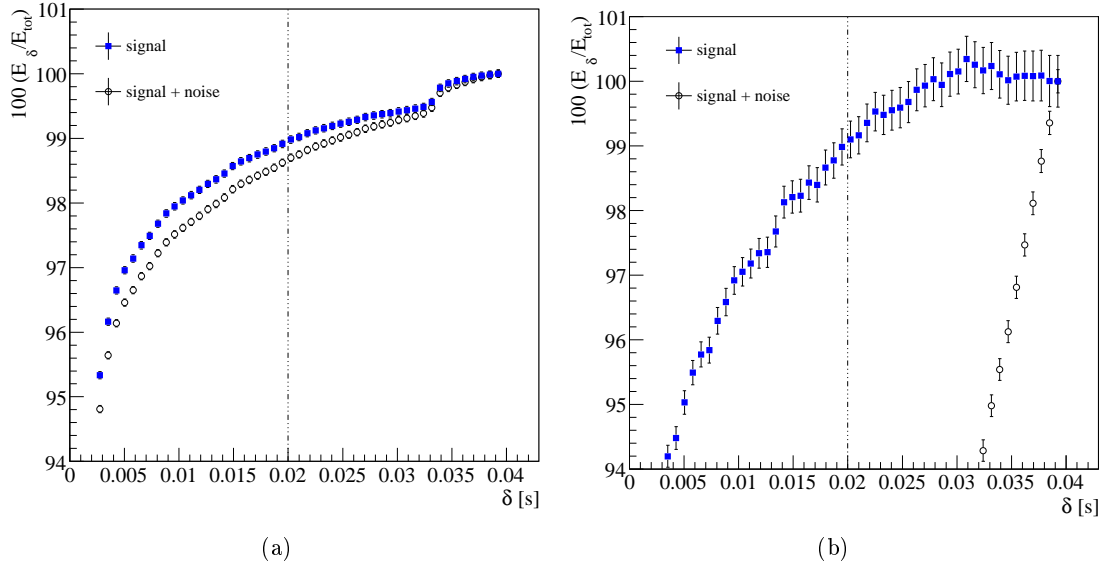
Figure 5.5: The percentage of signal energy, $100 \cdot (E_\delta/E_{\text{tot}})$, as a function of δ for the signal+noise (black open circles) and signal-only (blue filled squares) energies. The vertical dashed black line indicates the δ that was chosen for the inter-string analysis. E_{tot} is the energy for $\delta = 0.04 - 0.001$ s. (a): (BT6, AS6-2) has a large pressure pulse and also a clear shear wave. The shear wave is responsible for the sudden increase around 0.032 s. (b): For (DT4, AS6-2), the signal-to-noise ratio is low.

waveform as a measure for the strength of the pressure wave. A better measure of this quantity is the energy of the pulse. For the signal+noise waveform this energy is defined as:

$$E_{\text{S+N}} = \sum_i A_i^2, \text{ for } t_{\max} - 0.001\,\text{s} < t_i < t_{\max} + \delta \tag{5.2}$$

where $t_{\max}$ is the time of the maximum amplitude. The summation over i therefore goes over a certain number of amplitudes in the sensor waveform. The δ needs to be set in such a way that the summation mainly goes over amplitudes A_i that are recognisable above the background noise. The amplitudes are corrected for the possible offset of the Gaussian noise in that channel. The total length of the time-window over which the energy is calculated is $\delta + 0.001$ s. The energy is also extracted for the complete noise waveform for the same sensor channel. Thus, the energy of the transmitter signal as detected by the sensor is:

$$E_{\text{S}} = E_{\text{S+N}} - E_{\text{N}}, \tag{5.3}$$

where E_{N} is the energy of the noise in that sensor channel, scaled to the same number of samples. δ was chosen to be 0.02 s, as a compromise between having at least 99% (within error) of the pressure wave energy and excluding the shear wave energy (see § 5.2.4). This choice of δ excludes the shear wave contributions for the (T, S) combinations where they are above noise. From the extracted energies E_{S}, one can calculate the effective amplitude:

$$A_{\text{eff}} = \sqrt{E_{\text{S}}}. \tag{5.4}$$

The statistical errors are propagated throughout. All effective amplitudes are extracted for all available (T, S) combinations.

5.2.4 Optimising l and δ

l is the number of transmitter pulses that are averaged to obtain the averaged waveform. The higher l, the higher the signal-to-noise ratio. Figure 5.4(b) shows the comparison of the raw (i.e. unprocessed) transmitter pulse to the averaged waveform, using $l = 250$. The averaged waveform contains most of the features of the pulse (also compare Figs. 5.1(c) and 5.1(d)). Therefore it was decided to use $l = 250$ for the inter-string analysis presented here.

$\delta + 0.001\,\mathrm{s}$ is the length of the time-window around the pressure pulse for which the energy is calculated. If the window is too small, a significant fraction of the pressure pulse energy can be cut away. For a larger δ, the small pulses risk to be drowned inside the noise and the energy of the shear wave is possibly included. For example, in the event for (BT6, AS6-2), see Fig. 5.4(a), $\delta > 0.032\,\mathrm{s}$ would also include the shear wave. In order to find an optimal value for δ, the percentage of waveform energy (either the signal+noise or signal-only), $100 \cdot (E_\delta/E_{\mathrm{tot}})$ is plotted as a function of δ. E_{tot} is the energy for $\delta_{\max} = 0.04 - 0.001\,\mathrm{s}$. This means that the summation in Eq. 5.2 then goes over all samples of the waveform. Figure 5.5 shows two examples for (DT4, AS6-2) and (BT6, AS6-2). With $\delta = 0.02$ at least 99% of the total pressure wave energy is included in both cases. Fig. 5.5(a) illustrates the fact that, although this is not clearly visible with the naked eye (see Fig. 5.4(a)), the pressure pulse is still contributing to the amplitude $0.02\,\mathrm{s}$ after $t_{\max}$. In other words, the pressure pulse has a long tail.

$E_{0.02}/E_{\mathrm{tot}}$ is extracted, using the signal-only energies, for all channels from all available (T, S) combinations and the distribution is shown in Fig. 5.6(a). The distribution of $E_{0.02}/E_{\mathrm{tot}}$ for (T, S) combinations that have signal-only energy at least as high as the statistical error on that energy are compared to the ones for which the signal-only energy is at least 3 and 40 times the statistical error on that energy. This shows that the outliers are typically combinations with a low signal-to-noise ratio. Figure 5.6(b) shows $E_{0.02}/E_{\mathrm{tot}}$ as a function of E_{tot} for $E_{\mathrm{S}} > 3\sigma(E_{\mathrm{S}})$. The events with low energy have larger deviations from $E_{0.02}/E_{\mathrm{tot}} = 1$ but also larger statistical errors.

For the presented inter-string analysis, $\delta = 0.02\,\mathrm{s}$ was chosen. It ensures that at least 99% of the total pressure pulse energy is included.

5.2.5 Missed or disqualified combinations

Some (T, S) combinations are missing because the data acquisition program failed during the recording of that specific configuration. In addition, the following quality cuts are applied before the (T, S-c), where S-c stands for channel c from sensor S, combination is accepted for the attenuation length analysis:

- All saturated pulses are excluded. This means that a (T, S-c) combination is excluded if $A_{\max} > +3.5\,\mathrm{V}$ or $A_{\min} < -3.5\,\mathrm{V}$, where $A_{\max}$ ($A_{\min}$) is the maximum (minimum) amplitude in the raw signal+noise waveform.

- The effective amplitude (see Eq. 5.4) at a given channel is required to be higher than $\gamma\sigma(A_{\mathrm{eff}})$, with $\gamma = 3.0$ for the same-level inter-string analysis and $\gamma = 1.5$ for the ratio

(a)   (b)
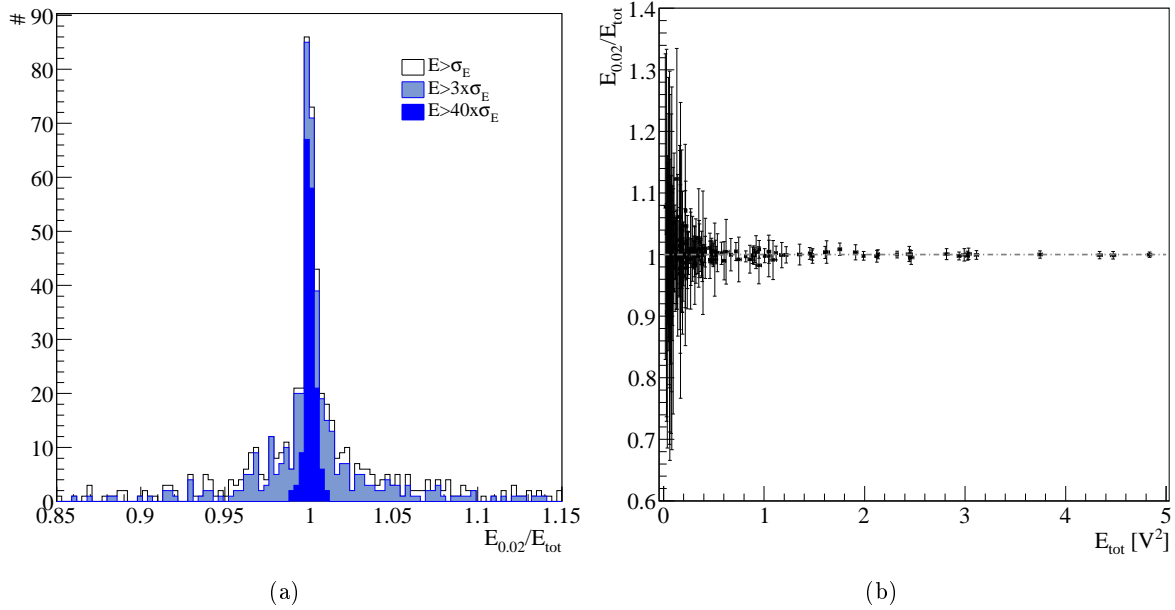
Figure 5.6: (a): The distribution of E_δ/E_{tot} for different quality cuts. (b): $E_{0.02}/E_{\text{tot}}$ as a function of E_{tot} for the quality cut $E_S > 3\sigma(E_S)$. The gray dashed line indicates $E_{0.02}/E_{\text{tot}} = 1$.

Amplitude reduction mechanism	Physical process	Behaviour
Absorption	Energy conversion	$e^{-\alpha_a d}$
Scattering	Energy diversion	$e^{-\alpha_s d}$
Beam spreading	Energy redistribution	$\frac{1}{d^2}$ (spherical), $\frac{1}{d}$ (cylindrical)

Table 5.1: Mechanisms by which an sound wave amplitude is attenuated. Adapted from [168].

inter-string analysis. This cut excludes channels that have signals which are too close to noise and possible false pulses (these are signals that are not from the transmitter).

- Channels with known problems are excluded: AS3 (all three channels) and CS1 (all three channels).

5.3   Attenuation length analysis

5.3.1   Acoustic attenuation

The attenuation of a sound wave by absorption or scattering can be mathematically represented by an exponential decay. In the case of plane wave propagation, the acoustic pressure P at a distance d can be written as:

$$P = P_0 e^{-\alpha d}, \tag{5.5}$$

where P_0 is the initially measured acoustic pressure and α is the attenuation coefficient for acoustic pressure in the material. The attenuation length λ is defined as $\lambda = 1/\alpha$.

All acoustic sources have a finite extent and also, a true plane wave does not exist. A wave from an acoustic point source propagates and diverges and, as it does so, the amplitude will be geometrically attenuated. The energy is spread over an increasingly large area and the amplitude will decrease.

For the SPATS array, the signal amplitude in voltage depends linearly on the acoustic pressure arriving at the piezo-ceramic element within the linear working range of the amplifiers. For a point source (like the SPATS transmitters in the inter-string geometry) the signal amplitude scales due to geometry as $1/d$ (spherical emission) and attenuation as $e^{-d/\lambda}$:

$$A_{\text{eff}}(d) = \frac{A_0}{d} e^{-\alpha d} = \frac{A_0}{d} e^{-d/\lambda}, \tag{5.6}$$

where A_0 is a constant. We then define:

$$y := -\frac{d}{\lambda} + \ln(A_0) = \ln(A_{\text{eff}} d) \tag{5.7}$$

where A_{ef} is the effective amplitude (in V) and d is the transmitter to sensor distance (in m). A linear fit can be performed using the model:

$$y = -\alpha d + b, \tag{5.8}$$

where α is the acoustic attenuation coefficient (in m^{-1}) and b is a free parameter. A fit to the data then directly determines the two parameters, α and b, and their respective errors.

5.3.2 DT4 same-level attenuation length

Every transmitter pulse is recorded by, amongst others, the sensors that are positioned at the same depth as the transmitter. So if we only consider those same-level sensors, there are three different distances (i.e. three strings) at which the same transmitter pulse is recorded. To start with, an example of a same-level analysis using the inter-string data is presented for string D transmitter DT4 at a depth of 320 m. For this level, all 9 (DT4, S-c) same-level combinations pass the quality cuts discussed in §5.2.5 and the corresponding extracted energies E and effective amplitudes A_{eff} are listed in Table 5.2. The errors are the propagated statistical errors. For each sensor channel, both E and A_{eff} are in general agreement with the analysis presented in [167], where the same data but different analysis codes were used.

Now $y = \ln(A_{\text{eff}} d)$ is calculated for each (DT4, S) combination. The statistical errors for A_{eff} and d are propagated. The spread between the three different amplitudes for the three channels in the same sensor module is much larger than the statistical fluctuations, see Fig. 5.7(a). Indeed, the unknown orientation of the SPATS sensors gives rise to a "random" systematic error. This means that the amplitude will always be systematically higher or lower for a certain channel from a certain angle. The direction-dependent sensitivity for each sensor channel was investigated using the pinger data, as discussed in §4.3.2. If it is assumed that the variation in sensitivities measured in the pinger analysis is a good estimate for other directions too, then the ± 0.86 systematic uncertainty on y for each of the channels can be used in this same-level inter-string analysis. The statistical and systematic errors are subsequently quadratically added to obtain the total error on a measured amplitude.
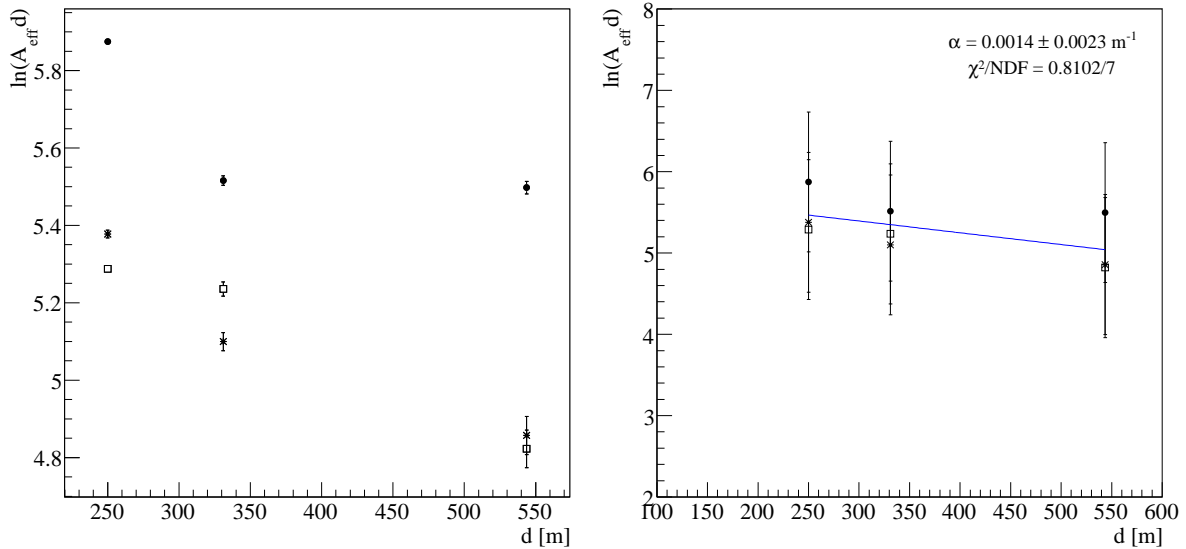
(a)

(b)
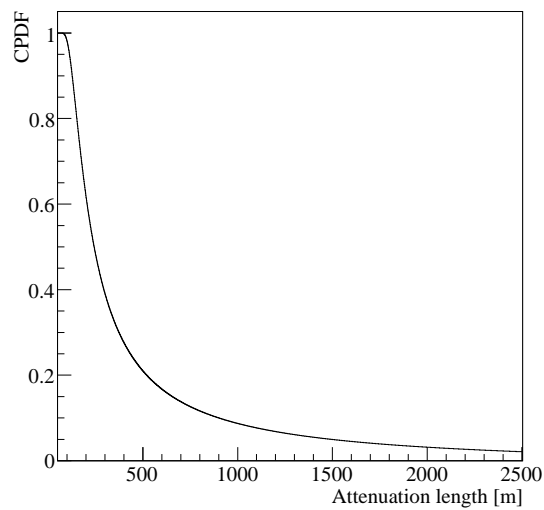
(c)

Figure 5.7: The DT4 same-level data: three sensor modules with each three sensor channels (0 (open square), 1 (filled circle) and 2 (black star)) record the same transmitter pulse at different distances. (a): With statistical errors only, the spread between the points is much larger than the expected statistical fluctuations. (b): With the ± 0.86 systematic uncertainty included and MINUIT fitresult. (c): The Cumulative Probability Density Function (CPDF) for the fit from (b)

.

Sensor-Channel	Distance [m]	E [V^2]	$\sigma(E)$ [V^2]	A_{eff} [V]	$\sigma(A_{\mathrm{eff}})$ [V]
AS6-0	250.0 ± 0.7	0.63	0.01	0.79	0.01
AS6-1	250.0 ± 0.7	2.03	0.02	1.42	0.01
AS6-2	250.0 ± 0.7	0.75	0.01	0.87	0.01
BS6-0	331.1 ± 0.7	0.32	0.01	0.57	0.02
BS6-1	331.1 ± 0.7	0.56	0.01	0.75	0.01
BS6-2	331.1 ± 0.7	0.25	0.01	0.49	0.02
CS6-0	543.6 ± 0.7	0.05	0.01	0.23	0.05
CS6-1	543.6 ± 0.7	0.20	0.01	0.45	0.02
CS6-2	543.6 ± 0.7	0.06	0.01	0.24	0.05

Table 5.2: All inter-string distances, energies and amplitudes for the same-level attenuation length analysis for transmitter DT4. Errors are statistical only.

Figure 5.9(f) shows $\ln(A_{\mathrm{eff}}d)$, with the systematic error included, as a function of distance d for the three available distances. For each distance there are three data-points, one for each of the three sensor channels. The fit is obtained with the MINUIT numerical minimisation package [169] as it is implemented in ROOT [170]. The fit values for α and b were also calculated with a C++ function that extracts the analytical solution (errors on y only) described in [171]. Both results agree and only the results from the MINUIT procedure (taking into account both errors on the d and y values) are quoted.

The single fit yields $\alpha = 0.0014 \pm 0.0023\,\mathrm{m}^{-1}$, with $\chi^2/\mathrm{NDF} = 0.810/7$. This does not constrain the acoustic attenuation length in ice due to the large systematic error that is introduced by using different sensor channels. The Cumulative Probability Density Function (CPDF) for this fit is shown in Fig. 5.7(c) for the case where the attenuation length is constrained to be positive. The χ^2/NDF is very small, indicating that the errors on the single amplitudes have been overestimated. This means that the estimation of the systematic error is too conservative for this set of (T, S) combinations, since it dominates the error on a single amplitude.

5.3.3 Combined same-level analysis

Now the same-level analysis as described in the previous section is performed for all levels and all possible combinations. There are 28 SPATS transmitters in total, of which 24 were used during the inter-string data taking. Since there are only 5 levels in common between strings A, B and C and string D, there are only 20 possible same-level fits. Of these 20 possible fits, it is required that:

- All sensor channels and extracted effective amplitudes pass the quality cuts presented in § 5.2.5.

- There is at least 1 data point (i.e. one channel above noise) per distance for a minimum of two different distances.

- The MINUIT minimisation converges.

12 transmitters pass these requirements. All fits are shown in Fig. 5.8 and Fig. 5.9 and the fit parameters are summarised in Table 5.3. In this table, the results from an independent analysis

on the same data [167] are also shown. Combining all results by calculating the weighted mean, where the weight of a attenuation coefficient result α_i is defined as $1/\sigma_i^2$, gives:

$$\alpha = 0.0031 \pm 0.0008\,\mathrm{m}^{-1}, \tag{5.9}$$

Transmitter-Depth [m]	This work			[167]
	$\alpha \pm \sigma_\alpha$ [m^{-1}]	$b \pm \sigma_b$	χ^2/NDF	$\alpha \pm \sigma_\alpha$ [m^{-1}]
AT-140				0.0065 ± 0.0026
AT-250	**0.0066 ± 0.0024**	7.4 ± 0.7	$0.536/7$	0.0065 ± 0.0026
AT-320	**0.0043 ± 0.0024**	6.6 ± 0.7	$1.489/7$	0.0043 ± 0.0025
AT-400	**0.0039 ± 0.0033**	5.9 ± 0.8	$1.769/5$	0.0038 ± 0.0035
BT-140	-0.0087 ± 0.0273	2.0 ± 8.0	$0.485/3$	-0.019 ± 0.027
BT-190	**0.0008 ± 0.0036**	5.8 ± 0.9	$4.535/5$	-0.00024 ± 0.0043
BT-320	**0.0069 ± 0.0036**	7.8 ± 1.0	$1.769/6$	0.0078 ± 0.0034
BT-400	-0.0022 ± 0.0032	3.7 ± 0.8	$4.032/6$	-0.00054 ± 0.0049
CT-250	**0.0035 ± 0.0029**	6.4 ± 1.3	$0.732/7$	0.0050 ± 0.0043
CT-320	**0.0050 ± 0.0033**	6.8 ± 1.4	$0.531/6$	0.0045 ± 0.0042
DT-250	-0.0011 ± 0.0027	4.9 ± 1.0	$2.241/6$	-0.00095 ± 0.0029
DT-250	**0.0043 ± 0.0024**	6.7 ± 0.9	$0.402/7$	0.0036 ± 0.0025
DT-320	**0.0014 ± 0.0023**	5.8 ± 0.9	$0.810/7$	0.0014 ± 0.0025
α weighted mean [m^{-1}]	0.0031 ± 0.0008			0.0031 ± 0.0009
λ [m]	323 ± 83			321 ± 95

Table 5.3: Fit parameters for the SPATS inter-string same-level fits. For comparison, the results from an independent analysis on the same data is shown.

It is possible to argue in favour of selecting a subset of the same-level results. Indeed, some of the MINUIT minimisations yield negative, and therefore non-physical, attenuation coefficients. If these results for α are excluded, nine extracted attenuation coefficients remain. They are marked in bold lettertype in Table 5.3, see also Fig. 5.10. The result for the weighted mean is then:

$$\alpha = 0.0041 \pm 0.0009\,\mathrm{m}^{-1}, \tag{5.10}$$

which corresponds to an attenuation length λ of (propagating the error):

$$\lambda = 245 \pm 54\,\mathrm{m}. \tag{5.11}$$

The error includes both statistical and systematic propagated errors. The uncertainty on the azimuthal behaviour and inherent sensitivity of each individual sensor dominates the error in this analysis. b allows a shift in $\ln(A_{\mathrm{eff}}d)$ and is linked to the initial transmitter amplitude. For these 9 fits, the spread in b is not in contradiction with the possible 40% expected variability due to differences in azimuthal orientation and transmittivity of the different transmitters.

For the final same-level analysis here, only high quality fits are retained for the final result. Indeed, only positive attenuation coefficients from fits to amplitudes at three different distances are used. In the end, including 2-distance fits or negative attenuation coefficients increases the

(a) AT5 (250 m)   (b) AT6 (320 m)

(c) AT7 (400 m)   (d) BT3 (140 m)

(e) BT4 (190 m)   (f) BT6 (320 m)
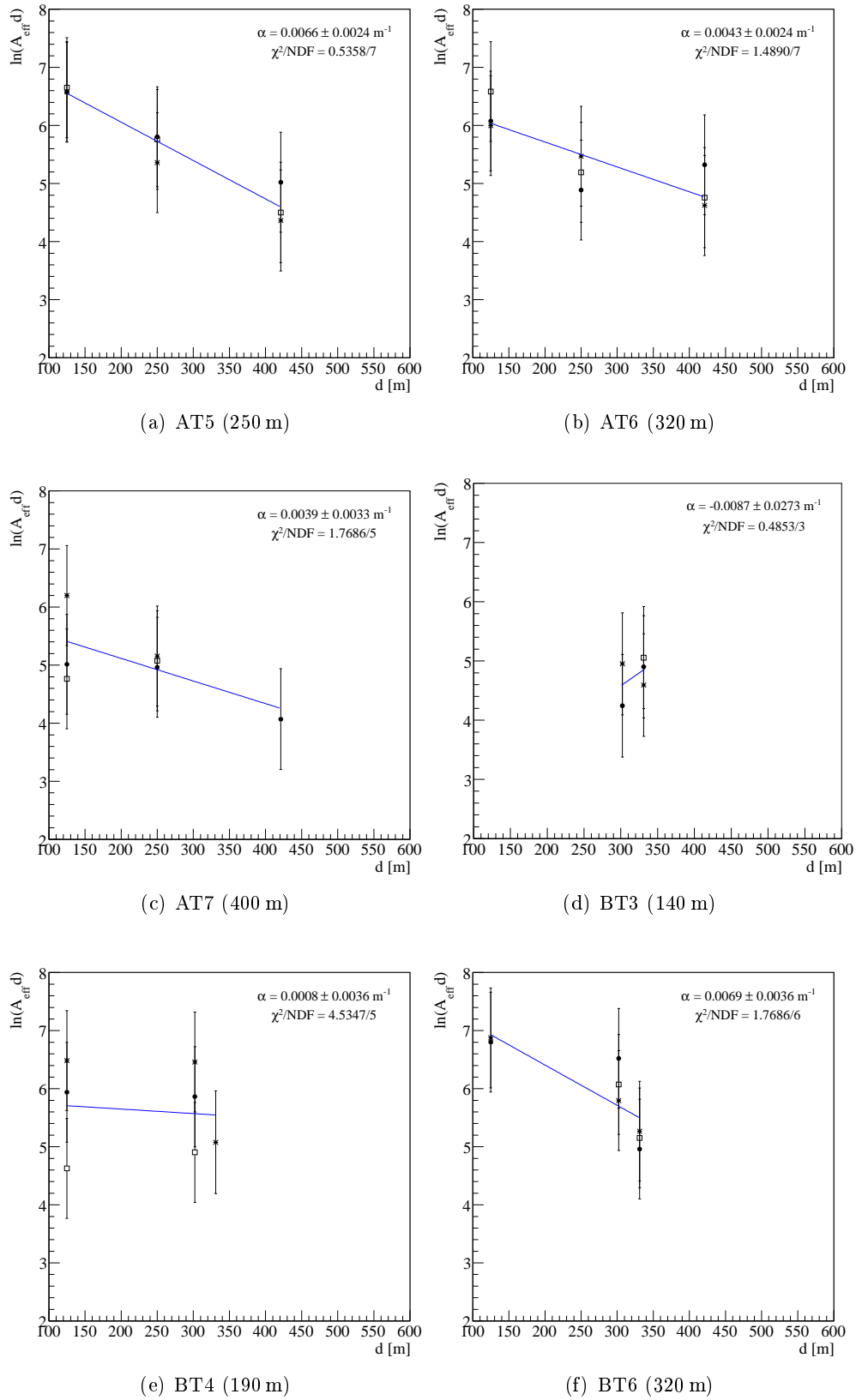
Figure 5.8: The SPATS inter-string same-level attenuation length fits. The depths of the stages are indicated.

117

(a) BT7 (400 m)

(b) CT5 (250 m)

(c) CT6 (400 m)

(d) DT2 (190 m)

(e) DT3 (250 m)

(f) DT4 (320 m)
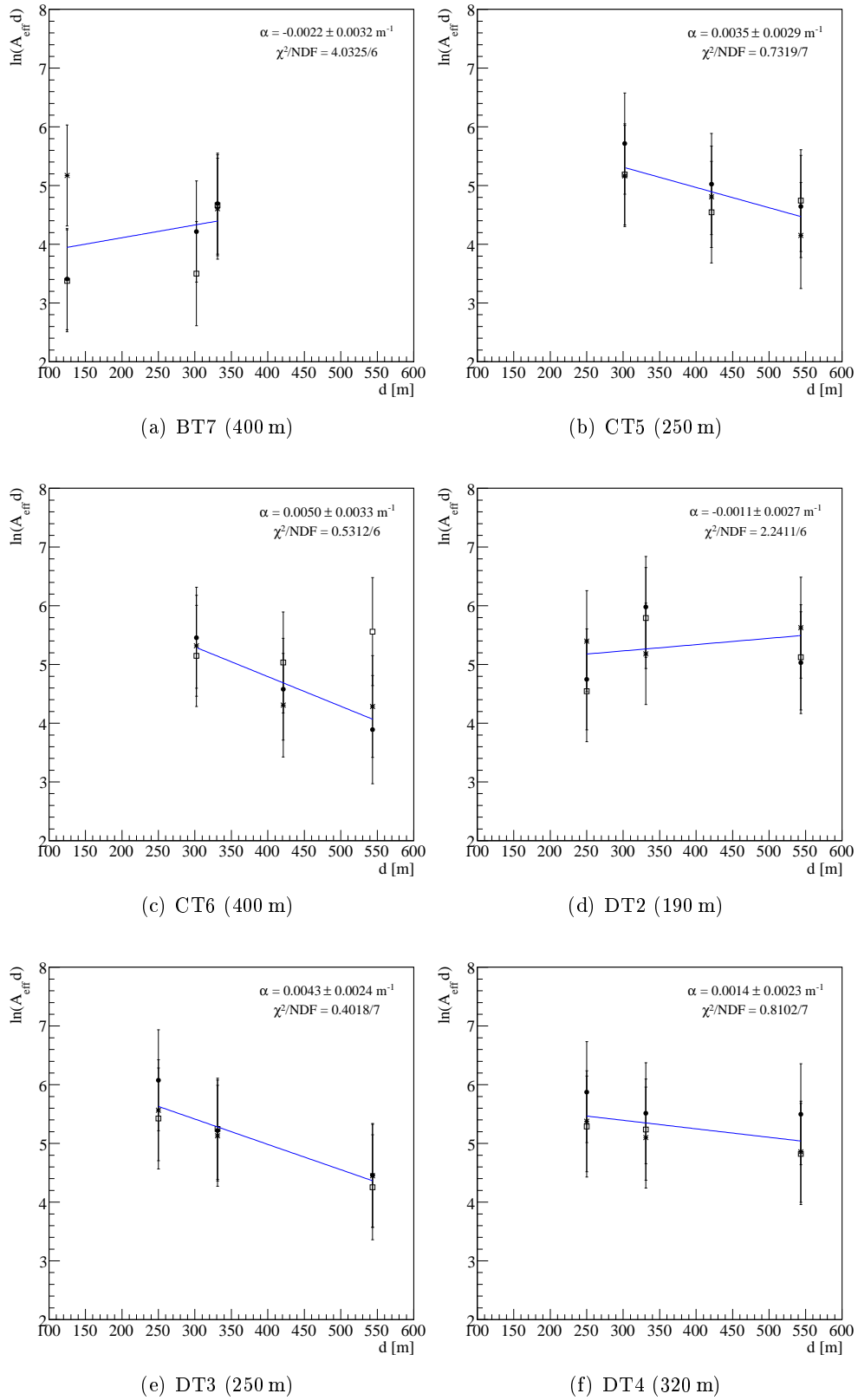
Figure 5.9: The SPATS inter-string same-level attenuation length fits (continued).
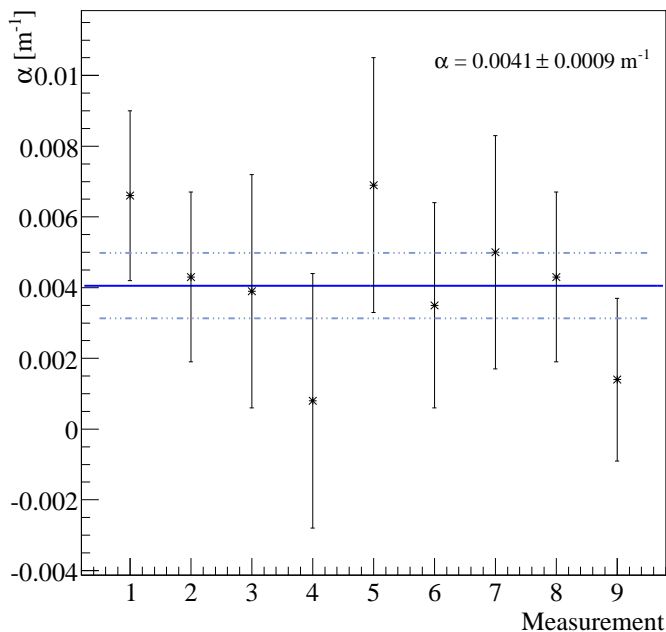
Figure 5.10: The SPATS inter-string same-level attenuation length results for $\alpha > 0$. The weighted mean is indicated by the blue solid line, the dashed blue lines are $\pm\sigma$.

attenuation length but also the error, see Table 5.3. Again, all results stay in agreement with each other within error. The quality cuts automatically select the measurements with the lowest error and the error on the final result does not reflect the complete spread in the same-level measurements. Also, in Fig. 5.10, the spread of the different measurements does indicate that, even with the systematic error on a single amplitude possibly overestimated, the final error for each measurement of α does not seem to be overestimated.

In the analysis presented here, all same-level data points were fitted individually. A global fit can also be extracted, forcing the fit parameter α to be the same for each transmitter combination. This global fit will be done in the near future.

There are some interesting differences (within error) with the results presented in [167] that can presumably be explained by a different choice in δ and different noise-subtraction methods. A more detailed comparison of all amplitudes between the two independent analyses is needed to investigate possible systematic deviations. Some of the same-level fits are very sensitive to long distance combinations. For these, the pulses at long distances have low amplitudes and therefore are prone to larger fluctuations with varying δ. As a verification, the complete same-level analysis was also done with $\delta = \delta_{\mathrm{max}}$. All results are in agreement within error. The complete same-level analysis presented in this section has allowed to gain confidence in the obtained effective amplitudes for the single (T, S-c) combinations by comparing the results of each step to the results of the analysis presented in [167].

5.3.4 Ratio attenuation length analysis

In [157] a numerical study was presented, introducing the "ratio method" for attenuation length analysis with the SPATS inter-string data. In the following this method is discussed and applied to the SPATS 4-string inter-string data set.

Method

As mentioned previously, none of the permanently deployed transmitters and sensors has been calibrated in ice. This means that both an unknown inherent sensitivity and unknown transmitter transmittivity enter the equation for a single inter-string amplitude measurement:

$$A_{ij} = \frac{\mathcal{T}_i \mathcal{S}_j}{d_{ij}} e^{-\alpha d_{ij}}, \tag{5.12}$$

where A_{ij} is the amplitude of the pulse emitted by transmitter i as detected by sensor j, $\mathcal{T}_i$ is the initial transmitter amplitude, $\mathcal{S}_j$ is the sensor sensitivity and d_{ij} is the distance between transmitter i and sensor j. In the same-level analysis, the same transmitter pulse is recorded by up to 9 different sensor channels from different angles. In that case the variation in sensitivity due to inherent sensitivity differences and azimuthal angle was taken into account through the systematic error.

If we now take two transmitter-sensor pairs, i.e. transmitters i and k both heard by sensors j and l (Fig. 5.11), it is possible to construct a ratio of amplitudes:

$$\frac{A_{ij}A_{kl}}{A_{il}A_{kj}} \frac{d_{ij}d_{kl}}{d_{il}d_{kj}} = \frac{\mathcal{T}_i \mathcal{S}_j}{\mathcal{T}_i \mathcal{S}_l} \frac{\mathcal{T}_k \mathcal{S}_l}{\mathcal{T}_k \mathcal{S}_j} e^{-\alpha([d_{ij}-d_{il}]-[d_{kj}-d_{kl}])}, \tag{5.13}$$

which can also be written as

$$\ln(\mathcal{R}_A \mathcal{R}_d) = -\alpha D_x + p, \tag{5.14}$$

where $\mathcal{R}_A$ and $\mathcal{R}_d$ are ratios of amplitudes and distances respectively. D_x is the difference in difference in distance between the two transmitter combinations ($[d_{ij} - d_{il}] - [d_{kj} - d_{kl}]$). p is a free fit parameter introduced to allow a systematic shift in $\ln(\mathcal{R}_A \mathcal{R}_d)$. The ratio $\mathcal{R}_A$ does not depend on the particular transmitter strengths and intrinsic sensor channel sensitivities involved.

Systematics

A single ratio measurement should yield the attenuation coefficient α if the transmitters and sensors all are perfectly isotropic. However, it was shown in Chapter 4 that the sensor sensitivity and the transmitter power depend on the azimuthal and polar orientation of the devices. Therefore, both $\mathcal{T}$ and $\mathcal{S}$ have a dependence on θ (polar angle) and ϕ (azimuthal angle). This means that the effect of the unknown azimuthal orientation of each sensor module and the significant polar dependence of the transmitter power still remain after constructing the ratios. The following selection and processing of data was introduced in order to minimise this geometrical effect.

- Only transmitter-sensor combinations from neighbouring levels with enough statistics were used: $(190, 250)$ m, $(250, 320)$ m and $(320, 400)$ m depth. This is the 2-level ratio fit. No sufficient amount of ratios was available for the other levels. The difference in polar angle, for an amplitude ratio used in the 2-level ratio fit presented here, is therefore maximum
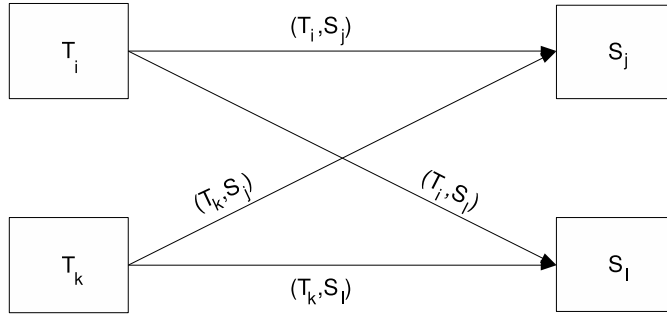
Figure 5.11: Illustration of an inter-string amplitude ratio.

$18°$ for $(190, 250)\,\mathrm{m}$, $29°$ for $(250, 320)\,\mathrm{m}$ and $32°$ for $(320, 400)\,\mathrm{m}$. Many of the ratios, however, have smaller differences in polar angles.

- The polar angle is assumed to be the dominant factor for the transmitter power $\mathcal{T}(\theta)$. From the results discussed in § 4.1.1 it follows that a possible 40% variation in the transmittivity has to be taken into account.

- The maximum difference in azimuthal angle in the inter-string setup is roughly $120°$, for example for a sensor channel on string B recording a pulse from a string D transmitter followed by one emitted by a string C transmitter. It is therefore expected to see a large difference between the two amplitudes on top of the inherent difference in transmitter power. Therefore, an average sensor module response is used. This means that the three recorded waveforms are processed and an effective amplitude is extracted for each of the three individual sensor channels in the sensor-module. These three amplitudes are then averaged and their errors are propagated. This average sensor module amplitude is used for the ratio calculations. If the sensitivity of each sensor channel has a similar dependence on the azimuthal orientation of the channel relative to the arrival direction of the pulse, the averaging makes the azimuthal dependence less prominent.

- It is assumed that the azimuthal effect is the dominant factor in sensor sensitivity $\mathcal{S}(\phi)$. As for the same-level analysis, a 68% possible variation of the sensor sensitivity has to be taken into account due to the unknown orientation of the sensor module.

An upper limit on the possible variation on a single amplitude measured by a certain sensor listening to a transmitter, a 68% variation of the sensor sensitivity and a 40% variation in the transmitter power is assumed. This leads to an 80% possible systematic shift for a single amplitude. A single amplitude ratio then has a systematic uncertainty of 160%, which translates as ± 1.6 in $\ln(\mathcal{R}_A)$.

Data set

Figure 5.12(a) shows the distribution of available distances between the transmitter and sensor for the entire inter-string data set. Figure 5.12(b) shows the pulse from the diagonal combination (DT7, CS6-1). For this example, the distance between transmitter and sensor is $573\,\mathrm{m}$, and the

(a)

(b)
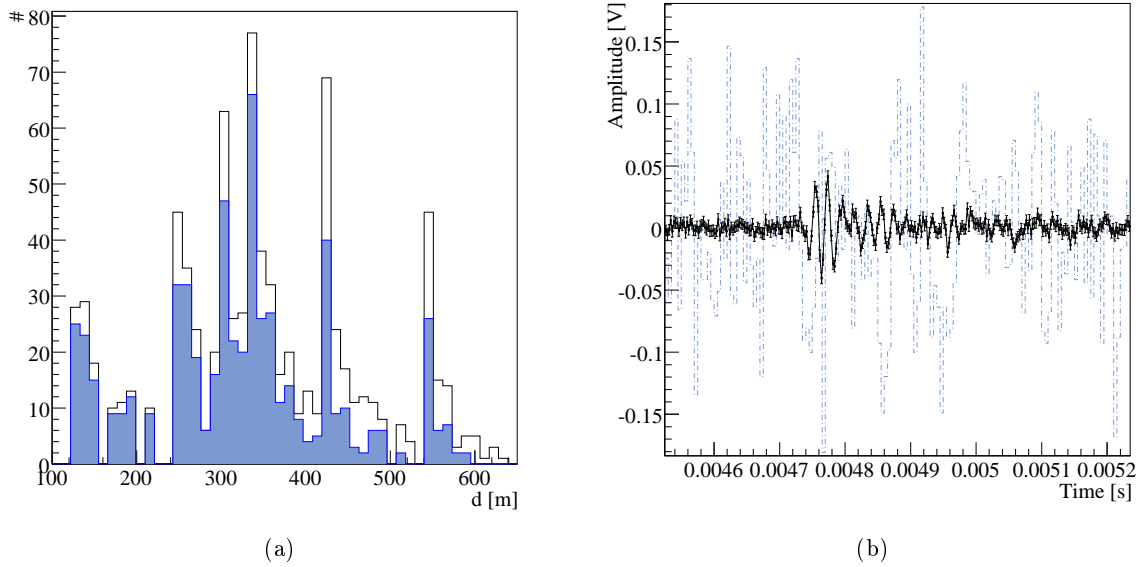
Figure 5.12: (a): The distribution of distances for the complete inter-string data set, for all (T, S) combinations that have $A_{\text{eff}} > \sigma(A_{\text{eff}})$ (white, background) and that have $A_{\text{eff}} > 3.0\sigma(A_{\text{eff}})$ (blue, foreground). (b): An example of an event at large distance: (DT7, CS6-1), the averaged waveform in black (foreground) and non-processed waveform in light blue (background).

diagonal path between the transducers has an polar angle of $18°$ compared to the horizontal plane.

The parameter γ that was introduced in § 5.2.5 is a measure of required signal-to-noise for the detected pulses. In order for an amplitude ratio to make the quality cut, all three channels of both sensor modules need to have $A_{\text{eff}} > 1.5\sigma(A_{\text{eff}})$. This is a less severe cut than the one that was used in the same-level analysis. The reason for this choice is that the chance of having all three channels seeing a false signal simultaneously is small; therefore the required A_{eff} for a channel to pass the cut can be smaller.

Figure 5.13(a) shows $\ln(\mathcal{R}_A \mathcal{R}_d)$ as a function of D_x for the complete inter-string data set (2439 ratios) compared to the 2-level selection (172 ratios). Only the statistical errors are plotted. The spread on the ratios that were built using all levels simultaneously (complete inter-string data set) is larger than the spread on the 2-level selection. This is expected since the maximum difference in polar angle is much larger for the full set than for the 2-level selection.

Figure 5.13(b) shows the comparison of the same data sets for the distribution of α, where each α was obtained by dividing $\ln(\mathcal{R}_A \mathcal{R}_d)$ by the corresponding D_x. This can be done if $p = 0$ is assumed, which theoretically should be the case. The distribution of the full data set is broad and does not have a Gaussian shape. The distribution resembles a Cauchy function, which is characterised by infinite tails and the fact that the mean is not better defined when increasing the number of measurements. The long tails in the distribution presented here can be understood as follows. Due to the large possible systematic shift on each of the four amplitudes used in a single amplitude ratio, it is likely that some ratios will use amplitudes for which the systematic effects
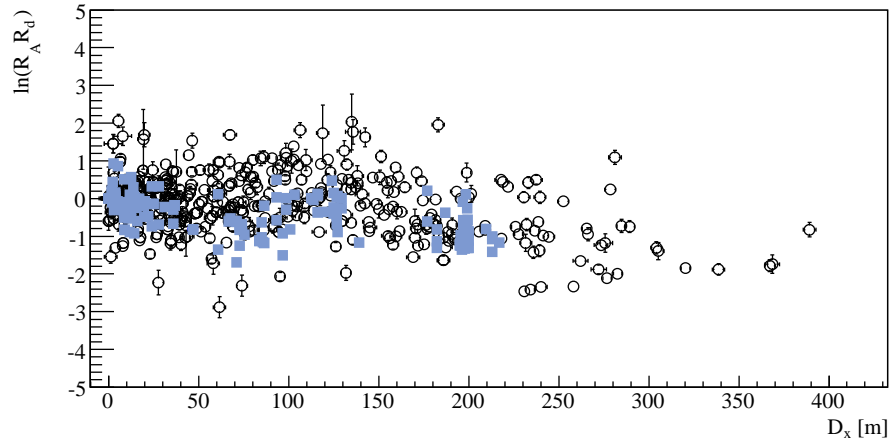
(a)
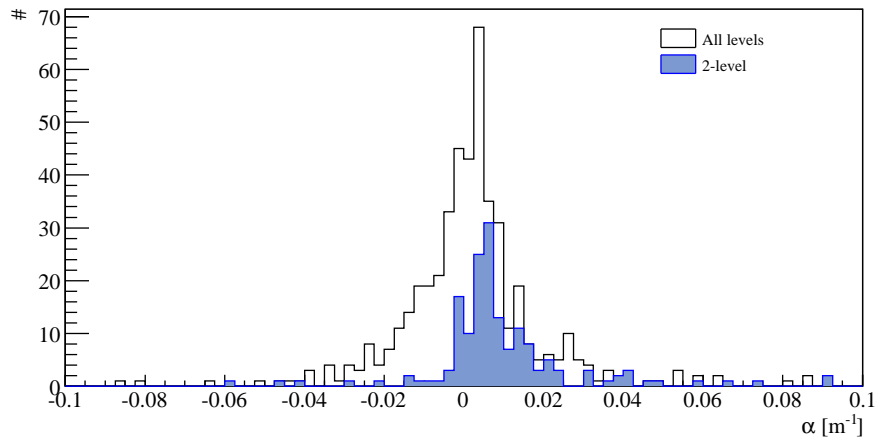
(b)

Figure 5.13: (a): $\ln(\mathcal{R}_A\mathcal{R}_d)$ as a function of D_x for the complete inter-string data set (2439 ratios, black open circles, background) compared to the 2-level selection (172 ratios, blue filled squares, foreground). Only the statistical errors are plotted. (b): Distribution of α for the complete inter-string data set (white, background) compared to the 2-level selection (blue, foreground).

are working in the same direction for the final attenuation coefficient result. The distribution for the 2-level data set is more narrow and excludes the most extreme cases. Also, there is an indication that more negative than positive α are cut away by applying the 2-level condition. Including larger polar angles increases systematically the attenuation length in ice in this case. This systematic dependence on polar angle is worth investigating further.

123

Results

It is clear that a single ratio calculation is useless as estimator for the attenuation coefficient due to the large systematic error. In total, 172 ratios were built for the three selected 2-level combinations. Figure 5.14 shows all 172 ratios and the 2-parameter fit. Table 5.4 lists the fit parameters. The error bars include both the systematic uncertainty and the statistical error on both the effective amplitudes and the distance ratio. The 2-parameter fit gives as a result for the attenuation coefficient $\alpha = 0.0040 \pm 0.0016 \, \text{m}^{-1}$. Converted to attenuation length, this leads to

$$\lambda = 250 \pm 100 \, \text{m}. \tag{5.15}$$

The small χ^2/NDF could give an indication that the error on this ratio result is overestimated. Indeed, the spread of the ratios around the fit is much smaller than the assumed systematical (dominant) error of ± 1.6 on $\ln(\mathcal{R}_A)$. This can either be due to an overestimation of the polar variation of the transmitter transmittivity or the azimuthal sensitivity variation of the sensor response. Currently, we cannot discriminate between these two possible causes, but both are likely in play. The $\pm 68\%$ that was extracted using the 2008/2009 pinger data is an estimation of the variability between the sensor channels due to both the difference in azimuthal orientation and in intrinsic sensitivity. In the ratio analysis, however, the intrinsic differences have been eliminated and the azimuthal effect is presumably partially averaged out by taking the mean response of each sensor module. On top of that, the systematic errors are likely correlated as, for example, the amplitudes from a certain transmitter will be systematically higher for a specific polar angle. If indeed the errors on the effective amplitudes are correlated, then the presented $\sigma(\lambda)$ is an upper limit on the error. If the only dominating systematic error is assumed to be the transmitter polar behaviour, then the total systematic error on a single amplitude is reduced to 40%, or 0.8 on $\ln(\mathcal{R}_A)$. The fit parameters for different systematic errors are also indicated in Table 5.4.

There is an interesting large population of ratios around $D_x = 200 \, \text{m}$, possibly related to an optimal ratio geometry. This is currently under study. It also needs to be noted that many of the 172 calculated ratios are not independent of each other, as individual amplitudes can be used in the construction of several ratios. These correlations and the effect on the final result are still to be investigated.

However, when fitting all ratios, with no selection on angles, the obtained attenuation length is still compatible with the result of the presented inter-string ratio analysis. This is already an indication that, although not all aspects of the correlation between ratios and the residual polar and azimuthal effects have been investigated yet, the error of 100 m of the final result presented here likely takes these possible effects into account.

σ_{sys}	$\alpha \pm \sigma_\alpha$ [m^{-1}]	$p \pm \sigma_p$	χ^2/NDF
1.6	0.0040 ± 0.0016	-0.11 ± 0.18	$13/170$
0.8	0.0040 ± 0.0008	-0.11 ± 0.09	$50/170$
0.4	0.0040 ± 0.0004	-0.11 ± 0.05	$199/170$

Table 5.4: Fit parameters for the SPATS ratio analysis fit.
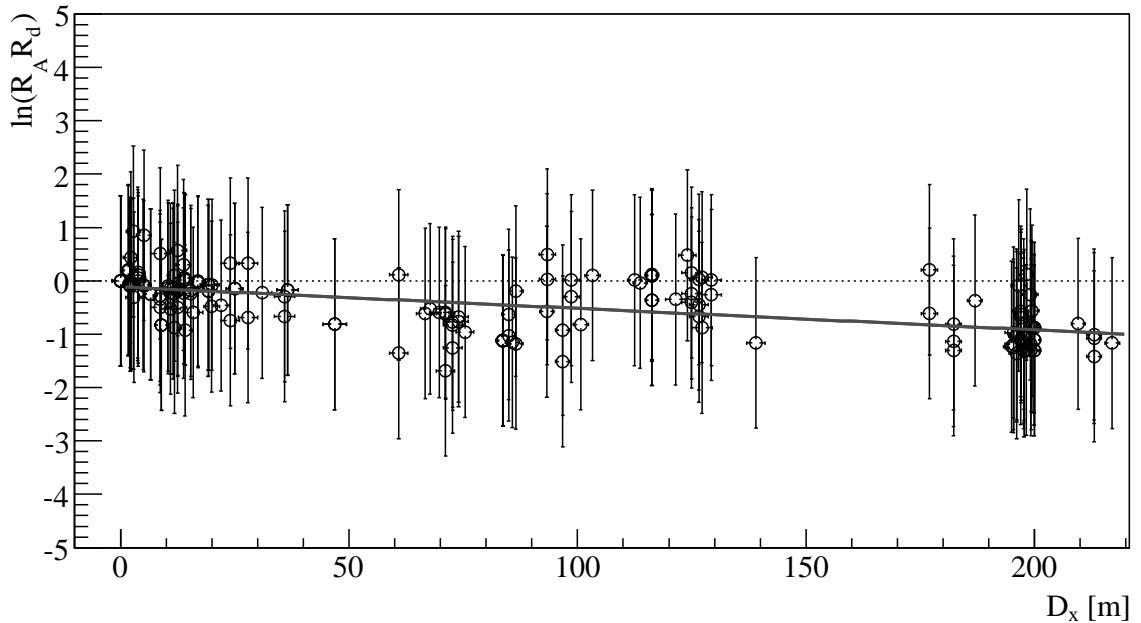
Figure 5.14: The interstring ratios for levels $(190, 250)$, $(250, 320)$ and $(320, 400)$ m as a function of $D_x = [d_{ij} - d_{il}] - [d_{kj} - d_{kl}]$. The spread on the points is an indication for the remaining polar and azimuthal systematic dependencies. This possible variation is accounted for by the introduction of a systematic error of $\pm$ 1.6 on $\ln(\mathcal{R}_A)$. The statistical error for each individual ratio is also propagated but is in general very small in comparison. The solid black line shows the 2-parameter fit as obtained by MINUIT and the dotted black line shows $y = 0$ as reference.

5.4 Conclusion

The SPATS inter-string analysis might initially seem to be completely dominated by systematic uncertainties. The azimuthal and polar behaviour of both the transmitters and the sensors introduce a large variability of the recorded pulses. In some cases, a sensor channel that is installed at a certain distance from a transmitter yields a larger (uncalibrated) signal amplitude than another channel that is much closer to the same transmitter. There are certain configurations, let's call it "detector conspiracies", where the amplitude increases with increasing distance and the same-level fit converges on a negative attenuation coefficient.

Indeed, whereas a single same-level fit or amplitude ratio theoretically should yield the attenuation length, the systematic effects prevent putting any constraint on the attenuation length, as became clear from the results for the DT4 same-level analysis.

The power of the inter-string analysis lies in the abundance of (T, S) combinations. For the combined same-level analysis, what are the odds that the sensor and transmitter modules are oriented in precisely such a way that the 9 fits would all yield a systematically too high or too low attenuation coefficient? However, the remark about being too selective in this analysis and the extreme sensitive fits casts a shadow upon the results presented in § 5.3.3.

Constructing ratios of the effective amplitudes eliminates the inherent sensitivity and transmitter power factors. However, the uncertainties due to differences in receiving and transmitting angles remain. A specific subset of data was therefore chosen, keeping the polar angle under control. The individual amplitudes for sensor channels were averaged in order to minimise the dependence of the sensor response on the azimuthal angle.

Both the same-level and the ratio inter-string analyses use subsets from the same inter-string data set but they are sensitive to different systematic effects. The same-level analysis fits amplitudes seen at different distances and from different angles with different sensor channels. Therefore those amplitudes are sensitive to the inherent sensitivity and angular dependence of the sensor channels. Also the azimuthally dependent transmitter power can influence the single amplitude measurement. No polar effects are expected if it is assumed that the ring-shaped piezo-ceramic elements are more or less aligned with the horizontal plane. The ratio method is not influenced by inherent differences in performance between the transmitters and sensors, but does include large differences in azimuthal and polar angles. The effects of correlations between the ratios and the remaining polar and azimuthal dependencies are still to be investigated.

Both analyses yield attenuation lengths on the order of 250 m. They are in agreement with each other and with an independent same-level analysis of the inter-string data presented in [167]. The inter-string attenuation length results are also compatible with the results obtained with the 2008/2009 pinger data, see for example [161].

The extracted attenuation length is unexpectedly small. Indeed, in Chapter 2 the absorption effect was argued to be the dominating attenuating effect in the South Pole ice and attenuation lengths of 9 ± 3 km were predicted. For a comparison of all attenuation length results and a discussion on the possible theoretical mechanism behind this unexpectedly short attenuation length, see Chapter 6.

Overview of SPATS results

Ice was proposed as a possible excellent candidate medium for acoustic neutrino detection. SPATS was designed to measure the three critical acoustic parameters of the Antarctic ice in the 1 kHz to 100 kHz frequency region: the sound speed, the background noise level and stability (both for transient and constant noise), and the attenuation length. In this chapter, the most recent SPATS results and their impact on the future of acoustic neutrino detection are discussed.

6.1 Background noise

6.1.1 Gaussian noise

The continuous noise is monitored in SPATS through a forced read-out at a sampling frequency of 200 kHz of all sensor channels for 0.5 s every hour. The distribution of ADC counts in each of the sensor channels is Gaussian (see Appendix. A) and stable. The typical deviation of the mean noise level is $\frac{\sigma_{RMS}}{<RMS>} < 10^{-2}$ with the exception of the period of IceCube drilling season. The in-water calibration of the string A, B and C sensors together with the pressure and temperature tests (see §4.1.1) allows to estimate the sensitivity of the SPATS sensors after they were deployed in the cold Antarctic ice.

The noise level and fluctuations are high for all 4 strings in the firn region, where the transition from a snow/air mixture to compact bulk ice takes place. This is consistent with the effect of a large sound speed gradient in that layer (see Fig. 6.2) which causes the surface noise to be refracted back to the surface. In the fully compacted ice, below the firn, noise conditions are more stable and an average noise level can be derived. This has been done with both the SPATS and the HADES sensors and the current results are currently not in agreement. Therefore, no final result can be given at this moment. More investigation and analysis are needed.

6.1.2 Transients

The SPATS detector has been operated in "transient mode"[1] for 45 minutes of every hour since August 2008. If the number of ADC counts on any of the twelve monitored channels exceeds $5.2\,\sigma_{\mathrm{noise}}$[2], a 5 ms window of data is recorded around the trigger on that channel. The resulting raw trigger rate is stable and on the order of a few triggers every minute for each of the twelve monitored channels. Most of these events are Gaussian noise events, where only one ADC bin is outside the trigger boundaries. The fraction of the triggered events that are true transient events are processed offline and analysed for time-coincidence clustering. Figure 6.1 shows the spatial distribution of a total of 4235 reconstructed transient events as detected by SPATS between 1

---

[1] The SPATS DAQ runs in "transient mode" when it records any transient event that triggers one of the selected sensor channels.

[2] σ_{noise} is the standard deviation of the Gaussian fitted to the noise ADC histogram.
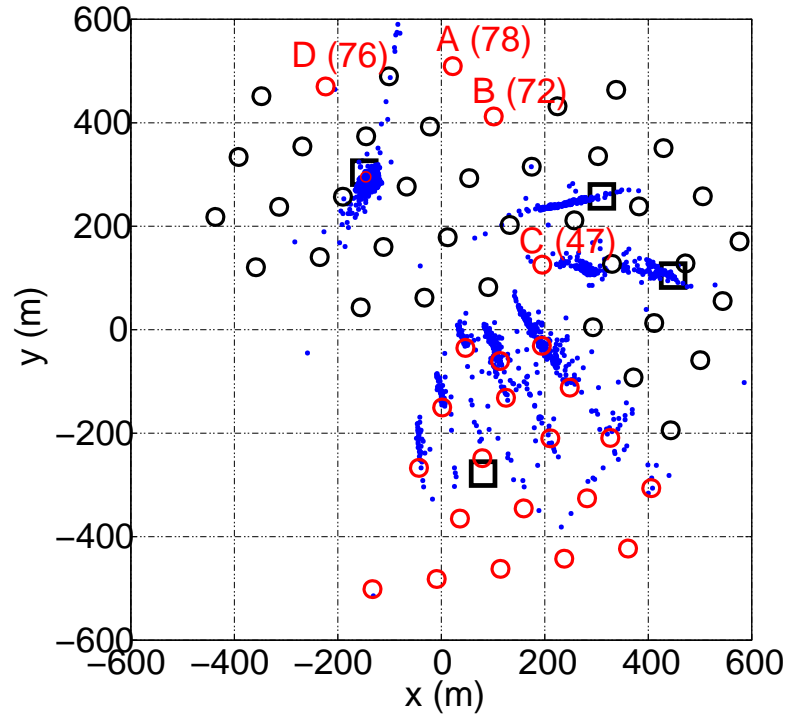
Figure 6.1: An overview of the spatial distribution of transient events as detected by SPATS between 1 September 2008 and April 2009. The regular (black and red), numbered (red) circles and open squares (black) indicate the positions of the IceCube holes, SPATS strings and "Rodriguez wells" respectively. The smearing-effect is an artefact of the event reconstruction algorithm. Figure from [167].

September 2008 and 23 April 2009 (4422 hours integrated lifetime) [167]. About 10 4-string events, meaning that at least one channel for each string has triggered on the transient event, with more than 5 sensors hit are reconstructed each day, most of which correlated to known anthropogenic in-ice sources [172]. The data shows a clear and steady source or "hot spot" that can be correlated with the man-made sub-surface cavern "Rodriguez well" (RW) that was used as a water reservoir during IceCube drilling in the 2007/2008 drilling season. This RW2007/2008 became silent in 4-string triggers around 23 May 2009 [172]. There is also likely steady detection of 2006/2007 and 2005/2006 (2004/2005) RWs. The 2008/2009 RW has not yet been detected. Transient data-taking continued during the IceCube 2008/2009 drilling season and the refreezing of 12 holes nearest to the SPATS array are audible whereas 7 of the farthest are not. No vertices have been reconstructed deeper than 400 m depth.

6.2   Sound speed

The sound speed analysis is presented in [167] and uses the 2007/2008 pinger data in geometries where the pinger and sensor are at the same depth and 125 m apart. Transit times are extracted from the data for both pressure and shear waves for all instrumented SPATS levels. Figure 6.2
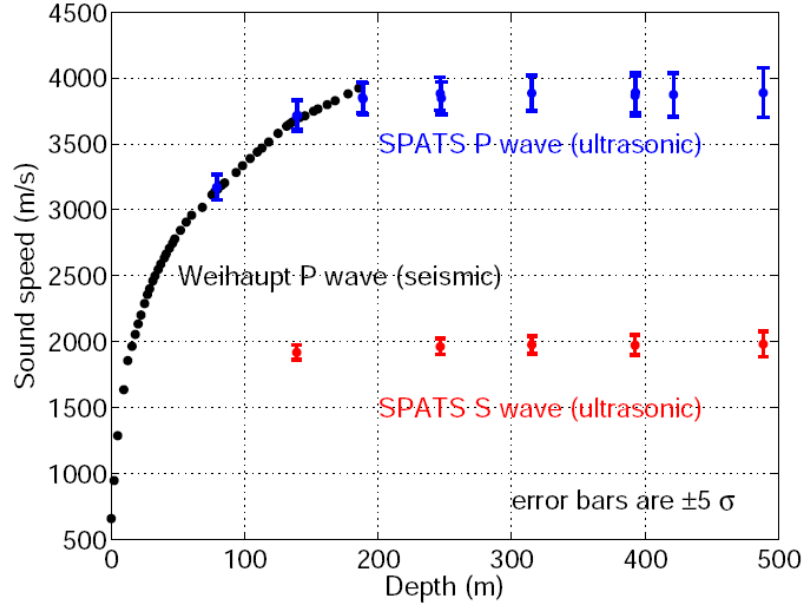
Figure 6.2: SPATS results for the sound speed of both pressure and shear waves versus depth. A previous measurement made at seismic (on the order of 1 Hz) frequencies [146] is shown for comparison. Note: the SPATS error bars are $\pm 5\sigma$ in order to be visible. No uncertainty estimate is available for the result in [146]. Figure from [167].

shows all SPATS sound speed data points for depths from 80 m to 500 m. There is agreement with [146] in the firn region for the pressure wave sound speed measurement. The extracted shear wave sound speed is about half of the pressure wave speed, as expected from the theoretical predictions presented in [147]. A linear fit was made to the data in the deep and fully compacted ice (bulk ice) between 250 m and 500 m depth. The following results were found for the pressure and shear wave sound speeds and their variation with depth (gradient g) [167, 173]:

$$v_p(375\text{m}) = (3878.3 \pm 12.2)\text{m/s},$$
$$g_p = (0.087 \pm 0.133)(\text{m/s})/\text{m},$$
$$v_s(375\text{m}) = (1975.0 \pm 8.0)\text{m/s},$$
$$g_s = (0.067 \pm 0.086)(\text{m/s})/\text{m}.$$

The gradient for both pressure and shear wave sound speeds is consistent with zero. Both sound speed measurements are performed with a better than 1% precision, taking into account the errors on the horizontal distance, pinger and sensor depths, emission and arrival times.

6.3 Attenuation length

Three types of attenuation length analyses have been performed with the SPATS array. Each of those analyses uses the same sensors, those that are permanently frozen in the ice on the four strings, but different sources. The sound sources are either the retrievable pinger, the frozen-in SPATS transmitters or the transient events. All results are also shown in Fig. 6.3.

6.3.1 Pinger

Two types of analyses have been performed on the 2008/2009 pinger data, using the energy of the full waveform calculated in the time domain and the energy calculated in the frequency domain [161, 174]. The pinger signal is recorded simultaneously by all SPATS sensors for each of the 4 IceCube holes in which it is deployed. These pinger holes are almost perfectly aligned relative to the SPATS array, making the single-channel analysis independent of polar and azimuthal sensitivity variation. The energy of the signal, which dominates in the frequency range from $5\,\mathrm{kHz}$ to $35\,\mathrm{kHz}$, is extracted both from the waveforms in the time domain and from the frequency power spectrum. For each sensor channel, a same-level fit is performed and the mean of all fits with the standard deviation as error is taken as the estimate for the attenuation length. This gives the following result for the time domain [161]:

$$\lambda = 306 \pm 64 \text{ m,} \tag{6.1}$$

and for the frequency domain energy analysis [174]:

$$\lambda = 277 \pm 89 \text{ m.} \tag{6.2}$$

There is no evidence for a depth and/or frequency dependence of the attenuation length in either analysis.

6.3.2 SPATS transmitters

Two types of analyses have been performed using the frozen-in SPATS transmitters: the same-level analysis and the ratio analysis, both presented in this thesis. Every transmitter in SPATS can be detected by 3 sensors at the same depth and different distances (strings). This means that only the unknown sensor sensitivities have to be included into the systematic error for a same-level attenuation length fit. All data of the transmitters that are recorded at minimum two different distances were fitted. Each single fit does not constrain the attenuation length very well due to the large sensor-to-sensor variations in sensitivity. By combining all fits, the resulting weighted mean and the standard deviation of the weighted mean give the attenuation length and its error [167]:

$$\lambda = 321 \pm 95 \,\mathrm{m.} \tag{6.3}$$

In §5.3.3, the same-level analysis for the same inter-string data is presented, using completely independent analysis codes. After constraining the attenuation coefficient to be positive, only 9 same-level fits remain. By combining all fits, the resulting weighted mean and the standard deviation of the weighted mean give the attenuation length and its error:

$$\lambda = 245 \pm 54 \,\mathrm{m.} \tag{6.4}$$

The ratio method was proposed as a way around the missing in-ice calibration of the sensors and transmitters. The method and results are described in detail in §5.3.4. This ratio method yields the following estimate for the attenuation length and its error:

$$\lambda = 250 \pm 100 \,\mathrm{m.} \tag{6.5}$$

Attenuation analysis	λ [m]	Error [m]	Error type
Pinger TD [161]	309	64 (9)	SD of distribution (SD of mean)
Pinger FD [174]	277	89 (3)	SD of distribution (SD of mean)
Inter-string SL (1) [167]	321	95	SD of mean
Inter-string SL (2) (this work)	245	54	SD of mean
Inter-string R (this work)	250	100	SD
Transient [172]	275	46	SD

Table 6.1: Overview of the current results from the Pinger Time Domain (TD) and Frequency Domain (FD) analysis, the Inter-string Same-Level (SL) and Ratio (R) analyses and the Transient analysis. SD stands for standard deviation.

6.3.3 Transients

A third source for attenuation length analysis in ice are the transient events (see § 6.1.2) originating from refreezing IceCube holes from the 2008/2009 IceCube drilling season. The retrievable pinger was deployed in 4 of those holes. This means that the transient events originating from the refreezing holes reach the sensors from the same direction as the pinger pulses in the 2008/2009 pinger analysis. So, the calibration constants (b as defined in § 4.3.2) can be used if the depths are comparable. To this end, transient events that have their vertex near the location of refreezing IceCube holes and for which the amplitudes in the SPATS sensors are within the dynamical range of the amplifiers, are selected. 13 of such transient events have been reconstructed, the effective amplitudes are extracted and the sensitivity correction factor is applied. Each individual transient event is then fitted and the extracted attenuation lengths are between 230 m and 400 m. The average attenuation length is [172]:

$$\lambda = 275 \pm 46 \text{ m.} \tag{6.6}$$

6.3.4 Overview and discussion

Table 6.1 and Fig. 6.3 show a compilation of the results of the SPATS attenuation length analyses. An overview of the transducer-related systematic effects is given in Table 6.2. The 2008/2009 pinger analyses are less sensitive to the systematic effects compared to the inter-string and 2007/2008 pinger data for the following reasons:

- In the pinger data, the same transmitter (pinger) is heard by the same sensor channel for 4 different distances. Therefore no inherent sensitivity or transmitter transmittivity differences need to be taken into account, assuming isotropic emission from the pinger.

- The geometry of the 2008/2009 pinger setup assures that the pinger holes are roughly aligned with the SPATS strings, the maximum azimuthal angle between different pinger holes is seen by string D and is 13°. On top of that, at the stop depths, the pinger is horizontally aligned with the SPATS stages within roughly 5 m. This means that the variation in polar angle is minimal.

- The new mechanical design of the pinger stage includes centralisers that assure a central position of the pinger piezo-ceramic element in the water-filled hole. This way, the pulse
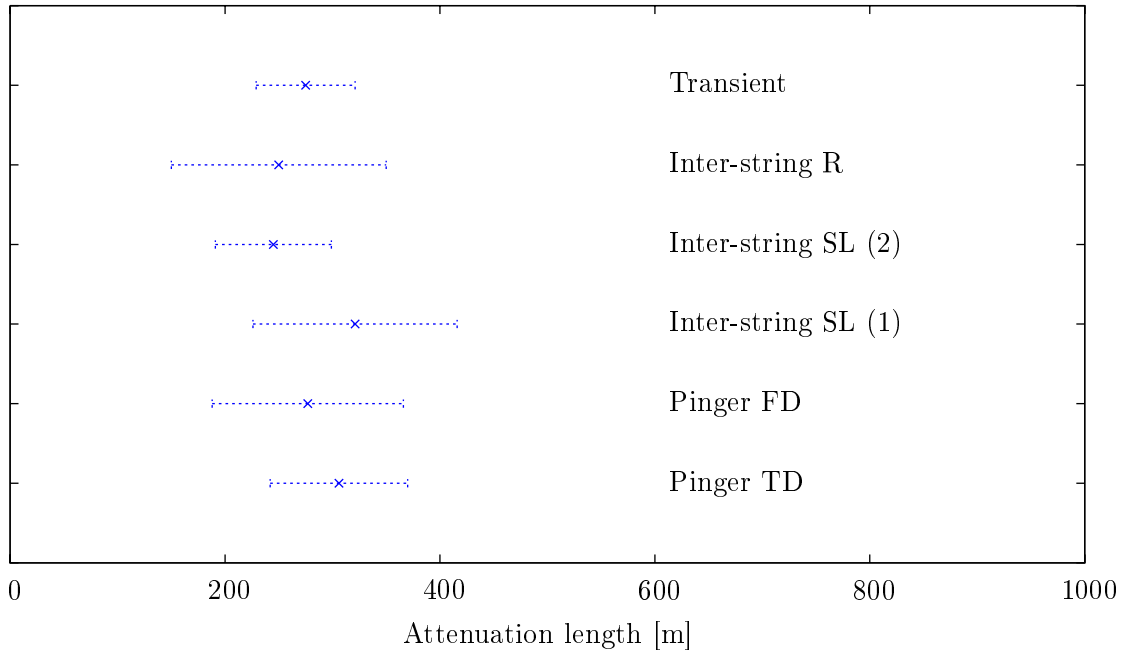
Figure 6.3: Summary of all current SPATS attenuation length analysis results. The error bars do not all represent the same type of error, see Table 6.1 for details. These results are intermediate since discussion on the precise errors and cross-checks are still ongoing.

reflecting off the back of the hole has a minimal delay compared to the main pulse. The delay is also stable. This results in reproducible pulse shapes, even between different holes. Also, the stable position of the transducer with respect to the hole wall reduces significantly the fluctuations in transmission coefficients and shear wave production at the water-ice boundary, again making the pulses more reproducible.

Therefore, compared to the other analyses that were performed on different types of data, the pinger attenuation length analysis is least subject to the various systematic effects although this is not necessarily reflected in the quoted errors. However, a few remarks on the different choice of uncertainty estimations are needed.

The agreement is that, in general, systematic effects should be identified and reduced to negligible (i.e. smaller than the random uncertainty) levels, as was done for the pinger data set after investigation of the systematic effects in the 2007/2008 pinger data. For both pinger analyses, the standard deviation (SD) of the distribution of the different single channel fits is quoted as the error on the weighted mean of the data set. This SD is a good estimator of the error on a single measurement but might be too large for the error on the mean of the distribution. Indeed, if all systematic effects have been reduced to such an extent that all sources of uncertainty are small and random, then the mean of the distribution will be better defined as more measurements (i.e. more sensor channels) are included.

However, the attenuation length is assumed to be the same for all included depths and there is indeed no significant depth dependence observed. Nevertheless, if the attenuation length

Systematic effect		P-TD	P-FD	I-SL	I-R	TR
Sensor	inherent sensitivity	no	no	yes	no	min
	azimuthal	min	min	yes	yes	min
	polar	min	min	no	yes	min
Transmitter	inherent power	no	no	no	no	no
	azimuthal	no	no	yes	yes	no
	polar	no	no	no	yes	no
External	Hole ice	min	min	yes	yes	min
	IceCube cable	min	min	yes	yes	min

Table 6.2: Overview of the systematic effects involved in the SPATS attenuation length analyses.

is depth dependent then the SD on the mean will be an underestimation of the error. The actual uncertainty on the attenuation length extracted from the pinger data is likely somewhere between the SD on the mean and the width of the distribution. The latter is therefore quoted as a conservative error on the pinger attenuation length result.

In contrast to the pinger setup, for the SPATS inter-string analyses, it is not possible to eliminate the systematic effects. However, they have been estimated using in-water calibration and pinger data. The sensor channel sensitivities and transmitter transmittivity depend on the specific geometric situation. On top of that, none of the transducers are calibrated in ice. There are indications that the orientation of the sensor module is the dominant factor in the sensitivity of a channel to a pulse arriving from a certain direction.

The same-level analysis presented in [167] and in § 5.3.3 include a systematic error due to the unknown azimuthal orientation and inherent sensitivity of the sensor channels. The quoted error is the standard deviation of the weighted mean of the attenuation lengths that were extracted for the transmitters. However, with amplitudes that are dominated by sensor orientation and sensitivity it is not straightforward to assume an underlying limiting distribution. The mean might not be better defined if more transmitters would be added.

In the inter-string ratio analysis, the inherent differences between transducers are eliminated. The variations in polar angle are kept to a minimum and the signals in the sensor channels from the same sensor module are combined. The total of the 172 ratios were fitted for the attenuation coefficient and the quoted error is the estimate for the standard deviation as returned by the MINUIT minimisation program. For both inter-string analyses, no extra systematic error was introduced to account for the possible variation in the transmitter signal due to bubbles and cracks in the hole ice or the effect of the position of the IceCube main cable.

The analysis of the transient data has the smallest quoted error of all attenuation length analyses that are presented here. The spread on the 13 measurements, after correcting for the sensor channel sensitivities b, from transients originating from different refreezing IceCube holes and depths is small. The reasonable quoted error is the estimator for the standard deviation using the calculated mean. The statistics is still low, more data might be expected from the refreezing of the 2009/2010 IceCube holes. The technique looks promising also because the transient events seem to have significant power up to 60 kHz. This might allow for the study of the frequency dependence of the attenuation length.

To conclude, all three independent types of SPATS attenuation length analyses yield results that are consistent with each other within errors. A conservative estimate for the attenuation length of acoustic pressure waves in the 5 kHz to 40 kHz region[3] in glacial ice at a temperature of $-51\,^{\circ}$C is $\lambda \sim 290\,$m with an estimated conservative error of $\pm100\,$m. There is no significant depth dependence measured in the 190 m to 500 m region. There is no frequency dependence observed in the 5 kHz to 35 kHz region. The attenuation length results presented here are intermediate since discussion on the precise errors and cross-checks are still ongoing.

If the error is interpreted as the 68% confidence limit and no systematic effect has been underestimated or missed then a 700 m attenuation length can be excluded with more than 99% certainty. Therefore, the discrepancy between the theory and the experimental result is significant. The strength of this result lies in the fact that three independent measurement methods (although all using the same sensors) have provided a set of consistent measurements.

The measured value is much smaller than the estimates presented in [150, 117] (see also §2.4.3), where an attenuation length of several km is predicted. In those predictions, the absorption due to molecular reorientation is assumed to be the dominant effect, see Fig. 6.4. The SPATS results have pushed for a new experimental investigation of the ice quality near the South Pole, using old ice cores from the SPRESO bore holes. The data are subsequently used as input for the model of scattering and absorption in ice, from which the results are presented in [151]. Strong scattering at grain boundaries is suggested but disfavoured since grain scattering increases as f^4, where f is the frequency, and there is no evidence for a frequency-correlated attenuation length measured by SPATS. The absorption of acoustic energy by dislocation lines in the ice might also account for the measured attenuation length.
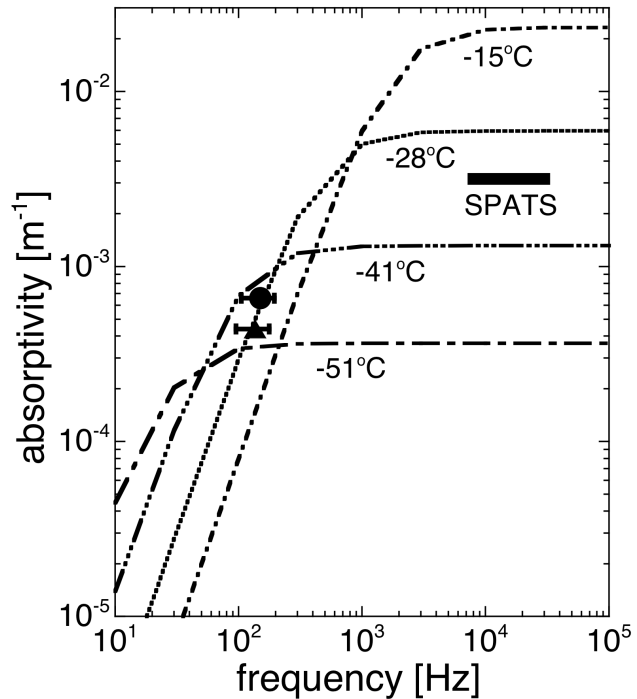
Figure 6.4: Contribution to absorptivity due to molecular reorientation in glacial ice, same as Fig. 2.13(a). The black band is the attenuation length as measured by SPATS in ice at a temperature of $-51\,^{\circ}$.

6.4 Pinger 2009/2010

A new pinger will be deployed in 3 IceCube holes during the 2009/2010 IceCube construction season. It has two main goals:

---

[3] The pinger has maximal output between 5 kHz to 35 kHz. The SPATS transmitters have a more variable frequency output roughly between 10 kHz and 60 kHz.

- The current data set does not allow a distinction to be made between absorption- or scatter-dominated attenuation length. However, elastic theory predicts that absorption is frequency independent, while scattering is expected to increase as f^4. Thus, a frequency dependent measurement would allow us to discriminate between the two cases. The old pinger design emits acoustic power strongly peaked in the 5 kHz to 35 kHz frequency band. New electronics now allows for the emission of more broadband pulses with up to 80 kHz bandwidth. The distribution of distances of the planned IceCube holes to the SPATS array and the frequency bandwidth of 100 kHz of our sensors will allow us to measure the attenuation length at different frequencies and to distinguish between constant attenuation length (absorption) and attenuation length decreasing as f^4 (scattering).

  In addition, in the next pinger runs there will be one or several stops at the shallowest instrumented depths (80 m to 140 m). In this firn region, the grain size is known to be very different from the grain size in the bulk ice below 200 m depth. Therefore, measuring the attenuation length at shallower depths is a good probe of the grain scattering hypothesis.

- No vertices for transient events are reconstructed deeper than 400 m. Whether there are no deep transient sources or if there is some mechanism that prevents us from detecting them, can be studied by lowering the retrievable pinger to deeper depths as in previous seasons. The mechanical design of the pinger allows its operation down to 1000 m depth, where the specification of the transducer is the limiting parameter. Lowering the pinger to that depth while continuously recording the signal with the SPATS sensors will allow us to distinguish between attenuation and other mechanisms that might be responsible for the disappearance of deep transient signals.

6.5   Conclusion

After 3 years of smooth data taking, SPATS is well on its way to achieve all of the initial goals. Table 6.3 gives an overview of these goals, the status of the analyses and investigations, and future plans.

Goal	Current result	Theory?	Plans
Continuous noise	Gaussian very stable level?	No final result.	Further tests and analysis are needed.
Transient noise	Low raw rates $< 1\,\mathrm{Hz}$. anthropological sources identified, no surface noise. No events below $400\,\mathrm{m}$?	Within expectations.	Include more channels? New DAQ? Go to $1000\,\mathrm{m}$ with new pinger.
Sound speed	$v_p = (3878.3 \pm 12.2)\mathrm{m/s}$ $v_s = (1975.0 \pm 8.0)\mathrm{m/s}$, gradient $= 0$.	Consistent with theory and other in-situ experimental results.	Publication in preparation.
Attenuation	$\lambda \sim 290$ with a conservative error of $\pm 100\,\mathrm{m}$.	Inconsistent w. theory. Scattering/absorption?	New pinger runs to investigate frequency dependence. Publication in preparation.

Table 6.3: The status of the SPATS analyses.

Discussion and outlook

Currently, one of the main objectives in the neutrino astrophysics community is to detect, or to put challenging limits on, the flux of UHE neutrinos. These neutrinos are considered ideal astrophysical messengers as they travel on straight paths from their source to Earth, carrying information about the – still mysterious – hadronic accelerators in the Universe or about the GZK process. Their main advantage, the fact that they rarely interact with matter, also translates to the main experimental challenge in neutrino astrophysics. Indeed, detection of neutrino interactions requires observation of a large volume of detector medium. We have seen that the expected fluxes for the UHE neutrinos, both created at the hadronic astrophysical accelerators and from interaction of the charged CRs with the CMB, are very low. Even IceCube, currently the largest neutrino detector, will likely only skim the relevant energy and flux regions. New detection methods, detecting the radio and acoustic signatures produced by the UHE neutrino interactions, are needed in order to instrument at a reasonable cost the required large volumes of detector medium.

In this work, the investigation of the feasibility of acoustic neutrino detection in the South Pole ice with the South Pole Acoustic Test Setup (SPATS) was presented. The aim of SPATS is to measure the acoustic properties of the ice in the relevant frequency region and at the relevant depths so that the optimal detector design and resulting sensitivities to neutrino fluxes can be predicted. The current SPATS results confine the future design of an acoustic neutrino detection array in the South Polar ice:

- **Sound speed**
  The SPATS sound speed result is in agreement with theoretical predictions and previous in-situ experimental results. The sound speed gradient in the South Pole ice below 200 m is consistent with zero, so that the acoustic waves will not be refracted while propagating in the bulk ice. As a result, the location of an acoustic source can be reconstructed quickly and precisely using analytical methods. The pancake-shaped pattern that originates from the neutrino-induced cascades in the ice will also remain intact and can be used as a way to recognise a neutrino signature. The neutrino arrival direction could then be estimated by fitting a plane to the hit sensors. Also, if both a pressure and a shear wave pulse are generated by a neutrino interaction in the ice, and they are both also detected by a single acoustic sensor, then the time difference between them can be used to estimate the distance to the source, and from this the neutrino energy, with a single sensor.

- **Transient noise**
  Transient noise events originate mainly from known fixed sources and the rate is very low compared to ocean environments. Currently, no vertices have been reconstructed deeper than 400 m depth. The low transient rate could simplify the neutrino event candidate selection.

- **Attenuation length**

  The acoustic attenuation length in ice measured by SPATS is much smaller than predicted by theory. This has a large impact on the geometry of a possible future acoustic neutrino detector since the horizontal distances will need to be much smaller than initially foreseen and simulated. This means that the acoustic detection technique is not as economically advantageous as was assumed at first. In the hybrid detector design presented in § 1.4.4, the radio/acoustic strings are placed 1 km apart while the acoustic attenuation length was assumed to be on the order of kms, not ~ 290 m. In the light of the experimentally determined attenuation length, this simulated hybrid detector is now too sparsely instrumented in order to achieve the necessary sensitivities. Other acoustic array designs are possible and have been simulated, although these might be less easy to combine with a radio array.

  The result of recent simulations shows that an acoustic addition to a radio GZK detector with overall spacing of 500 m could give valuable information to confirm radio observations [175].

- **Gaussian noise**

  The continuous noise has been proven to be Gaussian and very stable. There is no influence from on-ice activity or ambient temperature. A stable noise level allows for a fixed trigger level and easier analysis of transient events and possible neutrino candidates.

  There is no consistent result yet on the absolute level of the continuous background noise in the bulk ice at South Pole. It is therefore too early to conclude, although current results point towards higher levels than initially expected. The absolute noise level sets the possible trigger level for a certain design of an acoustic array and therefore directly influences the energy threshold. High noise levels strongly disfavour self-triggering acoustic neutrino detector designs.

The SPATS transient rate and vertex location as well as the sound speed gradient results are favourable to acoustic neutrino detection in ice, also compared to the ocean as detector medium. However, the attenuation length λ is significantly lower than the theoretically predicted value and no final results are available for the absolute noise levels. The anticipated long attenuation length was one of the main appeals of the acoustic neutrino detection technique since the distance between instrumented cables is directly influenced by the attenuation of the signal in the ice. Also, a low continuous background noise level implies a better general signal-to-noise ratio. This means that the more silent the medium, the lower the energy threshold.

Do the presented SPATS results, and more specifically the presented short attenuation length, mean the end of the ambition to detect the acoustic signal of UHE neutrino interactions in ice? At this point, in the light of the latest SPATS results, it is too early to draw such a final and global conclusion. If the attenuating effect is scattering off grain boundaries, then the acoustic energy is not lost, only redirected. This effect might again increase the sensitivity of an acoustic array. If absorption is the dominant effect, then the acoustic energy is converted and therefore lost. In the next polar season, a new set of pinger runs will allow us to discriminate between these two options. It is, however, already clear that the attenuation length is too small to foresee a stand-alone, self-triggering acoustic array within a reasonable cost- and time-scale.

On the other hand, the hybrid idea remains powerful, since a fast trigger given by the radio detector can force the read out of the much slower acoustic signal. Still, the optimal hole spacing for such a radio detector does not coincide with the acoustic needs. In addition, current designs

of IceCube centred radio detectors foresee only shallow holes ($< 200\,\mathrm{m}$ deep) which is not ideal for the acoustic detection.

SPATS will continue by focussing on the remaining hurdles. The first challenge lies in the understanding of the mechanism behind the short attenuation length. Second, the absolute noise level in the ice needs to be estimated. On top of that, the detector will continue to run in transient mode (with the exception of dedicated pinger runs), possibly extending the amount of channels that are read out simultaneously. The transient data can be used to extract a limit on the UHE neutrino flux, the power of which depends on the absolute noise level. In any case, SPATS was not designed as a neutrino detector and the limit is not expected to constrain any realistic neutrino flux model.

In the end, while contemplating the SPATS achievements, one can but appreciate the vast amount of understanding of the South Pole ice acoustic environment that was gained with the total of the SPATS tests and measurements. We were able to confirm certain, and contradict other, theoretical predictions by producing the first ever experimental results for the acoustic attenuation length and both the pressure and shear wave sound speeds in the South Pole bulk ice. Clearly it has been an adventurous trip, filled with , sometimes surprising, discoveries, to be continued with new experimental data-taking and insights.

SPATS noise levels

In this appendix, the noise-histogram for each sensor-channel is shown for a total of roughly 10^6 ADC counts (about $5\,\text{s}$ at $200\,\text{kHz}$). There are 21 histograms for each string, ordered in 7 rows and 3 columns. The rows are the sensor-modules from the most shallow stage to the deepest one from top to bottom. Each column corresponds to an FADC board (i.e. to a sensor channel): board 0, 1 and 2 from left to right. This is a snapshot taken on 20 August 2009. Appendix B shows the evolution, over the complete lifetime, of the standard deviation σ of the Gaussian fitted these noise ADC histogram for each channel.

A.1 String-A

Figure A.1: String-A noise histograms for all channels. The sensor module at 190 m depth (level 3, third row) has one saturated channel and therefore the entire sensor module is unusable.

A.2 String-B

Figure A.2: String-B noise histograms for all channels. Channels BS1-2 and BS4-2 have a slighly asymetric behaviour. This might be a feature of the FADC board 2 of string B.

A.3 String-C

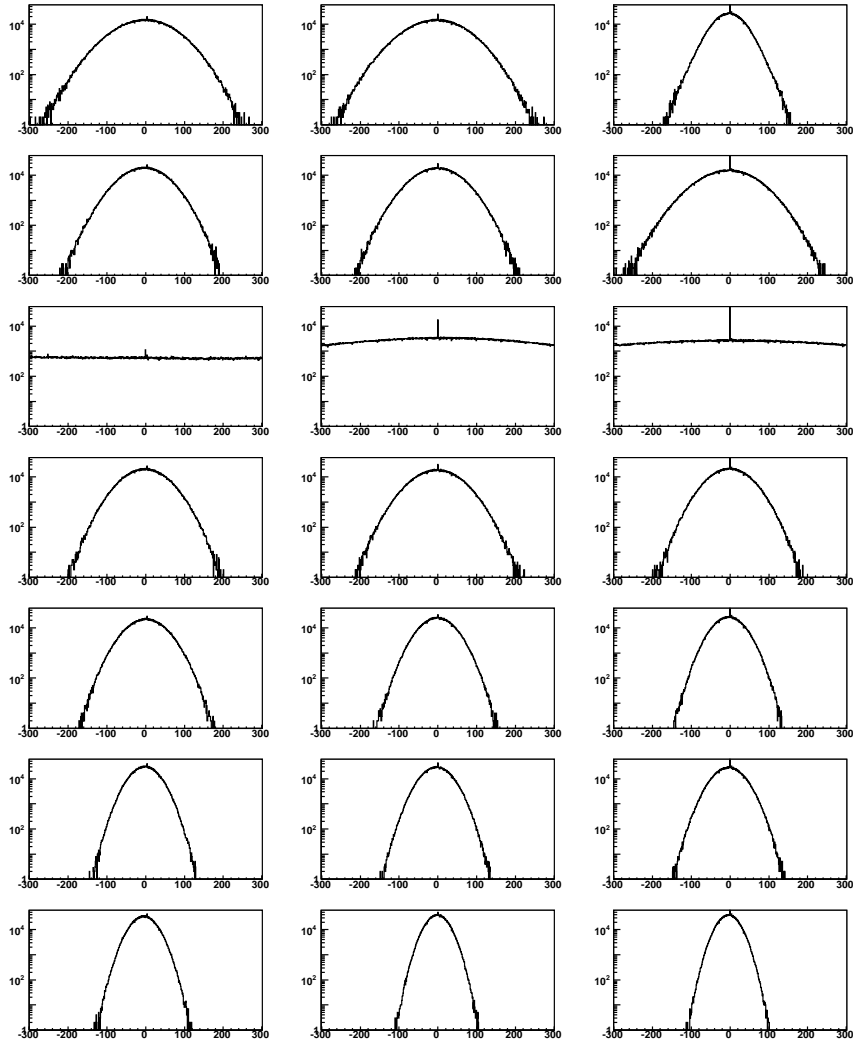**Figure A.3:** String-C noise histograms for all channels. The sensor module at 80 m depth (level 1, top row) has one saturated channel and therefore the entire sensor module is unusable.
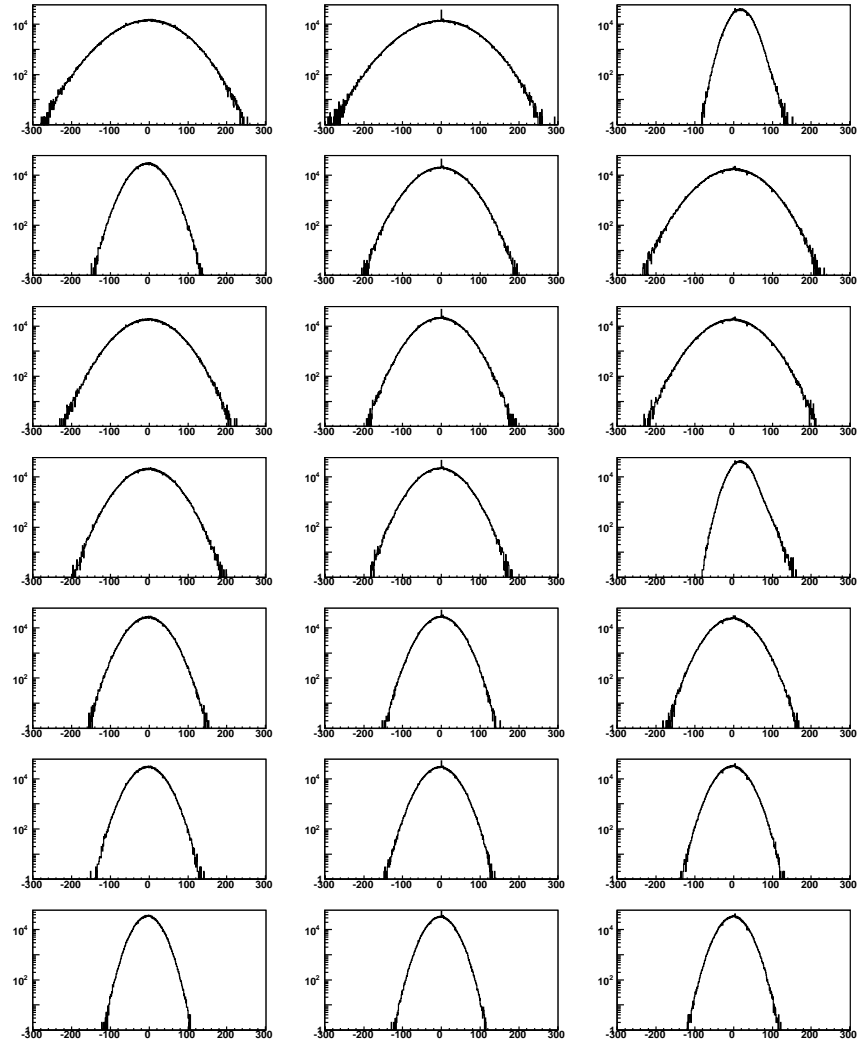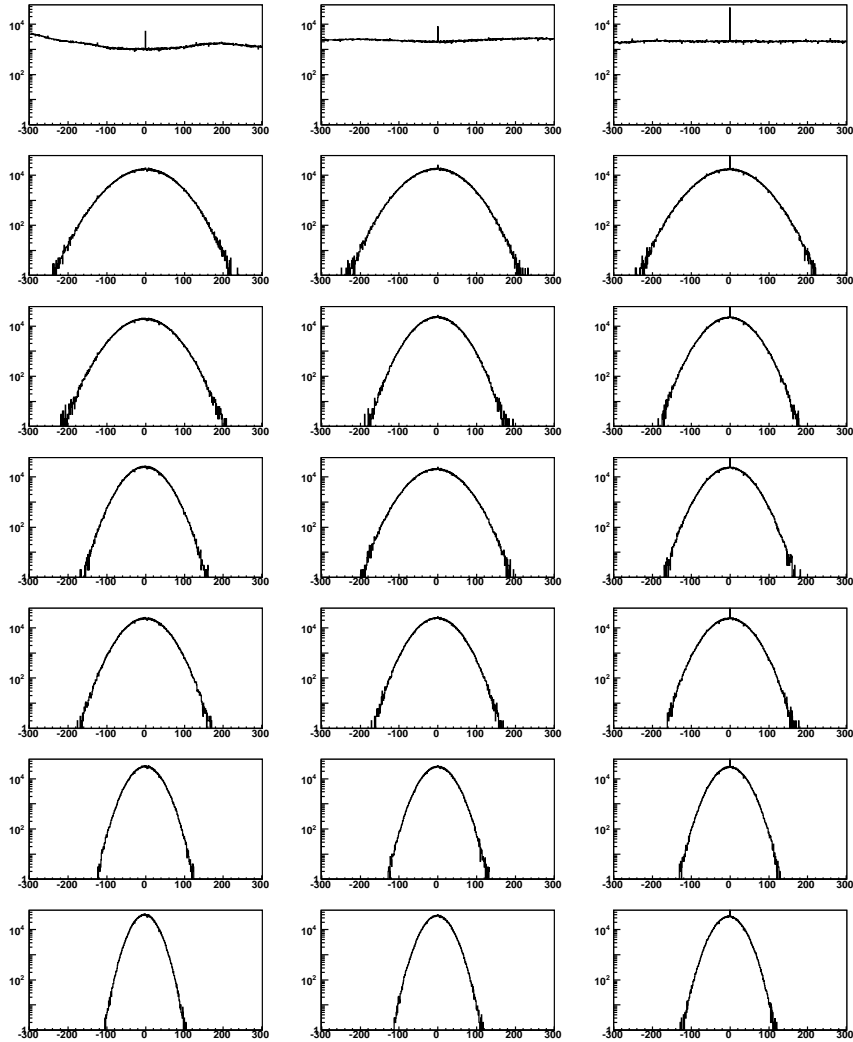
A.4 String-D
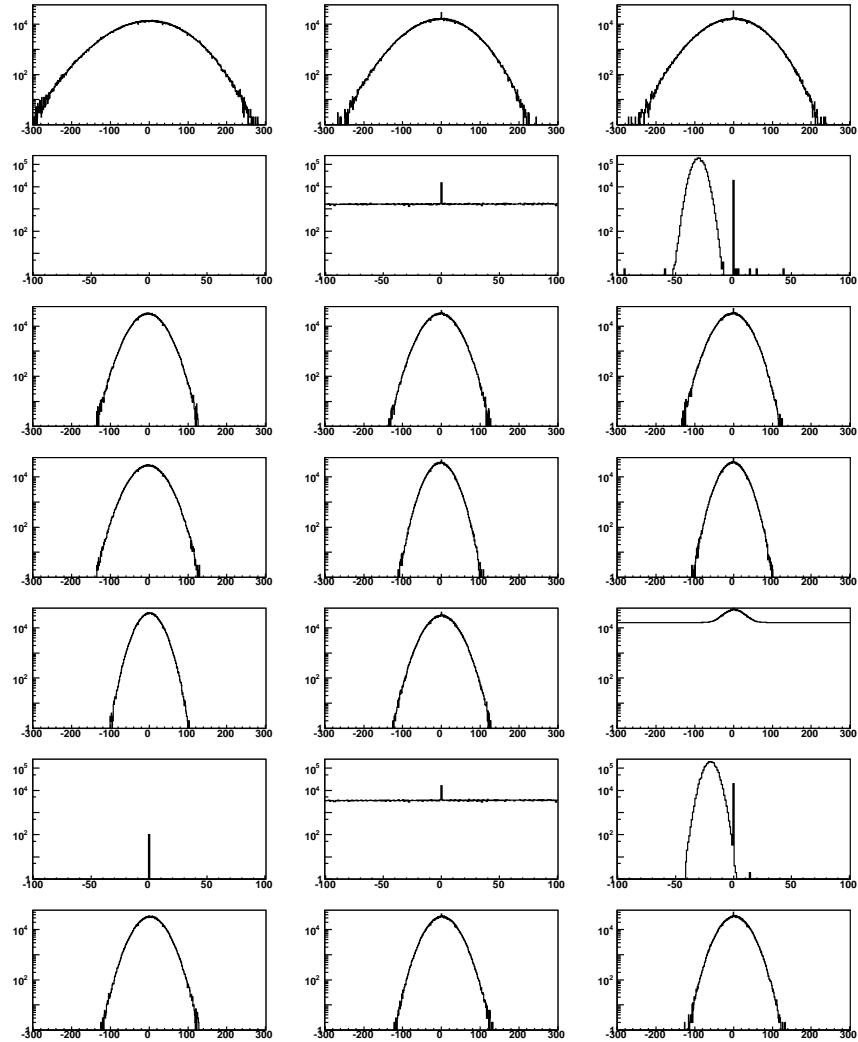
Figure A.4: String-D noise histograms for all channels. The HADES sensors have a single channel and are deployed at positions DS2 (190 m depth) and DS6 (430 m depth). Channel DS5-2 has an unknown problem.

SPATS noise evolution in time

In Appendix A, a single noise ADC histogram is shown for each SPATS sensor channel. This histogram data is recorded at least once ever hour. The standard deviation σ of a Gaussian fitted to such a noise histogram can be used as an indicator of the noise level in that sensor channel. In this appendix, the σ is plotted as a function of time for each sensor-channel. There are 7 graphs for each string, ordered in 7 rows. The rows are the sensor-modules from the most shallow stage to the deepest one from top to bottom. Each colour corresponds to an FADC board (i.e. sensor channel): board 0 in red, board 1 in green and board 2 in blue. For strings A, B and C, the noise-histogram data-taking started in July 2007. String-D has data from its deployment in December 2007. The 2007/2008 drilling season is clearly visible on all strings.

The noise-levels are more erratic before that drilling season since the sensors were powered on and off contineously. The 2008/2009 drilling season is less clearly visible. Two reasons for this are possible. First, the IceCube drilling took place at a larger distance from the SPATS array than in the 2007/2008 drilling season. Indeed, string C, which was positioned closest to the 2008/2009 IceCube drilling site, does show an increase in noise levels. The other strings only show a much smaller effect. Second, for the 2007/2008 drilling season, only 1 point/hour is plotted in contrast to 1 point/5 min for the 2007/2008 drilling season.

B.1 String-A
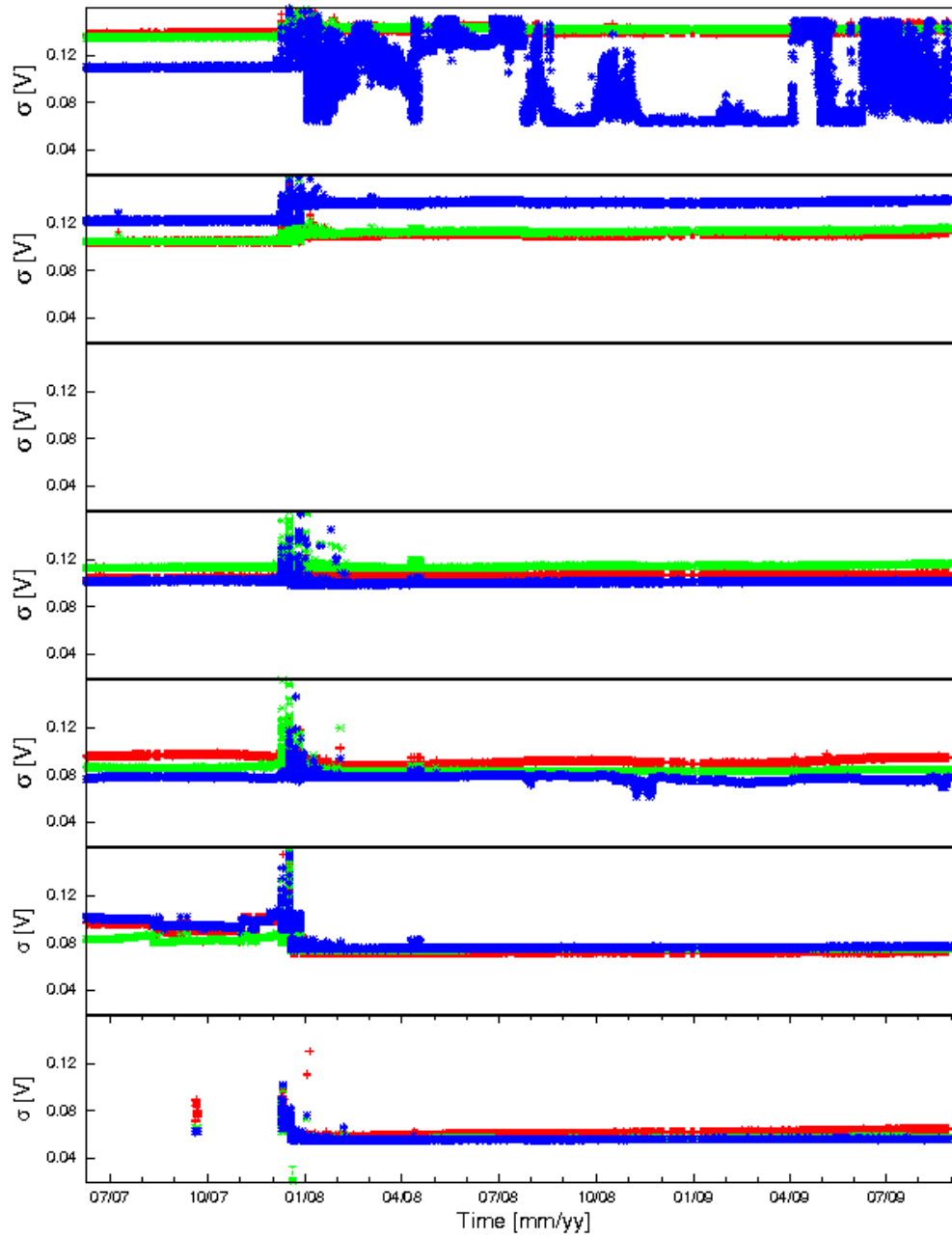
Figure B.1: String-A noise evolution for all channels.

B.2 String-B
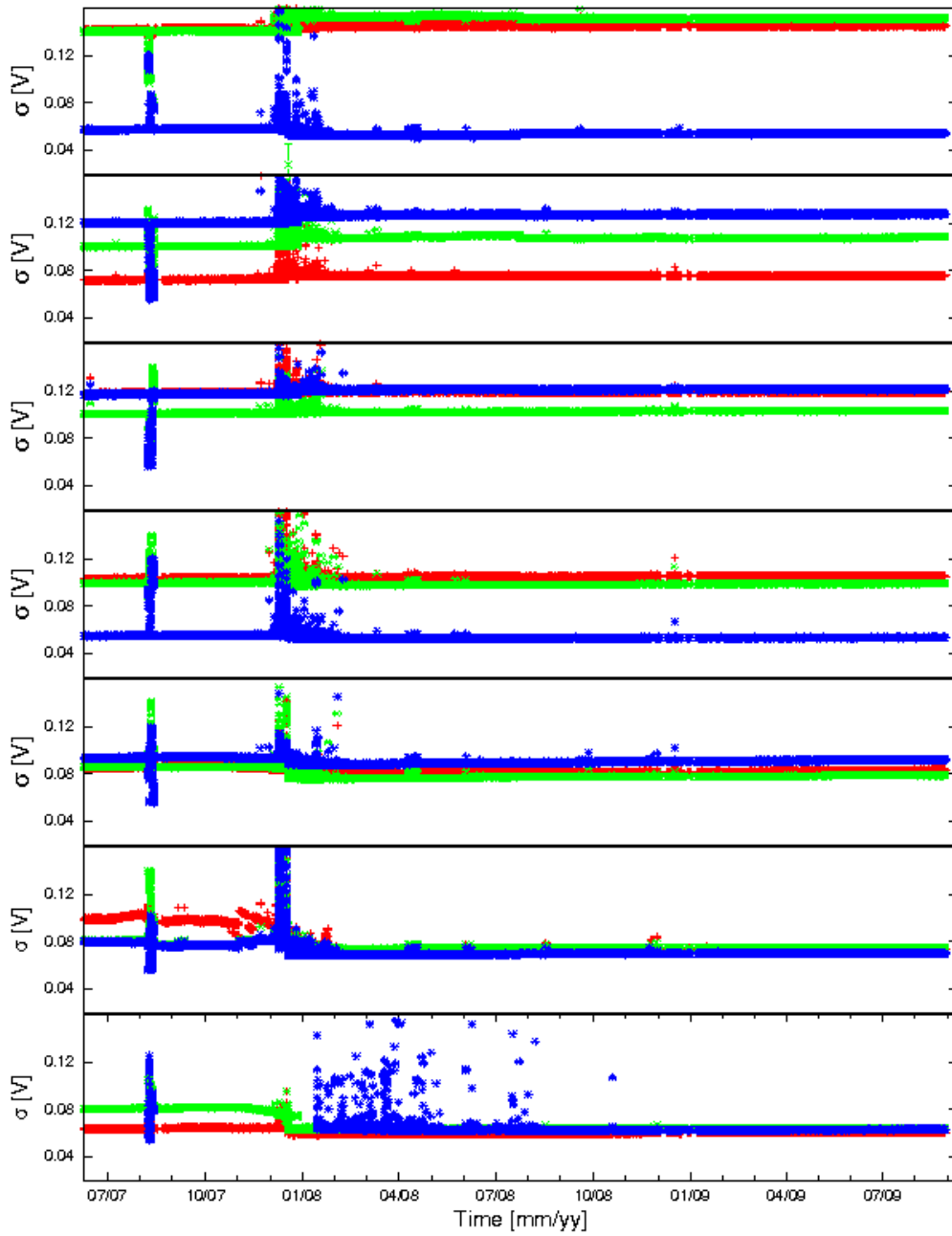
Figure B.2: String-B noise evolution for all channels.

B.3 String-C
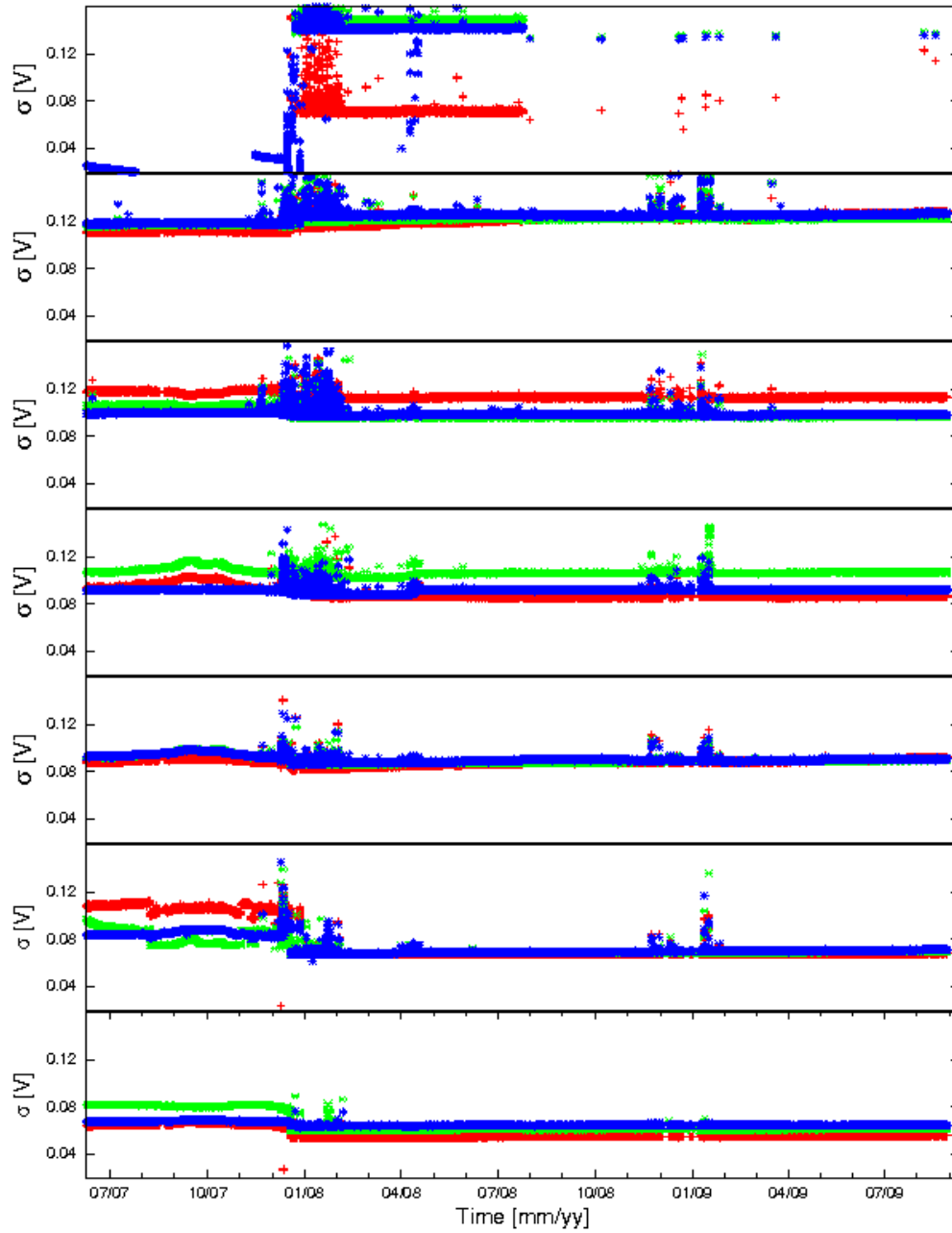
Figure B.3: String-C noise evolution for all channels.

B.4 String-D
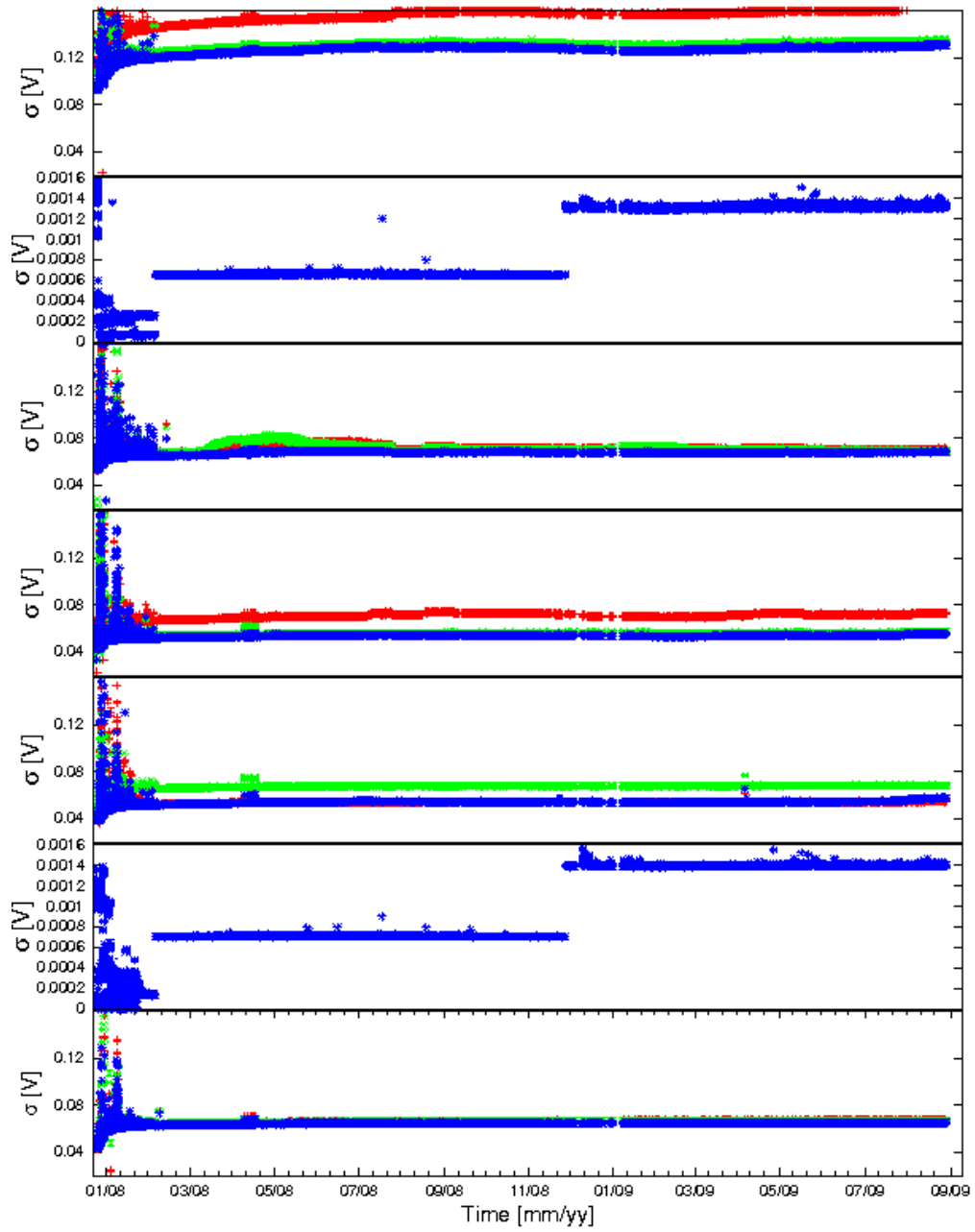
Figure B.4: String-D noise evolution for all channels. The gain setting was changed for the HADES channels at two occasions.

Transmitter results of the Abisko SPATS test

C.1 Transmitter variability
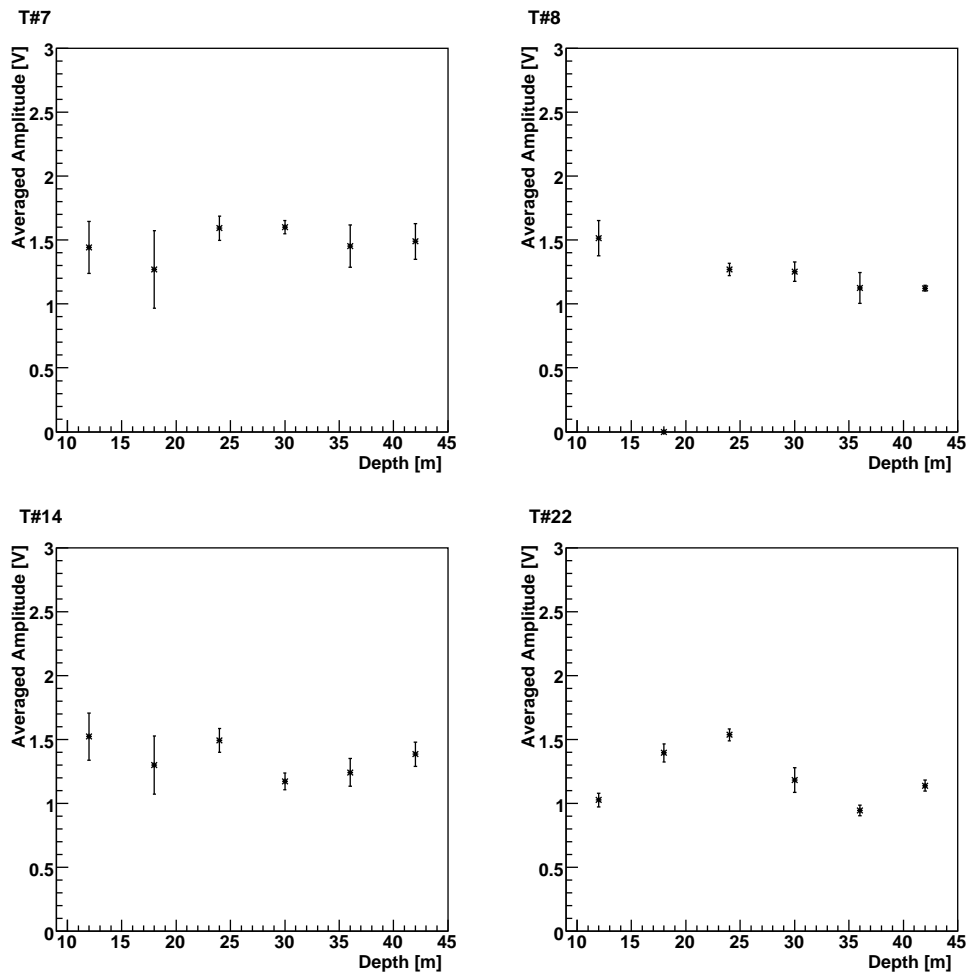
Figure C.1: The transmitter module variability in the Abisko SPATS test. Transmitter amplitudes averaged over 10 recorded events as a function of depth. The error bars are the standard deviation of a single measurement. The sensor was located at a distance of 400 m and at a depth of 30 m.

C.2 Transmitter-piezo variability
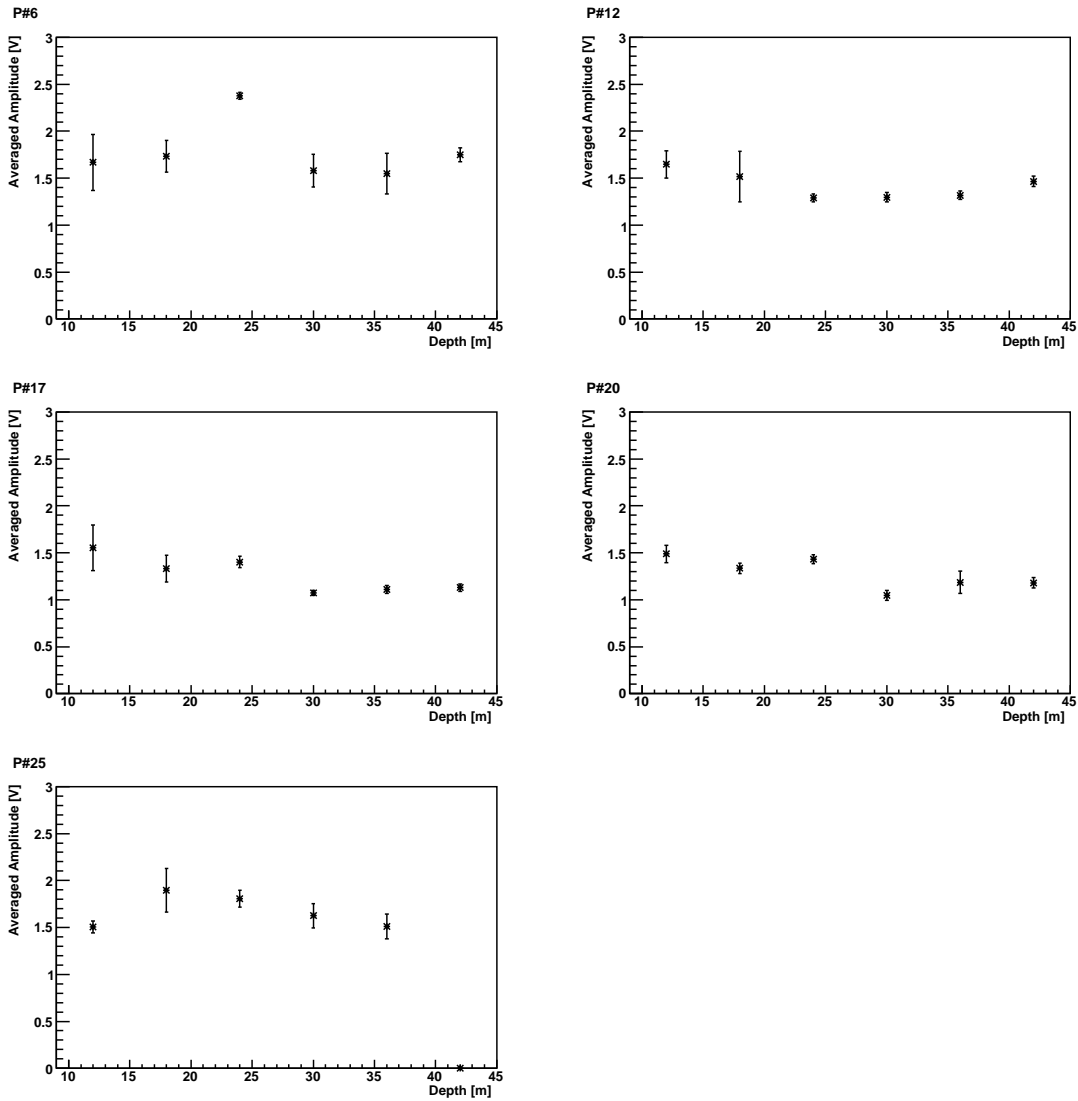
Figure C.2: The transmitter piezo-ceramic element variability in the Abisko SPATS test. The amplitudes are averaged over 10 recorded events at each depth. The error bars are the standard deviation for a single measurement. The sensor was located at a distance of 400 m and at a depth of 30 m.

Nederlandstalige samenvatting

Motivatie

Kosmische straling is gedefinieerd in dit werk als alle deeltjes (geladen of niet) die vanuit de kosmos op de atmosfeer van de aarde invallen. De ontdekking van deze straling wordt meestal toegekend aan V. F. Hess, nadat hij aan de hand van ballonvluchten in 1912 het bestaan van sterk doordringende geladen straling in de atmosfeer had aangetoond. Bijna een eeuw na de eerste ballonvlucht van Hess, is het spectrum van geladen kosmische straling gemeten over meer dan 28 grootteordes in flux en 13 grootteordes in energie. Het is een bijna structuurloos spectrum volgens $\frac{dN}{dE} \sim E^{\gamma}$, waarbij $\frac{dN}{dE}$ de differentiële flux is, E is de energie van de kosmische straling en γ is de spectrale index.

Verscheidene theorieën bestaan die de productie van dergelijke hoog-energetische kosmische straling modelleren. Deze modellen kunnen opgesplitst worden in twee soorten: de zogenaamde "bottom-up" modellen en de, meer exotische, "top-down" modellen. In de bottom-up modellen worden geladen deeltjes versneld tot hun uiteindelijke energie aan de hand van elektrische en magnetische velden: dit zijn de versnellingsmodellen. Aan de andere kant gaan de top-down modellen ervan uit dat de hoog-energetische deeltjes die we hier observeren de producten zijn van verval van deeltjes met nog hogere energie, zoals bijvoorbeeld topologische defecten.

Het spectrum van de geladen kosmische straling bevat 3 transitieregio's. De spectrale index gaat van -2.7 tot -3.1 tussen 10^{15} en 10^{16} eV, deze regio is genaamd de knie. Een verdere daling in spectrale index zou kunnen geassocieerd worden met een tweede knie voor energieën rond $4 \cdot 10^{17}$ eV. Bij de zogenaamde enkel tussen 10^{18} en 10^{19} eV gaat de spectrale index terug naar -2.7, deze kosmische straling heeft ultra hoge energie (UHE).

Het geheel van de data beschikbaar op dit moment lijkt te wijzen op een standaard model voor de kosmische straling. De metingen zijn in overeenstemming met de aanname dat de deeltjes tot aan de knie van galactische origine zijn, versneld in schockfronten van, bijvoorbeeld, restanten van supernova's. Het ten einde lopen van de versnellingsmogelijkheden van de galactische bronnen is een mogelijk mechanisme achter het steiler worden van het spectrum bij de knie. De galactsche kosmische deeltjes die versneld worden tot hoge energieën kunnen ook ontsnappen uit ons Melkwegstelsel en dit draagt ook bij tot de daling van de spectrale index bij de knie. Tussen de knie en de enkel is er mogelijk reeds een overgang van galactische deeltjes naar extragalactische kosmische straling. De algemene consensus is dat de deeltje voorbij de enkel van extragalactische origine zijn. Er bestaat echter nog geen sluitende experimenteel bewijs in verband met de preciese herkomst en samenstelling van de UHE kosmische straling. Zowel de P. Auger Observatory (PAO [27]) als de HiRes [26] detectors hebben het steile einde van het spectrum rond $4 \cdot 10^{19}$ eV experimenteel vastgesteld in 2007/2008.

Een mechanisme achter het beëindigen van het spectrum van de kosmische straling werd voorgesteld in 1966 door Greisen, Zatsepin en Kuz'min (GZK, zie [36, 37]). De zogenaamde GZK-grens wordt gevormd door de interactie van de UHE geladen deeltjes met de laag energetische fotonen van de kosmische microgolf achtergrondstraling (CMB). Inderdaad, de hoog energetische protonen kunnen interageren met de CMB fotonen via de Bethe-Heitler (BH) e^+e^- paar productie:

$$p + \gamma_{\mathrm{CMB}} \rightarrow p + e^+ + e^-, \tag{C.1}$$

en ook via pion productie processen, bijvoorbeeld via de Δ^+-resonantie [38]:

$$p + \gamma_{\text{CMB}} \rightarrow \Delta^+ \rightarrow N + \pi, \tag{C.2}$$

waar de finale staat $p+\pi^0$, $n+\pi^+$, $p+\pi^+ + \pi^-$, enzovoort, kan zijn. De zwaardere atoomkernen verliezen energie via foto-desintegratie. De neutrale mesonen vervallen dan in fotonen, terwijl de geladen mesonen vervallen in, onder andere, neutrino's. Deze voorspelde GZK neutrino flux wordt vaak de gegarandeerde neutrino flux genoemd. De precieze fluxgrootte varieert met meer dan een grootteorde tussen verschillende modellen en hangt af van de samenstelling van de UHE kosmische straling. Inderdaad, een puur proton samenstelling levert een veel hogere flux rond 10^{18} eV dan een gemengd proton en ijzer samenstelling. Het zetten van limieten op, of de detectie van, de GZK flux kan een waardevolle bijdrage leveren in het onderzoek naar de samenstelling van de UHE geladen kosmische straling. Er bestaan ook andere mogelijke bronnen voor neutrino's, zowel in ons eigen Melkwegstelsel als extragalactisch. De voorspelde fluxen van deze bronnen variëren enorm en veel modellen zijn reeds uitgesloten door huidige waarnemingen [54, 50]. Vanuit alle huidige neutrinoflux modellen is het reeds duidelijk dat de verwachtte flux op aarde zeer klein is.

Een neutrino interageert via diep inelastische botsingen met een nucleon uit het doelwitmateriaal met als eindproducten een neutrino of een geladen lepton, telkens met een hadronisch overshot. Voor hoge energieën zal de hadronische cascade steeds ongeveer 20% van de initiële energie meekrijgen.

Een hoog-energetisch neutrino dat interageert in een detectormedium heeft drie mogelijke detecteerbare signalen:

- **Optische golven**
  Geladen deeltjes zenden Cherenkov straling uit indien ze sneller gaan dan de lichtsnelheid in dat medium. Dit licht kan dan opgevangen worden met lichtvermeningvuldigingsbuizen (PMT). Voor een UHE neutrino interactie zijn er dus twee mogelijke optische signalen: een spoor van licht uitgaande van een enkel deeltje en een meer uitgestrekt lichtsignaal van de kaskade van deeltjes.

- **Radio golven**
  Een netto lading in de elektromagnetische kaskade zorgt voor een coherent radio Cherenkov effect dat eventueel kan opgevangen worden door antenna's.

- **Akoestische golven**
  Een hoog-energetische cascade zal lokaal en ogenblikkelijk het detectormedium opwarmen en zodoende een drukgolf creëren die eventueel kan opgevangen worden met akoestische sensoren. De mogelijkheid van het detecteren van UHE neutrino's aan de hand van het akoestische signaal dat ze bij interactie creëren is het onderwerp van dit proefschrift.

De zwakheid waarmee neutrino's interageren heeft een belangrijk gevolg voor de detectie ervan: men heeft enorme hoeveelheden detectormateriaal nodig om een redelijk aantal interacties per jaar te observeren. Er wordt dan ook vaak gebruik gemaakt van natuurlijke reservoirs, zoals bijvoorbeeld meren, zeeën en Zuidpoolijs. Er zijn reeds heel wat neutrino detectors operationeel of onder constructie. Een groot deel daarvan bestaan uit een rooster van PMT's in een bepaald optisch transparant natuurlijk medium, zoals zeewater of ijs. De huidige data bestaat enkel uit

atmosferische neutrino's. Het kan dan ook gesteld worden dat de optische Cherenkov detecti-etechniek zeer goed begrepen en getest is. De radiotechniek heeft reeds verscheidene projecten lopen in en op het Antarctische ijs.

IJs is een ideale kandidaat voor de bouw van een hybride detector die gebruik maakt van de drie detectietechnieken. IceCube, de eerste neutrinotelescoop op kilometerschaal met optische detectormodules, wordt momenteel geconstrueerd in het Antarctica-ijs [48]. IceCube zal echter naar schatting maar 1 UHE neutrino per jaar observeren. Simulaties en onderzoek hebben dan ook geleid tot het ontwerp van een veel grotere, zogenaamde hybride detector [88, 108]. De hybride detector zou de drie detectiemethodes combineren door IceCube, die alleen bestaat uit optische modules, uit te breiden met akoestische detectoren en radioantennes. Een veel groter volume van ongeveer $100\,\mathrm{km}^3$ zou zo met een redelijk beperkt aantal nieuwe detectoren (en dus tegen een redelijke kostprijs) bereikt worden.

De mogelijkheid van detectie van het akoestische signaal dat uitgezonden wordt door een cascade van geladen deeltjes in water is eerst geopperd door G. A. Askaryan in 1957 [110]. Ondertussen zijn er reeds vele referenties die de akoestische signalen berekenen of simuleren afkomstig van de cascades veroorzaakt door de interactie van UHE neutrino's in water en ijs. Een dergelijke akoestisch signaal heeft volgende eigenschappen:

- De drukgolf heeft een bipolaire vorm en de lengte is afhankelijk van de radiale uitgestrektheid van de cascade en van de geluidssnelheid in het medium. In ijs, de verwachtte frequentie-inhoud is gemiddeld $40\,\mathrm{kHz}$.

- De amplitude is lineair afhankelijk van de energie bevat in de cascade.

- Het akoestische veld heeft een zogenaamde pannenkoekvorm: de amplitude is het grootst in het vlak loodrecht op de as van de cascade.

Verscheidene experimenten hebben reeds het thermoakoestische model getest door middel van deeltjesversnellers. Ook aan de universiteit van Gent werd er in 2006/2007 een experimentele opstelling verwezenlijkt ter verificatie van het thermoakoestische model in water. Hierbij werd er een elektronbundel op een vat met water gericht. In een eerste instantie werd de gedeponeerde dosis opgemeten en ook gesimuleerd. Aan de hand van deze simulatie werd dan het akoestische signaal voorspeld. Een commerciële hydrofoon werd vervolgens in het akoestische veld geplaatst en het geobserveerde signaal was in redelijke overeenstemming met de gesimuleerde puls.

De akoestische detectietechniek bevind zich echter nog in kinderschoenen. De akoestische eigenschappen van ijs veelbelovend zijn voor deze detectie techniek. Inderdaad, de voorspelde dempinglengte is $9 \pm 3\,\mathrm{km}$, het geluidsniveau is mogelijk lager dan voor oceanen. Daarom was de South Pole Acoustic Test Setup (SPATS) ontworpen. Deze detector heeft de voorbije 3 jaar de akoestische eigenschappen van de eerste $500\,\mathrm{m}$ van de ijslaag aan de geografische Zuidpool in het relevante frequentie-interval onderzocht.

SPATS

SPATS (South Pole Acoustic Test Setup) is ontworpen in functie van het onderzoek van de akoestische eigenschappen van het Zuidpoolijs. The permanent geïnstalleerde hardware bestaat uit 4 verticale geïnstrumenteerde kabels, genaamd strings. Ze zijn geïnstalleerd in de bovenste $500\,\mathrm{m}$ van geselecteerde IceCube gaten zodat een trapezoïdale geometrie wordt bekomen. De

maximale afstand tussen twee strings is 543 m tussen string C en string D. Strings A, B en C hebben akoestische stations op 80, 100, 140, 190, 250, 320 and 400 m diepte. String D heeft geïnstrumenteerde niveaus op 140, 190, 250, 320, 400, 430 and 500 m diepte.

Een akoestisch station bestaat uit een zendermodule en een sensormodule. De zendermodule heeft een stalen drukbestendig vat waarin de electronica zit die toelaat een korte puls met hoge elektrische spanning (high voltage, HV) te genereren bij het ontvangen van een triggersignaal. Er is ook een temperatuur- of druksensor in elke zendermodule. De gegenereerde HV pulsen worden gestuurd via een stevige HV kabel naar het piëzo keramisch element dat ongeveer 13 cm onder het drukbestendige vat gepositioneerd is. Het piëzo keramisch element zend dan een akoestische kort signaal uit. De amplitude van de uitgezonden akoestische puls kan aangepast worden.

De SPATS sensormodule heeft drie sensorkanalen, elk 120° van elkaar gescheiden. Elk sensorkanaal bestaat uit een cylindrisch piëzo keramisch element dat direct aan een 3-stadia versterker gesoldeerd is. Het element is dan tegen de wand van het stalen drukbestendige vat gedrukt. Een tweede type sensor was ontworpen: HADES (Hydrophone for Acoustic Detection at South Pole) is een alternatieve sensor met een totaal ander dynamisch bereik en resonant gedrag

Ieder akoestisch station is verbonden met een akoestische knooppunt (Acoustic Junction Box, AJB). Dit is een robuuste aluminium doos die begraven ligt onder ongeveer 3 m sneeuw juist naast de positie van de string. Het bevat de elektronische componenten die nodig zijn voor de locale digitalisering van alle signalen. Elke AJB is verbonden via een oppervlaktekabel met een PC in het IceCube laboratorium die lokaal de data opslaat voordat het gekopieerd wordt via satelliet. Deze PC is ook verbonden met een GPS klok die instaat voor de precieze tijdsbestempeling van alle data.

Inter-string dempiinglengte

De SPATS inter-string data bestaat uit een 3 types files: ruis, sensor-string signaal en zender-string signaal. Aan de hand van deze drie files kan de energie van een bepaalde puls bekomen worden. De effectieve amplitude is gedefinieerd als de vierkantswortel van de pulsenergie.

Inter-string gelijk-niveau analyse

In een eerste instantie is er een analyse van de inter-string data uitgevoerd voor zender-sensor combinaties waarvoor de polaire hoek ten opzichte van het horizontaal vlak nul is. Aangezien er vier SPATS strings zijn, kan er met een enkele zender die gehoord wordt door de drie sensors op gelijk niveau maar op drie afstanden (dit zijn drie verschillende strings) een dempinglengtemeting uitgevoerd worden. In totaal zijn er 28 SPATS zenders, waarvan 25 deelnamen aan de inter-string dataproductie. Voor 12 zenders zijn er genoeg datapunten voor een dempinglengtemeting en het gewogen gemiddelde van alle metingen geeft voor de dempingscoëfficient $\alpha = 0.0031 \pm 0.0008 \, \text{m}^{-1}$. Indien enkel de positieve dempingscoëfficienten behouden worden voor de berekening van het gewogen gemiddelde, bekomt men $\alpha = 0.0041 \pm 0.0009 \, \text{m}^{-1}$. Dit geeft een dempinglengte van $245 \pm 54 \, \text{m}$.

Inter-string ratio analyse

Geen enkel van de in SPATS geïnstalleerde zenders of sensors zijn gekalibreerd in ijs, vandaar dat een ongekende intrinsieke gevoeligheid $\mathcal{S}_j$ of transmittiviteit $\mathcal{T}_i$ meespelen voor een enkele inter-string amplitude:

$$A_{ij} = \frac{\mathcal{T}_i \mathcal{S}_j}{d_{ij}} e^{-\alpha d_{ij}}, \tag{C.3}$$

waar A_{ij} de amplitude van de zenderpuls is, uitgezonden door zender i en gedetecteerd door sensor j en d_{ij} is de afstand tussen zender i en sensor j. Als we dan twee zender-sensor paren nemen, bijvoorbeeld zenders T_i en T_k gehoord door zowel sensor S_j als S_l, dan kan een ratio van amplitudes geconstrueerd worden:

$$\ln(\mathcal{R}_A \mathcal{R}_d) = \ln\left(\frac{A_{ij}A_{kl}}{A_{il}A_{kj}}\frac{d_{ij}d_{kl}}{d_{il}d_{kj}}\right) = -\alpha D_x + b, \tag{C.4}$$

waar $\mathcal{R}_A$ en $\mathcal{R}_d$ de ratios zijn van de amplitudes en afstanden respectievelijk. $D_x = ([d_{ij} - d_{il}] - [d_{kj} - d_{kl}])$ en b is een vrije parameter die een systematische verschuiving in y toelaat. De drie kanalen van beide sensormodules moeten voldoen aan $A > 1.5\sigma_{\text{stat}}(A)$, waar $\sigma_{\text{stat}}(A)$ de statistische fout is op de amplitude A. Dode en gesatureerde kanalen zijn uitgesloten.

Een enkele ratio zou dan theoretisch de dempingscoëfficiënt moeten opleveren indien alle zenders en sensoren een perfect isotroop gedrag hebben. Er is echter de azimutale oriëntatie van elke sensormodule die ongekend is en het zender signaal is is afhankelijk van de polaire oriëntatie. Beide effecten moeten dus geminimaliseerd en in rekening gebracht worden. Vandaar dat in de analyse enkel de zender-sensor combinaties van aangrenzende niveaus gebruikt worden: (190,250), (250, 320) and (320,400) m diepte. Dit limiteert het verschil in polaire hoek voor een amplitude ratio tot maximaal of 32°. Het maximale verschil in azimutale hoek is grofweg 120°. Daarom wordt er in deze analyse gebruik gemaakt van een gemiddelde sensoramplitude. Een 68% variatie van de gevoeligheid van de sensor en een 40% variatie in the zender wordt aangenomen. Dit geeft dan een totale onzekerheid op een enkele amplitude ratio van 160%.

Het is dus duidelijk dat een enkele ratio berekening geen nut heeft als een schatter voor de dempingscoëfficiënt. In totaal werden er 172 ratio berekend, deze ratio in functie van D_x werden dan gefit met een 2-parameter fit functie, met als resultaat voor $\alpha = 0.0040 \pm 0.0016$ m^{-1}. Dit geeft voor de dempinglengte

$$\lambda = 250 \pm 100 \, \text{m}. \tag{C.5}$$

Conclusie

SPATS was ontworpen en geïnstalleerd in het ijs nabij de geografische Zuidpool. Het geheel van de huidige experimentele resultaten hebben een impact op de haalbaarheid van een grote akoestische neutrino detector in het Zuidpoolijs:

- Geluidssnelheid.
  De SPATS resultaten voor de geluidssnelheid van de longitudinale en transversale golven zijn in overeenkomst met de theoretische voorspellingen en voorgaande experimentele data. Eenmaal dieper dan 200 m, blijven de geluidssnelheden constant. De longitudinale geluidssnelheid is 3878.3 ± 1.2 m/s en de transversale geluidssnelheid is 1975.0 ± 8.0 m/s.

Het feit dat de geluidssnelheid constant is onder 200 m zorgt ervoor dat de akoestische golven niet afbuigen als ze door het diepe ijs propageren. Dit vergemakkelijkt de reconstructie van de aankomstrichting van het neutrino. Daarboven, indien een neutrino interactie zowel longitudinale als transversale golven voortbrengt, dan kan het tijdsverschil tussen de twee golven voor een enkele sensor gebruikt worden voor het berekenen van de afstand tot de interactie.

- Achtergrondgeluid.
  Het achtergrondgeluid bestaat uit twee componenten: het continu geluid en voorbijgaande geluiden die mogelijks verkeerdelijk als neutrino signalen kunnen geinterpreteerd worden. De flux en herkomst van deze voorbijgaande achtergrondgeluiden zijn bepaald geweest door de SPATS detector. De flux is heel laag en het overgrote deel komt van gekende bronnen van menselijke makelij.

  De continue achtergrondruis is heel stabiel en de distributie is Gaussisch. De menselijke activiteit en de temperatuursschommelingen op het oppervlak hebben geen invloed op het geluidsniveau in het ijs. Op dit moment is er nog een resultaat voor het absolute niveau van de achtergrondruis.

- Attenuatielengte.
  De door SPATS gemeten dempinglengte is veel kleiner dan voorspeld. Dit heeft een grote impact op de geometrie van een mogelijke toekomstige akoestische neutrino detector aangezien de horizontale afstanden veel kleiner moeten zijn. Vandaar dat de akoestische detectietechniek minder financieel aantrekkelijk is dan verwacht.

Enkel het absolute geluidsniveau is nog niet bepaald. De dempinglengte is veel kleiner dan verwacht, mogelijks door een foutieve aanname over de korrelgrote in het ijs. Om dit verder te onderzoeken zijn er verdere metingen gepland in het komende Antarctisch seizoen.

Acknowledgements

First of all, I would like to thank my advisor, Dirk Ryckbosch, for supporting my PhD work. Not only did he offer excellent advice and guidance but, on top of that, has allowed both espresso and pingpong to provide a exquisite balance throughout the long days at the INW lab.

Many thanks are also owed to Dr. Rolf Nahnhauer, who has introduced me into the SPATS group and supported my PhD work in many ways. The SPATS group has proven to be a very invigorating work environment and special thanks are needed for all members of this dynamic group of people; Sebastian Boser, Allan Hallgren, Justin Vandenbroucke, Delia Tosi, Timo Karg, Benjamin Semburg and all the others. I have learned much from all of them in many ways and on many levels: thank you!

It was great to have the opportunity to work together with the two UGent master students, Piet Verwilligen and Filip Thyssen. They explored together the realm of interesting stuff to do with an industrial freezer, some transducers and an electron accelerator! Their research and results have given me more insight in the experimental challenge of investigating the thermo-acoustic model in water and ice.

The INW has proven to be a very pleasant work environment filled with cool, funny and interesting people. Thanks everyone for all the great moments, especially my office mates Arne Van Overloop and Tom Feusels. A special thanks goes to Hyon-Suk Jo for his help, patience, down-to-earth guidance and proof-reading carefully the entire thesis. Also thanks to Garmt de Vries-Uiterweerd for proof-reading parts of the thesis.

I also had much support from my distant friends, Sarah Goossens, Katleen de Hert, Carol Aboudib, Jeanne Edwards and Chad Carpenter. Thanks guys, for being diverting, funny, patient and understanding.

I feel indebted to the Abisko and Amundson Scott research stations and the people working in those extreme places, their hospitality has allowed for SPATS to effectively produce all results presented here. More specifically I would like to thank Tom Ham, Gary Hill, Mike Kleist, Tim Murray, Perry Sandstrom and the Raytheon support crew.

I would also like to thank the members of the reading committee (Prof. Dr. Dirk Ryckbosch (WE05), Dr. Michael Carson (WE05) and Dr. Rolf Nahnhauer(DESY, Zeuthen, Germany)) for their suggestions to improve this thesis, and the remaining members of the examination committee: Prof. Dr. J. Ryckebusch (chair), Prof. Dr. M. Grünewald (WE05), Prof. Dr. C. De Clercq (VUB), Prof. Dr. D. Botteldooren (IR05), Dr. M. Tytgat (WE05).

Thanks mum, dad, Rien and Febe for all your support!

Bibliography

[1] L. Knox, N. Christensen, and C. Skordis, "The Age of the Universe and the Cosmological Constant Determined from Cosmic Microwave Background Anisotropy Measurements," *Astrophys. J.*, vol. 563, pp. L95–L98, 2001.

[2] C. L. J. Cowan, F. Reines, F. B. Harrison, H. W. Kruse, and A. D. McGuire, "Detection of the Free Neutrino: A Confirmation," *Science*, vol. 124, p. 103, 1956.

[3] R. Davis, "Solar neutrinos. II: Experimental," *Phys. Rev. Lett.*, vol. 12, pp. 303–305, 1964.

[4] H. Becquerel, "Sur les radiations émises par phosphorescence," *Comptes Rendus*, vol. 122, pp. 420–421, 1896.

[5] J. J. Thomson, "Cathode rays," *Philosophical Magazine*, vol. 44, p. 293, 1897.

[6] T. Wulf, "About the radiation of high penetration capacity contained in the atmosphere," *Physikalische Zeitschrift*, vol. 5, pp. 152–157, 1910.

[7] A. Gockel *Phys. Z.*, vol. 11, p. 280, 1910.

[8] A. Gockel *Phys. Z.*, vol. 12, p. 597, 1911.

[9] V. F. Hess, "Messungen der durchdringenden Strahlung bei zwei Freiballonfahrten," *Wien. Sitz. Ber.*, vol. 120, pp. 1575–1585, 1912.

[10] V. F. Hess, "Beobachtungen der durchdringenden Strahlung bei sieben Freiballonfahrten," *Wien. Sitz. Ber.*, vol. 121, pp. 2001–2032, 1912.

[11] W. Kohlhorster, "Uber eine Neukonstruktion des Apparates zur Messung der durchdringenden Strahlung nach Wulf und die damit bisher gewonnen Ergebnisse," *Phys. Z.*, vol. 14, 1913.

[12] J. Bluemer, R. Engel, and J. R. Hoerandel, "Cosmic Rays from the Knee to the Highest Energies," 2009. arXiv 0904.0725.

[13] D. J. Bird *et al.*, "The Cosmic ray energy spectrum observed by the Fly's Eye," *Astrophys. J.*, vol. 424, pp. 491–502, 1994.

[14] J. W. Elbert and P. Sommers, "In search of a source for the 320 EeV Fly's Eye cosmic ray," *Astrophys. J.*, vol. 441, pp. 151–161, 1995.

[15] E. Fermi, "On the Origin of the Cosmic Radiation," *Phys. Rev.*, vol. 75, pp. 1169–1174, 1949.

[16] R. Blandford and D. Eichler, "Particle Acceleration at Astrophysical Shocks: A Theory of Cosmic Ray Origin," *Phys. Rept.*, vol. 154, pp. 1–75, 1987.

[17] A. M. Hillas, "The Origin of Ultra-High-Energy Cosmic Rays," *Ann. Rev. Astron. Astrophys.*, vol. 22, pp. 425–444, 1984.

[18] S. D. Wick, T. W. Kephart, T. J. Weiler, and P. L. Biermann, "Signatures for a cosmic flux of magnetic monopoles," *Astropart. Phys.*, vol. 18, pp. 663–687, 2003.

[19] P. Bhattacharjee and G. Sigl, "Origin and propagation of extremely high energy cosmic rays," *Phys. Rept.*, vol. 327, pp. 109–247, 2000.

[20] R. Basu and P. Bhattacharjee, "On the injection spectrum of ultrahigh energy cosmic rays in the top-down scenario," *Phys. Rev.*, vol. D70, p. 023510, 2004.

[21] T. J. Weiler, "Cosmic ray neutrino annihilation on relic neutrinos revisited: A mechanism for generating air showers above the Greisen-Zatsepin-Kuzmin cut-off," *Astropart. Phys.*, vol. 11, pp. 303–316, 1999.

[22] T. K. Gaisser, *Cosmic Rays and Particle Physics*. Cambridge, 1990.

[23] R. K. Saha, R. Majumdar, P. Pal, and D. P. Bhattacharyya, "Estimation of anti-p/p flux ratio from leaky box and closed galaxy models using CERN accelerator results on anti-p production," *Mod. Phys. Lett.*, vol. A13, pp. 1997–2011, 1998.

[24] A. Codino and F. Plouin, "The Misleading Nature of the Leaky Box Models in Cosmic Ray Physics," 2008. arXiv 0806.1346.

[25] A. D. Erlykin and A. W. Wolfendale, "The knee in the cosmic ray energy spectrum," 2009. arXiv 0906.3949.

[26] R. Abbasi *et al.*, "First Observation of the Greisen-Zatsepin-Kuzmin Suppression," *Phys. Rev. Lett.*, vol. 100, p. 101101, 2008.

[27] J. Abraham *et al.*, "Observation of the suppression of the flux of cosmic rays above 4×10^{19} eV," *Phys. Rev. Lett.*, vol. 101, p. 061101, 2008.

[28] T. Chiarusi and M. Spurio, "High-Energy Astrophysics with Neutrino Telescopes," 2009. arXiv 0906.2634.

[29] R. Aloisio, V. Berezinsky, P. Blasi, and S. Ostapchenko, "Signatures of the transition from galactic to extragalactic cosmic rays," *Phys. Rev.*, vol. D77, p. 025007, 2008.

[30] J. Belz, "Overview of recent HiRes results," *Nucl. Phys. Proc. Suppl.*, vol. 190.

[31] M. Unger *et al.*, "Study of the Cosmic Ray Composition above 0.4 EeV using the Longitudinal Profiles of Showers observed at the Pierre Auger Observatory," 2007. arXiv 0706.1495.

[32] J. Abraham *et al.*, "Correlation of the highest-energy cosmic rays with the positions of nearby active galactic nuclei," *Astropart. Phys.*, vol. 29, pp. 188–204, 2008.

[33] J. Abraham *et al.*, "Correlation of the highest energy cosmic rays with nearby extragalactic objects," *Science*, vol. 318, pp. 938–943, 2007.

[34] M. Lemoine and E. Waxman, "Anisotropy vs. chemical composition at ultra-high energies," 2009. arXiv 0907.1354.

[35] A. A. Penzias and R. W. Wilson, "A Measurement of Excess Antenna Temperature at 4080 Mc/s.," *Astrophysical Journal*, vol. 142, pp. 419–421, 1965.

[36] K. Greisen, "End to the cosmic ray spectrum?," *Phys. Rev. Lett.*, vol. 16, pp. 748–750, 1966.

[37] G. T. Zatsepin and V. A. Kuzmin, "Upper limit of the spectrum of cosmic rays," *JETP Lett.*, vol. 4, pp. 78–80, 1966.

[38] D. Hooper, S. Sarkar, and A. M. Taylor, "The intergalactic propagation of ultra-high energy cosmic ray nuclei," *Astropart. Phys.*, vol. 27, pp. 199–212, 2007.

[39] F. W. Stecker, "Photodisintegration of ultrahigh-energy cosmic rays by the universal radiation field," *Phys. Rev.*, vol. 180, pp. 1264–1266, 1969.

[40] D. Hooper, S. Sarkar, and A. M. Taylor, "Intergalactic propagation of ultrahigh energy cosmic ray nuclei: An analytic approach," *Phys. Rev.*, vol. D77, no. 10, p. 103007, 2008.

[41] I. Ribas, C. Jordi, F. Vilardell, E. L. Fitzpatrick, R. W. Hilditch, and E. F. Guinan, "First determination of the distance and fundamental properties of an eclipsing binary in the andromeda galaxy," *Astrophys. J.*, vol. 635, p. L37, 2005.

[42] P. Fouqué, J. M. Solanes, T. Sanchis, and C. Balkowski, "Structure, mass and distance of the Virgo cluster from a Tolman-Bondi model," *Astron. Astrophys.*, vol. 375, pp. 770–780, 2001.

[43] G. L. Fogli, E. Lisi, A. Mirizzi, D. Montanino, and P. D. Serpico, "Oscillations of solar atmosphere neutrinos," *Phys. Rev.*, vol. D74, p. 093004, 2006.

[44] D. V. Ahluwalia, "Ambiguity in source flux of cosmic and astrophysical neutrinos: Effects of bi-maximal mixing and quantum- gravity induced decoherence," *Mod. Phys. Lett.*, vol. A16, pp. 917–926, 2001.

[45] W. Cui, "TeV Gamma Ray Astronomy," *Res. Astron. Astrophys.*, vol. 9, pp. 841–860, 2009.

[46] R. Abbasi *et al.*, "Determination of the Atmospheric Neutrino Flux and Searches for New Physics with AMANDA-II," *Phys. Rev.*, vol. D79, p. 102005, 2009.

[47] M. Ackermann *et al.*, "Search for Ultra High-Energy Neutrinos with AMANDA-II," *Astrophys. J.*, vol. 675, p. 1014, 2008.

[48] A. Achterberg *et al.*, "First year performance of the IceCube neutrino telescope," *Astropart. Phys.*, vol. 26, pp. 155–173, 2006.

[49] E. Waxman and J. Bahcall, "High Energy Neutrinos from Astrophysical Sources: An Upper Bound," *Phys. Rev.*, vol. D59, p. 023002, 1999.

[50] J. K. Becker, "High-energy neutrinos in the context of multimessenger physics," *Phys. Rept.*, vol. 458, pp. 173–246, 2008.

[51] R. Engel, D. Seckel, and T. Stanev, "Neutrinos from propagation of ultra-high energy protons," *Phys. Rev.*, vol. D64, p. 093010, 2001.

[52] L. A. Anchordoqui, H. Goldberg, D. Hooper, S. Sarkar, and A. M. Taylor, "Predictions for the Cosmogenic Neutrino Flux in Light of New Data from the Pierre Auger Observatory," *Phys. Rev.*, vol. D76, p. 123008, 2007.

[53] T. Stanev, *High energy cosmic rays.* Springer, 2004.

[54] W. Bednarek, G. F. Burgio, and T. Montaruli, "Galactic discrete sources of high energy neutrinos," *New Astron. Rev.*, vol. 49, pp. 1–21, 2005.

[55] L. S. Sparke *et al.*, *Galaxies in the universe.* Cambridge, 2000.

[56] E. Waxman, "GRB after-glow: Supporting the cosmological fireball model, constraining parameters, and making predictions," *Astrophys. J.*, vol. 485, p. L5, 1997.

[57] E. Waxman, "Extra galactic sources of high energy neutrinos," *Phys. Scripta*, vol. T121, pp. 147–152, 2005.

[58] R. Abbasi, "Search for high-energy muon neutrinos from the naked-eye GRB 080319B with the IceCube neutrino telescope," *Astrophys. J.*, vol. 701, pp. 1721–1731, 2009.

[59] A. Loeb and E. Waxman, "The cumulative background of high energy neutrinos from starburst galaxies," *J. Cosm. Astropart. Phys.*, vol. 0605, p. 003, 2006.

[60] F. W. Stecker, "Are diffuse high energy neutrinos from starburst galaxies observable?," *Astropart. Phys.*, vol. 26, pp. 398–401, 2007.

[61] K. Mannheim, R. J. Protheroe, and J. P. Rachen, "On the cosmic ray bound for models of extragalactic neutrino production," *Phys. Rev.*, vol. D63, p. 023003, 2001.

[62] A. Achterberg *et al.*, "Multi-year search for a diffuse flux of muon neutrinos with AMANDA-II," *Phys. Rev.*, vol. D76, p. 042008, 2007.

[63] R. Fiore *et al.*, "Ultra-high energy neutrino nucleon interactions," *Phys. Rev.*, vol. D68, p. 093010, 2003.

[64] R. Gandhi, C. Quigg, M. H. Reno, and I. Sarcevic, "Neutrino interactions at ultrahigh-energies," *Phys. Rev.*, vol. D58, p. 093009, 1998.

[65] J. Kwiecinski, A. D. Martin, and A. M. Stasto, "Penetration of the earth by ultrahigh energy neutrinos predicted by low x QCD," *Phys. Rev.*, vol. D59, p. 093002, 1999.

[66] C. E. Navia, C. R. A. Augusto, H. M. Portella, and H. Shigueoka, "How opaque is the earth to ultrahigh energy neutrinos?," *Phys. Rev. D*, vol. 67, no. 10, p. 103008, 2003.

[67] H. L. Lai *et al.*, "Improved parton distributions from global analysis of recent deep inelastic scattering and inclusive jet data," *Phys. Rev.*, vol. D55, pp. 1280–1296, 1997.

[68] M. Gluck, S. Kretzer, and E. Reya, "Dynamical QCD Predictions for Ultrahigh Energy Neutrino Cross Sections," *Astropart. Phys.*, vol. 11, p. 327, 1999.

[69] J. V. Jelley, *Cherenkov radiation and its applications.* Pergamon Press, 1958.

[70] G. A. Askarian, "Excess negative charge of an electron-photon shower and its coherent radio emission," *Sov. Phys*, vol. JETP14, p. 441, 1962.

[71] C. Amsler *et al.*, "Passage of particles through matter," *Phys. Lett.*, vol. B667, 2008.

[72] J. Alvarez-Muniz and E. Zas, "EeV neutrinos," in *Proceedings of 2nd Interational Workshop on New Worlds in Astroparticle Physics*, (Faro, Portugal), 1998. astro-ph/9902187.

[73] V. Bertin and V. Niess, "Acoustic signal computations in the Mediterranean Sea," *J. Phys. Conf. Ser.*, vol. 81, p. 012019, 2007.

[74] S. Bevan *et al.*, "Study of the acoustic signature of UHE neutrino interactions in water and ice," *Nucl. Inst. Meth.*, vol. A607, no. 2, pp. 398–411, 2009.

[75] L. D. Landau and I. Pomeranchuk, "Electron cascade process at very high-energies," *Dokl. Akad. Nauk Ser. Fiz.*, vol. 92, pp. 735–738, 1953.

[76] A. B. Migdal, "Bremsstrahlung and pair production in condensed media at high-energies," *Phys. Rev.*, vol. 103, pp. 1811–1820, 1956.

[77] J. Alvarez-Muniz and E. Zas, "The LPM effect for EeV hadronic showers in ice: implications for radio detection of neutrinos," *Phys. Lett.*, vol. B434, p. 396, 1998.

[78] M. A. Markov, "On high energy neutrino physics," *Proceedings of the 1960 Annual International Conference on High-Energy Physics*, p. 578, 1960.

[79] V. S. Berezinskii and G. T. Zatsepin, "Possible experiments with very high energy cosmic neutrinos: the DUMAND project," *Sov. Phys. Usp.*, vol. 20, no. 5, pp. 361–380, 1977.

[80] R. J. Wilkes *et al.*, "DUMAND-II progress report," Presented at Conf. on Intersection between Particle and Nuclear physics, Tucson, AZ, May 24–29, 1991.

[81] A. Roberts, "The Birth of high-energy neutrino astronomy: A Personal history of the DUMAND project," *Rev. Mod. Phys.*, vol. 64, pp. 259–312, 1992.

[82] V. Aynutdinov *et al.*, "The BAIKAL neutrino experiment: Physics results and perspectives," *Nucl. Instrum. Meth.*, vol. A602, pp. 14–20, 2009.

[83] J. A. Aguilar *et al.*, "First results of the instrumentation line for the deep-sea ANTARES neutrino telescope," *Astropart. Phys.*, vol. 26, pp. 314–324, 2006.

[84] P. A. Rapidis, "The NESTOR underwater neutrino telescope project," *Nucl. Instrum. Meth.*, vol. A602, pp. 54–57, 2009.

[85] R. Arnold *et al.*, "Technical design and performance of the NEMO-3 detector," *Nucl. Instrum. Meth.*, vol. A536, pp. 79–122, 2005.

[86] P. Sapienza, "The NEMO project: Achievements and perspectives," *J. Phys. Conf. Ser.*, vol. 120, p. 062010, 2008.

[87] S. Kuch, *Design studies for the KM3NeT neutrino telescope.* PhD thesis, Erlangen, Nuremberg U., 2007.

167

[88] D. Besson, S. Boeser, R. Nahnhauer, P. B. Price, and J. A. Vandenbroucke, "Simulation of a hybrid optical / radio / acoustic extension to IceCube for EHE neutrino detection," *Int. J. Mod. Phys.*, vol. A21S1, pp. 259–264, 2006.

[89] J. F. Beacom, N. F. Bell, D. Hooper, S. Pakvasa, and T. J. Weiler, "Measuring flavor ratios of high-energy astrophysical neutrinos," *Phys. Rev.*, vol. D68, p. 093005, 2003.

[90] L. A. Anchordoqui, H. Goldberg, F. Halzen, and T. J. Weiler, "Neutrinos as a diagnostic of high energy astrophysical processes," *Phys. Lett.*, vol. B621, pp. 18–21, 2005.

[91] I. Kravchenko, "Limits on the Ultra-High Energy Electron Neutrino Flux from the RICE Experiment," *Astropart. Phys.*, vol. 20, p. 195, 2003.

[92] S. W. Barwick *et al.*, "Constraints on cosmic neutrino fluxes from the ANITA experiment," *Phys. Rev. Lett.*, vol. 96, p. 171101, 2006.

[93] J. Abraham *et al.*, "Upper limit on the diffuse flux of UHE tau neutrinos from the Pierre Auger Observatory," *Phys. Rev. Lett.*, vol. 100, p. 211101, 2008.

[94] R. Abbasi *et al.*, "An upper limit on the electron-neutrino flux from the HiRes detector," 2008. arXiv 0803.0554.

[95] N. G. Lehtinen, P. W. Gorham, A. R. Jacobson, and R. A. Roussel-Dupre, "FORTE satellite constraints on ultra-high energy cosmic particle fluxes," *Phys. Rev.*, vol. D69, p. 013008, 2004.

[96] P. W. Gorham *et al.*, "Initial results from the ANITA 2006-2007 balloon flight," *J. Phys. Conf. Ser.*, vol. 136, p. 022052, 2008.

[97] C. W. James *et al.*, "Limit on UHE Neutrino Flux from the Parkes Lunar Radio Cherenkov Experiment," *Mon. Not. Roy. Astron. Soc.*, vol. 379, pp. 1037–1041, 2007.

[98] P. W. Gorham, K. M. Liewer, R. Milincic, C. J. Naudet, D. Saltzberg, and D. Williams, "Status of Goldstone Lunar Ultra-High Energy Neutrino Experiment (GLUE)," *Part. Astrophys. Instrum.*, vol. 4858, no. 1, pp. 171–178, 2003.

[99] R. D. Dagkesamansky, A. R. Beresnyak, A. V. Kovalenko, and I. M. Zheleznykh, "The upper limit to the EHE neutrino flux from observations of the moon with Kalyazin radio telescope," *Int. J. Mod. Phys.*, vol. A21S1, pp. 142–146, 2006.

[100] C. W. James *et al.*, "Results of LUNASKA lunar Cherenkov observations at the ATCA," 2009. arXiv 0907.4332.

[101] O. Scholten *et al.*, "Status report of the NuMoon experiment," 2008. arXiv 0810.3426.

[102] H. J. A. Rottgering *et al.*, "LOFAR: Opening up a new window on the Universe," in *Proceedings of Conference on Cosmology, Galaxy Formation and Astro-Particle Physics on the Pathway to the SKA*, 2006. astro-ph/0610596.

[103] P. Allison *et al.*, "IceRay: An IceCube-centered Radio-Cherenkov GZK Neutrino Detector," 2009. arXiv 0904.1309.

[104] S. W. Barwick *et al.*, "ARIANNA: A New Concept for UHE Neutrino Detection," *J. Phys. Conf. Ser.*, vol. 60, pp. 276–283, 2007.

[105] M. Chiba *et al.*, "Measurement of attenuation length for radio wave in natural rock salt samples concerning ultra high energy neutrino detection," *Int. J. Mod. Phys.*, vol. A21S1, pp. 25–29, 2006.

[106] R. Milincic, "The status of SalSA detector," *AIP Conf. Proc.*, vol. 928, pp. 77–82, 2007.

[107] D. Saltzberg *et al.*, "Introduction to the SalSA, a saltdome shower array as a GZK neutrino observatory," *Int. J. Mod. Phys.*, vol. A21S1, pp. 252–253, 2006.

[108] D. Besson *et al.*, "Simulation of a hybrid optical-radio-acoustic neutrino detector at the South Pole," *Nucl. Instrum. Meth*, vol. A604, 2009.

[109] P. Askebjer *et al.*, "Optical properties of deep ice at the South Pole: Absorption," *Appl. Opt.*, vol. 36, pp. 4168–4180, 1997.

[110] G. A. Askarian *Atomnaya Energiya*, vol. 3, p. 152, 1957.

[111] G. A. Askarian, B. A. Dolgoshein, A. N. Kalinovsky, and N. V. Mokhov, "Acoustic detection of high-energy particle showers in water," *Nucl. Instrum. Meth.*, vol. 164, pp. 267–278, 1979.

[112] J. G. Learned, "Acoustic radiation by charged atomic particles in liquids: an analysis," *Phys. Rev.*, vol. D19, p. 3293, 1979.

[113] T. Bowen, "Sonic particle detection," *Proceedings of the 23rd ICRC*, vol. 6, pp. 277–282, 1978.

[114] L. M. Lyamshev, "Radiation acoustics," *Soviet Physics Uspekhi*, vol. 35, no. 4, pp. 276–302, 1992.

[115] H. F. Pollard, *Sound waves in solids*. Pion, 1977.

[116] L. M. Lyamshev, *Radiation acoustics*. CRC press LLC, 2004.

[117] P. B. Price, "Attenuation of acoustic waves in glacial ice and salt domes," *Journal of Geophysical Research*, vol. 164, pp. 267–278, 2006.

[118] M. J. P. Musgrave, *Crystal acoustics*. Holden-Day, 1970.

[119] L. G. Dedenko *et al.*, "Acoustic signal from neutrinos of ultrahigh-energy and background conditions for an acoustic neutrino telescope in the Ionian Sea," *Bull. Russ. Acad. Sci. Phys.*, vol. 58, pp. 2075–2077, 1994.

[120] L. R. Sulak *et al.*, "Experimental Results on the Acoustic Detection of Particle Showers," Presented at Int. Conf. on Neutrino Physics and Astrophysics, Elbrus, USSR, Jun 18-24, 1977.

[121] G. De Bonis, "Acoustic signals from proton beam interaction in water.," *Nucl. Instrum. Meth.*, vol. A604, pp. S199–S202, 2009.

[122] K. Graf *et al.*, "Testing thermo-acoustic sound generation in water with proton and laser beams," *Int. J. Mod. Phys.*, vol. A21S1, pp. 127–131, 2006.

[123] J. Stegmaier, "Optimierung akustischer Detektoren zum Nachweis hochenergetischer kosmischer Teilchen," Master's thesis, Johannes-Gutenberg-Universtät Mainz, 2004.

[124] P. I. Golubnichy, G. S. Kaljuzny, S. I. Nikolsky, and V. I. Yakovlev, "Utilization of Lasers for Modeling Acoustic Effects Arising in the Interactions of Particles with Liquids," *16th International Cosmic Ray Conference. Published by the Institute for Cosmic Ray Research, University of Tokyo*, vol. 11, p. 202, 1979.

[125] L. M. Lyamshev, "Radiation acoustics," *Moscow Izdatel Nauka*, 1987.

[126] V. B. Bychkov *et al.*, "Experimental Study of the Acoustic Field Generated by a 50 MeV Electron Beam in Water," 2006. arXiv:physics/0610241.

[127] F. Thyssen, "Akoestische detectie van leptonen in water en ijs," Master's thesis, Universiteit Gent, Belgium, 2007.

[128] W. Mondelears, K. van Laere, A. Goedefroot, and K. van den Bossche, "The Gent university 15 MeV high-current linear accelerator facility.," *Nucl. Instrum. Meth.*, vol. A368, pp. 278–282, 1996.

[129] P. Cauwels, *Modelling of bremsstrahlung phase-space parameters for the production of homogeneous and monochromatic fields.* PhD thesis, Universiteit Gent, Belgium, 2001.

[130] K. U. Ingard, *Fundamentals of waves and oscillations.* Cambridge University Press, 1988.

[131] J. Perkin, "The sensitivity of km^3 hydrophone arrays to fluxes of ultra high energy neutrinos," *Nucl. Instrum. Meth.*, vol. A604, no. 1-2, Supplement 1, pp. S193 – S195, 2009. Conference ARENA 2008.

[132] R. Lahmann *et al.*, "Deep-Sea Acoustic Neutrino Detection and the AMADEUS System as a Multi-Purpose Acoustic Array," *Nucl. Instrum. Meth.*, vol. A602, pp. 255–261, 2009.

[133] C. Richardt, G. Anton, K. Graf, J. Hossl, U. Katz, R. Lahmann, and M. Neff, "Position reconstruction of acoustic sources with the amadeus detector," *Nucl. Intrum. Meth.*, vol. A604, no. 1-2, Supplement 1, pp. S189 – S192, 2009. Conference ARENA 2008.

[134] K. G. Kebkal, R. Bannasch, O. G. Kebkal, A. I. Panfilov, and R. Wischnewski, "3D acoustic imaging applied to the Baikal Neutrino Telescope," *Nucl. Instrum. Meth.*, vol. A602, pp. 177–179, 2009.

[135] J. Vandenbroucke, G. Giorgio, and N. Lehtinen, "Experimental study of acoustic ultrahigh-energy neutrino detection," *Astrophys. J.*, vol. 621, pp. 301–312, 2005.

[136] S. Danaher, "First data from ACoRNE and signal processing techniques," *J. Phys. Conf. Ser.*, vol. 81, p. 012011, 2007.

[137] J. D. Perkin, *The Acoustic Detection of Ultra High Energy Neutrinos.* PhD thesis, University of Sheffield, 2008.

[138] P. W. Gorham, K. M. Liewer, C. J. Naudet, D. P. Saltzberg, and D. R. Williams, "Radio limits on an isotropic flux of >100 EeV cosmic neutrinos," 2001. arXiv astro-ph/010243.

[139] P. B. Price, "Attenuation of acoustic waves in glacial ice and salt domes," *J. Geophys. Res.*, vol. 111, p. B0220, 2006.

[140] R. Nahnhauer, A. A. Rostovtsev, and D. Tosi, "Permafrost: An Alternative Target Material for Ultra High Energy Neutrino Detection?," *Nucl. Instrum. Meth.*, vol. A587, pp. 29–34, 2008.

[141] N. H. Fletcher, *The chemical physics of ice*. Cambridge monographs on physics, 1970.

[142] M. Choukroun and O. Grasset, "Thermodynamic model for water and high-pressure ices up to 2.2 GPa and down to the metastable domain," *J. Chem. Phys.*, vol. 127, p. 124506, 2007.

[143] J. R. Blackford, "Sintering and microstructure of ice: a review," *J. of Phys.*, vol. D40, no. 21, pp. R355–R385, 2007.

[144] D. S. Wilkinson, "A pressure-sintering model for the densification of polar firn and glacier ice," *Journal of Glaciology.*, vol. 34 no116, pp. 40–45, 1988.

[145] N. Maeno and T. Ebinuma, "Pressure sintering of ice and its implication to the densification of snow at polar glaciers and ice sheets," *J. Phys. Chem.*, vol. 87 (21), pp. 4103–4110, 1983.

[146] J. G. Weihaupt, "Seismic and gravity studies at the South Pole," *Geophysics*, vol. 28, pp. 331–359, 1963.

[147] D. G. Albert, "Theoretical modeling of seismic noise propagation in firn at the South Pole, Antarctica," *Geophys. Res. Lett.*, vol. 25(23), pp. 4257–4260, 1998.

[148] P. B. Price *et al.*, "Temperature profile for glacial ice at the South Pole: Implications for life in a nearby subglacial lake.," *PNAS*, vol. 99, pp. 7844–7847, 2002.

[149] P. B. Price, "Kinetics of conversion of air bubbles to air hydrate crystals in antarctic ice," *Science*, vol. 267, no. 5205, pp. 1802–1804, 1995.

[150] P. B. Price, "Mechanisms of attenuation of acoustic waves in Antarctic ice," *Nucl. Instrum. Meth.*, vol. A325, pp. 346–356, 1993.

[151] D. A. Meese, P. B. Price, and J. Vandenbroucke, "Mechanisms for attenuation of 10–30 kHz acoustic waves at -51°c in glacial ice near South Pole," *J. Geophys. Res.*, 2009. In preparation.

[152] S. Boeser *et al.*, "Feasibility of acoustic neutrino detection in ice: Design and performance of the South Pole Acoustic Test Setup (SPATS)," *Proceedings of the 30th International Cosmic Ray Conference*, vol. 5 (HE part 2), pp. 1597–1600, 2008.

[153] S. Boeser *et al.*, "Feasibility of acoustic neutrino detection in ice: First results from the South Pole Acoustic Test Setup (SPATS)," *Proceedings of the 30th International Cosmic Ray Conference*, vol. 5 (HE part 2), pp. 1605–1608, 2008.

[154] B. Semburg *et al.*, "HADES - Hydrophone for Acoustic Detection at South Pole," *Nucl. Instrum. Meth.*, vol. A604, no. 1-2, Supplement 1, pp. S215 – S218, 2009. Conference ARENA 2008.

[155] J. H. Fischer, "Acoustic transducers for the South Pole Acoustic Test Setup," Master's thesis, Humboldt Universität Berlin, 2006.

[156] B. Semburg. Private communication, 2009.

[157] S. Boser, *Acoustic Detection of Ultra-High-Energy Cascades in Ice*. PhD thesis, Humboldt Universität, Berlin, 2006.

[158] S. Boeser *et al.*, "SPATS data aqcuisition overview." IceCube internal document.

[159] T. Karg. Private communication, 2009.

[160] J. Vandenbroucke. Private communication, 2009.

[161] D. Tosi, *Measurement of acoustic attenuation in South Pole ice with a retrievable transmitter*. PhD thesis, Humboldt Universität, Berlin, 2010.

[162] Hamburger Schiffbauversuchsanstalt. http://www.hsva.de/.

[163] R. Heller. Private communication, 2009.

[164] D. Tosi. Private communication, 2009.

[165] Swedish River Basin District Authorities. http://www.vattenmyndigheterna.se/ (in Swedish).

[166] Abisko Scientific Research Station, The Royal Swedish Academy of Sciences. http://www.linnea.com/~ans/ans.htm.

[167] J. Vandenbroucke, *Experimental study of acoustic ultra-high-energy neutrino detection*. PhD thesis, Berkeley University, USA, 2009.

[168] P. J. Shull, *Nondestructive evaluation: theory, techniques, and applications*. M. Dekker, 2002.

[169] F. James and M. Roos, "MINUIT: A System for Function Minimization and Analysis of the Parameter Errors and Correlations," *Comput. Phys. Commun.*, vol. 10, pp. 343–367, 1975.

[170] "The ROOT System Home Page." http://root.cern.ch/, 2008.

[171] W. H. Press, S. A. Teukolsky, W. T. Vetterling, and B. P. Flannery, *Numerical recipes*. Cambridge, 2007.

[172] R. Nahnhauer. Private communication, 2009.

[173] R. Abbasi *et al.*, "Measurement of sound speed vs depth in south pole ice for neutrino astronomy," *Submitted to Astropart. Phys.*

[174] M. Schunck. Private communication, 2009.

[175] J. Berdermann, M. Carson, and R. Nahnhauer, "Possible Acoustic Additions To A Radio UHE Neutrino Detector." IceCube internal document, 2009.